



UNIVERSITÀ
DEGLI STUDI
FIRENZE

**DOTTORATO DI RICERCA IN
*SCIENZE DELLA TERRA***

CICLO XXIX

COORDINATORE Prof. Lorenzo Rook

*Vent Opening Probability map and Pyroclastic Density
Currents hazard assessment at Somma-Vesuvio through
a multidisciplinary approach based on physical
volcanology and numerical modeling*

Settore Scientifico Disciplinare GEO/08

Dottorando

Dott. Alessandro Tadini

Tutori

Dott. Augusto Neri

Prof. Raffaello Cioni

Prof. Roberto Santacroce

Coordinatore
Prof. Lorenzo Rook

Anni 2013/2016

Abstract

This three year-long Ph.D. project focused on the following objectives: a) implementation of a database with the most significant volcanological data useful for the development of a vent opening probability map within the Somma-Vesuvio (SV) caldera; b) development of probability density maps for each volcanological dataset defined in a) and linear combination of such maps (each of them with appropriate weights assigned after an expert elicitation procedure) to obtain a first vent opening probability map with specific focus on explosive volcanism; c) field and laboratory studies of selected deposits of pyroclastic density currents (PDCs) at SV for better characterizing Total-Grain Size Distributions, invasion areas and total volumes of such PDCs; d) application of simplified physical models and numerical simulation of PDC formation and propagation using the new parameters defined in c); e) volcanic hazard assessment at SV in the case of a future reactivation of the volcano through a preliminary PDC probabilistic invasion map.

With respect to point a), it was possible to realize a database on a GIS platform (ESRI ArcGIS 10) which collects bibliographic data related to: i) distribution of volcanic vents of high magnitude/intensity eruptions (i.e. Plinian and SubPlinian I-II), for which appropriate uncertainty areas related to their positioning were also defined on the basis of geological-morphological evidences; ii) uncertainty areas related to the distribution of volcanic vents for moderately explosive eruptions (Violent Strombolian-VS to Continuous Ash Emission-AE); iii) distribution of parasitic vents related to effusive eruptions, defined after a critical review of cartographic data (including historical maps from IGM-Istituto Geografico Militare related to 1876 and 1906 years); iv) distribution of eruptive fissures related to effusive eruptions, defined after a critical review between cartographic data and historical accounts; v) distribution of deep faults obtained after the digitalization of bibliographic data related to seismic profiles and gravimetric data (54 faults in the Vesuvian area, 7 of which within the SV caldera). Moreover, this database has been integrated with the digitalization in vector format of the latest SV Geological Map.

With respect to point b), the development of density probability maps for each dataset has been performed using, as density functions, Gaussian kernels centered on single data (volcanic vent or fault). Kernel bandwidth for each dataset has been estimated considering different parameters. For what concerns the development of the first vent opening probability maps for the SV caldera in the case of a Plinian/Sub-Plinian eruption, different weights have been attributed to the above-mentioned datasets for their linear combination by using expert elicitation techniques. The result after two elicitation sessions, which involved 15 experts with different experiences and backgrounds (all of them volcanology-related), was the implementation of 3 sets of maps each of

them constituted by three maps (representing a mean value and an uncertainty range represented by the 5° and 95° percentiles) obtained with 3 different expert's pooling methods (Classical Model-CM, Expected Relative Frequency-ERF and Equal Weight-EW). Among these sets, those related to the CM method have been adopted as reference ones, since they are more suitable to capture the uncertainty of the obtained estimations. Among the most significant results obtained it is worth mentioning that: i) there is a peak of vent opening probability in correspondence of the present crater rim of the edifice; ii) there is a non-negligible (despite highly uncertain) contribution given by deep faults (even if their weight is less than 10%) ; iii) there is a cumulative probability of vent opening less than 30% located in the western part of SV caldera (Piano delle Ginestre). Other maps that have been developed have been derived considering subgroups of experts, whose members share similar backgrounds and/or experience, confirmed that, although with some differences, there is a general consensus among all the experts interviewed. Moreover, elicitation sessions highlighted that, with respect to a specific question asked to experts, the mean probability that the next Plinian or Sub-Plinian eruption could have its initial vent located outside the present outline of the SV caldera is between 6% and 10%: this non-negligible value indicates the need for future investigations. As a further development, a vent opening probability map was implemented that takes into account that the next Plinian eruption, after an initial phase of vent opening inside the caldera, results in a caldera enlargement, a common situation for all the past Plinian eruptions at SV.

With respect to point c), field and laboratory analyses have been performed with the goal of estimating the Total-Grain Size Distributions (TGSD), the volumes and the invasion areas of two PDC units (EU3pf and EU4) belonging to the AD 79 “Pompeii” eruption and one PDC lobe from the “Fg” unit of the AD 472 “Pollena” eruption (the “Cupa Fontana” lobe) which could be employed in the following studies of physical modelling. These units and lobes have been chosen since they are representative of two end-members the vast spectrum of possible PDCs, a more dilute one (EU3pf and EU4 units) and a denser one (Fg unit). To this purpose, two field work sessions expanded the vast database of granulometric analyses which helped in the calculation of the TGSD of the EU3pf and EU4 units; with respect to the Fg “Cupa Fontana” PDC lobe instead, bibliographic data related to several samples collected and measured stratigraphic sections allowed, also in this case, to calculate the three above-mentioned parameters (maximum runout, volume and TGSD). Quantitative estimations of maximum runouts and total volumes (and partially for the TGSD estimations) have been also performed for all the units/lobes. Moreover, the samples collected and the measured stratigraphic sections allowed to formulate several hypotheses related to the type of collapse (asymmetric versus axisymmetric collapse) and a possible influence exerted by

the wind which influenced PDC propagation. Finally, an approximate reconstruction of SV morphological appearance prior to the AD 79 eruption (related to the caldera area) has been performed: this reconstruction has been employed as input data for numerical simulations.

With respect to point d), progress was made on validation of simplified physical models using as input data the estimations of maximum runout, volume and TGSD measured for the above-mentioned PDC units/lobes. The two models tested were the Box-Model and TITAN2D. The first one is a model with a kinetic approach, which approximates mass conservation through equal area geometrical elements (boxes in 2D and cylinders in 3D) and calculates the kinetic energy at the flow front comparing it with the potential energy needed to overcome topographic obstacles. The code has a dam-break configuration and combines three equations which describe the conservation of momentum, the conservation of mass and particle sedimentation (according to the Stoke's law). This code has been employed to reproduce more dilute PDCs (concentration of solid particles from 0.5% to 5% in volume, EU3pf and EU4 units) with different configurations, that is considering polydisperse cases (with 10 granulometry classes from the TGSD estimations), monodisperse cases (with a single granulometry class corresponding to the $Md\phi$), axisymmetric collapses and asymmetric collapses; direct versions of the code (simulation starting from an initial volume) and inverse versions of the code (simulation starting from a value of invasion area) have been employed as well. The TITAN2D code instead is a depth-averaged approach which solves shallow-water equations with Coulombian constitutive equations. The code was employed to simulate denser PDCs (solid particles concentration >10% in volume), Fg "Cupa Fontana" PDC lobe) by considering a flux source with a continuous feeding of material for a fixed amount of time. Validation was performed i) from the point of view of the degree of overlapping between the inundation area given by the model and the one from the real deposit, ii) from the point of view of the comparison between the variation of the thickness of the model and the thickness of the real deposit from the vent area with increasing distances and iii) from the point of view of the comparison between the weight percentage of coarse versus fine particles in the model output and in the real deposit at specific distances from the vent area. The validations allowed estimation of the input parameters on which there is the highest degree of uncertainty (the initial concentration of solid particles and the settling velocities of the different particles) for which the Box-Model in its simpler formulation (monodisperse inverse version) is capable of reproducing in a satisfactory way at least the order of magnitude of the inundation area of the EU4 unit (representative of a Plinian-like eruption at SV). From the point of view of the TITAN2D code instead, it has been assessed how this code is capable to capture at least the general trend of a real deposit (from the point of view of inundation area and thicknesses): however, at this stage this code has now been employed

for the definition of PDC probabilistic invasion maps from the point of view of the more dense-like part of PDCs.

Finally, with respect to point e), thanks to the above-mentioned parameters (EU4 unit, monodisperse inverse code), it was possible to produce a preliminary PDC probabilistic invasion map for a specific scenario (Plinian eruption, axisymmetric collapse with no wind) at SV. This map takes into account the uncertainty related to vent position (defined by the set of maps from point b) and the uncertainty linked to invasion areas (defined for the EU4 unit – point c). Despite this is a very specific scenario which has low probability of occurrence for the next eruption at SV, still this preliminary map represents a first attempt for volcanic hazard assessment from the point of view of PDC invasion for the Vesuvian area and a quantitative estimation of the sources of uncertainty which might influence the final result.

The results obtained with this project might also be easily applied to other volcanic context since it provides procedures for: a) the development of a probabilistic vent map for a caldera-forming volcano through fusion of multiple datasets and expert elicitation; b) the development and application of methods for volume and total grain size distribution from PDC deposits; c) an integrated use of dense and dilute PDC models and validation against field data. This study provides moreover a contribution to the volcanic hazard assessment from the point of view of PDC inundation areas by identifying different types of column collapse scenarios and possible developments of PDC probabilistic invasion maps that take into account such scenarios.

Table of contents

Abstract	ii
Table of contents	1
Acknowledgements	5
1. Introduction	7
1.1 Overview of the project	7
1.2 The Somma-Vesuvio area	10
<i>1.2.1 Tectonic setting</i>	10
<i>1.2.2 Eruptive history of SV</i>	11
1.3 Pyroclastic Density Currents	14
<i>1.3.1 General features</i>	14
<i>1.3.2 Transport mechanism and sedimentation</i>	16
<i>1.3.3 PDC deposit features</i>	18
1.4 A geo-database for Somma-Vesuvio	21
1.5 Vent Opening Probability maps for Somma-Vesuvio	22
1.6 From field data to numerical modeling: reconstructing key input parameters from eruptive units for model validations	23
1.7 Application of numerical models using field data	24
1.8 Pyroclastic Density Currents invasion maps	25
2. A geo-database for Somma-Vesuvio	26
2.1 Introduction	26
2.2 The geo-database and its properties	27
2.3 Uncertainty description and quantification	29
2.4 The datasets	31
<i>2.4.1 Geological mapping and caldera information</i>	31
<i>2.4.2 Vent location of large-medium scale explosive eruptions</i>	32
<i>2.4.3 Vent location of small scale explosive eruptions</i>	34
<i>2.4.4 Vent location of effusive eruptions</i>	36
<i>2.4.5 Deep Faults</i>	43
2.5 Concluding remarks	44
Appendix A: analysis of epistemic uncertainties for parasitic vents	46
Appendix B: analysis of epistemic uncertainties for eruptive fissures	49
3. Vent Opening Probability maps for Somma-Vesuvio	56
3.1 Introduction	56
3.2 Methods	59
3.3 Data sets description and associated spatial density distributions	60

3.3.1 Vent location of large-medium scale explosive eruptions	60
3.3.2 Small scale explosive eruptions	62
3.3.3 Effusive eruptions	63
3.3.4 Deep Faults	65
3.4 Results	67
3.4.1 The weights of the variables considered.....	67
3.4.2 Sensitivity of variable weights to group composition	71
3.5 Vent opening probability maps	71
3.5.1 Probability distribution within the caldera boundary	71
3.5.2 Vent position during caldera enlargement	74
3.6 Discussion	77
3.6.1 Expert elicitation procedure, scoring methods and vent opening probability maps	77
3.6.2 Implications for volcanic hazard assessments	78
3.7 Concluding remarks	80
Appendix A: kernel density estimations	81
Appendix B: experts' pooling methods	82
4. From field data to numerical modeling: reconstructing key input parameters from eruptive units for model validations	85
4.1 Introduction	85
4.2 The Pompeii and Pollena eruptions	86
4.2.1 The AD 79 “Pompeii” eruption.....	86
4.2.2 The AD 472 “Pollena” eruption	92
4.3 Methods	95
4.3.1 Maximum runout.....	95
4.3.2 Volume estimation	96
4.3.3 Total Grain Size Distribution (TGSD).....	98
4.3.4 Reconstruction of paleotography.....	99
4.4 Results	100
4.4.1 Maximum runout for the EU3pf and EU4 units and for the Fg “Cupa Fontana” lobe	100
4.4.2 Volume estimation for the EU3pf and EU4 units and for the Fg “Cupa Fontana” lobe.....	104
4.4.3 TGSD for the EU3pf and EU4 units and for the Fg “Cupa Fontana” lobe.....	112
4.4.4 Paleotopography before the AD 79 “Pompeii” eruption and before the AD 472 “Pollena” eruption.....	122
4.5 Discussion	124

4.5.1 Maximum runouts	124
4.5.2 Volume estimations	126
4.5.3 TGSD estimations	128
4.6 Conclusions	132
5. Application of numerical models using field data.....	134
5.1 Introduction	134
5.2 Numerical modeling of PDCs	135
5.2.1 The Box-model code	137
5.2.2 The TITAN2D code	139
5.2.3 Numerical modeling of PDCs at Somma-Vesuvio	141
5.2.4 Model validations with field data	144
5.3 Numerical simulations and validations	145
5.3.1 Choice of input parameters	145
5.3.2 Box-Model simulations	150
5.3.3 TITAN2D simulations	158
5.4 Discussion	162
5.4.1 Box-Model simulations	162
5.4.2 TITAN2D simulations	166
5.5 Conclusions	169
Appendix A: derivation of Shallow water equations from Navier-Stokes equations.....	171
Appendix B: the Box-Model equations.....	175
Appendix C: the TITAN2D equations.....	177
6. Pyroclastic Density Currents invasion maps	180
6.1 Introduction	180
6.2 Methods	181
6.3 Results and Discussion	181
6.3.1 Input parameters.....	181
6.3.2 PDC invasion map.....	182
6.4 Conclusions	185
7. Conclusions	187
7.1 Main conclusions and achievements	187
7.2 Open questions and future perspectives.....	189
8. Supporting information	192

8.1 Accessory datasets for SV geo-database	192
8.1.1 <i>Dikes or tabular intrusions</i>	192
8.1.2 <i>Subsurface faults/lineaments</i>	194
8.1.3 <i>Seismic activity</i>	195
8.1.4 <i>CO₂ emissions</i>	197
8.2. Expert elicitation	200
8.2.1 <i>First questionnaire: outcomes and preliminary maps</i>	200
8.2.2 <i>Second questionnaire: outcomes and definitive results</i>	204
8.2.3 <i>Maps obtained with different scoring methods (CM, ERF and EW methods)</i>	208
8.2.4 <i>Sub-groups of experts (CM and EW methods): elicited values</i>	209
8.2.5 <i>Sub-groups of experts (CM method): different maps</i>	211
8.2.6 <i>Maps obtained without the “Deep faults” dataset (CM and EW methods)</i>	212
8.2.7 <i>Maps obtained considering caldera enlargements in case of a Plinian eruption only</i>	213
8.3 Maximum runout for PDCs from the Avellino eruption, the AD 472 Pollena eruption and the AD 1631 eruption	214
8.3.1 <i>Avellino</i>	214
8.3.2 <i>Pollena</i>	215
8.3.3 <i>AD1631</i>	216
8.4 Sections used for volume and TGSD estimations	218
8.4.1 <i>EU3pf</i>	218
8.4.2 <i>EU4</i>	228
8.4.3 <i>Fg “Cupa Fontana”</i>	239
8.5 List of samples used for TGSD estimation	240
8.5.1 <i>EU3pf</i>	240
8.5.2 <i>EU4b</i>	244
8.5.3 <i>EU4c</i>	246
8.5.4 <i>Fg Cupa Fontana</i>	246
References	247

Acknowledgements

This PhD project which I worked on for three years features the contributions, support and advises of many people which I would like to thank warmly. First of all, this work has been partially supported by the project V1 “Stima della pericolosità vulcanica in termini probabilistici” funded by Dipartimento della Protezione Civile (Italy). Dr. Marco Bocci and Dr. Mauro Papucci from Istituto Geografico Militare (IGM) are greatly acknowledged for kindly allowing the consultation of the IGM archive for the retrieval of historical maps for the Somma-Vesuvio area. Dr. Giuseppe Vilardo (INGV-OV, Naples, Italy) and Dr. Domenico Granieri (INGV-PI, Pisa, Italy) are acknowledged for providing some of the datasets described in the present thesis. Special thanks go to Dr. Lucia Gurioli (Blaise Pascal University, Clermont-Ferrand, France) and Dr. Maurizio Mulas (Universidad de Guayaquil, Guayaquil, Ecuador) for allowing the employment of their field data related to Somma-Vesuvio Eruptive Units. A huge thank goes to two people in particular: Marina Bisson from INGV-PI (who helped me in learning basic and advanced functions in the Geographical Information Systems world, participated in the Expert Elicitation and constantly and kindly advised me during this long three years) and Andrea Bevilacqua from Scuola Normale Superiore Pisa (who allowed me to use a revised version of the Box-Model code developed during his PhD project, participated in the Expert Elicitation procedure as facilitator and generously dedicated a lot of his time helping me in creating some of the fundamental results of this thesis). Tomaso Esposti Ongaro (INGV-PI) is also greatly acknowledged for providing an updated version of the Box-Model code for model validations, for all the numerous advices and discussions about the basics of numerical modeling and the outputs of the simulations and for participating into the Expert Elicitation procedure. I would like to thank all the people who participated in the elicitation procedure, that is: Willy Aspinall (who participated as facilitator), Roberto Isaia, Francesco Mazzarini, Greg Valentine, Stefano Vitale, Peter Baxter, Antonella Bertagnini, Matteo Cerminara, Mattia De’ Michieli Vitturi, Alessio Di Roberto, Samantha Engwell, Franco Flandoli and Marco Pistolesi. Greg Valentine is also greatly acknowledged for all the support and advises provided during my stay at the University at Buffalo and for allowing me to participate in a wonderful field trip in Southwestern USA. From the University at Buffalo I would also like to thank Dr. Abani Patra, Dr. Marcus Bursik, Ali Akhavan Safaei and Renette Jones for the big support provided while trying to learn how to use the TITAN2D code.

Finally, this project which I worked on for three years, would have not been possible without my advisors (Dr. Augusto Neri, Prof. Raffaello Cioni and Prof. Roberto Santacroce) who strongly supported myself and strengthened my passion for volcanology.

Last but not least, I would really like to dedicate this thesis to three people in particular: my parents (Cristina and Luigi), who always truly believed in my skills and allowed me, through their teachings and their model, to become the person that I am today; Giulia, who is always (and I hope will always be) next to me sharing happy moments and constantly warming my heart.

Chapter 1

Introduction

1.1 Overview of the project

The area of the Campania region near the city of Naples (Fig. 1.1) is worldwide famous for its natural landscapes (Gulf of Napoli, gulf of Pozzuoli and the Sorrentina Peninsula among others) but it is also well-known for all the volcanoes (Somma-Vesuvio-SV, Campi Flegrei and Ischia) that constantly threatens all the inhabitants living on their feet.

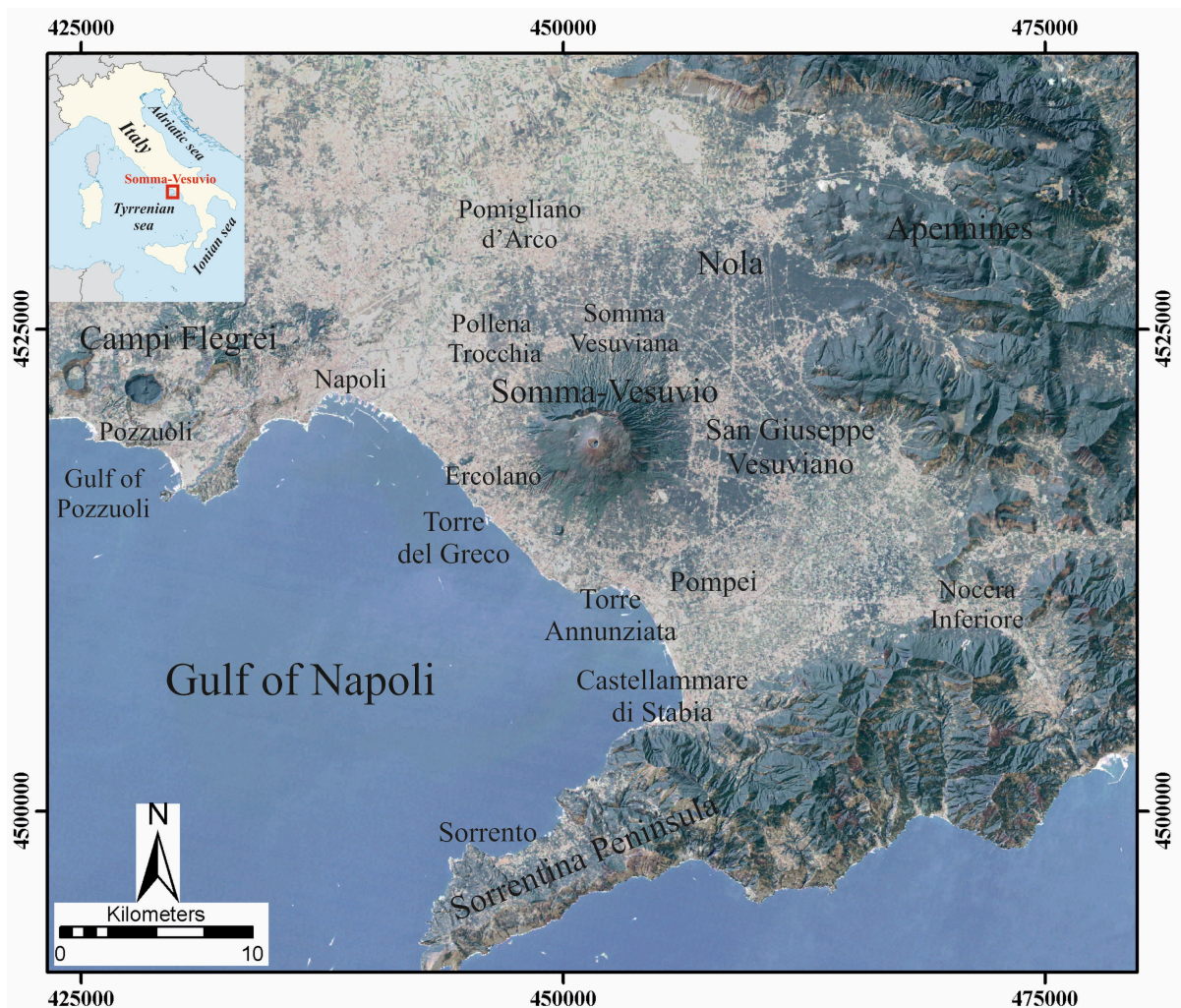


Fig 1.1: landsat image of the SV area with highlighted some of the localities cited in the text . Coordinates are expressed in the UTM WGS84 33N system.

The strategic position of this area, coupled with good climate conditions and extremely fertile soils (due to the high amount of volcanic material), have always favored the development of human settlements. Due to the high amount of potentially hazardous phenomena linked to volcanic eruptions, the Neapolitan area has been long hit by catastrophic events: besides the already mentioned eruption of AD 79 (which destroyed Pompeii, Herculaneum and Stabiae), other significant and catastrophic eruptions of SV hit the area, like the AD 472, AD 1631 (the latter one causing more than 4,000 deaths; Rosi et al. 1993). Moreover, the effusive/explosive activity of SV which characterized the period 1631-1944, caused several damages to the buildings and the infrastructures of the area. Notwithstanding this actual source of risk, the present state of repose since 1944 has allowed a massive growth of population around the flanks of SV, which now presents scientists and decision makers with a major challenge (Baxter et al. 2008). As in fact shown by Zuccaro et al. (2008), the potential consequences of even a sub-Plinian eruption at SV (one of the most probable next eruptive event at SV according to Neri et al. 2008), due to the structural and social vulnerability of the area, could be extremely severe.

For all of these reasons, SV is constantly monitored and emergency planning in the case of a future reactivation of SV has been periodically updated (DPC 1995, 2014), taking advantage of the considerable amount of studies aimed at unraveling the behavior and the stratigraphy of the SV volcano. A key aspect of volcanic hazard that need to be carefully evaluated is the one related to the probability on invasion of Pyroclastic Density Currents (PDC), one of the most destructive phenomena linked to volcanic eruptions. Presently, several studies have described qualitatively some potential inundation area of PDCs (Sheridan and Malin 1983; Rossano et al. 1998; Esposti Ongaro et al. 2008) and a “Red Zone” (i.e. an area that will be surely invaded by PDC during an eruption, and that need to be completely evacuated) has been drawn for the SV area, considering a sub-Plinian-like eruption as the maximum expected event (DPC 2014). However, a quantitative PDC probabilistic invasion map for SV (that takes advantage of the latest, well-established numerical models of PDCs) has been only partially developed (Tierz et al. 2016), despite this tool could be extremely useful for civil protection authorities. Such an approach has been pursued by Bevilacqua (2016), who developed a PDC invasion map for the Campi Flegrei volcano where the quantification of the uncertainties of the most important variables (vent position variability and PDC inundation area being the most important) have been explicitly accounted for. This project largely adopt the same approach (although with some important

differences) and aims at partially filling the gap at SV, trying to evaluate all the possible variables and to quantify all the sources of uncertainties that could affect the final product.

In order to present the results of this Ph.D. project, this thesis collects in this first introductory Chapter a review of the SV area (both from a tectonic and eruptive history point of view) and of some key aspects of PDCs, along with a brief summary of all the main achievements of the project itself. The following Chapters instead will describe in detail all the main research topics of the thesis, which are: a) the organization of geological information suitable for creating a vent opening probability map into a Geo-Database with the quantification of epistemic uncertainty for each dataset (Chapter 2); b) the development of a vent opening probability map for the SV caldera in the case of a Plinian or sub-Plinian I eruption, derived after the linear combination of Probability Density Function for each of the datasets described in the previous Chapter with a Structured Expert Judgment (SEJ) procedure for defining weights assigned to each dataset (Chapter 3); c) the collection of new field data and their integration with other field data from previous works (Cioni R., Gurioli L. and Mulas M., unpublished) in order to reconstruct key eruptive parameters (maximum runouts, volumes and Total Grain Size Distributions) for some eruptive units and PDC lobes (from the AD 79 and the AD 472 eruptions) that could be used as input parameters for numerical modeling (Chapter 4); d) the application of two simplified numerical models (the Box-Model and the TITAN2D codes) using as input parameters the data described in the previous Chapter (Chapter 5); e) the development of the first preliminary PDC probabilistic inundation map, targeted to a specific scenario and which considers all the possible sources of uncertainty described in the previous Chapters, integrated with the vent opening probability map for the SV caldera (Chapter 6). Finally, Chapter 7 presents the main conclusions and achievements of this project along with possible future developments, while Chapter 8 collects several supporting information which help in the PDC hazard assessment for the SV area.

1.2 The Somma-Vesuvio area

1.2.1 Tectonic setting

The SV volcanic complex lies in the Campanian plain (Fig.1.2a), a structural depression of Plio-Quaternary age filled with marine, alluvial and volcanic sediments of Early Pleistocene-Holocene age laying over a variously dissected Mesozoic carbonate basement (limestones and dolostones) (Bianco et al. 1998; Bruno et al. 1998; Brocchini et al. 2001). Crustal thickness varies between 25 km in the Campi Flegrei area to 35 km in the SV area (Locardi and Nicolich 1988; Ferrucci et al. 1989).

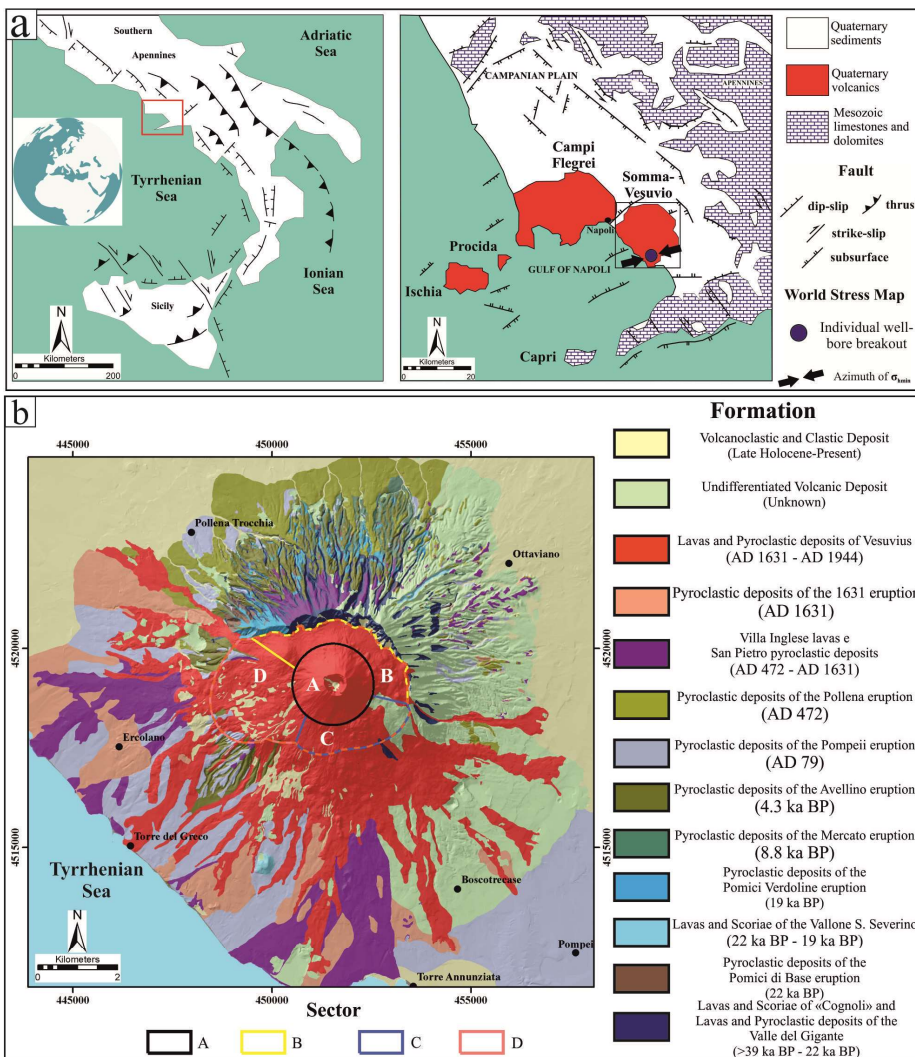


Fig.1.2: a) Morphostructural sketch of southern Italy and Campanian plain with highlighted the most important tectonic features (redrawn after Bianco et al. 1998) and World Stress Map data (Heidbach et al. 2008); b) Geological units of Somma-Vesuvio volcanic complex (Santacroce and Sbrana 2003). SV caldera (outlined in dark orange dashed line) and caldera sectors as defined in Section 2.4.1.

Gravimetric data (Finetti and Morelli 1974; Berrino et al. 1998) suggests that in the Vesuvian area the carbonate basement is about 11 km thick, with the top at a depth of 2 km (as also confirmed by the results of the geothermal drilling Trecase 1, on the southern lower slopes of the volcano; Cassano and La Torre 1987).

Tectonic structures affecting the Campanian plain consist of NW–SE/NNW–SSE and NNE–SSW/NE–SW trending faults with normal to sinistral movements for the NW–SE-trending faults, and normal to dextral for

the NE–SW-trending structures (Fig. 1.2a), in agreement with the NNE-SSW orientation of the σ_{Hmin} axis of the regional stress field (Hippolyte et al. 1994; Bianco et al. 1998). This trend of regional σ_{Hmin} is also confirmed, although only from a single analysis of an individual well-bore breakout of “C” quality (Fig. 1.2a), from World Stress Map Data (Heidbach et al. 2008), which indicates σ_{Hmin} oriented NE-SW (N76°). E-W faults with normal component of movement are recognized also in the area of SV caldera (Bianco et al. 1998).

Movements of faults in the SV area are mostly related to the regional stress field, although a local stress field (ESE-WNW trending σ_{Hmin}), linked to fault reactivation processes, has been proved responsible for second-order movements of faults (Bianco et al. 1998). Shear-wave splitting analysis performed at SV revealed that NW-SE discontinuities (faults and fractures) might extend down to at least 6 km depth and may thus represent the main group of structural discontinuities that affect the volcano.

The asymmetric shape of the western slope of SV has been variably interpreted by the different authors. Ventura et al. (1999) and Milia et al. (2007; 2012) attributed this to several flank failures that occurred in association with major Plinian eruptions. Such failures could have eventually modified the shallow plumbing system of SV so that effusive activity of Mount Somma changed to a more explosive nature after the oldest Plinian eruption of SV (“Pomici di Base” Plinian eruption; Ventura et al. 1999). However, recent stratigraphic data from a borehole drilled SW of SV volcanic edifice (Di Renzo et al. 2007) excludes the presence of debris avalanche deposits related to flank collapses, at least in the last 20 ka, while Sulpizio et al. (2008) rebutted the interpretations of Ventura et al. (1999) and Milia et al. (2007) on the grounds of stratigraphic inconsistencies between the suggested age of collapses and the primary deposits still present inside the inferred collapsed area.

1.2.2 Eruptive history of SV

The SV is a composite volcano with an old edifice (Mount Somma) dissected by multiple summit caldera collapses (Cioni et al. 1999). A stratocone grew discontinuously inside the summit caldera after the *AD 79 Pompeii* Plinian eruption, and the present cone (Vesuvio or Gran Cono) is related to the activity after the *AD 1631* sub-Plinian I eruption. SV activity has been reconstructed in

several papers, including Cioni et al. (2008), who also suggested the classification scheme used in the following.

Volcanic activity of SV complex began after the Campanian Ignimbrite eruption of Campi Flegrei (39 ka BP) and continued up to AD 1944, with periods of quiescence alternating with periods of intense explosive and effusive activity. The eruption of 1944 marked the transition from an ‘open conduit’ condition, which characterized the activity of SV in the period 1631-1944, to the present quiescent state. Recent tomographic investigations of the SV substratum (Auger et al. 2001; Iuliano et al. 2002; Scarpa et al. 2002; Zollo et al. 2002; Del Pezzo et al. 2006) have a) evinced the presence of a high-velocity anomaly below the crater area, b) discounted the presence of large magma bodies (volume bigger than 0.1-0.2 km³) within the shallowest 5 km of depth and c) suggested the presence of a regionally wide magma reservoir at the depth of 8-10 km.

Mount Somma activity (from 39 up to 22 ka BP) has been prevalently effusive, producing a thick pile of thin lava flows interbedded with spatter and cinder deposits (Fig. 1.2b). Conversely, starting from the *Pomici di Base* eruption (22 ka BP; Fig. 1.2b), at least four high-magnitude Plinian eruptions (i.e. *Pomici di Base*, *Mercato*, *Avellino* and *Pompeii*) occurred, interspersed by three major sub-Plinian I eruptions (*Greenish Pumices*, *Pollena* and *AD 1631*), three minor sub-Plinian II eruptions (*AP1*, *AP2* and *AD 512*) and several minor events, characterized by a quite large range of magnitudes and intensities, falling in the categories of Violent Strombolian and Continuous Ash Emission eruptions (see Cioni et al. 2008, for further details).

Plinian eruptions approximately range in magnitude between 1 and 5 km³ of deposits, and in intensity between 10⁷-10⁸ kg/s. They are characterized by widely dispersed fallout tephra sheets (less than 2,000 km² covered by 10 cm of deposit: Cioni et al., 2008) and variable thicknesses (up to 35 m) of pyroclastic density current (PDC) deposits dispersed up to a maximum distance of about 20 km (Gurioli et al. 2010). Each of the four Plinian eruptions resulted in a caldera collapse that contributed to the present asymmetric shape of the SV polyphased caldera (Cioni et al. 1999). The length of the quiescence preceding each Plinian eruption decreased with time; conversely, the activity became more and more frequent at least starting from about 4 ka (following the *Avellino* eruption), while generally decreasing its intensity (Cioni et al. 2008).

Sub-Plinian I eruptions approximately range in magnitude between 0.1 and 1 km³, with intensities of 10⁷ kg/s as order of magnitude. Similar in character to Plinian eruptions, they have mainly

dispersed tephra fallout sheets (less than 1,000 km² covered by 10 cm of deposit in each eruption) and PDC deposits (up to 20 m thick), spread up to a maximum distance of about 8-10 km from the vent (Gurioli et al. 2010). Plinian and sub-Plinian I PDC deposits crop out in the different sectors of the edifice and its apron (Fig. 1.2b), showing variable dependence on pre-existing topography (Santacroce and Sbrana, 2003). Only the PDC deposits of the 1631 Sub-Plinian I eruption do not crop out along the northern sector of Mt. Somma.

Sub-Plinian II eruptions (*API*, *AP2*, and *AD 512*) range in magnitude between 10⁻² and 10⁻¹ km³ and in intensity between 10⁶ and 10⁷ kg/s (Andronico and Cioni, 2002; Cioni et al. 2011). Deposits from these eruptions are represented by relatively small tephra sheets (less than 400 km² covered by 10 cm of deposit) and minor, thin PDC beds, deposited only within 2-3 km around the vent.

Violent Strombolian (VS) eruptions, with approximate magnitude of 10⁻³-10⁻² km³ and intensity of 10⁵-10⁶ kg/s, are associated with lapilli and ash fallout deposition and minor avalanching of hot materials, mainly confined to the slopes of the cone (e.g. 1822 and 1944 eruptions). Continuous Ash Emission (AE) eruptions (e.g. *AP3*, 4 and 5, several events of Middle Age activity, 1794, 1660) - with magnitudes up to 10⁻² km³ and intensities <10⁵ kg/s - resulted in the deposition of sequences (from few centimeters up to several decimeters thick) of ash deposits interlayered with minor lapilli beds. The most important feature of this latter type of activity is its prolonged duration (from weeks to months) (details in Cioni et al. 2008 and Barsotti et al. 2015).

Effusive activity at SV, except for the Mount Somma lavas, apparently has been mostly confined during the last 1000 years of activity (Arrighi et al. 2001; Cioni et al. 2008; Scandone et al. 2008), and has been especially intense following the AD 1631 eruption. Effusive activity could have occurred also during other inter-plinian periods, confined to the progressively enlarged and deepened caldera structure. During the period of semi-persistent activity between 1639 and 1944, a total of 99 eruptions occurred (sometimes predominantly effusive but very often accompanied with Strombolian to Violent Strombolian activity), each separated by an average of 3-4 years repose period but none exceeding 7 years (Arrighi et al. 2001; Scandone et al. 2008). Other periods of mild Strombolian to effusive activity occurred between the *Pompeii* Plinian eruption and the *Pollena* sub-Plinian I eruption (S. Maria cycle: Cioni et al. 2008) and discontinuously after the *AD 512* sub-Plinian II eruption up to *AD 1139* (Cioni et al. 2008; Scandone et al. 2008).

The Somma-Vesuvio products (Cioni et al. 2008; Santacroce et al. 2008) are mostly Potassic (trachytes and latites erupted in the period from the *Pomici di Base* to the *Greenish Pumices*) to K-rich in composition (phonolites to phonotefrites/tefriphonolites for the following period), exhibiting a wide variability from nearly silica-saturated to strongly silica-undersaturated. The degree of both silica undersaturation and alkali contents increased with time: the products of the last 2 ka of activity (following the AD 79 Pompeii eruption) show the most alkali-rich compositions and the lowest SiO₂ content of the whole set of erupted products (Santacroce et al. 2008).

For a complete review of the compositional features of SV volcanic products, which is beyond the scope of this study, please refer to Cioni et al. (2008), Santacroce et al. (2008) and references therein.

1.3 Pyroclastic Density Currents

1.3.1 General features

Pyroclastic Density Currents (PDC) are among the most amazing and devastating natural phenomena (Fig.1.3), whose complex mechanisms of generation, transport and deposition (despite still partly not understood) have been deeply investigated over the past decades. This sub section is not intended to provide a complete description of all the features of this phenomena, which would imply a dedicated project and for which excellent reviews already exists (Branney and Kokelaar 2002; Sulpizio et al. 2014). It is rather more useful to the purposes of this project to provide a general overview of PDCs features focusing on some key aspects that will be discussed throughout the text.

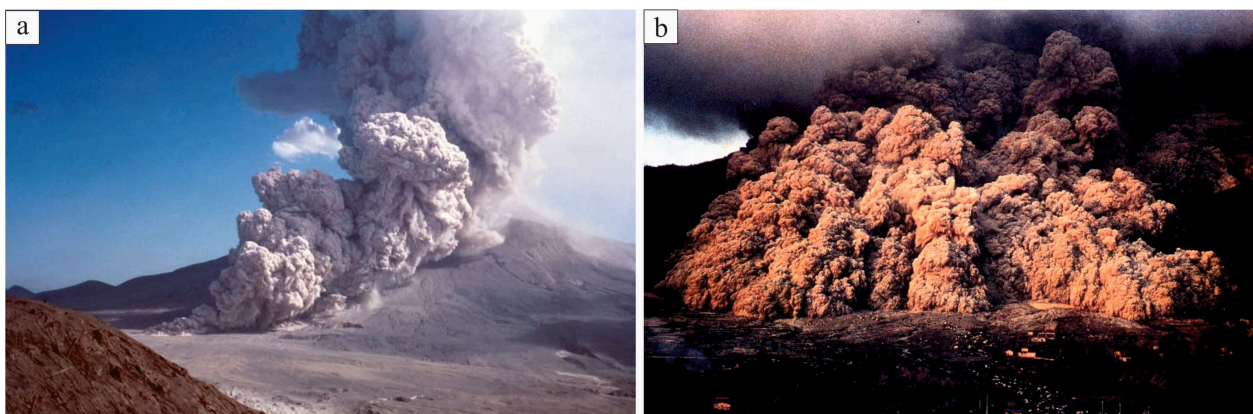


Fig.1.3: two examples of Pyroclastic Density Currents (PDC) from a) the August 7, 1980 Mt. S. Helens (USA) eruption (photo courtesy P.W. Lipman, USGS) and b) the June 3, 1991 Mt. Unzen (Japan) dome collapse (photo courtesy Nagasaki Photo service).

PDCs are multiphase currents that move across the landscape under the effect of gravity. They macroscopically can be seen as a system composed of a denser mixture of pyroclastic particles (pumices, scoriae and loose crystals) and gas immersed in a less dense, almost isotropic fluid (the atmosphere). Traditionally (Sparks 1976), these phenomena have been subdivided into two distinct groups, the high-particles concentration “Pyroclastic flows” and the low-particles concentration “Pyroclastic surges”. However, numerous field data have shown that many deposits could not be linked univocally to one of these two groups, since lithofacies associations from single deposits describe depositional mechanisms ascribed to both of them. Several authors over the past years (Cas and Wright 1987; Valentine 1987; Druitt 1992; Wilson and Houghton 2000; Branney and Kokelaar 2002; Sulpizio et al. 2014) have therefore rejected this simple categorization, proposing the more general term of “Pyroclastic Density Currents” that encloses a natural continuum between two end members, dilute (fluid-dominated) and concentrated (solid-dominated) PDCs. These two end-members have been termed by Branney and Kokelaar (2002), “Fully-dilute PDCs” (where particles are supported mainly by fluid turbulence throughout the whole current) and “Granular fluid-based PDCs” (where particle concentration is sufficiently high in the basal part for grain-grain interactions and fluid escape to be the dominant support mechanisms) respectively. This terminology (used throughout this manuscript) has the advantage of being directly related to transport processes, also retrievable from lithofacies analysis of the related deposits.

PDCs are mostly non-uniform (i.e. with high spatial variability of their features), unsteady to quasi-steady (i.e. temporally variable to quasi-stable) phenomena (Branney and Kokelaar 2002) that can be short (few minutes) to relatively long-lived events (up to 10^4 - 10^5 s for larger ignimbrites; Bursik and Woods 1996); velocities of PDCs can vary from 10 to 300 m/s (Gurioli 1999). Volume estimations for PDC flow units (see section 4.3.2) have yielded highly variable values, ranging from less than 1 km³ (Gurioli 1999; Sulpizio et al. 2005) up to several hundreds and even thousands of km³ (Bachmann and Bergantz 2003; Cook et al. 2016) for larger ignimbrites sheets.

Propelling forces for PDCs mobility derive from either magmatic or phreatomagmatic magma fragmentation (Cas and Wright 1987; Carey 1991; Branney and Kokelaar 2002). PDCs can be triggered from various explosive volcanism phenomena, including: a) total or partial collapse of a sustained (Plinian/sub-Plinian; Fig.1.3a) or transient (Vulcanian) eruptive column (Gurioli 1999; Branney and Kokelaar 2002); b) sustained low pyroclastic fountaining (“boil-over”; Cas and Wright 1987); c)

collapse of lava domes (Fig.1.3b; Rose et al. 1976; Bardintzeff 1984; Yamamoto et al. 1993; Cole et al. 2002) or loose ignimbrites (Branney and Kokelaar 2002); d) lateral blasts (Hoblitt 1986); e) expansion of over-pressurized jets (Cas and Wright 1987); f) phreatic explosions (Sheridan 1980).

PDCs derive usually from a wide range of intermediate to acid magmas (andesites to rhyolites), with varying particle densities from 2500 to 500 kg/m³ (Gurioli 1999), a key factor that influences flow mobility and sedimentological features of associated deposits.

1.3.2 Transport mechanism and sedimentation

As in all gravity-driven flows, PDCs can be described from the point of view of flow regime (laminar or turbulent), rheology (Bingham, Newtonian or non-Newtonian) and particle support mechanisms (fluid turbulence, particle interactions, fluidization). Each of these features shows a high degree of variability even within a single PDC unit which is highly influenced by the complex interaction of the current with the underlying topography (Gurioli 1999; Branney and Kokelaar 2002). A conceptual framework useful for understanding how different processes acting within PDCs could affect deposition and therefore lithofacies association is the concept of “flow-boundary zone” (FBZ; Fig.1.4) described by Branney and Kokelaar (2002). According to the authors, this zone can be identified with the lowermost part of the current and the uppermost part of the forming deposit, where lithofacies characteristics are largely determined. During steady or quasi-steady PDCs, deposition proceeds at a constant rate with the FBZ layer surface that rises steadily with time (Branney and Kokelaar 2002): the subsequent aggradation of the deposit can be ‘gradual’ (not necessarily implying a slow rate of deposition) or ‘stepwise’ (i.e., which proceeds with a series of abrupt jumps). Within this framework, the observed deposit is not the actual representation of the current but more precisely an indication of the prevailing features of the FBZ through time and space. Any clast, while descending, has in fact to cross the FBZ layer, responding to the prevailing combination of support mechanism and segregation effect. The features of the FBZ (density or concentration of solid particles, shear rate, rate of deposition of solid particles) determine therefore the lithofacies association visible in the deposit. A total of four intergradational end-members have been proposed (Fig.1.4).

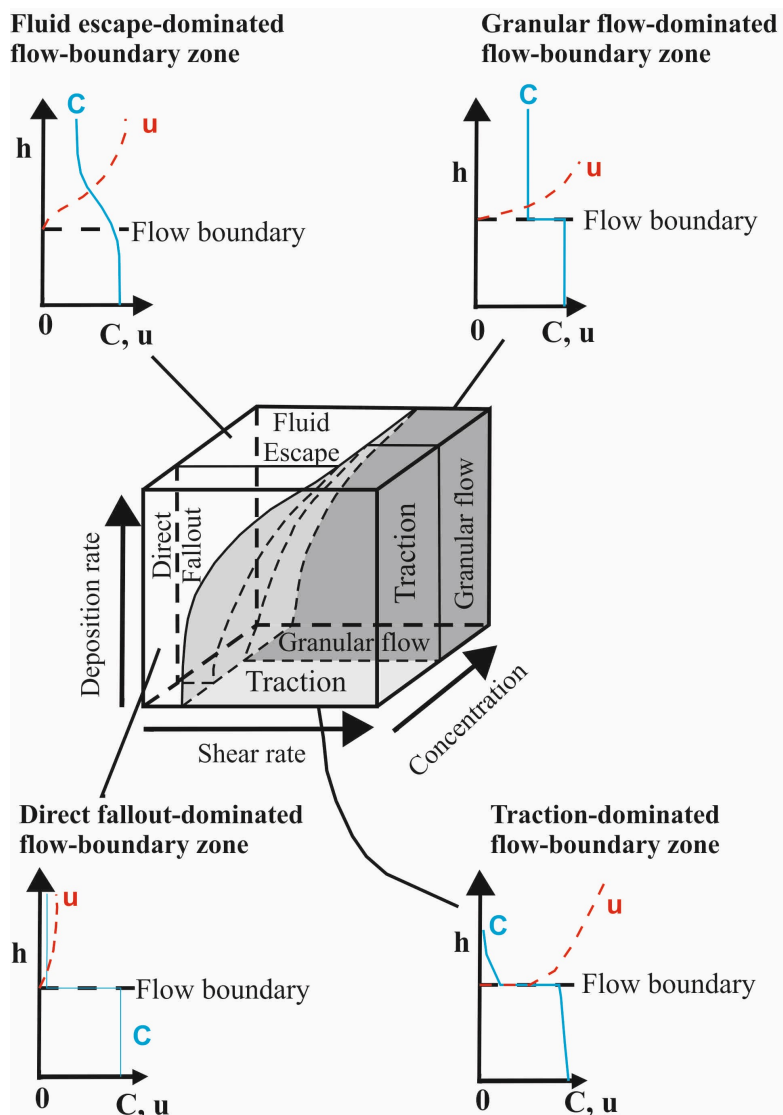


Fig. 1.4: conceptualization of the relative fields of the four types of flow-boundary zone defined by Branney and Kokeelar (2002). Rate of deposition is the mass-flux of pyroclasts into the deposit per unit area of the flow boundary. C is the concentration of particles, u is the velocity of the current. Modified from Branney and Kokelaar (2002) and Sulpizio et al. (2014).

For each of these types of FBZ, different features of the most important parameters describe end member situations with: a) low particle concentrations and low shear velocities (“Direct fallout-dominated FBZ”); b) fluid turbulence as the major supporting mechanism, with low particles concentration resulting in minimal interactions between moving clasts (“Traction-dominated FBZ”); c) clast concentration and shear intensity sufficient for grain interactions to dominate clast support (“Granular flow-dominated FBZ”); d) fluid escape (due to fluid expelled after deposition) as the prevailing clast support mechanism (“Fluid escape-dominated FBZ”).

A third type of depositional mechanism (“en masse”) has been classically proposed by Sparks (1976) for plug flows with Bingham rheology.

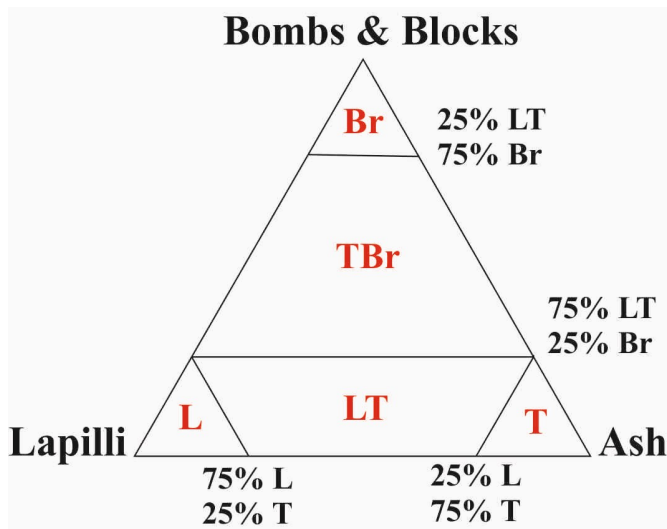
In this case, deposition occurs when flow velocity drops below a certain value, and the resulting deposit maintains all the features and the architecture of the flow itself. However, Branney and Kokelaar (2002) limited this particular type of deposition to few cases (i.e. slow moving terminal pumice dams and levees) since i) many of the observed deposits show chemical zonation (reflecting chemical variation of magma through time), ii) lateral variations from massive to stratified deposit show progressive deposition, iii) clast orientations throughout the whole deposit show evidences of laminar

flow (incompatible with the development of an upper non-shearing plug) and iv) there are no evidences in PDC deposits of compressional structures commonly observed in other natural plug flow deposits.

1.3.3 PDC deposit features

The recognition and description of different lithofacies (character of the deposit or part of it which is distinct according to stratification, grain-size, grain shape, sorting, fabric and composition) within PDC deposits is a key element. The processes occurring in the flow-boundary zone determine in fact lithofacies for the associated pyroclastic deposits, which can be described on the basis of non-genetic terms with reference to the sedimentary structures, grain-size, sorting and composition (Sulpizio et al. 2014). Lithofacies changes through time (vertical variations in the deposit) and space (horizontal variations in the deposits) define the lithofacies architecture of the pyroclastic successions, whose study allows inference of the time- and space-dependent changes of the depositional regime (for a given PDC or for a series of PDCs generated during the same eruption).

The importance of providing objective terms for describing PDC deposits lithofacies is crucial, as this capability will allow a clear understanding of what has been observed in the field by all the possible audiences. In this manuscript it is therefore used the primary lithological description defined



by White and Houghton (2006) and displayed in Fig.1.5 (note that the term “Lapillistone” is not a synonym for “Lapilli-Tuff”, as intended by Schmid 1981). With this initial characterization, several abbreviations (following Branney and Kokelaar 2002) are added in order to describe structures of the deposit: the list of lithofacies symbol used throughout this manuscript are listed in Table 1.1.

Fig. 1.5: non-genetic classification scheme of primary volcanic rocks (modified from White and Houghton 2006). Abbreviations used: L – Lapillistone; T – Tuff; LT – Lapilli-Tuff; TBr – Tuff-Breccia; Br – Breccia.

Lithofacies symbol	Description
mlBr	Massive lithic Breccia
mlBr _{ipoor}	Massive lithic Breccia poor in fines
lensL	Lens of lapillistone
mLT	Massive Lapilli Tuff
mLT _i	Massive Lapilli Tuff with inverse grading pattern
mLT _n	Massive Lapilli Tuff with normal grading pattern
mLT _(nl, ip)	Massive Lapilli Tuff with normal grading for lithics and inverse grading for pumices
mLT _{accr}	Massive Lapilli Tuff with accretionary lapilli
emLT _f	eutaxitic Massive Lapilli Tuff with directional fabric
bLT	Thin-bedded Lapilli Tuff
dbLT	Diffuse thin-bedded Lapilli Tuff
//sLT	Parallell-stratified Lapilli Tuff
xsLT	Cross-stratified Lapilli Tuff
mT _{accr}	Massive Tuff with accretionary lapilli
dbT _{accr}	Diffuse thin-bedded Lapilli Tuff with accretionary lapilli
sT	Stratified Tuff
//sT	Parallell-stratified Tuff
xsT	Cross-stratified Tuff

Table 1.1: list of abbreviations for PDC lithofacies description used throughout the text.

A general feature that identify PDC deposits (including ignimbrites, which are deposits from PDC rich in pumice and pumiceous ash shards, with evidences of being deposited in relatively high temperature conditions) is their poor sorting (Branney and Kokelaar 2002): this is commonly due to i) poor sorting at the source, ii) abrasion/breakage of larger pumice clasts during transport (which determines the general roundness of pumiceous clasts of PDC deposits), iii) particle agglomeration and clustering of fine ash particles (due to electrostatic forces), iv) particle interlocking (clasts being trapped with adjacent clasts moving coupled with them), v) simultaneous existence of multiple transport mechanism and vi) rapidity of emplacement from PDC currents. One of the final goal for the detailed description of lithofacies association in a PDC deposit is to clarify if, within Eruptive Units related to PDCs, more than one flow unit can be identified. Flow-unit is a genetic term meaning the deposit of a discrete current, and the recognition of more flow-units within a PDC deposit requires evidences for cessation of the current (i.e. fallout deposit related to fine particles decantation or to a renewal of a sustained column). This recognition is of great importance when dealing with numerical simulations and hazard assessment related to PDC invasion areas. With the terminology introduced above, it is possible to provide synthetic, non-genetic and objective description of all the different types of PDC deposits, and to link them with depositional features determined by different FBZs (Fig.1.6).

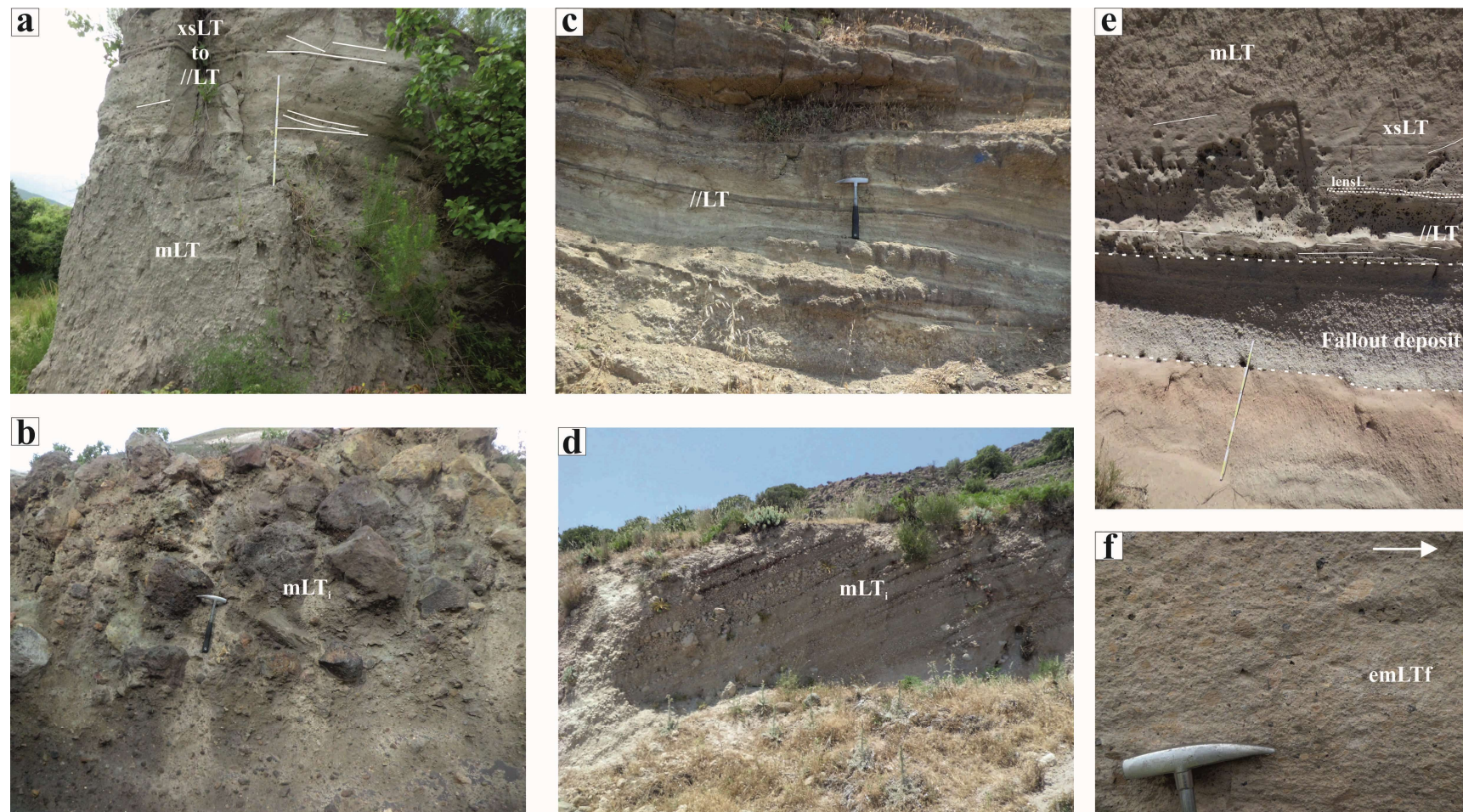


Fig. 1.6: examples of PDC lithofacies from different volcanic areas. a) Somma-Vesuvio, Italy; b) Vulcano island, Italy – Caruggi unit; c) Nysiros island, Greece; d) Nysiros island, Greece – Upper Pumice unit; e) New Mexico, USA – Otawi member of the Upper Bandelier tuff; f) New Mexico, USA – Battleship rock (white arrow indicates flow direction).

1.4 A geo-database for Somma-Vesuvio

This Chapter presents new and revised datasets about the spatial distribution of past volcanic vents, eruptive fissures and regional and local structures of the SV volcanic system. The key innovative features of the study are the identification and quantification of the main sources of uncertainty affecting interpretations of the datasets. In this regard, the spatial uncertainty of each volcanological feature is modeled by an uncertainty area, i.e. a specific geometric element typically represented by an ellipse or polygon drawn around points or lines. The dimensions of these areas have been estimated on the basis of established available knowledge and, in some cases, taking also into account the accuracy and reliability of the information sources and the precisions of the various analysis techniques (i.e. for seismic profile resolutions). The new datasets have been assembled as an updatable geo-database that aims to integrate and complement existing databases for SV. The data are organized into four datasets with characteristics stored as eleven feature classes (points and lines for feature locations and polygons for the associated uncertainty areas), totaling more than 1700 elements. More specifically, volcanic vent and eruptive fissure elements are subdivided into feature classes according to their associated eruptive styles: i) Plinian and sub-Plinian eruptions (i.e. large-medium scale explosive activity); ii) Violent Strombolian and Continuous Ash Emissions eruptions (i.e. small-scale explosive activity), iii) effusive eruptions (including eruptions from both parasitic vents and eruptive fissures). The regional (i.e. deep faults) and local structures are represented as linear feature classes. In order to better interpret the data and analyze results, additional datasets include SV geological units and caldera morphological features. In the following section, the database is used to develop a first vent opening probability map for the Somma-Vesuvio caldera, with specific attention focused on the occurrence of large-medium explosive events. Further developments of the geo-database are in progress with the goal of extending it with data describing dispersal of eruptive products and their properties, as well as other geophysical and geochemical datasets relevant for hazard assessment purposes. The datasets developed during this PhD project but not employed for the development of the vent opening probability maps are displayed in Section 8.1.

1.5 Vent Opening Probability maps for Somma-Vesuvio

Quantifying uncertainty is crucial for producing hazard assessments for developing emergency plans and mitigating the associated risks. In this Chapter, volcanological/structural datasets (defined in the previous Chapter) and inputs from Structured Expert Judgment (SEJ) are combined together to produce a first background (i.e. long-term or base-rate) probability map for vent opening location in the next Plinian or Sub-Plinian eruption of SV. The SV volcano has, over its history, exhibited a large variability in eruptive styles, and a moderate but significant spatial variability in vent locations. In particular, the vent positions associated with large explosive eruptions, i.e. Plinian and Sub-Plinian, have shown shifts within the present caldera. Notwithstanding this moderate shift, the location of a new vent could have a major effect on the run-out and dispersal of pyroclastic density currents mainly due to the presence of the Mt. Somma barrier, as also evidenced by past deposit patterns and illustrated by 3D numerical simulations, and therefore will have important implications for hazard mitigation. The implementation of a vent opening probability map has been performed through i) the development of spatial probability density maps with Gaussian kernel function modelling to use with different volcanological and structural datasets (defined in Chapter 2), and ii) the production of a background probability map for vent opening position, using weighted linear combination of spatial density maps for the identified volcanological and geophysical parameters, with uncertainties (related to both epistemic and aleatoric uncertainties) explicitly included by using SEJ. Outcomes obtained during two elicitation sessions involving about 15 experts are reported for three expert judgment weighting and pooling models: a) the Classical Model (CM) of Cooke (1991); b) the Expected Relative Frequency (ERF) model of Flandoli et al. (2011), and c) the Equal Weights (EW) combination. The results of combining expert judgements with our spatial modeling of the identified variables illustrate that: a) vent opening probabilities are evenly distributed around the caldera with a peak in correspondence with the area of the present crater but with about 50% mean probability that the vent will open in other areas of the caldera; b) there is a mean cumulative probability of about 30% that the next vent will open west of the present edifice in the so-called “Piano delle Ginestre” area; c) there is a mean probability of more than 20% that next Plinian eruption will enlarge the present SV caldera and a not negligible probability (of almost 10%) that the next Plinian or sub-Plinian eruption will have its initial vent opening outside the present outline of the SV caldera. Robustness of results have been tested by considering the effects of alternative pooling methods, sub-groups of experts with different backgrounds and experiences and

sub-groups of volcanological datasets. Uncertainty analysis also allowed identification of the most controversial issues and to have a first estimate of the associated ranges.

1.6 From field data to numerical modeling: reconstructing key input parameters from eruptive units for model validations

In this chapter new and revised field data on selected deposits of Pyroclastic Density Currents (PDC) from two different, large-scale eruption of SV (the EU3pf and EU4 from the AD 79 “Pompeii” eruption, and unit Fg from the AD 472 “Pollena” eruption) are employed for the quantification of key parameters (maximum runout, volume, Total Grain-Size Distribution and paleotopography) that could be employed as input data for validating the results of two available numerical models for PDC. The research included also a synthesis of the stratigraphic features of the different PDC deposits from the two eruptions described in different sources. A general objective of the research was also the need to quantify the uncertainties associated with each parameter, an objective that has been fully achieved for the quantification of the maximum runout outlines, the volume estimations and partly for the Total Grain-Size Distribution (TGSD).

Main conclusions achieved include also some interpretations about the mobility of PDCs with respect to the volcanic plume collapse: i) the EU3pf unit (at the end of the magmatic phase of the AD 79 “Pompeii” eruption) was probably emplaced after an axisymmetrical collapse, but the strong wind at the time of the eruption partitioned the finer-grained particles in the downwind direction, asymmetrically enhancing PDC mobility and maximum runout; ii) the EU4 unit (at the beginning of the final phreatomagmatic phase of the AD 79 “Pompeii” eruption) featured instead a probable asymmetrical collapse of the eruptive column, which caused the more coarse grained particles to be partitioned toward the N and NW. Finer-grained particles of the EU4 unit were instead forced toward the direction of wind blowing, with the same implications described for the EU3pf unit; iii) the effect of the pre-existing Mt. Somma scarp to the N does not seem to have influenced the partitioning of fine/coarse particles.

Results described in this Chapter will be employed in the next Chapter as input parameters for numerical model validations with field data. Further analyses of PDCs maximum runouts from other major explosive eruptions at SV (Plinian and sub-Plinian) are displayed in section 8.3.

1.7 Application of numerical models using field data

In this Chapter it is intended to deal with the outputs of the numerical models when trying to reproduce known PDCs from eruptive units: this step is necessary since an uncertainty evaluation provides more robustness to an hypothetical PDC probabilistic invasion map produced using numerical models. To this purpose, values for the EU3pf, EU4 and Fg “Cupa Fontana” calculated in the previous chapter (i.e. maximum runouts, volumes and Total Grain Size Distributions) will be used as input parameters. Two different codes (the Box-Model and TITAN2D; Dade and Huppert 1996; Patra et al. 2005) will be employed to reproduce two specific end-member of the complex spectrum of PDCs, that is the dilute, turbulent part of PDCs (concentration of solid particles in volume between 0.5% and 10%) and the more dense, laminar part of PDCs (concentration of solid particles in volume more than 10%). The Box-Model (which calculates the kinetic energy of the flow front and compares it with the potential energy needed to overcome topographic obstacles) will be employed for the validation of the more dilute and turbulent part of PDCs (i.e. for the EU3pf and EU4 units) while the TITAN2D code (depth-averaged approach with a Coulombian friction law) will be employed for the reproduction of the more dense and laminar part of PDC spectrum (i.e. the Fg “Cupa Fontana PDC lobe). Validation of numerical model outputs has been performed with respect to inundation areas (with the calculation of the True Positive, True Negative and False Positive values), thickness of the real deposit versus thickness of the model output with distance and mass fractions of different granulometry classes with distance for the real deposit versus the numerical model output (this latter one for the Box-Model code only). For the Box-Model code, several simulations have been performed considering i) polydisperse (with 10 grain size classes) and monodisperse (with the $Md\phi$ values of the TGSD calculated in Chapter 4) situations; ii) a direct version (where the initial volume is released and the invasion area is computed) and an inverse version (where the initial collapsing volume is a function of an inundation area defined by the user); iii) axisymmetrical and asymmetrical collapses. Values of settling velocities (w_s) have been calculated as well for all the different grain sizes. Empirical calibrations led to the conclusion that the modeling for the EU4 unit better approximates the real deposit outline and thickness, and will be therefore employed as input data for the generation of the first PDC probabilistic map (Chapter 6).

Results with the TITAN2D code, instead, highlighted that this code is able to capture the general trend of PDC deposits, both from the point of view of the inundation area and the thickness of

the deposit; it is however true that some parameters (i.e. basal friction angle and total simulation time) are affected by a certain degree of uncertainty. This is primarily due to the absence, at the moment, of a reliable stopping criteria which is able to stop the flow autonomously without user inputs. Therefore, for the more dense part of the PDC spectra, at this stage of the project the TITAN2D code has not been employed for PDC hazard assessment.

1.8 Pyroclastic Density Currents invasion maps

This final Chapter is intended to summarize all the achievements of the previous chapters and produce a preliminary PDC probabilistic invasion map, targeted to a specific scenario. Since in fact it has been highlighted how at SV PDCs are the result of different processes, different type of eruptive column collapses and different mechanisms of emplacement and interaction with topography, a single PDC invasion map is not realistic. More useful is the possibility to have different maps for all the different possible scenarios. With this in mind, this first PDC probabilistic invasion map is aimed at reproducing a scenario of a Plinian eruption with an axisymmetrical collapse in absence of wind. The parameters employed are referred to the EU4 unit, whose parameters have been empirically calibrated in the previous Chapter. The resulting maps (representing the 5th, Mean and 95th percentiles) have been produced using a similar procedure to the one adopted by Bevilacqua (2016), which involves (at the same time) a Montecarlo sample of 1000 i) vent location using the vent opening probability maps (defined in Chapter 3) and ii) values of inundation area (linked to the three percentiles of inundation area calculated for the EU4b/c unit in Chapter 4) used by an inverse version of the Box-Model. These maps (which have been compared to a set of three maps where the position of the vent has been kept fixed with the position of the centroid of the present Gran Cono crater) indicate that in this specific case the control of vent position on the total inundation area is minimum (an expected result for Plinian eruptions). These results could be linearly combined with another set of three maps which represent the same type of situation (i.e. axisymmetrical collapse in the absence of wind) but in case of a sub-Plinian I eruption.

Chapter 2

A geo-database for Somma-Vesuvio

2.1 Introduction

Somma-Vesuvio (SV) is one of the most dangerous volcanoes in the world. Its surroundings are very densely inhabited with more than 600,000 people living within 6 km of the present crater, the Gran Cono. Moreover, SV eruptive styles are significantly variable, ranging from relatively gentle lava effusions to devastating Plinian eruptions (Cioni et al. 2008).

In the last few decades, many studies have been carried out on SV with a variety of aims such as reconstructing and classifying its eruptive history (e.g. Principe et al. 2004; Cioni et al. 2008), characterizing the properties of its eruptive products (Santacroce et al. 2008 and references therein), describing the distributions of geological and morphological features (Santacroce and Sbrana 2003; Ventura et al. 2005; Vilardo et al. 2009; Gurioli et al. 2010; Principe et al. 2013) and recording its activity through geophysical and geochemical monitoring (Vilardo et al. 1996; Aiuppa et al. 2004; Federico et al. 2004; Frondini et al. 2004; De Natale et al. 2006; Cella et al. 2007; De Siena et al. 2009; Granieri et al. 2013).

The work presented here is intended to complement the available volcanological information with new and revised datasets, and with elaborations that address specifically the locations of past vents and eruptive fissures, as well as other structural features. The reconstruction of past activity of SV highlights the significant past variability in vent locations of both explosive (Cioni et al. 2008 and references therein) and effusive (Nazzaro 1997; Ricciardi 2009) activity. Such variability had a remarkable influence on the distribution of eruptive products around the volcano, particularly those associated with the emplacement of pyroclastic density currents. Clear evidence for such effects is found in the mapped deposits (Gurioli et al. 2010), and shown as well by outcomes of 3D simulations of column-collapse scenarios at SV (Esposti Ongaro et al. in preparation).

A key feature of the present study is the inclusion of information about the uncertainties affecting the datasets. Particular attention is given to the definition of the spatial uncertainty affecting the locations of vents and fissures. This uncertainty can be particularly substantial for the oldest and bigger explosive events, given the largely incomplete reconstruction of volcanic deposits (particularly

in the most proximal localities and in distal areas) and to the uncertainty related to possible shifts of vent location during a single event. In some cases, uncertainty bounds for specific features were also estimated by critically comparing and integrating data derived from different sources (for instance, for the location of effusive vents) or by accounting for the accuracy of the methods used to obtain them (in the case of structural data). A similar approach was followed by Bevilacqua et al. (2015) for the characterization of the uncertainty of past vent locations and structural features at Campi Flegrei caldera (Italy).

The new datasets are organized into a new updatable geo-database adopting a geographically referenced framework. In particular, the database adopts GIS methodology based on the ESRI platform (Mitchell 1999) for data storage and representation, although the datasets are also readable with different GIS platforms. Such a new database integrates and complements already existing databases of SV such as those of Vilardo et al. (2009) which includes, on a webGIS platform, geographical, territorial, morphological and geophysical data (raster and vector), as well as seismicity catalogues (<http://ipf.ov.ingv.it/siscam.html>).

The quantification of the different sources of uncertainty affecting the datasets is a crucial step for volcanological studies, particularly for those aimed at the assessment of volcanic hazard and risk mitigation. A first application of the new datasets presented here is described in Chapter 3, where a first vent opening probability map for SV has been produced with specific reference to the occurrence of large-medium explosive events.

In the following sections, a brief technical description of the geo-database (Section 2.2), of the epistemic/aleatoric uncertainty definitions (Section 2.3) and the presentation of the new and revised datasets (Section 2.4) are described. Finally, Section 2.5 briefly concludes with a few remarks about potential uses and applications of the new geo-database.

2.2 The geo-database and its properties

For the development of the geo-database presented here, it has been adopted the ArcGIS 10.1® geo-database platform since it is a repository that offers efficient storage and logical organization of spatial data. The geo-database of SV contains more than 1,700 elements stored in 11 feature classes (point, linear and polygonal) and grouped as four main volcanological and structural datasets.

Polygonal feature classes represent the spatial uncertainty areas of the related data, which are represented through point or linear feature classes. The four main datasets have been complemented with data about geological mapping (1 feature class) and caldera information (2 feature classes), which are both stored in a fifth dataset. In total, the geo-database (Fig. 2) therefore comprises 14 feature classes grouped in 5 datasets, as follows:

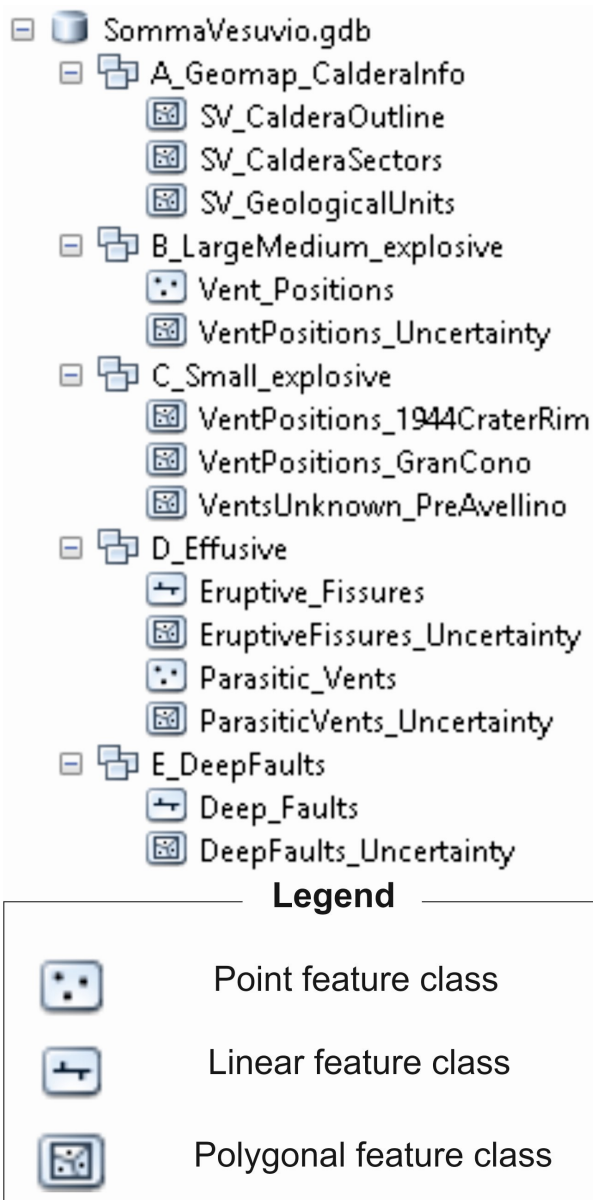


Fig. 2.1: framework of Somma-Vesuvio (SV) geodatabase. Different datasets are extensively discussed in the text.

1) Geological mapping and caldera information (see subsection 2.4.1); this dataset records the spatial distribution of volcanic products as displayed in the latest geological map of SV (Santacroce and Sbrana 2003) along with geomorphological data about the SV caldera outline and SV caldera sectors;

2) A dataset recording the spatial distribution of vents associated with large-medium scale explosive activity (i.e. Plinian and sub-Plinian I and II eruptions - see subsection 2.4.2);

3) A dataset recording the spatial distribution of vents associated with small scale explosive activity (i.e. Violent Strombolian to Continuous Ash Emission eruptions - see subsection 2.4.3);

4) A dataset recording the spatial distribution of volcanic features associated with effusive activity (i.e. parasitic vents and eruptive fissures - see subsection 2.4.4) and subdivided into Parasitic vents and Eruptive fissures sub-datasets;

5) A dataset containing spatial information on regional/local structures and locations of deep faults (see subsection 2.4.5).

All the data presented in the following sections have been imported into the geo-database and geocoded to WGS84 UTM ZONE 33 coordinate system. A 10 m cell size digital elevation model (Tarquini et al. 2007) is used as the reference topographic basis for dataset visualizations. In the following sections, the datasets so far included in the geo-database are described in detail, with specific reference to the sources used and to additional elaborations made to quantify the uncertainties associated with each element.

2.3 Uncertainty description and quantification

The datasets construction is based on the organization of vector data that can be queried. The vector data are obtained by transforming - into digital format - information from bibliographic sources, direct measurements and field surveys. As several sources of uncertainty can affect the final quality of data, evaluating their accuracy (in our case, the uncertainty in feature locations) is not straightforward. Sources of errors could be due to many factors related to technical operations (e.g. data acquisition during field work, instrumental precision, transformation of analogue data to digital, etc.). However, a full discussion of these sources of uncertainties is beyond the scope of this study, which instead is focused on the quantitative representation of the epistemic uncertainty affecting the knowledge of vent location of past events and of controlling structural features of the volcano. Such sources of uncertainty are significant and, as mentioned above, ideally should be properly accounted for, especially in the assessment of any associated volcanic hazards (Aspinall 2006).

Epistemic uncertainties, related to the incomplete knowledge of the behavior of the system being investigated (Aspinall 2006; Matthies 2007), are due, in our specific case study of SV, to possible ambiguity of field data and paucity or lack of elements that help to constrain the reconstruction of precise positions of volcanological and structural features. For instance, when dealing with vent locations, the position of a past vent is typically inferred by reconstructing the pattern of the different deposits (fallout isopachs, distribution of pyroclastic density currents, venting area of lava flows, etc.). However, as is clearly evident, isopach reconstruction introduces a subjective degree of interpretation (and thus an uncertainty) which is inversely proportional to the number of suitable outcrops where thickness of proximal fall deposits can be estimated (Engwell et al. 2015). As a consequence, uncertainties are higher for older eruptions whose deposits have been eroded, partially covered by

younger deposits or affected by recent urbanization (particularly dense in the Vesuvius area), or where the area close to the vent has been deeply modified by subsequent volcanic activity (either destructive or constructive).

In relation to vent areas and especially for Plinian events, aleatoric and epistemic uncertainties associated with the temporal evolution of the process should be accounted for. In these cases, intrinsic complexities of the dynamics of the eruption, such as possible vent migration during the event, or the simultaneous activity of multiple vents or eruptive fissures produced by caldera collapse, significantly increase such sources of uncertainty. For past events, elements of aleatoric uncertainty are difficult to distinguish from epistemic uncertainty and have been considered together in the assessment of uncertainty of vent location, as described in the following sections.

Besides these sources of uncertainty, for some of the datasets we have also considered other uncertainties which are related to possible misinterpretation of the nature of volcanological features (e.g. uncertainties in the location of presumed effusive parasitic vents) or resolution limits of available data acquired in the field (e.g. uncertainty in the location of deep faults and some buried parasitic vents for which positions are determined indirectly from interpretation of seismic reflection profiles).

The uncertainty areas, built around the features, are drawn differently, according to feature geometry. The size and shape of the uncertainty areas were defined on the basis of the available data and of the specific knowledge of the SV complex. As is more deeply discussed in Chapter 3, it is assumed that such uncertainty areas enclose 100% of probability of vent location and that, for the sake of simplicity, such probability is uniformly distributed over the uncertainty area. In general, in case of a point feature, the uncertainty area is proscribed as a circle or a polygon centered on the feature itself, with a radius representing the spatial uncertainty associated with the point position. For linear features, in contrast, the uncertainty area is a polygon that can be drawn by putting its boundaries at a constant distance from the line itself. The lengths of segments represent the spatial uncertainty related to the line position. In particular, in the present study on SV, we define uncertainty areas with a variable radius (and shape) for large-medium scale explosive eruptions, small-scale explosive eruptions datasets and for the eruptive fissures sub-dataset. For representing the uncertainty areas of parasitic vents, we use a circular area with fixed radius and, to represent the uncertainty in the location of deep faults, a rectangular buffer area with fixed width.

At this stage, structured expert elicitation techniques (Cooke 1991; Aspinall 2006) for ascribing detailed uncertainty distributions to spatial parameterizations - have not been applied in the present study. The same basic assumption (i.e. uniform 100% probability density within the uncertainty area) was adopted by Bevilacqua et al. (2015) in a similar study on Campi Flegrei caldera, and found appropriate for the aims of that study.

2.4 The datasets

2.4.1 Geological mapping and caldera information

Geological mapping and caldera morphological features are included in the geo-database with the specific aim of facilitating the characterization of the other volcanological datasets and of helping in their elaboration (see also Chapter 3).

Geological units from the latest geological map of SV (Santacroce and Sbrana 2003) were digitized and included in the geo-database in order to integrate volcanological, structural and geological data, particularly for the attribution of a given period of activity to parasitic vents and eruptive fissure ages, as detailed in the following discussion. Fig. 1.2b displays a simplified version of such feature classes, where different formations have been grouped into major units representing specific temporal intervals of SV activity or specific type of deposits. Geological units have been stored in a polygonal feature class where each record is classified according to the information provided in the geological map (formation, code of formation, type of deposit, age and labels). A total of 13 formations for primary volcanic deposits (lava flows, PDC deposits, fallout deposits) and two formations for alluvial and clastic/volcanoclastic deposits comprise the feature class. Deposits cover the whole volcanic history of SV, starting from Mount Somma activity (“Lave e Piroclastiti della Valle del Gigante” and “Lave e Scorie dei Cognoli”; Fig. 1.2b) through to the more recent activity of the volcano (“Lave e Piroclastiti del Vesuvio”; Fig. 1.2b).

The SV caldera morphological outline and a simplified morphological partitioning of it are also included in the geo-database. The present SV caldera outline (Fig. 1.2b) has been drawn by taking into consideration morphological limits (the foot of Mount Somma northern scarp) and the caldera collapse extent of Plinian eruptions based on other morphological features (sharp changes in the slope,

evidences from the hydrographic network, etc., Cioni et al. 1999). The surface area enclosed by this caldera outline is 12.98 km².

In order to provide more information about parasitic vents and eruptive fissures location (see section 2.4.3 for more details), as well as to facilitate considerations about the potential areas of vent openings (Chapter 3), SV caldera is also subdivided into four sectors (named A, B, C and D), whose definition is mostly related to the morphological features of SV caldera (Fig. 1.2b). In detail, sector A encloses the present area of Gran Cono, and it is bordered by the break in slope at the base of the cone; sector B refers to the N-NE part of SV caldera (delimited by the Mount Somma scarp) and approximately corresponds to the “Valle del Gigante” area; sector C encloses the SE part of SV caldera and approximately corresponds to the “Valle dell’Inferno” area; sector D refers to the W part of SV caldera and includes the “Piano delle Ginestre” area. The areal size of the four sectors varies between about 2.1 km² for sector C up to about 4 km² for sector D.

2.4.2 Vent location of large-medium scale explosive eruptions

The dataset of large-medium explosive eruptions groups two feature classes that account for the vent positions and their associated uncertainty areas (Fig. 2.2) related to four Plinian, three sub-Plinian I and three sub-Plinian II events, according to the classification introduced by Cioni et al. (2008).

For Plinian eruptions (Fig. 2.2a), uncertainty areas are taken to be equal to the area of the associated caldera collapse, as defined in Cioni et al (1999). Despite several data related to fallout isopachs (Bertagnini et al. 1998; Cioni et al. 2000b; Gurioli et al. 2005; Gurioli et al. 2010; Mele et al. 2011) that help to constrain possible vent positions for these eruptions, there are wide uncertainties associated with them, likely due to possible vent migration during each Plinian eruption (e.g. following caldera collapse). For these Plinian events, dimensions and shapes of uncertainty areas are linked to the accuracy of morphological constraints used by Cioni et al. (1999) to delineate caldera collapsed areas.

As a result, *Pompeii* and *Avellino* eruptions have uncertainty areas better defined with respect to the older *Mercato* and *Pomici di Base* eruptions, which have fewer morphological constraints (see Cioni et al. 1999).

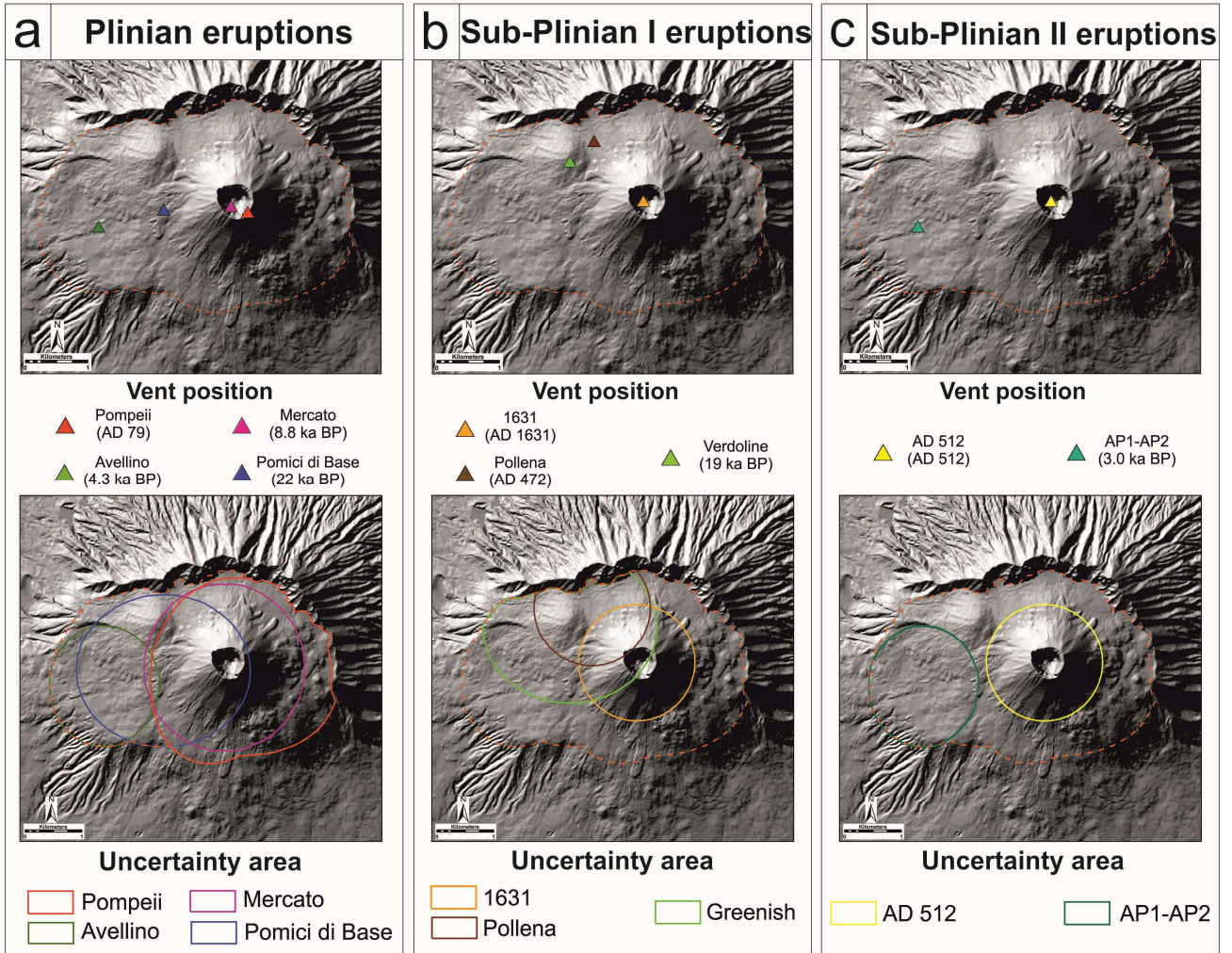


Fig. 2.2: large explosive eruptions dataset comprising a) 4 Plinian eruptions, b) 3 sub-Plinian I eruptions and c) 3 sub-Plinian II eruptions. Each group of eruptions is composed of a feature class indicating vent positions (from Gurioli et al. 2010) and a feature class representing the spatial uncertainty area. SV caldera outlined in dark orange dashed line.

With respect to sub-Plinian I eruptions (Fig. 2.2b), several data from fallout isopachs (Rosi et al. 1993; Cioni et al. 2003b; Sulpizio et al. 2005) allowed Gurioli et al. (2010) to display inferred vent locations also for these eruptions. Uncertainty areas affecting the vent location are defined in a way similar to that for Plinian eruptions. The definition of uncertainty areas suffers from the limitation that no, or very limited, morphological constraints are available, as the sub-Plinian eruptions resulted in less pronounced caldera collapses/enlargements (Cioni et al. 2008). For this reason, we have to rely on additional information for the definition of such areas - in more detail: a) for the *AD 1631* eruption, the vent uncertainty area, approximately coinciding with the base of the Gran Cono, is mainly based on

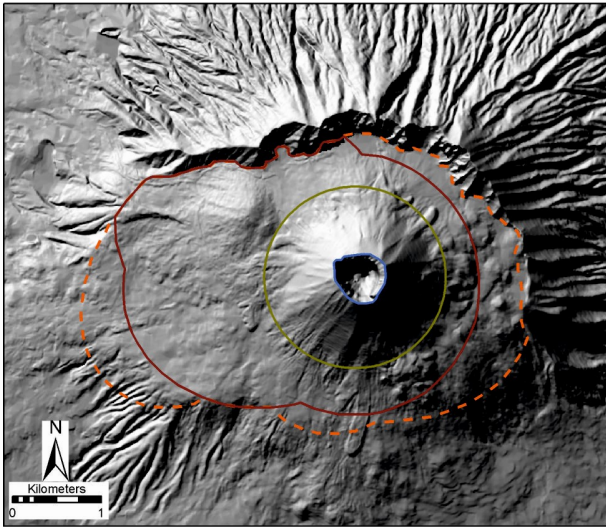
historical accounts (Rosi et al. 1993; Scandone et al. 1993; Nazzaro 1997; Ricciardi 2009); b) for the *AD 472 Pollena* eruption, due to similarities in magnitude and intensity values, the extent of the vent uncertainty area has been assumed similar to that of *AD 1631* eruption, centered on the *Pollena* inferred vent location and reshaped according to the SV present caldera outline; c) for the *Greenish Pumices* eruption (the oldest among the sub-Plinian I eruptions), uncertainties are higher, as no clear morphological constraint exists due to following activity. For these reasons, the uncertainty area related to this eruption is larger and has been put equal to the one of the closest Plinian eruption (Pomici di Base), centered on the *Greenish Pumices* inferred vent location and again reshaped according to the SV present caldera outline (similarly as for the *Pollena* eruption).

For sub-Plinian II eruptions (Fig. 2.2c), difficulties are also greater than for the sub-Plinian I eruptions. We adopt however a similar approach: a) for the *AD 512* eruption, field data (Cioni et al. 2011) and sporadic historical accounts (Alfano 1924) constrain the vent position within the area presently occupied by the Gran Cono, and for this reason we place the uncertainty area equal to the one of the sub-Plinian I *AD 1631* eruption; b) for *AP1* and *AP2* eruptions, Andronico and Cioni (2002) provided a reconstruction of fallout isopachs which suggest a vent position in a similar location of the preceding *Avellino* Plinian eruption. For these reasons, the extent of the uncertainty areas associated to these two eruptions is the same as the *Avellino* eruption.

2.4.3 Vent location of small scale explosive eruptions

The small scale explosive eruptions dataset (Fig. 2.3) encloses the Violent Strombolian (VS) and Continuous Ash Emission (AE) categories, which have been placed here into the same dataset reflecting the similar magnitudes and intensities, although deposits and related hazards are quite different (Cioni et al. 2008; Neri et al. 2008; Barsotti et al. 2015).

Cioni et al. (2008) report a total of 32 events with field evidences that span a wide temporal window between the *Avellino* Plinian eruption (4.3 ka BP) and the last eruption of 1944. However, the degree of confidence in the vent location of these eruptions is quite variable with respect to time, related to the level of preservation of the associated deposits (which might be easily remobilized and also have a smaller areal extent with respect to higher magnitude/intensity eruptions).



Violent Strombolian to Continuous Ash Emissions

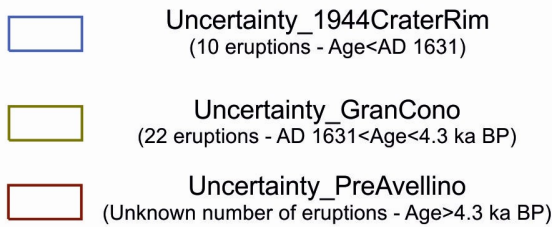


Fig. 2.3: Small scale explosive eruption data set. The data set includes 32 eruptions whose vents are distributed over three uncertainty areas: 1) the area included within the 1944 crater rim, where 10 eruptions occurred since the AD 1631 sub-Plinian event, 2) the area of Gran Cono, where, in the period between the Avellino (4.3 ka BP) and AD 1631 eruptions, there occurred the remaining 22 eruptions and 3) the area related to VS and AE eruptions that have been possibly lost in the eruptive sequence (possibly older than the Avellino Plinian eruption). SV caldera is outlined in dark orange dashed line.

For the younger VS to AE eruptions, i.e. 10 events that occurred after the *AD 1631* eruption and which have the most preserved deposits, Arrighi et al. (2001) were able to reconstruct detailed fallout isopachs, and accordingly vent positions could be all placed within an area that is approximately coincident with the present rim of Vesuvius crater. For the remaining 22 eruptions that date back to the period between the *Avellino* and the *AD 1631* eruption, sparse information has been provided by several authors. Among them, only the AP3 to AP6 eruptions have been systematically studied by Andronico and Cioni (2002) and the reconstruction of their fallout isopachs indicate that vent locations of these eruptions were confined to the area of the present edifice of Gran Cono. The remaining eruptions have been cited differently within the bibliographic sources (PM2, PM3, PM4, PM5, PM6 in Santacroce and Sbrana 2003; AS1a-d, AS2, AS2a-f, AS3, AS4, AS4a-c, AS5 in Cioni et al. 2008) and the available unpublished field data indicate that also for these eruptions the

approximate location of the eruptive vent was confined within the area of Gran Cono.

However, the eruptive records of this type of eruptions might not be complete because, as mentioned before, the older the eruption the more unlikely it is that the deposit would be well-preserved. We therefore consider the possibility that an unknown number of VS to AE events have been “lost” in the eruptive sequence, and we propose to locate these eruptions within an uncertainty area whose extent has been drawn by joining the uncertainty areas of the large-medium scale eruptions that occurred before the *Avellino* eruption (i.e. *Pomici di Base*, *Greenish Pumices*, *Mercato*). The presence of some scoria cones on the outer SV slopes suggests that mid-intensity activity sporadically

occurred also outside the present SV caldera at different ages (e.g. Pollena and Vallone San Severino scoria cones, between Pomici di Base and Greenish pumices eruptions; Camaldoli della Torre scoria cone, between the *Avellino* and the *Pompeii* eruptions; several Middle-Age scoria cones especially in the southern and western sector of the volcano).

In summary, for the small-scale explosive eruptions dataset, three main uncertainty areas for the spatial location of vents are defined, each based on the associated time period (Figs. 2.1 and 2.3). These are represented through three feature classes. The first one accounts for an unknown number VS to AE eruptions that possibly occurred before the *Avellino* eruption (Uncertainty_PreAvellino); the second one, with extent matching the area of the Gran Cono (Uncertainty_GranCono), is a feature class that represents the uncertainty area of 22 vents from eruptions between the *Avellino* Plinian eruption and the *AD 1631* sub-Plinian I eruption; and the third one, which is represented by the present crater area, encloses the last 10 VS to AE events, that occurred between the *AD 1631* and *1944* eruptions (Uncertainty_1944CraterRim).

2.4.4 Vent location of effusive eruptions

The *Effusive eruptions* dataset is composed of two separate sub-datasets, i.e. *Parasitic vent locations* and *Eruptive fissures*, which describe the two possible surface manifestation of effusive activity.

Parasitic vents

With the term “parasitic vents” we refer to any punctual surface expression of lava or scoria emission on the flanks of the main edifice; scoria cones, vents aligned along eruptive fissures (described below), isolated vents (“bocche”) and exogenous tholoids (local accumulation of lava that creates significant reliefs) are included in this dataset, whereas rootless vents (“hornitos”) are not considered. A total of 95 vents (47 with surface exposure, 45 buried and 3 inferred) and 4 exogenous tholoids totaling 99 parasitic vents have been mapped over the whole SV complex (Fig. 2.4), after integration of several bibliographic sources (IGM 1876, 1906; Santacroce 1987; Bertagnini et al. 1991; Bruno and Rapolla 1999; Santacroce and Sbrana 2003; Ventura et al. 2005; Cioni et al. 2008; Principe et al. 2013).

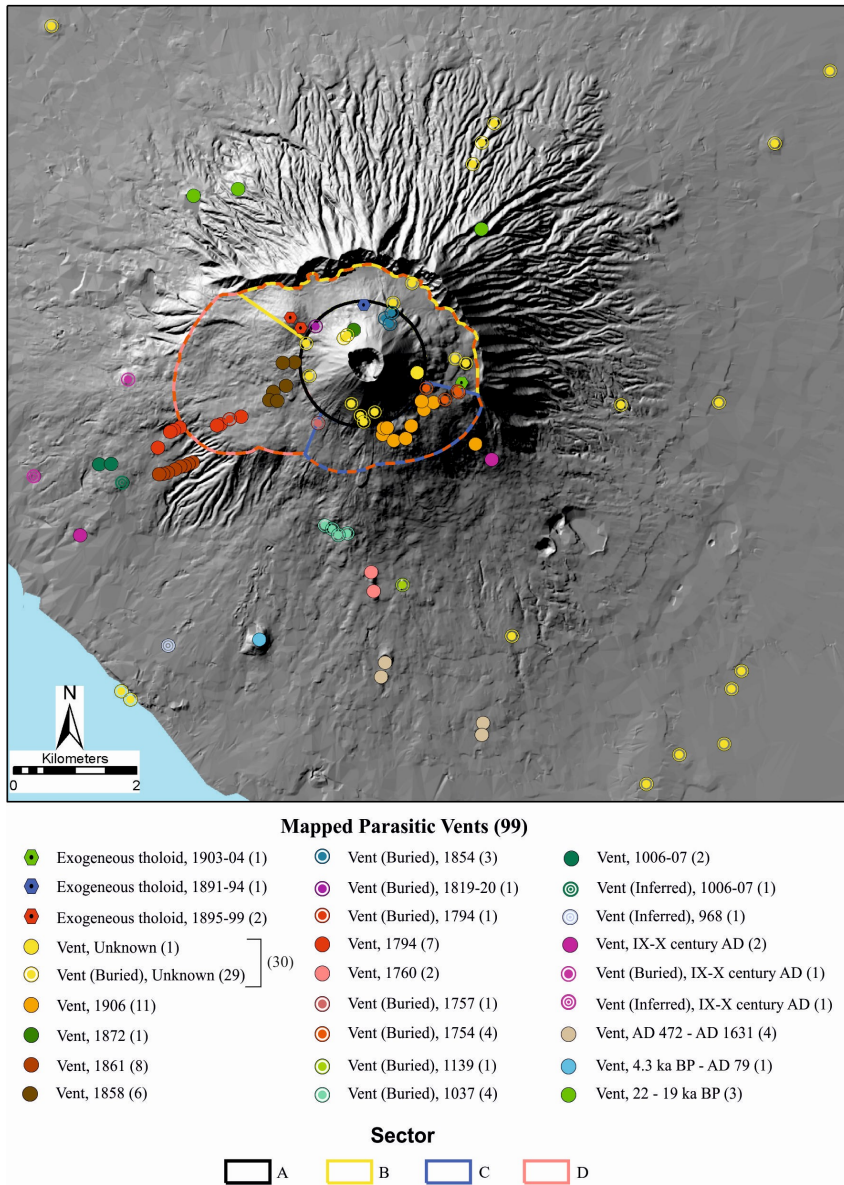


Fig. 2.4: parasitic vents dataset compiled after integration of bibliographic sources (for details see text). SV caldera is outlined in dark orange dashed line.

occurred after the *AD 1631* eruption, 21 to eruptions that occurred between the *Pomici di Base* and the *AD 1631* eruptions, while 30 vents were not assigned to any of the known eruptions of SV (Table 2.1 and Fig. 2.4).

With respect to spatial location (Table 2.1), 46 out of 99 vents/tholoids are located within the SV caldera and, among them, 15 are located within Sector A, 7 within Sector B, 14 within Sector C and 10 within Sector D (Fig. 2.4). Parasitic vents located outside SV caldera (53 vents) are more concentrated in the south, where most of them have surface exposure, while several of them have been identified after seismic surveys (Bruno and Rapolla 1999; Ventura et al. 2005) or have been inferred from considerations about lava flow morphologies (Principe et al. 2013).

As far as times of vent formation are concerned (Table 2.1), 48 vents out of 99 are related to eruptions which

	MAPPED			BIBLIOGRAPHY (MIN-MAX)	LOST VENTS (MIN-MAX)
Sector	Age Known	Age Unknown	TOTAL	TOTAL	TOTAL
A	6	9	15	29-42	<u>14-27</u>
B	3	4	7	11-13	<u>4-6</u>
C	14	-	14	14	=
D	10	-	10	10	=
UNKNOWN	-	-	-	19-23	<u>19-23</u>
INSIDE CALDERA	33	13 (<AD1631)	46	83-102	<u>37-56</u>
OUTSIDE CALDERA (Age<AD 1631)	15	-	15	15-21	<u>0-6</u>
TOT (Age<AD 1631)	48	13	61	98-123	<u>37-62</u>
OUTSIDE CALDERA (All Ages)	27	26	53	-	-
TOT (All Ages)	69	30	<u>99</u>	-	-

Table 2.1: Summary table of parasitic vents as discussed in the text. Sectors as defined in Fig. 1.2 and Section 2.4.1. The notations min and max refer, respectively, to the minimum and maximum values of vents cited in the bibliographic sources considered and of “lost vents” (difference between vents cited in bibliography and mapped vents, see Section 2.4.4 and Appendix 1 for more details).

Several assumptions about their ages can be made: i) it is reasonable to assume that vents within the SV caldera (13 vents) are likely to be representative of the period 1631-1944 (Plinian caldera-forming eruptions and sub-Plinian eruptions likely obliterated vents that preceded them); ii) for the rest (16 vents), the possibility that they took place within the period 1631-1944 can be excluded because all the vents within this period outside SV caldera have been mapped from reliable historical chronicles; iii) vents outside SV caldera and located to the north/northeast/northwest of Mount Somma scarp (6 vents) are probably related to Mount Somma activity or to Vesuvius activity up to the *Pompeii* eruption - there is an absence of records of eccentric activity in historical chronicles for this sector, and the three parasitic vents on Mount Somma scarp date to before the *Pomici di Base* eruption; iv) for vents outside SV caldera and located to the east/west/southeast/southwest (10 vents), it is too speculative to attribute ages since, in this part of the volcano, eruptive centers opened even after the *Pompeii* eruption,

although some of them might be related to effusive volcanic activity that occurred between the IX and X centuries AD (Principe et al. 2004).

When assessing location uncertainties related to parasitic vents, two different sources of uncertainty need to be considered. The first is related to spatial uncertainties in feature location, related to possible errors due to inaccurate placement of vents from field data to maps, for which we have defined appropriate uncertainty areas; the second arises from the comparison between the positions of vents mapped in the field and the locus of vents cited in historical accounts (from which we derive an estimate of the number of “lost vents”). Due to several residual ambiguities and discrepancies among the different historical accounts considered (for instance, different source might cite different numbers of parasitic vents for the same eruption), the number of lost vents could be estimated only as a range (minimum and maximum values).

In the case of parasitic vents, their locations have been determined mostly from existing databases and maps with precise geographic coordinates and reference points, resulting in apparent very low positioning errors. However, several mapped vents have presently limited exposure or are completely buried, whereas others have been deduced from seismic reflection surveys (Bruno and Rapolla 1999). Based on these limitations and considering the typical measured radii of scoria cone craters in different volcanic settings (Porter 1972; Hasenaka and Carmichael 1985; Corazzato and Tibaldi 2006; Dóniz et al. 2008), a circular uncertainty area with radius 75 m is assumed for all parasitic vents.

With the goal of estimating the second element of uncertainty, i.e. the number of lost vents, a detailed analysis and comparison of bibliographic sources dealing with parasitic vent locations is carried out by analyzing bibliographic sources which summarize observations recorded in historical accounts (Scandone et al. 1993; Nazzaro 1997; Ricciardi 2009). Chronicles and historical accounts about this topic are very poor before the year 1631 and therefore the comparison performed in this work was restricted to the period 1631-1944. The detailed comparative table and more details about the procedure are reported in Appendix 1. Table 2.1 reports the minimum and maximum (min; max), number of parasitic vents as deduced from such bibliographic sources and historical accounts and hence indicates the potential numbers of lost vents. With the information available it is also possible to define qualitatively the position of several vents cited in the bibliography by using SV caldera morphological sectors (Fig. 1.2b). It is estimated that 37-62 vents should be considered “lost vents”;

apart from these latter ones, it is worth noting that 5 vents have been mapped but are not cited in the historical records (1757, 1854 and 1872 eruptions). Among these, it is estimated that between 14-27 lost vents could have been located in Sector A, 4-6 in Sector B, 19-23 within the whole caldera and 0-5 outside the SV caldera.

Eruptive Fissures

The term “eruptive fissure” (or fracture) refers here to any linear element within the volcanic edifice from which emission of volcanic materials (lava, ash, scoriae) took place. Eruptive fissures at SV generally resulted in the emission of lava through gentle effusions and/or lava fountains (e.g. 1779 and 1872 eruptions; Scandone et al. 1993). In one case, during the *AD 1631* eruption (Rosi et al. 1993), the initial fracture rapidly evolved into a point vent, and was clearly characterized by emission of ash, scoriae and incandescent blocks, without any lava effusions.

This sub-dataset is composed of 32 elements, derived from several articles and geological maps (Santacroce 1987; Santacroce and Sbrana 2003; Acocella et al. 2006b; Cioni et al. 2008), displayed in Fig. 2.5a.

Among them, only 6 cases out of the 32 can be mapped now in the field, while the locations of the rest are simply inferred from bibliographic sources by Acocella et al. (2006b). A total of 27 fissures developed wholly, or almost entirely, within the SV caldera. Ages of different eruptive fissures, as defined by Acocella et al. (2006b), have been confirmed by comparison with other bibliographic sources and dated geological units underlying or in proximity to the assumed eruptive fissure (Santacroce and Sbrana 2003). A total of 7 fissures drawn by Acocella et al. (2006b), whose positions are not attributable with a sufficient degree of confidence, have not been included in the present dataset. These fissures were related to the eruptions of 1631 (although Rosi et al. (1993) showed a preferred site of the fissure location within the W flank of the previous edifice), 1694, 1723, 1766, 1804-5 and 1822 (the latter associated to two fissures, as reported by Acocella et al. 2006b).

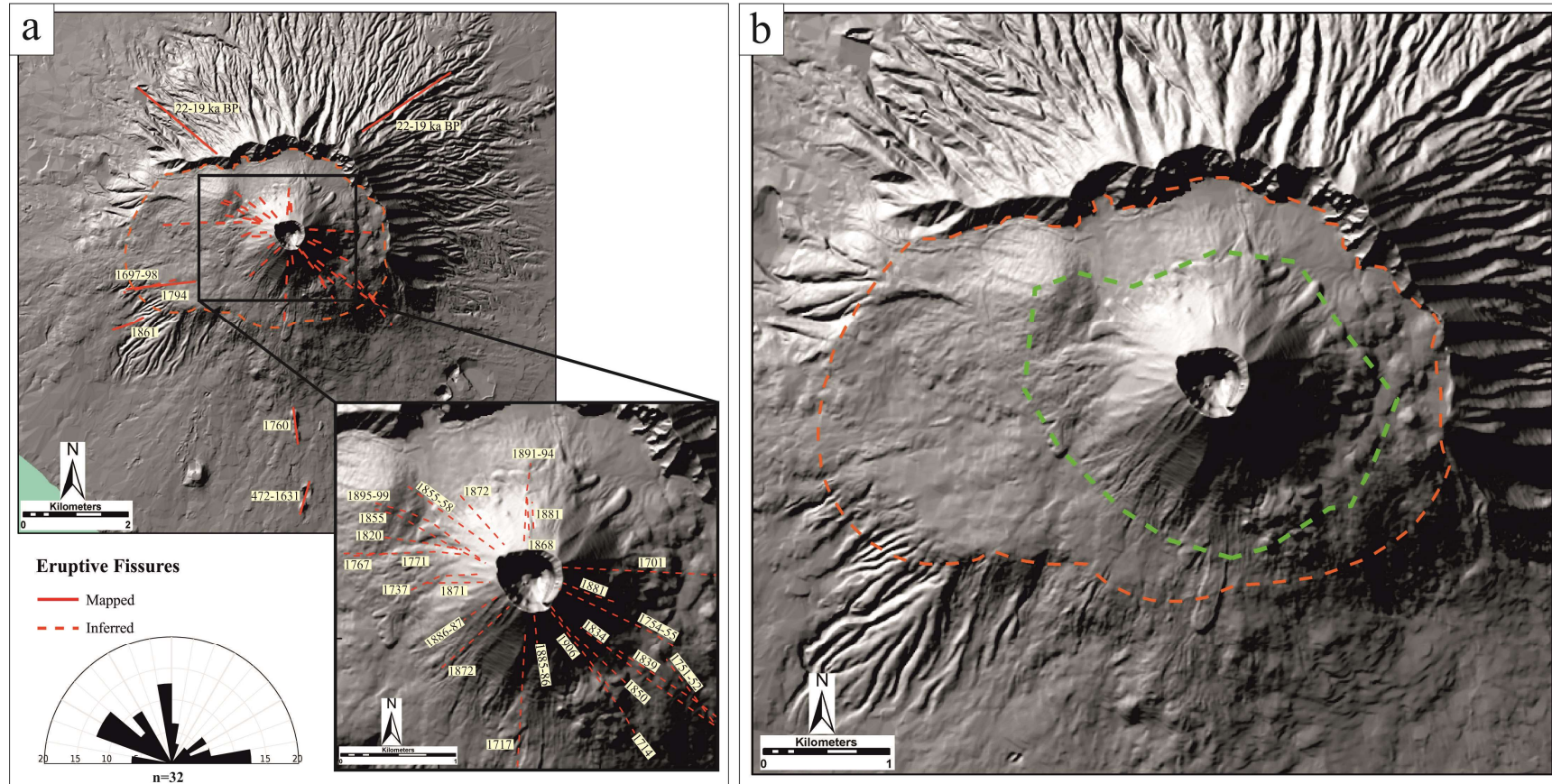


Fig. 2.5: a) eruptive fissures dataset compiled after integration of different bibliographic sources (for details see text). Numbers in yellow boxes are ages of eruptive fissures. SV caldera outlined in dark orange dashed line. Rose diagram refers to all the eruptive fissures in the dataset (petal size is 10°); b) high-density area for eruptive fissures (in light green dashed line) as discussed in Section 2.4.4. SV caldera outlined in dark orange dashed line.

From the point of view of ages, the bulk of eruptive fissures (29 out of 32) were related to the period 1631-1944. A comparison is made of different bibliographic sources which analyze historical accounts between the *AD 1631* and the 1944 eruptions (Scandone et al. 1993; Acocella et al. 2006b; Ricciardi 2009), similar to that performed for parasitic vents, in order to account for possible “lost eruptive fissures” and to provide robust estimates for the locations of the eruptive fissures included in the dataset. The result of this detailed comparison, and of the comparison between parasitic vents and eruptive fissures for a single eruption is available in Appendix 2. Considering the three sources cited in the previous paragraph as a whole, eruptive fissures have been reported from 52 eruptions within the period 1631-1944, resulting in the formation of 57-67 eruptive fissures (numbers have the same meaning of those used for parasitic vents, i.e. min-max range), and the number of “lost” features is 28-38.

Features location uncertainties for eruptive fissures are evaluated in a similar way as for parasitic vents. Eruptive fissures are digitized in vector format by georeferencing a raster image from Acocella et al. (2006b). However, as discussed before, these locations potentially are affected by substantial uncertainty as the positions of most (i.e. 26 out of 32) have been inferred from descriptions in the chronicles and not directly mapped in the field. This situation is particularly evident for the fissures located in the area of Gran Cono (Fig. 2.5a), today completely covered by the 1944 products. As a consequence, a possible approach for using this fissure dataset (limited to the area of Gran Cono) is to define a high-density area of eruptive fissures. Such an area (see Fig. 2.5b) roughly includes the entire Gran Cono up to its base and is slightly elongated along the NW-SE direction following one of the prevailing trends of eruptive fissures (see rose diagram inset in Fig. 2.5a). As further discussed in Chapter 3, within such area a circular uniform distribution of eruptive fissures can be assumed, as the general pattern of fissures around the Gran Cono is almost radially distributed (Fig. 2.5a).

Locations of the “lost eruptive fissures” can be qualitatively given with a certain degree of confidence by considering the disposition of past eruptive fissures with respect to the volcanic edifice. Acocella et al. (2006a, 2006b) have extensively treated this topic, showing an almost radial disposition of the fissures with respect to the Vesuvius cone for the 1631-1944 eruptive period. Fig. 2.5a clearly illustrates this radial trend, although it also shows a significant prevalence of fissures mainly along the NW-SE direction (and partially along E-W direction), consistently with the orientation of the regional stress field and NW-SE trending regional structures (Fig. 1a; see also Section 2.4.5). “Lost eruptive fissures” should thus be located in an area roughly corresponding to the above-mentioned uncertainty high-density area of eruptive fissures.

2.4.5 Deep Faults

The deep faults dataset (Fig. 2.6) is composed of a linear feature class with 54 elements representing faults detected in the substratum.

These faults were identified and characterized through seismic reflection methods (45 faults, 35 after interpolation and 10 after extrapolation; Bianco et al. 1998; Bruno et al. 1998; Bruno and Rapolla

1999), gravimetric data (6 faults; Cassano and La Torre 1987) or mixed gravimetric and seismic reflection data (3 faults classified as “Neotectonic structures” by Ciaranfi et al. 1981). Seven out of 54 faults cross the SV caldera, as defined in the present work, two of them being located with mixed gravimetric/seismic data and the remaining five with geophysical data. Notably, the two faults that cross SV caldera, as evidenced by Ciaranfi et al. (1981), mimic the position and strike of other faults extrapolated from seismic profiles by Bruno et al. (1998), suggesting that they likely represent the same fault planes.

Fault lengths vary between about 400 m to 13.5 km and show a rather tight distribution along the NE-SW and NW-SE directions (Fig. 2.6), consistent with the mean orientation of the regional stress field (Bianco et al. 1998). All these faults have been

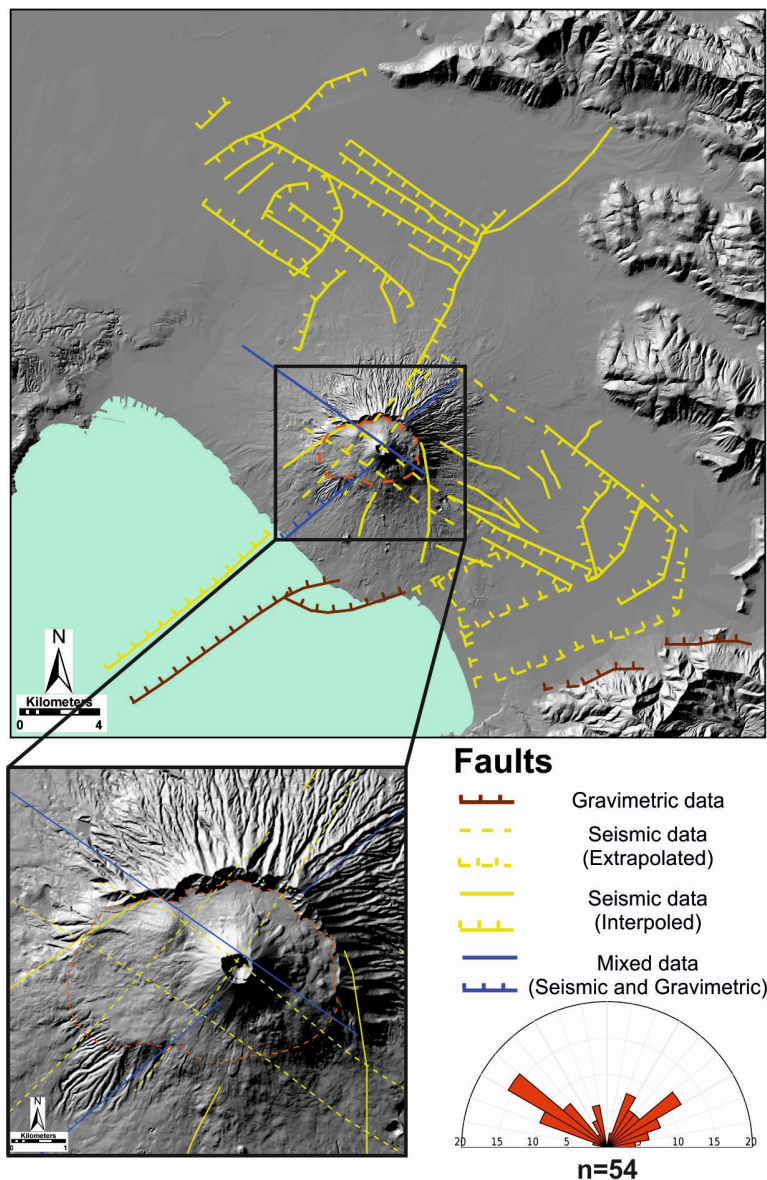


Fig. 2.6: deep faults dataset compiled after integration of different bibliographic sources (see text for details). Petal size of related rose diagrams is 10°.

located within the Mesozoic carbonate basement (Ciaranfi et al. 1981; Cassano and La Torre 1987; Bianco et al. 1998; Bruno et al. 1998) or within the shallower 150-200 m of alluvial/volcanic deposits (Bruno and Rapolla 1999). The top of the carbonate basement underneath the Campanian plain has been calculated from geophysical data inversion (Bruno et al. 1998) and gravimetric data (Cella et al. 2007) and varies from more than 2,000 m b.s.l. in the Acerra and Pompeii grabens, up to shallower depths (1,400-1,500 m b.s.l) below the SV area. Extrapolation of fault planes from geophysical profiles has been put forward by Bruno et al. (1998) as well, with specific focus on structures that cut the SV caldera (Fig. 2.6). These inferred faults are consistent with numerous observations of fault planes from other sources (Ciaranfi et al. 1981; Cassano and La Torre 1987; Florio et al. 1999). Local fault kinematics at SV are also consistent with regional fault kinematics, that is normal to sinistral for the NW–SE-trending faults and normal to dextral for the NE–SW-trending structures (Bianco et al. 1998; see Section 1.2.1).

For the deep faults dataset, a linear uncertainty area is assumed here with a width of 150 m, a value that takes into account the typical resolution limit of seismic profiles (F. Mazzarini, personal communication).

2.5 Concluding remarks

New and revised datasets of the eruptive and structural features of the Somma-Vesuvio volcanic complex have been developed with the aim of synthesizing a uniform geo-database that complements and extends existing datasets. These datasets relate specifically to a new reconstruction of the inferred locations of past eruptive vents and fissures of SV activity and to some regional/local structures, with particular emphasis being placed on enumerating associated uncertainties. Such information is relevant to reaching a better understanding of the eruptive behavior of the volcanic complex and to produce more accurate hazard assessment studies. SV clearly shows a significant spatial variability of its past activity as a function of time and type of eruption. Field evidence and theoretical studies show that such variability can significantly affect the areas impacted by erupted products, and specific attention is warranted for localities that might potentially be inundated by pyroclastic density currents.

The important specific attribute of the new datasets is the consideration and quantification of spatial uncertainty as it affects the reconstruction of such information through the use of uncertainty

areas and of topological elements drawn around the variables considered to encompass their positional imprecision. This innovative feature of the datasets serves to reflect quantitatively the intrinsic uncertainty that attends such information - due, on one side, to a lack of complete, detailed knowledge of past events (i.e. epistemic uncertainty) and, on the other, to the unpredictable variability of the dynamics of the system (i.e. aleatoric or physical variability).

All the new data about uncertainty areas and the revised datasets are assembled in a volcanological geo-database, complementing existing individual topic and separate subject matter SV databases. This unifying geo-database can be queried and updated, and is currently under further development with the inclusion of further fresh or revised data and information about past activity (i.e. isopachs of PDCs and fallout thickness, lahars inundation areas, geochemical and geophysical data, etc.). Because the new database includes specific information on some sources of uncertainty affecting the data, it also represents a valuable source of information for the development of hazard assessment products.

In Chapter 3 the datasets presented here is used to produce a first quantitative background (or long-term) vent opening probability map of the SV caldera, with specific reference to the occurrence of sub-Plinian and Plinian events. This approach is, therefore, consonant with good practice in other volcanic areas where sufficient information and plentiful data are available (Cappello et al. 2012; Connor et al. 2012; Bartolini et al. 2013; Bevilacqua et al. 2015).

Appendix A: analysis of epistemic uncertainties for parasitic vents

This appendix provides more details to the analysis about the discrepancies (among different bibliographic sources) of the number of parasitic vents occurred during different SV eruptions, which are here coded through the notation “x/y”: these two numbers indicate, respectively, the sum of all vents calculated using (for eruption with discrepancies) the minimum (x) and maximum (y) number of cited vents. For example, considering 1794 eruption, we have 4 vents from Scandone et al. 1993; 8 vents from Nazzaro 1997 and 6 vents from Ricciardi 2009. In this case the minimum and maximum are 4 and 8, respectively. Table 2.2 reports such values in the “Bibliography MIN/MAX” column. Considering the three sources as a whole, parasitic vents have been reported for 27 different eruptions between 1723 and 1906 eruptions with a total number of vents of 98-123 (Table 2.2). With the information available it was possible to define qualitatively the positions of the vents cited in bibliography using SV caldera morphological sectors (Fig. 2.1b): as an example, parasitic vents from the May 1858-Apr 1861 eruption cited by Scandone et al. (1993) were placed in Sector D of SV caldera because the authors provided as location site for these vents the “Piano delle Ginestre” area (see Additional file 1 for more details). Within SV caldera sectors (Fig. 2.4), 29-42 vents to sector A, 11-13 vents were assigned to sector B, 14 vents to sector C, 10 vents to sector D, 19-23 vents with an unknown localization within the whole caldera, 15-20 vents outside the SV caldera. In Table 2.2, for each record it is provided the number of vents reported in each source and, where possible, qualitative indications about vent locations. Black colored records represent eruptions with parasitic vents cited only in one source; light blue colored records represent eruptions with parasitic vents cited in two sources or cited in all the three sources but with differences in vents number; red colored records indicate eruptions with full agreement among the sources. Data from Nazzaro (1997) and Ricciardi (2009) are underestimated due to ambiguities in vent citations for some eruptions.

	SCANDONE 1993			NAZZARO 1997			RICCIARDI 2009		
Eruption	n° Vent(s)	Location	Notes	n° Vent(s)	Location	Notes	n° Vent(s)	Location	Notes
Apr-Jul 1723	2	?	-	-	-	-	-	-	-
May-Jun 1737	-	-	-	1	W flank of Gran Cono, in correspondence of the 1631 suture	-	-	-	-
Oct 1750	3	?	-	-	-	-	-	-	-
Oct-Nov 1751	2	?	-	1	SE base of Gran Cono, in correspondence of the 1631 suture	-	1	At the southeastern base of the Gran Cono, in correspondence of the 1631 suture	-
Mar 1752	3	?	-	-	-	-	3	1751 Lava flow	-
Dec 1754-Mar 1755	4	On the Gran Cono toward Ottaviano	Several vents	4	S flank of Atrio del Cavallo, in correspondence of the 1631 suture	-	1	Atrio del Cavallo	-
Dec 1760-Jan 1761	2	1.5 mile N of the Royal road	-	7	300 m a.s.l., "il Noto" locality	-	Some (2)	300 m a.s.l. between Camaldoli della Torre and Fosso della Monaca	-
Jan 1774	1	Near canale dell'Arena	-	-	-	-	-	-	-
Sep 1789	5	?	-	-	-	-	5	Base of Gran Cono toward Ercolano	-
Jun-Jul 1794	4	-	Location provided by Santacroce and Sbrana 2003	8	"Montedoro" W fracture, in between 480 and 320 m a.s.l.	"Some vents"	6	?	-
Sep 1810	-	-	-	3	S flank of Gran Cono, "Pedicino" locality	-	-	-	-
Dec 1819 - May 1820	6	NW side of the crater ("Coutrel" vent)	-	-	-	-	6	?	-
Oct 1821	2	?	-	-	-	-	6	?	-
Jan 1822	2	?	-	-	-	-	-	-	-
Feb-Oct 1822	1	?	-	-	-	-	-	-	-
Sep 1822	1	?	-	-	-	-	-	-	-

Oct-Nov 1822	3	In the crater and on the flank of Gran Cono toward Camaldoli	Several vents	-	-	-	-	-	-
Aug-Sep 1834	-	-	-	12	E base of Gran Cono, in correspondence of the 1631 suture	-	-	-	-
May 1855	3	N side of the Cone	-	11	N side of the cone, between 1068 and 898 m a.s.l.	-	11	N side of Gran Cono, between 1068 and 898 m a.s.l.	At the end of may only the lower group of cones (at 898 m a.s.l.) is still active
May 1858-Apr 1861	11	Piano delle Ginestre	-	9	NNW, SW (Piano delle Ginestre), N (near 1855 vents)	-	6	Atrio del Cavallo	Lava tube (exit near S. Vito di Ercolano)
Dec 1861	3	?	Location provided by Santacroce and Sbrana 2003	8	Near "Montedoro" fracture, in between 300 and 218 m a.s.l.	"Some vents"	-	-	-
Jun 1891-Jun 1894	4	N flank of Gran Cono at 900-1000 m AND at 830 m along 1868 fissure	Exhogenous tholoid (Colle Margherita)	8	N flank of Gran Cono and next to 1834 vents (900, 875 and 830 m a.s.l.)	Exhogenous tholoid (Colle Margherita)	-	-	-
Jul 1895-Sep 1899	4	1185, 1100, 900 and 750 m asl	Exhogenous tholoid (Colle Umberto)	6	1170, 1100, 900, 750 m a.s.l., to the E of such vents	Exhogenous tholoid (Colle Umberto)	6	?	Exhogenous tholoid (Colle Umberto)
Aug 1903-Sep 1904	1	Valle dell'Inferno	Exhogenous tholoid (Cupola 1937)	1	E zone of Valle dell'Inferno, near 1834 and 1850 vents	Exhogenous tholoid (Cupola 1937)	1	Valle dell'Inferno	Exhogenous tholoid (Cupola 1937)
Oct 1904-Feb 1906	2	NW side of the Gran Cono at 1245 m asl and 1180 m asl	-	2	NW side of the Gran Cono at 1245 m asl and 1180 m asl	-	-	-	-
Feb/Apr 1906	1	On the Gran Cono at 1180 m asl	-	-	-	-	-	-	-
Apr 1906	3	S side of the Gran Cono	11 vents according to Bertagnini et al. 1991 and IGM 1906	3	S side of the Gran Cono	11 vents according to Bertagnini et al. 1991 and IGM 1906	-	-	-
TOT	73			84	(Underestimation)		52	(Underestimation)	

Table 2.2: summary table for parasitic vents epistemic uncertainty analysis.

Appendix B: analysis of epistemic uncertainties for eruptive fissures

Similarly to parasitic vents, also the eruptive fissures show discrepancies among different bibliographic sources (Table 2.3) and between these and the fissures mapped, resulting in a certain amount of “lost eruptive fissures”. With respect to the 29 fissures mapped or inferred (over the period between AD 1631 and 1944), the number of “lost eruptive fissures” is 28-38 (here the notation is the same as that used for parasitic vents). For each record it is provided the number of fissures reported in each source and, where possible, qualitative indications about fissure locations. Black colored records represent eruptions with fissures cited only in one source; light blue colored records represent eruptions with fissures cited in two sources or cited in all the three sources but with differences in fissures number; red colored records indicate eruptions with full agreement among the sources.

Eruptive fissures could be closely related to parasitic vents, as for several fissures, their linear development is marked by the alignment of parasitic vents (e.g. 1760, 1794 and 1861 eruptions; Fig. 6a; Scandone et al. 1993). Table 2.4 provides a comparison between different eruptions (from the period 1631-1944) and the occurrence of vents versus eruptive fissures for each eruption. From this table it is possible to evaluate that for 17 eruptions, bibliographic sources report the contemporaneous occurrence of eruptive fissures and parasitic vents. Among these events it was possible to estimate that for 7 of them (1754-55, 1760-61, 1794, 1861, 1891-94, 1895-99, 1906) 24 mapped parasitic vents were located along their related eruptive fissures, while for the remaining 10 (1723, 1737, 1751, 1819-20, 1821, 1822, 1834, 1855, 1855-58, 1903-04) this relation is either absent or not demonstrable. Four other parasitic vents from earlier ages are located along eruptive fissures as well.

	SCANDONE ET AL. 1993			ACOCCELLA ET AL. 2006			RICCIARDI 2009		
Eruption	n° of Fissure(s)	Location	Notes	n° of Fissure(s)	Location	Notes	n° of Fissure(s)	Location	Notes
Dec 1631	-	-	-	1	Max distance from the Gran Cono: ? Azimuth: 220°	Lenght: ?	-	-	-
Apr 1694	-	-	-	1	Max distance from the Gran Cono: 1485 m Azimuth: 290°	Lenght: 450 m	-	-	-
Lug 1697	-	-	-	-	-	-	1	Base of Gran Cono (associated lava flow toward Torre del Greco)	-
Sep 1697- Jan 1698	3	On the Gran Cono	-	1	Max distance from the Gran Cono: 3645 m Azimuth: 255°	Lenght: 450 m	-	-	-
May 1698 - Jul 1698	1	SW of the crater	-	-	-	-	-	-	-
Jul 1701	1	E base of the Gran Cono	-	1	Max distance from the Gran Cono: 1840 m Azimuth: 135°	Lenght: 1330 m	-	-	-
Jun 1714	-	-	-	1	Max distance from the Gran Cono: 1645 m Azimuth: 150°	Lenght: 760 m	-	-	-
Jun 1717	2	S and E flank of the Gran Cono	-	1	Max distance from the Gran Cono: 1705 m Azimuth: 185°	Lenght: 1000 m	-	-	-
Apr-Jul 1723	-	-	2 vents	1	Max distance from the Gran Cono: ? Azimuth: ?	Lenght: ?	-	-	-
May-Jun 1737	1	SW flank of the Gran Cono	-	1	Max distance from the Gran Cono: 1025 m Azimuth: 260°	Lenght: 660 m	-	-	-
Oct-Nov 1751	1	SE flank of the Gran Cono toward Bosco	-	1	Max distance from the Gran Cono: 2565 m Azimuth: 140°	Lenght: 1280 m	-	-	-

Dec 1754- Mar 1755	1	On the Gran Cono toward Boscotrecase and toward Ottaviano	-	1	Max distance from the Gran Cono: 1225 m Azimuth: 145°	Lenght: 1000 m	-	-	-
May 1759	1	On the Gran Cono toward Boscotrecase	-	-	-	-	-	-	-
Dec 1760	1	1 mile N of Boscotrecase	-	1	Max distance from the Gran Cono: 4025 m Azimuth: 175°	Lenght: 2200 m	-	-	-
Apr 1766	2	SE and SW flank of Gran Cono	-	1	Max distance from the Gran Cono: ? Azimuth: ?	Lenght: ?	-	-	-
Oct 1767	1	Between N and NW near the top of the Gran Cono	-	1	Max distance from the Gran Cono: 2560 m Azimuth: 270°	Lenght: 1300 m	1	NW of Gran Cono	-
Mar 1770	1	E flank of Gran Cono	-	-	-	-	-	-	-
May 1771	1	Vallone dell'Arena	-	1	Max distance from the Gran Cono: 1585 m Azimuth: 270°	Lenght: 1050 m	1	E sector, 200 m from the crater	-
Jan-Mar 1776	2	1) NW of the cone toward Colle dei Canteroni (Oss. Vesuviano); 2) N-NW of the Gran Cono	-	-	-	-	-	-	-
May-Aug 1779	3	1) N-NE (of the cone?); 2) N side of the crater; 3) toward Ottaviano and Somma	-	-	-	-	-	-	-

Aug 1788	1	1.5 miles from the top of the Cone	-	-	-	-	-	-	-
Jun-Jul 1794	1	SW-NE	-	1	Max distance from the Gran Cono: 3360 m Azimuth: 250/260°	Lenght: 1300 m	2	1) N sector, NE direction; 2) S sector, SW direction	-
Aug 1804- Oct 1805	-	-	-	1	Max distance from the Gran Cono: 1120 m Azimuth: 225°	Lenght: 820 m	-	-	-
Sep 1809	1	SE flank of the crater	-	-	-	-	-	-	-
Jan-Feb 1812	1	SE side of the cone	-	-	-	-	1	Summit of Gran Cono (associated lava flow toward Torre del Greco)	-
Dec/24/1813	-	-	-	-	-	-	1	SW direction (associated lava flow toward Boscotrecase and Torre Annunziata)	-
Dec 1817	1	NE flank of the cone	-	-	-	-	-	-	-
Dec 1819 - May 1820	1	W (of the Gran Cono)	-	1	Max distance from the Gran Cono: 1200 m Azimuth: 250/275°	Lenght: 750 m	-	-	-
Oct 1821	-	-	2 vents	-	-	-	Some	NW of Gran Cono and in the Atrio del Cavallo	-
Oct-Nov 1822	1	On the Gran Cono to the E	-	2	1) Max distance from the Gran Cono: 895 m Azimuth: 285° 2) Max distance from the Gran Cono: 1255 m Azimuth: 180°	1) Lenght: 500 m 2) Length: 1000 m	-	-	-
Nov 1833- Jan 1834	1	SW base of the Gran Cono	-	-	-	-	-	-	-
Aug- Sep 1834	-	-	4 vents	1	Max distance from the Gran Cono: 2260 m Azimuth: 130°	Lenght: 1650 m	1	At the base of Gran Cono (associated lava flow on the E side of Gran Cono toward Caposecchi and S. Giovanni)	-

Jan 1839	2	On the Gran Cono to the E and W	-	1	Max distance from the Gran Cono: 2360 m Azimuth: 125°	Lenght: 1400 m	-	-	-
1847	-	-	-	1	Max distance from the Gran Cono: 1380 m Azimuth: 240°	Lenght: 1130 m	-	-	-
Feb 1850	2	1) On the Gran Cono to the N 2) Associated Lava Flow toward Poggiomarino	-	1	Max distance from the Gran Cono: 1980 m Azimuth: 135°	Lenght: 1100 m	1	At the base of Gran Cono (associated lava flow toward Boscotrecase)	-
May 1855	-	-	3 vents	1	Max distance from the Gran Cono: 1025 m Azimuth: 315°	Lenght: 1000 m	1	N side of Gran Cono, between 1068 and 898 m a.s.l.	-
May 1858	-	-	11 vents	1	Max distance from the Gran Cono: 1360 m Azimuth: 285°	Lenght: 1000 m	1	Atrio del Cavallo	6 vents
Dec 1861	1	2 km from Torre del Greco	-	1	Max distance from the Gran Cono: 3630 m Azimuth: 250°	Lenght: 600 m	1	Near Torre del Greco, between 300 and 218 m a.s.l.	-
Nov 1867- May 1868	2	SE flank of the crater and ESE flank of Gran Cono	-	-	-	-	1	NNE side of Gran Cono	-
Nov 1868	1	NW flank near 1855 vents	-	1	Max distance from the Gran Cono: 860 m Azimuth: 10°	Lenght: 520 m	-	-	-
Jan-Apr 1871	-	-	-	1	Max distance from the Gran Cono: 1530 m Azimuth: 290°	Lenght: 550 m	-	-	-
May 1871- Apr 1872	1	NW side (in Atrio del Cavallo)	-	-	-	-	-	-	-

Apr 1872	2	NW side of the Gran Cono and S side of the cone toward Camaldoli	-	1	Max distance from the Gran Cono: 1000 m Azimuth: 320°	Lenght: 640 m	2	1) NW side of Gran Cono (from summit up to Atrio del Cavallo, 300 m long); 2) S side of Gran Cono (associated lava flow toward Camaldoli hill)	-
Dec 1881-Jan 1884	-	-	-	1	Max distance from the Gran Cono: 1450 m Azimuth: 115°	Lenght: 1200 m	1	E side of Gran Cono	-
May 1885-Jul 1886	2	Toward Torre Annunziata and toward Boscotrecase	-	2	1) Max distance from the Gran Cono: 660 m Azimuth: 220° 2) Max distance from the Gran Cono: 900 Azimuth: 270°	1) Lenght: 600 m 2) Lenght: 600 m	-	-	-
Jun 1891-Jun 1894	1	NNW side of the Gran Cono (Colle Margherita)	-	1	Max distance from the Gran Cono: 1490 m Azimuth: 0-30°	Lenght: 1200 m	1	Colle Margherita	-
Jul 1895-Sep 1899	1	WNW side of the Gran Cono (Colle Umberto)	-	1	Max distance from the Gran Cono: 1460 m Azimuth: 310°	Lenght: 1080 m	1	Colle Umberto	-
Aug 1903-Sep 1904	1	WNW side of the Gran Cono	-	-	-	-	-	-	-
Apr 1906	-	-	3 vents (11 according to Bertagnini et al. 1991)	1	Max distance from the Gran Cono: 1480 m Azimuth: 140°	Lenght: 2000 m	1	SE side of the Gran Cono, from 1200 m a.s.l. up to 800 m a.s.l.	-
May-Jun 1913	-	-	-	1	Max distance from the Gran Cono: 1670 m Azimuth: 95°	Lenght: 1390 m	-	-	-
Jun 1929	-	-	-	1	Max distance from the Gran Cono: 1380 m Azimuth: 100°	Lenght: 930 m	-	-	-
Mar-Apr 1944	-	-	-	1	Max distance from the Gran Cono: ? Azimuth: 0.125°	Lenght: 700 m	-	-	-
TOT	46			38			19		

Table 2.3: summary table for eruptive fissures epistemic uncertainty analysis.

Eruption	Vent(s)	Fissure(s)	Eruption	Vent(s)	Fissure(s)
Dec 1631	N	Y	Dec 1817	N	Y
Apr 1694	N	Y	Dec 1819 - May 1820	Y	Y
Lug 1697	N	Y	Oct 1821	Y	Y
Sep 1697- Jan 1698	N	Y	Jan 1822	Y	N
May 1698 - Jul 1698	N	Y	Feb-Oct 1822	Y	N
Jul 1701	N	Y	Sep 1822	Y	N
Jun 1714	N	Y	Oct-Nov 1822	Y	Y
Jun 1717	N	Y	Nov 1833- Jan 1834	N	Y
Apr-Jul 1723	Y	Y	Aug-Sep 1834	Y	Y
May-Jun 1737	Y	Y	Jan 1839	N	Y
Oct 1750	Y	N	1847	N	Y
Oct-Nov 1751	Y	Y	Feb 1850	N	Y
Mar 1752	Y	N	May 1855	Y	Y
Dec 1754- Mar 1755	Y	Y	May 1858- Apr 1861	Y	Y
May 1759	N	Y	Dec 1861	Y	Y
Dec 1760- Jan 1761	Y	Y	Nov 1867- May 1868	N	Y
Apr 1766	N	Y	Nov 1868	N	Y
Oct 1767	N	Y	Jan-Apr 1871	N	Y
Mar 1770	N	Y	May 1871- Apr 1872	N	Y
May 1771	N	Y	Apr 1872	N	Y
Jan 1774	Y	N	Dec 1881- Jan 1884	N	Y
Jan-Mar 1776	N	Y	May 1885- Jul 1886	N	Y
May-Aug 1779	N	Y	Jun 1891- Jun 1894	Y	Y
Aug 1788	N	Y	Jul 1895- Sep 1899	Y	Y
Sep 1789	Y	N	Aug 1903- Sep 1904	Y	Y
Jun-Jul 1794	Y	Y	Oct 1904- Feb 1906	Y	N
Aug 1804- Oct 1805	N	Y	Feb/Apr 1906	Y	N
Sep 1809	N	Y	Apr 1906	Y	Y
Sep 1810	Y	N	May-Jun 1913	N	Y
Jan-Feb 1812	N	Y	Jun 1929	N	Y
Dec/24/1813	N	Y	Mar-Apr 1944	N	Y

Table 2.4: comparative table of parasitic vents versus eruptive fissures between the *AD 1631* and *1944* eruptions.

Chapter 3

Vent Opening Probability maps for Somma-Vesuvio

3.1 Introduction

Somma-Vesuvio (SV) is one of the most studied and risky volcanoes in the world. Its eruptive phenomena and record has been investigated through many studies since the very first eyewitness account of the famous *AD 79 Pompeii* eruption by Pliny the Younger (e.g. Sigurdsson et al. 1985; Cioni et al. 1992; Cioni et al. 2008). Volcanic risk is very high because surrounding areas are very densely inhabited, with over one million people directly threatened by the potential for devastating ash fallout, pyroclastic density currents and lahars (Cioni et al. 2008; DPC 1995, 2014; see Fig. 3.1).

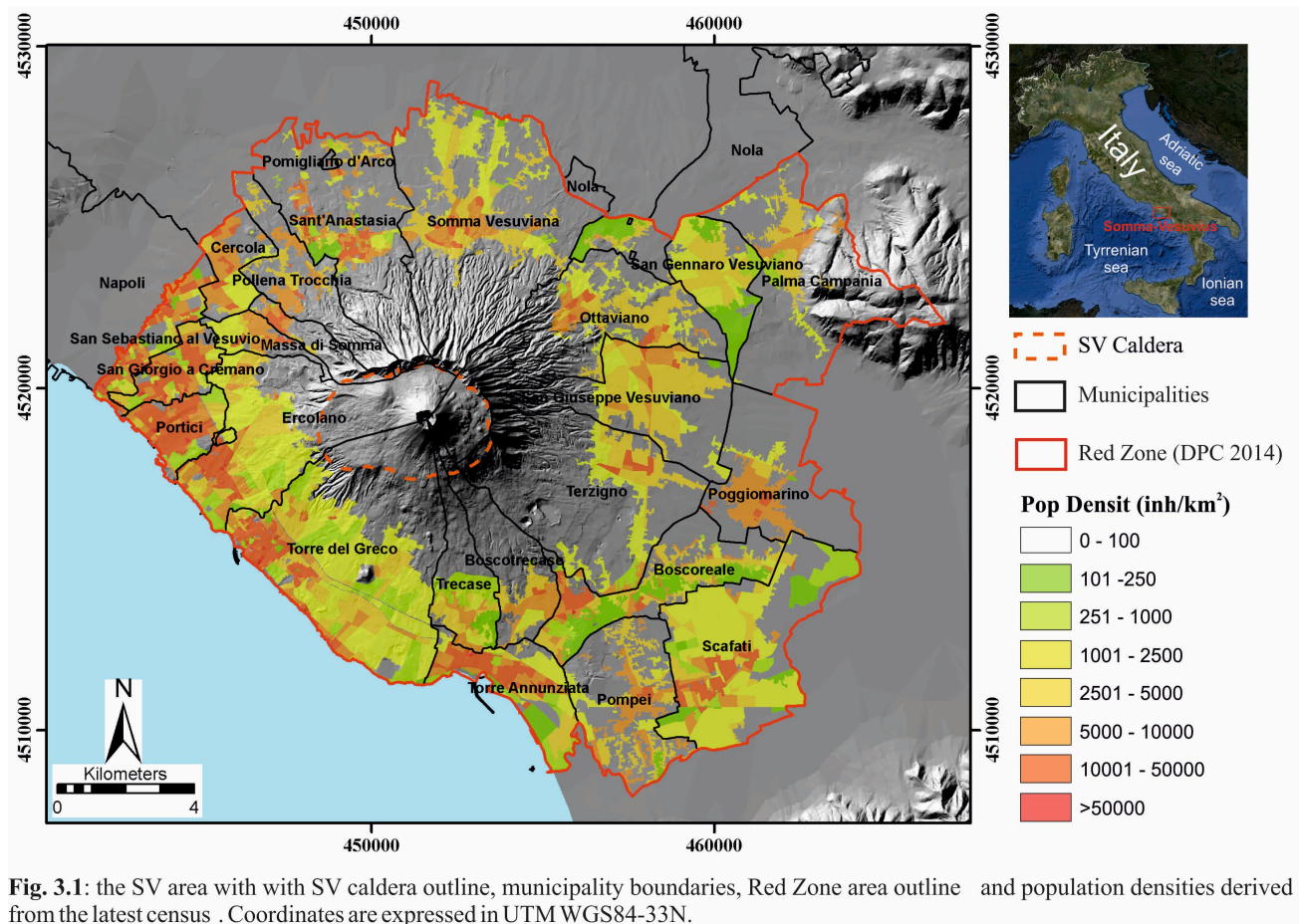


Fig. 3.1: the SV area with SV caldera outline, municipality boundaries, Red Zone area outline and population densities derived from the latest census. Coordinates are expressed in UTM WGS84-33N.

Over its history, SV volcano has exhibited a large variability in eruptive styles as well as a moderate but significant spatial variability in vent locations. In Chapter 2, a detailed reconstruction is presented of vent locations in past events, together with an assessment of some sources of associated

spatial uncertainties. For instance, it is now established that, especially over the last 2 ka, many volcanic vents opened outside the present SV caldera outline (Santacroce and Sbrana 2003; Principe et al. 2013) mainly on the western and southern flanks (Acocella et al. 2006b). In these cases, however, volcanic activity involved just effusive lava emissions or small-scale explosive eruptions from parasitic vents (e.g. Strombolian to Violent Strombolian events; Cioni et al. 2008).

As far as Plinian and sub-Plinian eruptions are concerned, field data indicate that their volcanic vents significantly varied in location but were always located within the present SV caldera. In particular, according to Cioni et al. (1999), the present outline of the SV caldera (an area about 4 km x 3 km) is the result of a multistage collapse after four major Plinian eruptions, with minor contributions from three sub-Plinian I eruptions (Cioni et al. 2008). In particular, during caldera-forming eruptions, the initial vent was always located inside the previously-formed caldera, or along its border, but field evidences suggest a subsequent migration of the vent as a result of collapse with consequent enlargement of the caldera itself. This variability appears to have had a strong influence on the distribution of eruptive products around the volcano, particularly those associated with pyroclastic density currents (PDC). Evidence for such effects are found in the reconstruction of PDC deposits (e.g. Gurioli et al. 2010) as well as in the outcomes of transient 3D numerical simulations of column-collapse scenarios which highlight a major effect of vent location and proximal topography of the volcano on the area invaded by the flows (Esposti Ongaro et al. in preparation).

Based on this knowledge, it is evident that a probability map of vent opening within the present SV caldera, together with estimates of associated uncertainties, would represent a crucial, objective basis for the assessment of volcanic hazards from a future explosive eruption at SV volcano. Vent opening probability maps, sometimes including information on associated uncertainty, have been produced to assess potential future activity in monogenetic volcanic fields (Connor et al. 2012), volcanic islands (Alberico et al. 2008; Marti and Felpeto 2010; Becerril et al. 2013), composite stratovolcanoes (Cappello et al. 2012) and calderas (Alberico et al. 2002; Selva et al. 2012; Bevilacqua et al. 2015). The only approach which considered vent opening variability at SV is the one proposed by Selva et al. (2014), who used a vent opening area solely for the evaluation of tephra fall hazard. In this latter case, the above-mentioned authors defined a vent opening area consisting of a circle of 6 km radius subdivided into five distinct areas, each with constant probability of vent opening. That area included several circum-Vesuvian towns like Torre del Greco and Ottaviano among others and

neglected any volcanological and structural information about past vents and faults. In contrast, numerical modeling for PDC hazard scenarios from SV explosive eruptions have, thus far, simply assumed a central vent corresponding to the present Gran Cono edifice (e.g. Neri et al. 2007; Esposti Ongaro et al. 2008; Macedonio et al. 2016).

The aim of this Chapter is to present the first background (also referred to as the long-term or base rate) probability maps of vent opening for the SV caldera that incorporates information and related uncertainty about some key parameters of the volcanic system: to do so, it is not presented a single map for a specific scenario but rather a set of three maps (a spatial distribution map of the mean probability of vent opening location with two maps of the associated confidence percentiles, based on epistemic uncertainty quantifications derived from a structured elicitation of specialists, using alternative pooling procedures to combine judgements). In particular, the set of three maps express the probability of vent opening conditional on the occurrence of either a new Plinian or sub-Plinian eruption in the foreseeable future. This is achieved by considering the known eruptive record of SV in the last about 20 ka, as well as the distribution of key structural features of the caldera. The probability model assumed is doubly stochastic, in the sense that the probability values representing the spatial physical (also called aleatoric) variability affecting the vent opening process are themselves affected by epistemic uncertainty (Sparks and Aspinall 2004; Bevilacqua et al. 2015; Bevilacqua 2016). Sources of epistemic uncertainty relate to the uncertain locations of past vents, the incompleteness of the eruptive record, and uncertain weights given to the different volcanic system variables under consideration (Bevilacqua et al. 2015; see also Chapter 2).

By accounting for the possible variability of vent location (e.g. as for the Campi Flegrei caldera: Selva et al. 2010; Neri et al. 2015), the derived maps represent an important information basis for producing long-term, or background, probabilistic hazard maps for the main phenomena associated to medium-large scale (such as Plinian and sub-Plinian) events at SV. In case of a future unrest, the maps will offer a “zero configuration” from which to elaborate new maps of vent position probability based also on real-time monitoring data.

3.2 Methods

The method that has been followed is based on the assumption that the probability of new vent opening can be computed as a weighted linear combination of the spatial distributions of key physical variables of the system that reflect, or can influence, this process. In other words, with such assumption we assume that new vents will likely open close to the previous ones, and their location will be influenced by the presence of geological structures such as major faults and fractures. A very similar approach was applied by Bevilacqua et al. (2015) for the definition of vent opening maps at Campi Flegrei caldera (Italy), whereas similar approaches, but involving some different techniques, have been applied, for instance, by Marti and Felpeto (2010), Cappello et al. (2012), Connor et al. (2012), Selva et al. (2012) and Bartolini et al. (2013) for mapping vent opening at other effusive and explosive volcanoes.

In this study data from literature have been used as well as new information as presented in Chapter 2. In particular, the data sets considered in the analysis were: 1) the distribution of eruptive vents which produced past Plinian and sub-Plinian events; 2) the distribution of vents which produced explosive events such as Violent Strombolian (VS) and Continuous Ash Emission (AE) eruptions; 3) the spatial distribution of effusive vents and eruptive fissures in the past, and 4) the distribution of structural data. Given the volcanological and geological data available, and based on the present understanding of the volcano, these distributions, here assumed representative of the aleatoric variability of the vent opening process, appeared to be the ones most closely correlated with vent opening potential, with major faults being indicative of sectors of crustal weakness inside the caldera.

This said, it is acknowledged that the probability of new intra-caldera vent opening could be correlated with other system variables or with complex processes that were not considered, due to lack of sufficient knowledge about them. To account for any contribution from these neglected factors and to represent missing information, we included a conservative spatial uniform distribution inside the SV caldera. For instance, with respect to the possible fault effect, it is important to point out that: i) a rising feeder dike could be captured by a pre-existing fault but only if it is favorably oriented (e.g. Gaffney et al. 2007) and ii) fault zones involve the development from a main fault plane of a broader volume of distributed brittle deformation, called the ‘damage zone’ (Kim et al. 2004) which might be important for defining the surface expression of the opening dyke (Mazzarini et al. 2013). Once the various datasets have been defined (see Chapter 2), Gaussian kernels (Appendix A) with different bandwidths

were applied to each variable considered in order to produce the associated continuous probability density maps.

For this project, the Structured Expert Judgement (SEJ) elicitation consisted of two elicitation sessions involving 15 participating specialists with different levels of experience, scientific interests, and from a variety of institutions. The main goal of the elicitation was to achieve transparent, robust, and shared distributional estimates for the weights to be attributed to the different variables considered. This objective was achieved by taking advantage of well-established experts' pooling methods, namely the Cooke's Classical Model (CM), the Expected Relative Frequency (ERF) and an Equal Weight (EW) rule (e.g. Cooke 1991; Aspinall 2006; Flandoli et al. 2011; Bevilacqua 2016]. A detailed description of the two elicitation sessions, along with the description of the different pooling methods is provided in Appendix B. This approach differs from previous studies where weights were deterministically assigned by the authors to variables with unknown values (e.g. Selva et al. 2012; Bartolini et al. 2013).

3.3 Data sets description and associated spatial density distributions

In this section the main features of the datasets considered in the study are briefly summarized. For a more detailed description of the data sets including the basis on which the uncertainty sources were quantified please refer to Chapter 2. For each data set, the corresponding continuous density functions representing the conditional probability of vent opening associated with it are also presented. Such maps were obtained by applying a Gaussian kernel with the specific bandwidth adopted for each data set, as reported in Appendix A.

3.3.1 Vent location of large-medium scale explosive eruptions

The data set of vent location of large-medium size explosive eruptions consists of four Plinian (i.e. *Pomici di Base*, *Mercato*, *Avellino*, and *AD 79 Pompeii* – Fig. 2a) and six sub-Plinian (i.e. *Greenish Pumices*, *AP1*, *AP2*, *AD 472 Pollena*, *AD 512*, *AD 1631* – Fig. 2c) eruptions (VEI range 3-5) occurred since 22 ka BP. The six sub-Plinian eruptions include both sub-Plinian I and sub-Plinian II as defined by Cioni et al. (2008) and discussed in Chapter 2.

For this data set, we considered uncertainty areas centered on vent positions deriving from the interpretation of isopachs/isopleths and caldera structural information (Chapter 2). Depending on the eruption type or the features of the specific event, various uncertainty area extents were assumed: i) for Plinian eruptions, the extent has been assumed equal to the area of the related caldera collapse as defined in Cioni et al. (1999); ii) for the sub-Plinian *AD 1631* and *AD 512* eruptions, the uncertainty area encloses the area of the Gran Cono; iii) for the *AD 472 Pollena* eruption, the extent was assumed similar to that of the *AD 1631* eruption, but centered on the *Pollena* vent location as inferred by Sulpizio et al. (2005) and cut according to the SV present caldera outline; iv) for the *Greenish Pumices* eruption, uncertainty area extent was assumed the same as the *Pomici di Base* eruption but was centered on the *Greenish Pumices* vent location and cut according to the SV present caldera outline; v) for the *AP1* and *AP2* eruptions the extent was the same as the *Avellino* eruption.

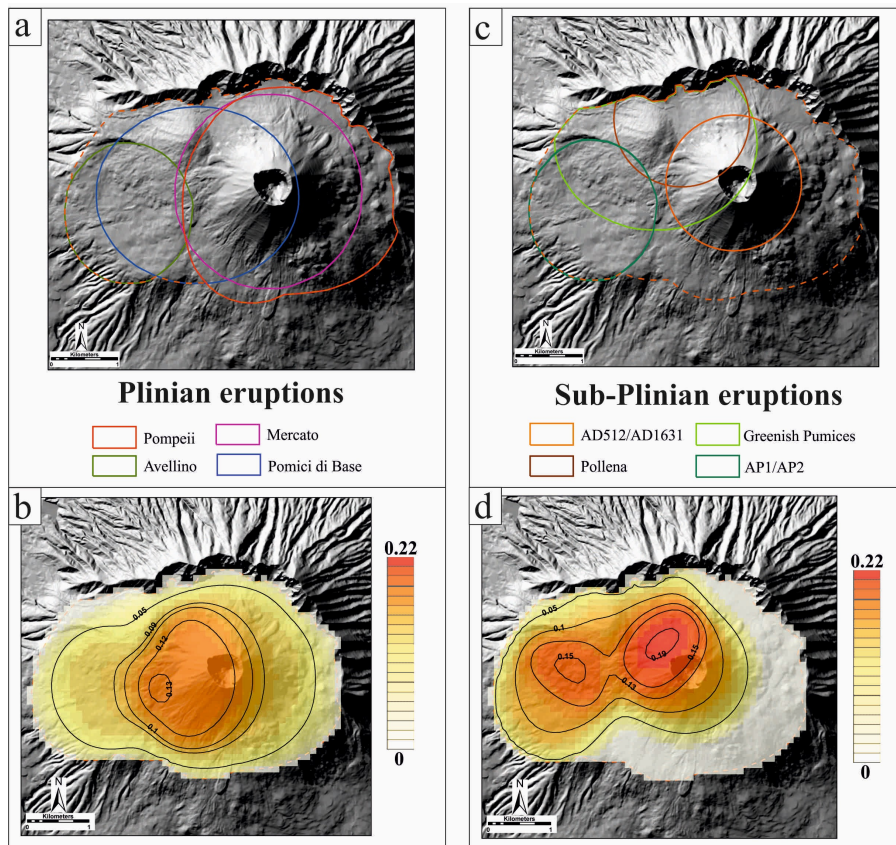


Fig. 3.2: a) vent uncertainty areas of 4 Plinian eruptions; b) probability density map for Plinian eruptions after the application of a Gaussian kernel (bandwidth is 220 m; cellsize is 100 m; values are probability percentages per cell; contour lines enclose areas where cell values are higher than the value of the line itself); c) vent uncertainty areas of 6 SubPlinian eruptions (I and II); d) probability density map for sub-Plinian eruptions after the application of a Gaussian kernel (bandwidth is 220 m; cellsize is 100 m; values are probability percentages per cell; contour lines enclose areas where cell values are higher than the value of the line itself). SV caldera is outlined in dark orange dashed line.

Based on the volcanological and structural evidences discussed in Chapter 2, each uncertainty area was assumed to enclose 100% probability of the location of the corresponding past vent. Within the area, probability was assumed uniformly distributed. As described in Appendix A, Gaussian kernel were applied to these latter uniform distributions, (Fig. 3.2b and 3.2d): the bandwidth (h) was assumed equal to the mean minimum distance between the

centroids of the circles/ellipses (220 m) since it is related to the spatial spread of the observed past vents. The distribution of the Plinian data set (Fig. 3.2b) shows that the density is quite smoothly spread over all the caldera, with maximal cell values located about 1 km west of the Gran Cono crater. Conversely, for the sub-Plinian data set (Fig. 3.2d) the density shows significantly higher values with two peaks concentrated about 500 m northwest and about 2 km west of the Gran Cono.

3.3.2 Small scale explosive eruptions

VS to AE eruptions have been included jointly into the small scale explosive eruptions data set, which comprises the vent location of 32 events that span a wide temporal window between the Avellino eruption (4.3 ka BP) and the last eruption of Vesuvio of AD 1944 (Cioni et al. 2008). The 32 vents of the VS eruptions and AE activity were mainly concentrated in the area of Gran Cono. However, due to relative low availability of field data (possibly related to the scale of these eruptions), we cannot exclude however that some events of a similar magnitude and intensity can be get lost in the stratigraphic record. As a consequence, for the VS to AE data set, three different uncertainty areas for spatial localization of vents are defined as a function of the temporal frame considered (see Chapter 2, for a detailed explanation of them). These are: i) the present crater of Gran Cono enclosing the last 10 VS to AE events that occurred between *AD 1631* and *AD 1944* eruptions (Fig. 3.3a); ii) the area of the Gran Cono representing the uncertainty area of 22 vents of eruptions occurred between the *Avellino* and the *AD 1631* eruptions (Fig. 3.3c) and iii) the portion of SV caldera that accounts for all the VS to AE eruptions that can be get lost in the stratigraphic record (Fig. 3.3e). This portion of the SV caldera corresponds to the extent of the SV caldera just before the occurrence of the Avellino eruption. As with the Plinian and sub-Plinian eruption cases, the uncertainty areas of these three maps are assumed to enclose 100% probability for the location of associated past vents and that such probability is distributed uniformly within the areas. However, in contrast with the Plinian and sub-Plinian data set, in this case each area refers to a group of eruptions, whose vent locations cannot be reconstructed, and not to a single event with an imprecise vent location. Figs. 3.3b, 3.3d and 3.3e show the density functions corresponding to the three areas (i.e. to Figs. 3.3a, 3.3c and 3.3e, respectively) respectively, obtained by application of symmetric Gaussian kernels. Kernel bandwidth was assumed fixed at 100 m, corresponding to the cell size of the grid adopted.

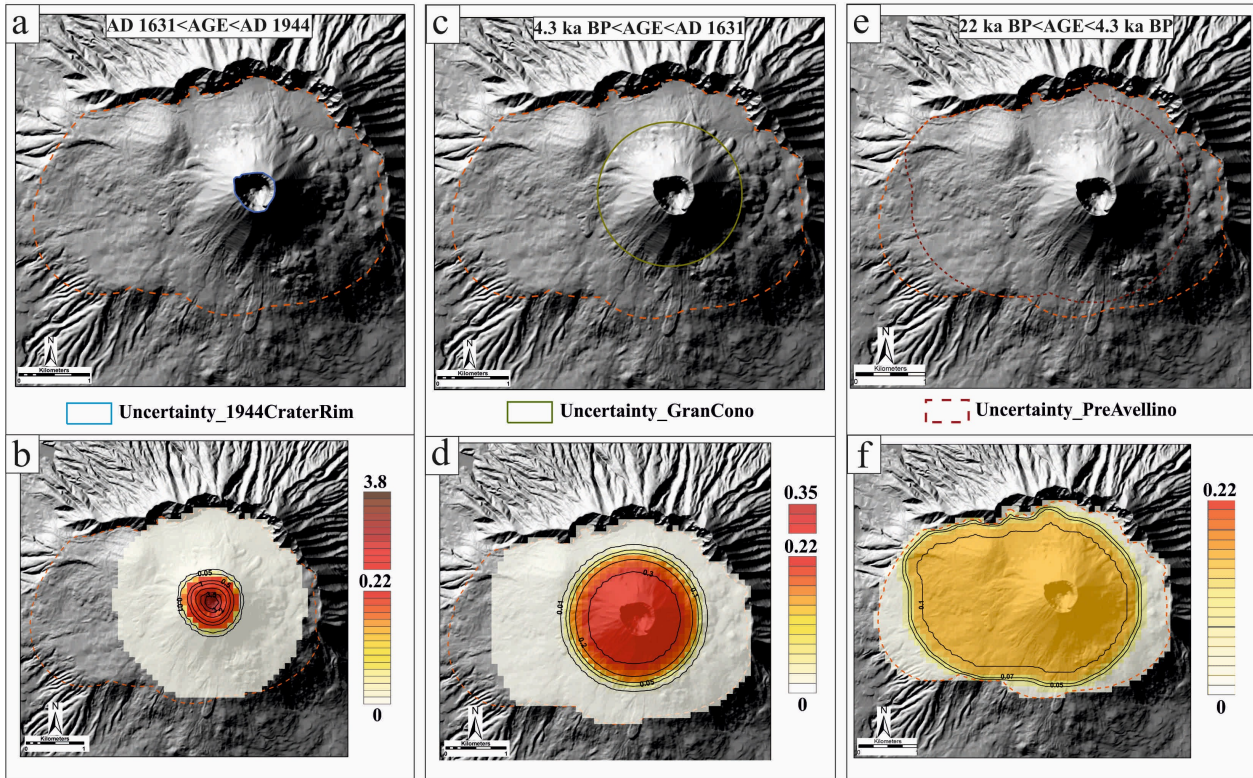


Fig. 3.3: Uncertainty areas of vent location of the small scale explosive eruption data set and associated probability density maps. a) vent uncertainty areas of 10 VS to AE eruptions occurred between AD 1631 and AD 1944 (area of the 1944 crater), b) probability density map associated to the uncertainty area in a) after the application of the Gaussian kernel (the bandwidth was assumed equal to 100 m as the cell size; values are probability percentages per cell); c) vent uncertainty area of 22 VS to AE eruptions occurred between 4.3 ka BP and AD 1631 (area of Gran Cono), d) probability density map associated to the uncertainty area in c) after the application of the Gaussian kernel (assuming the same parameters and meaning of b); e) vent uncertainty area of VS to AE eruptions occurred between 22 ka BP and 4.3 ka BP (portion of the SV caldera); f) probability density map associated to the uncertainty area in e) after the application of the Gaussian kernel (assuming again the same parameters and meaning of b). Colors the same for all the scale bars up to the value of 0.22. The extension of the SV caldera is outlined as orange dashed line.

3.3.3 Effusive eruptions

Following the description reported in Chapter 2, the effusive eruptions data set was sub-divided in two separate sub-data sets, the parasitic vents and the eruptive fissures.

Parasitic Vents

Among the parasitic vents cited in Chapter 2, 46 of them (referred to the period 1631-1944) are located within the SV caldera and have been directly used in this work (Fig. 3.4a). Each of these mapped parasitic vents were associated to a circular uncertainty area of 75 m radius (calculated from the mean radius of parasitic vents from different tectonic settings; see Chapter 2) which encloses their

localization. Also in this case the uncertainty areas of these three maps were assumed to enclose 100% of probability of the location of associated parasitic vents.

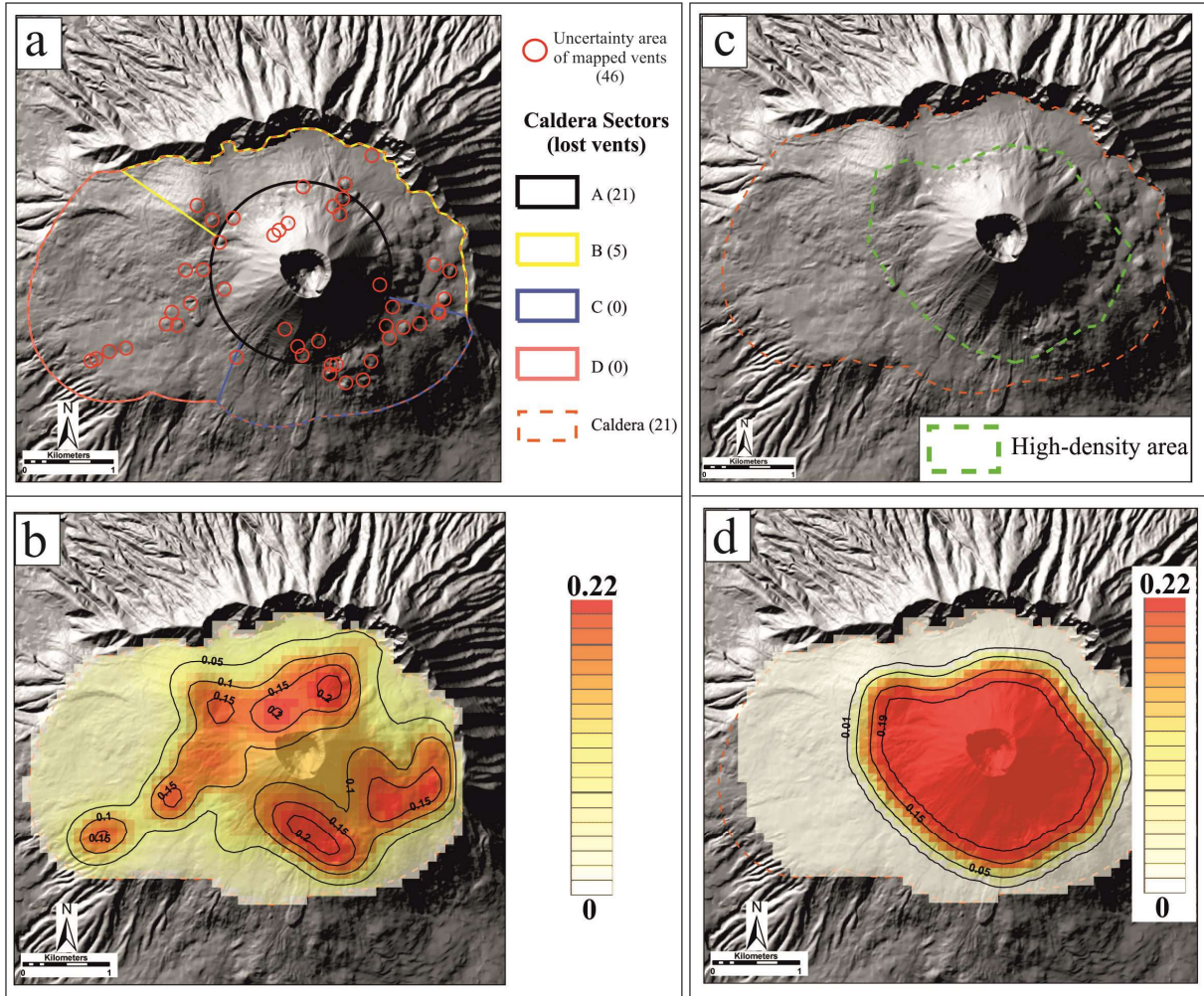


Fig. 3.4: a) map of uncertainty areas of 46 parasitic vents located within the SV caldera. 47 'lost' vents located in sector A (21), sector B (5) or within the whole caldera (21)(for details see Section 2.4.4); b) probability density map for Parasitic effusive vents after the application of a Gaussian kernel (bandwidth is 185 m; cellsize is 100 m; values are probability percentages per cell; contour lines enclose areas where cell values are higher than the value of the line itself); c) eruptive fissures high-density area related to eruptive fissures developed along Gran Cono; d) probability density map for Eruptive fissures after the application of a Gaussian kernel (bandwidth is 100 m; cellsize is 100 m; values are probability percentages per cell; contour lines enclose areas where cell values are higher than the value of the line itself). SV caldera is outlined in dark orange dashed line.

The major discrepancy between the number of vents cited in historical accounts and the number of mapped vents requires also the consideration of the so called "lost vent". With the information available, for a part of the lost vents it was possible in Chapter 2 to identify their position within

different sectors of the SV caldera (Fig. 3.4a). For the sake of the maps it is always assumed the arithmetic mean of the minimum and maximum values calculated in Chapter 2: lost vents are therefore four within sector A, five within sector B and 21 with an unknown localization within the whole SV caldera (Fig. 3.4a).

The related density function map for the effusive vent sub-dataset (Fig. 3.4b) has been produced by combining the map obtained after the application of the Gaussian kernel to the 46 mapped vents and with a map where the lost vents have been spread uniformly within their relative sectors. As with the Large explosive eruptions data set, the kernel bandwidth was assumed equal to the mean minimum distance between the centroids of the circles (185 m), since bandwidth is related to the spatial spread of observed past vents. Fig. 3.4b displays a map where the peaks of probability highlight the distribution of vents aligned along single eruptive fissures, and in this specific case two directions of elongation of peak areas can be envisaged (NW-SE and NE-SW).

Eruptive Fissures

Only 6 out of 32 eruptive fissures reported Chapter 2 can be mapped in the field, while (Acocella et al. 2006b) inferred the locations of the rest from historical accounts. Since there is a high uncertainty in eruptive fissure locations, it has been defined an uncertainty area of high-density eruptive fissures (Fig. 3.4c), which roughly corresponds to the extent of the Gran Cono itself. The probability of having had eruptive fissures within this area is considered uniform, as the general pattern of eruptive fissures around the Gran Cono is radial and almost equally distributed along all the directions (Chapter 2).

The resulting related density function, obtained using a bandwidth for the kernel equal to cell size dimension (Fig. 3.4d), indicates a uniform plateau, smoothly decaying towards the edges of the high-density area.

3.3.4 Deep Faults

The “Deep faults” dataset comprises faults detected mostly within the Mesozoic Quaternary carbonate basement (Chapter 2). Among the faults that cross the SV caldera described in Chapter 2 some of them have been identified only after extrapolation from seismic sections (Bruno et al. 1998), a procedure that possibly limits the reliability of the data. Therefore, in order to provide more

consistency to this data set, only faults that either have been interpolated from seismic profiles or that have been identified by at least two different bibliographic sources are considered here. This data set is thus composed of a total of 3 faults, 2 of them being fault planes extrapolated by Bruno et al. (1998)

(seismic reflection) but also confirmed by Ciaranfi et al. (1981) (identified from mixed gravimetric and seismic data), and the last one being a fault plane interpolated from seismic profile by Bruno and Rapolla (1999).

Following assumptions of Chapter 2, in order to take into account spatial uncertainty related to fault positions, it is considered an uncertainty area with a width of 150 m around each fault plane (Fig. 3.5a). For deep faults, the kernel bandwidth was assumed equal to the average damage zone (DZ) width which, in this study, has been considered proportional (linear) to the fault displacement. The latter one has been assumed equal to 190 m and has been estimated based on the fault length (L) according to Scholz (2002) for faults located within carbonate rocks ($DZ=3 \cdot 10^{-2} \cdot L$). The density map of Fig. 3.5d shows density probabilities focused very close to fault planes, even if peak values are only slightly higher with respect to peak values from other data set maps (see Section 3.3.1).

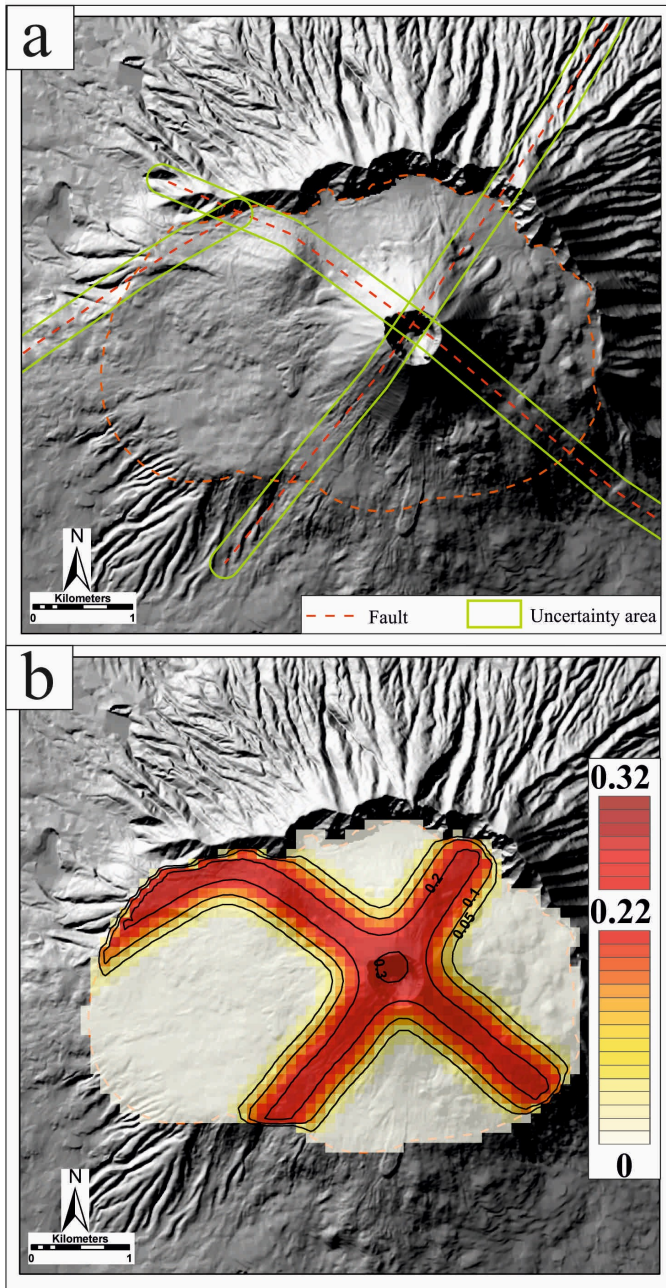


Fig. 3.5: a) map of uncertainty areas of deep faults. SV caldera is outlined in dark orange dashed line; b) probability density map for Deep faults after the application of a Gaussian kernel (bandwidth is 190 m; cellsize is 100 m; values are probability percentages per cell; contour lines enclose areas where cell values are higher than the value of the line itself.

3.4 Results

Once the spatial density maps described above were constructed, we applied the structured expert elicitation techniques described in Section 2 and Appendix B in order to attribute to each map a weight and combine them into a joint probability map. An alternative uniform distribution over the whole caldera area was also adopted to represent the possibility there may be no correlation between the vent opening distribution and the various mapped variables considered here.

As previously stated, three different expert judgment procedures have been applied to the elicitation data: i) Cooke Classical method (CM), ii) Expected Relative Frequency method (ERF), and iii) Equal weights rule (EW). The output probability percentiles of the Decision Maker have been represented by triangular distributions in the ERF case, while by Beta distributions in the other two cases (CM and EW). The approximation with Beta distributions was obtained choosing the shape parameters that minimize the maximum of the absolute errors on the three percentiles (shape parameters minimizing the sum of the absolute errors gave consistent results – differences below 1% on the weights estimates).

3.4.1 The weights of the variables considered

To simplify the quantification of weights for each spatial distribution, it was not asked to the experts to do this directly. Instead, as in Bevilacqua et al. (2015), a simple hierarchical logic tree has been defined (see Fig. 6), where most of the target questions quantify the relative importance, or relevance, of one variable or feature of the system versus others. It was followed a Monte Carlo simulation approach on the single branch weight estimates, multiplying the single estimates over each branch of the logic tree for obtaining the Beta probability distribution of the nine linear weights. In particular, in the logic tree of Fig. 3.6, each branch represents a pair or triplet of target questions asked to the experts. Sections 8.2.1 and 8.2.2 report respectively the initial and the revised questionnaires with target questions and the Decision Maker outcomes.

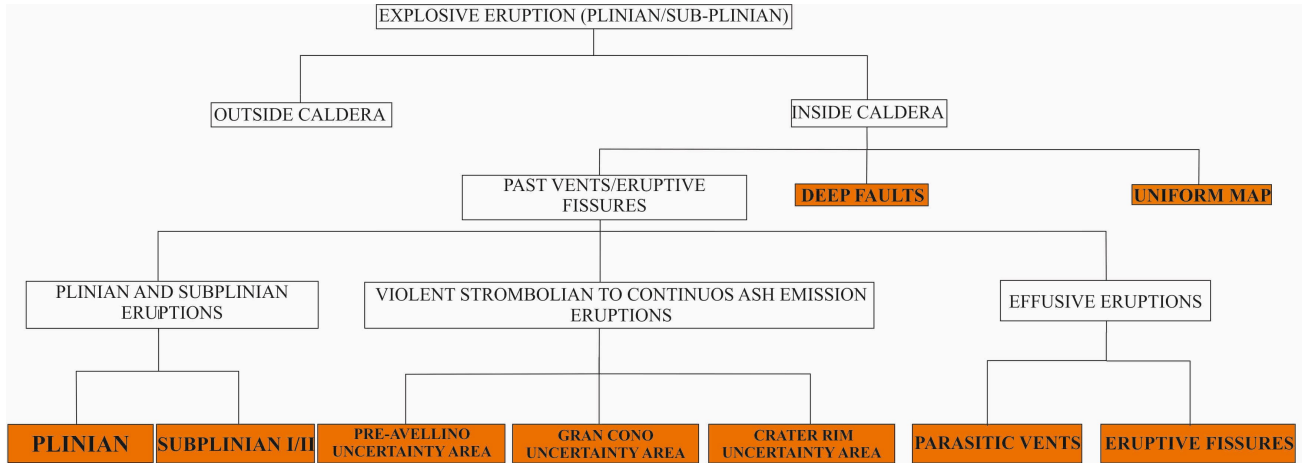


Fig. 3.6: logic tree for weights assignment to different questions during expert elicitation sessions. Orange colored boxes represent variables/datasets whose probability density maps have been linearly combined.

First, the experts were asked to evaluate the first tree branching probability: that the next Plinian/sub-Plinian eruption at SV will have its initial vent inside (versus outside) the present outline of the caldera. After that, when considering the location of the next future vent, the experts assessed the relative relevance of the information based on past volcanic activity compared to that for the distribution of deep faults and to a homogeneous distribution; this is at the second level of the tree in Fig. 3.6. At the next level down on the tree, the experts compared the relative importance of the volcanic features distributions associated with the different eruptive styles, i.e. Plinian/sub-Plinian versus VS/AE eruptions and versus effusive eruptions. And last, the perceived relative importance of past eruptive styles datasets was evaluated (i.e. Plinian versus sub-Plinian eruptions, VS to AE of different periods, parasitic vents versus eruptive fissures). In Table 3.1 are reported the median values and the 5th and 95th percentiles of the uncertainty distributions for the probability of having an initial vent inside or outside the caldera for the three different scoring rules considered. The medians values are those directly elicited from the experts (in the CM/EW cases), and they sum closer to 100% than the corresponding mean values. Since no other calculations have been done with these values, the relative mean values are not displayed here. For the opening of a new vent outside the caldera, these results suggest median values range from a minimum of about 6% (CM solution) to a maximum of about 10% (ERF solution), with corresponding upper credible range values (95th percentile) between 20.9% (ERF) and 31.8% (EW) and lower range values (5th percentile) between 0.4% (CM) and 2.4% (ERF).

	% - 5 th /Median/95 th								
	CM			ERF			EW		
<i>INSIDE CALDERA (initial vent)</i>	57.7	<u>93.2</u>	98.9	72.6	<u>89.9</u>	96.6	58.1	<u>89.3</u>	98.9
<i>OUTSIDE CALDERA (initial vent)</i>	0.4	<u>6.1</u>	27.6	2.4	<u>10.1</u>	20.9	0.7	<u>9.5</u>	31.8

Table 3.1: elicited values in percentiles of the probability of initial vent opening inside or outside the present SV caldera. CM=Classical Model; ERF=Expected Relative Frequency; EW=Equal Weight.

The medians are the values directly elicited from the experts (in the CM/EW cases), and these sum closer to 100% than the corresponding mean values. For the opening of a new vent outside the caldera, these results suggest median values from a minimum of about 6% (CM) to a maximum of about 10% (ERF), with an upper credible range value (95th percentile) between 20.9% (ERF) and 31.8% (EW). In Table 3.2 are reported the mean values and the 5th and 95th percentiles of the linear weights of the nine separate probability maps, obtained by simple Monte Carlo simulation following the logic tree framework of questions; these results are the base for producing the mean and percentile vent opening maps discussed in the following.

Dataset/Variable	Weight (% - 5 th /Mean/95 th)								
	CM			ERF			EW		
<i>Uniform Map</i>	8.2	<u>19.9</u>	33.9	8.7	<u>18.4</u>	28.0	5.7	<u>18.1</u>	33.5
<i>Deep Faults</i>	0.4	<u>9.4</u>	26.1	3.7	<u>11.2</u>	19.3	1.1	<u>11.2</u>	27.3
<i>Plinian Eruptions</i>	8.0	<u>16.3</u>	26.3	11.5	<u>17.9</u>	25.3	6.9	<u>18.0</u>	31.9
<i>Subplinian Eruptions</i>	14.3	<u>25.8</u>	38.9	14.3	<u>21.4</u>	29.9	8.6	<u>21.3</u>	36.7
<i>Violent Strombolian to Ash Emission Eruptions - 1944 Crater</i>	1.3	<u>6.6</u>	14.7	2.2	<u>5.6</u>	10.0	0.3	<u>5.1</u>	14.5
<i>Violent Strombolian to Ash Emission Eruptions - Gran Cono</i>	1.9	<u>7.4</u>	15.7	3.6	<u>7.9</u>	13.2	1.1	<u>8.1</u>	19.7
<i>Violent Strombolian to Ash Emission Eruptions - Caldera</i>	2.0	<u>8.1</u>	17.0	3.5	<u>7.7</u>	13.1	1.1	<u>8.3</u>	20.1
<i>Effusive Eruptions - Parasitic Vents</i>	0.5	<u>3.1</u>	7.8	2.1	<u>5.5</u>	10.0	0.1	<u>5.6</u>	16.4
<i>Effusive Eruptions - Eruptive Fissures</i>	0.5	<u>3.3</u>	8.1	1.6	<u>4.4</u>	8.2	0.1	<u>4.2</u>	12.9

Table 3.2: elicited values in percentiles of the weights assignment to different datasets/maps according to the logic tree approach described in the text.. CM=Classical Model; ERF=Expected Relative Frequency; EW=Equal Weight.

The weights assigned to different datasets/variables are found consistent between the three scoring rules (mean values differ for less than 2% in almost all the cases). With respect to the uncertainty ranges, outcomes show, as expected, that the ERF model produces narrower uncertainty intervals, the EW model the wider ones. The maps based on the CM results are adopted as reference here because these represent a rational, objective consensus on the key context of uncertainty quantification (tests of the CM and ERF methods have shown the former is generally more reliable for parameter uncertainty quantification, the latter for parameter central tendency accuracy, see Flandoli et

al. (2011) for more details on this subject). Moreover, this procedure has largely been adopted lately by the scientific community (e.g. Woo 1999; Bevilacqua et al. 2015).

The probability density functions of the weights for the various data sets, as derived from the CM method, are displayed in Fig. 3.7. It is worth pointing out that: a) to the vent location of Plinian and sub-Plinian eruptions, along with the uniform map, have been attributed the higher mean weights (equal to about 16.3%, 25.8% and 19.9% respectively) with respect to the vents for the other eruption types, and the resulting density

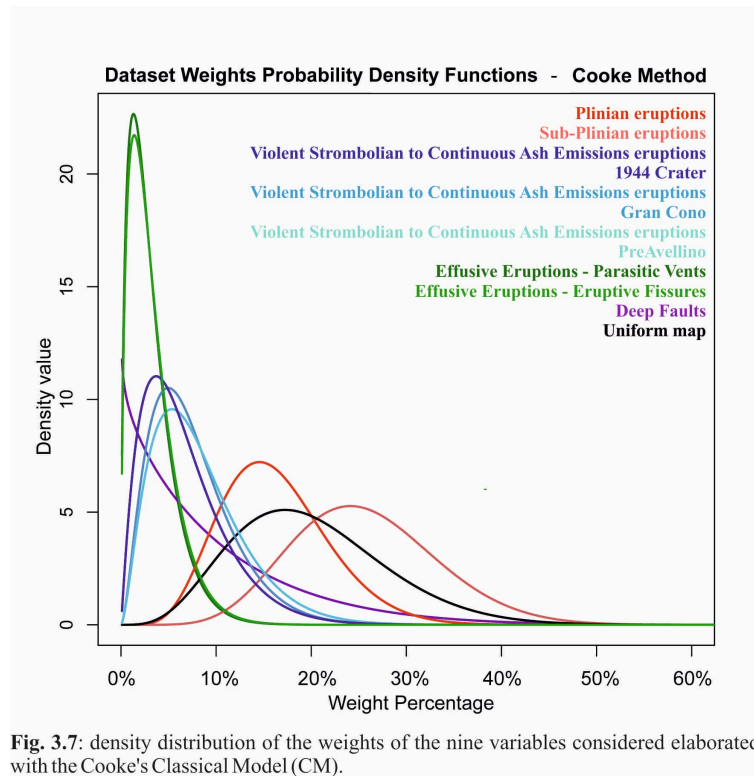


Fig. 3.7: density distribution of the weights of the nine variables considered elaborated with the Cooke's Classical Model (CM).

functions have a quasi-normal distribution with slightly wider uncertainty bounds; b) density distributions of the three VS to AE eruptions variables have lower mean weights (i.e. 6.6%, 7.4% and 8.1%) with a distribution skewed toward the upper bound of uncertainty (95th percentile), with a similar situation (even if with even lower mean values) observed also for the effusive eruptions variables; c) the deep faults variable has an extremely skewed distribution with a low mean value (i.e. 9.4%) but with a quite large upper 95th percentile value.

3.4.2 Sensitivity of variable weights to group composition

Sensitivity assessments on the elicitation outcomes were performed also with respect to individuals' experience and main scientific expertise, partitioning the participants into 2 couples of sub-groups: Group A1 (Seniors - 10 Experts), Group A2 (Juniors - 5 Experts), and also Group B1 (Geologists - 10 Experts) and Group B2 (Modelers - 5 Experts). Results are displayed in Sections 8.2.4 and 8.2.5. The DM from the CM method applied within the B1 (Geologists) sub-group shows wider uncertainty ranges and a higher probability value for initial vent opening outside SV caldera compared to the reference DM (similar results derive from A2 sub-group: Juniors). Other differences between sub-groups A1/A2 (Seniors/Juniors) and B1/B2 (Geologists/Modelers) sub-groups are quite small and overall consistent with the global weights DM results shown above. However, the following trends can be identified: i) experts in the A1 sub-group (Seniors) tend to assign less weight to the Deep faults dataset (around 6% - consistent with the CM Global results) than experts in the other sub-groups, which are all similar (around 10%); ii) experts in the A2 sub-group (Juniors) assigned quite low weights to the Effusive eruptions datasets; iii) experts in the B1 sub-group (Geologists) assigned less weight to the sub-Plinian eruptions dataset and, principally, gave higher weights to the Parasitic Vents dataset associated with effusive eruptions; iv) experts in the B1 sub-group also assigned a lower 5th percentile weight to the Uniform map compared to the other sub-groups, likely indicating they have higher confidence in the volcanological information used in the study. All the differences between groups are however small, demonstrating the large consensus generally reached by the group of experts on the topics to elicitate.

3.5 Vent opening probability maps

3.5.1 Probability distribution within the caldera boundary

Fig. 3.8 shows the probability vent opening maps, corresponding to the 5th, mean, and 95th percentiles, as obtained by weighting the density function maps of the different dataset according to the Cooke CM (taken here as reference model).

The strong similarities between the maps obtained by the application of the CM, ERF and EW methods (reported in Section 8.2.2) make the outcomes particularly robust. Alternative mean maps were produced (by the CM and EW methods) also within the above mentioned sub-groups of experts:

due to the strong similarity with the reference maps they are not presented here although they are available in Section 8.2.3. The maps were all represented on grids with cells of side 100 m and each probability density is expressed as percentage probability per cell (hm²) conditional on the occurrence of a Plinian/sub-Plinian eruption over the SV caldera (spatial integration of each mean map close to 100%).

Although maps of Fig. 3.8 show that the vent opening probability is widely diffused all over the SV caldera, it is obvious that, for each map, maxima are located in correspondence of the present crater summit (values range from 0.15% up to 0.69%). Moreover, a more pronounced effect of Deep Faults is found on the mean and 95th percentile maps, an effect of the high skewness of the higher values of the weight attributed to this dataset by the experts (see Table 3.2 and Fig. 3.7).

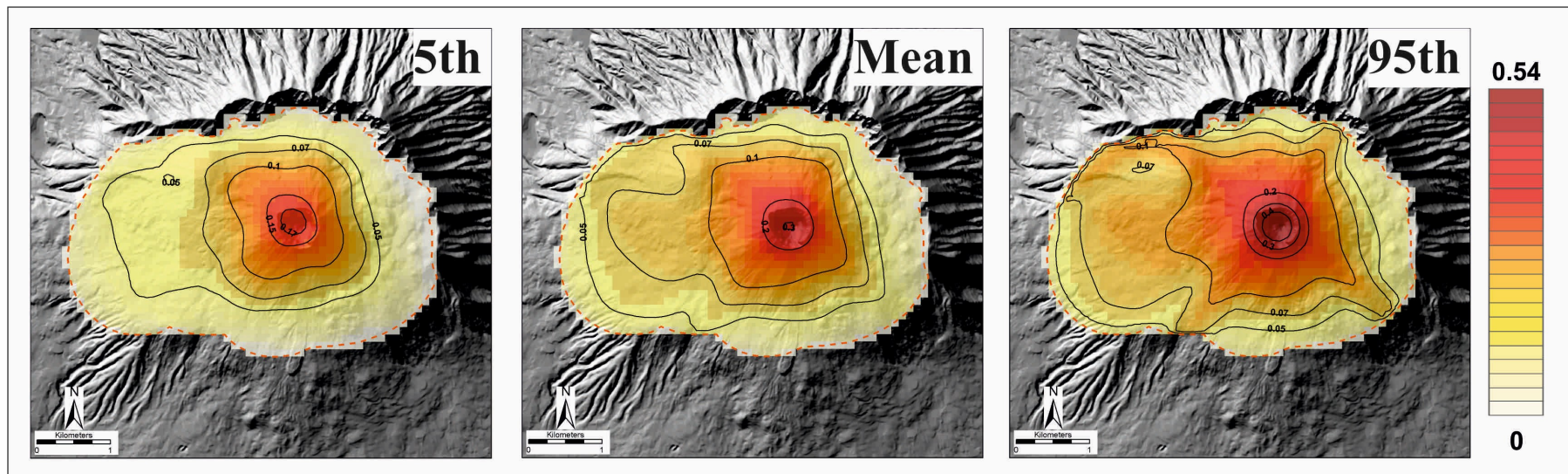


Fig. 3.8: a) maps of the 5th, mean and 95th percentiles obtained after the Classical Model (CM) expert pooling technique. Cellsize is 100 m; values are probability percentages per cell; contour lines enclose areas where cell values are higher than the value of the line itself.

3.5.2 Vent position during caldera enlargement

As previously mentioned, the effect of a possible caldera enlargement in the case of a next large scale explosive eruption on the position of the vent has been analyzed based on the following assumptions: a) caldera enlargement is possible due to the occurrence of a Plinian eruption; b) caldera enlargement can be neglected in case of a sub-Plinian (or lower magnitude) eruption; c) caldera enlargement can be modeled by assuming migration of the initial vent position of a Plinian eruption out to the limit of a collapse area related to the eruption. Given these assumptions, vent position following a caldera collapse has been modeled with a simplified kernel function, called here a “collapse kernel” (Fig. 3.9). The kernel function value is piecewise constant with respect to the distance from the origin. In particular, the function is null outside a circle radius 1.3 km, which is the mean size of collapsed areas in the four previous Plinian, caldera-forming eruptions. The kernel sums to one and its density is distributed such that 60% is located up to 0.25 km from the center, 5% from 0.25 km to 1.05 km, and 35% from 1.05 km to 1.3 km. The collapse kernel function is convolved with the values of the initial vent opening map, in case of a Plinian eruption. The choice of these limits would like to address a situation of caldera collapse where most of the erupted material is possibly discharged through the central conduit area and along ring faults.

Relying on the findings of Neri et al. (2008), the probability P of having a Plinian event (conditional only of having a Plinian or a sub-Plinian eruption), has been here estimated assuming independent Beta distributions (as in Neri et al. 2008): these results are significantly skewed and have $[5^{\text{th}}, 50^{\text{th}}, 95^{\text{th}}]$ uncertainty percentiles equal to $[0.5\%, 9.5\%, 40\%]$, and mean value 13.5%. During the Monte Carlo simulation for the ‘initial vent’ opening probability map we also sampled the caldera collapse probability value P , and we applied the collapse kernel function only to that case. Specifically, the individual samples for the final vent opening maps (Fig. 3.10) are the linear combinations of the maps after “collapse kernel” application (Fig. 8.8 from

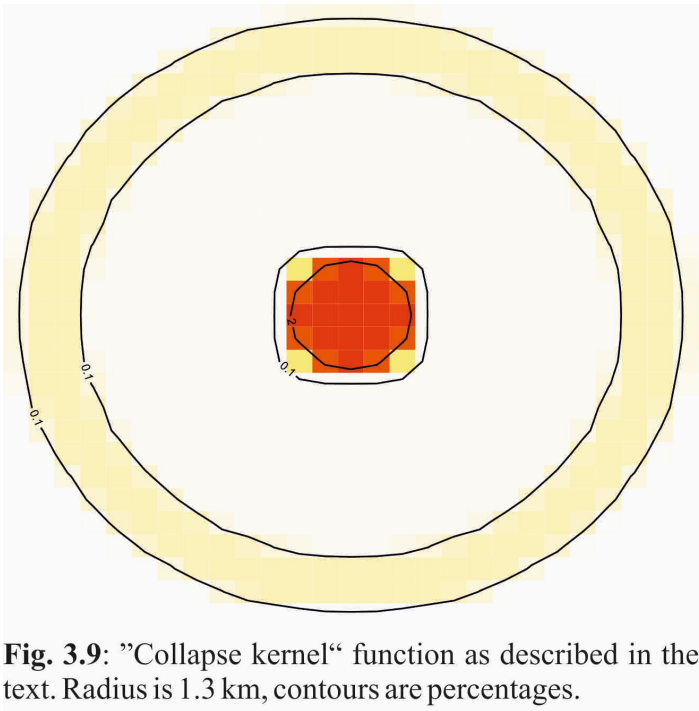


Fig. 3.9: "Collapse kernel" function as described in the text. Radius is 1.3 km, contours are percentages.

Section 8.2.7) and the maps without caldera collapse (Fig. 3.8), multiplied by their respective probabilities: P and $1-P$.

The maps reported in Fig. 3.10 thus represent the vent opening mean probability map and its companion credible range probabilities, such that these also include the possibility of caldera enlargement (associated only with Plinian events), conditional on the occurrence of a large eruption (Plinian or sub-Plinian) at SV. Probability percentiles of caldera enlargement (i.e. vent opening spatial probability integral outside the caldera boundary) are [0.8%, 1.9%, 5.8%], with a mean value of 2.4%.

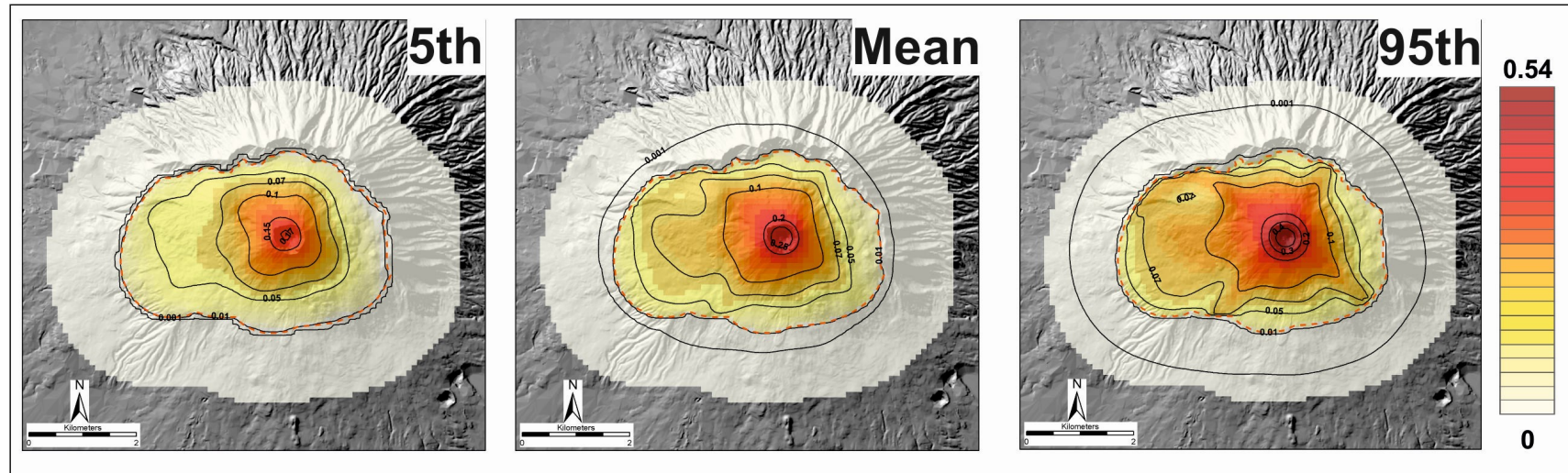


Fig. 3.10: maps of the 5th, mean and 95th percentiles for a vent opening probability map with caldera enlargement obtained after the Classical Model (CM) expert pooling technique in the case of a sub-Plinian or Plinian eruption. Cellsize is 100 m; values are probability percentages per cell; contour lines enclose areas where cell values are higher than the value of the line itself.

3.6 Discussion

3.6.1 Expert elicitation procedure, scoring methods and vent opening probability maps

During the elicitation sessions, some technical and understanding issues were raised by some of the experts. These issues led to repeating the elicitation for the most skewed responses (i.e. outside caldera probability, and deep fault weight estimation), after having discussed the initial elicitation results. Other skewness-related issues are evinced in the graphical representation of DM percentile estimates with continuous density functions. In case of relevant skewness, the mean value tends to shift towards the wider uncertainty side, with respect to modal or median values.

Despite these subtleties and challenges, and considering that each of the methods has its own advantages and drawbacks, the overall consensus among the different scoring methods underlines the general consensus among all the experts about the mean results, with strong similarity in the maps presented. Weights assigned to different datasets/variables are consistent between the three scoring rules (mean values differ for less than 2% for almost all the cases), a situation that suggests a fundamental consensus exists among the experts and is captured by the relevant Decision Makers. With respect to the uncertainty ranges, outcomes show, as expected, that the ERF model computes the smaller uncertainty intervals on central tendency, the CM provides intermediate credible intervals values, while the EW model produces the widest uncertainty distributions (as is usual).

It is also worth mentioning that the “deep faults” dataset significantly affects the final outcomes of vent opening probability maps, especially with regard to higher percentiles, because, as discussed before, the skewness of the PDFs is more pronounced toward higher values for this dataset. The contribution of this dataset to the density values is also increased because, despite the fact that the mean values of weights attributed to it do not reach extremely high values (i.e. about 10%), still it is the most spatially concentrated of the datasets, and the corresponding Gaussian kernel function does not spread the probability enough to offset that concentration. This issue needs to be carefully taken into account when evaluating the influence of this data set on the final vent opening location probability maps also considering the quality of the data, as two of the three faults that compose the dataset have been extrapolated from adjacent seismic profiles. However, it is undoubted that the presence of large crustal discontinuities can be a factor affecting vent distribution, and this suggests that a refinement of this dataset is advisable.

To properly evaluate the net effect of the deep faults dataset on the vent opening maps in case of a future Plinian/sub-Plinian eruption, we also produced maps using the CM and EW methods, in

which the contribution of the deep faults dataset was removed and its weight equally distributed back over the other datasets. The rationale for this further analysis was also due to the consideration that prevailing NW-SE and NE-SW trends (same as the structures in the “Deep faults” dataset) were recognizable also without including the “deep faults” dataset, which is, as mentioned above, the most controversial one. Results shown in Section 8.2.6 highlight that, while significantly less evident with respect to Fig. 3.8, the NE-SW and NW-SE trends can be still identified, particularly in the “Piano delle Ginestre” area and in the SE side of the Gran Cono (see Chapter 2). Possibly, these trends might indirectly reflect the presence of buried main structures with the same trend controlling the volcanic activity.

3.6.2 Implications for volcanic hazard assessments

The vent opening location probability maps have also important implications in terms of hazard assessment of Plinian and sub-Plinian eruptions. In particular, the mean map of the CM method indicates that less than 50% of the cumulative probability of vent opening location (lower and upper percentiles 36.0% and 55.6%, respectively) is found within the central area of the Gran Cono (Sector A of Fig. 3.4a), whilst there is about 30% of probability (lower and upper percentiles 22.4% and 36.7%, respectively) that the next Plinian/sub-Plinian eruption will have its initial vent within the area of the Piano delle Ginestre (Sector D of Fig. 3.4a), i.e. between about 1-3 km west of the axis of the Gran Cono crater. To give this context, PDCs from the Avellino Plinian eruption (4.3 ka BP), whose initial vent was located in the “Piano delle Ginestre” area, reached the area presently occupied by the city of Naples (Fig. 3.1). Considering the “Valle del Gigante” area (Sector B of Fig. 4a), the cumulative mean probability that a next vent of a Plinian/sub-Plinian eruption will open in this area is around 16% (lower and upper percentiles 11.9% and 19.4%, respectively). It is pertinent for assessing potential hazard impacts that a vent opening in this area, even if it is associated with a sub-Plinian scale eruption will have a high probability that resulting PDCs could invade areas and municipalities located on the North flank of the volcano (Fig. 3.1), overpassing the Mount Somma rim (Esposti Ongaro et al. in preparation). Finally, also the cumulative vent opening location probability for Sector C of Fig. 3.4a (the “Valle dell’Inferno” area) yields a non-negligible probability value of about 10% (lower and upper percentiles 7.5% and 13.7%, respectively).

Another noteworthy outcome of the present study relates to the relative probability that the next Plinian/sub-Plinian eruption might have its initial vent outside the present SV caldera. The elicitation and modelling results indicate that there is a mean probability value of this occurring of 6% from the CM method, 10% using the ERF method, and 12% using the CM method with sub-group B1 – Geologists. Potentially, this is a very significant finding from this work, and the implications should not be ignored. Recalling that the relatively limited number of Plinian/sub-Plinian events at SV (i.e. 10) have been located within or near the margin of the preexisting caldera, it is suggested that the estimated probability values for a Plinian/sub-Plinian vent opening located outside the SV caldera are likely conservative, but not necessarily unrealistic. Past eruptions of this intensity were also characterized by a large magnitude (erupted volume), so suggesting they are associated to important magma reservoirs that could be partially unrelated to the structure strictly controlling the growth of the SV edifice.

Since no other information are available, it is only possible to speculate (based on reasonable assumptions) that: a) in the case of an open conduit condition (see Acocella et al. 2006b) the areas more prone to vent opening outside the SV caldera in any scale new eruption would more likely be those facing the sea (i.e. in the SW/SE sector), rather than toward N sectors (considering the older ages of the volcanic features in the N side of the volcano) and within a distance of a few km from the SV crater rim (approximately corresponding also to the location of parasitic vents from Middle Age activity, see Fig. 2.4 from Chapter 2); b) in the case of a closed conduit condition (like the present one) no good constraints are presently available. These inferences have not been investigated further here but it certainly poses an interesting challenge for future research. In particular, it will be necessary to carefully evaluate: a) the extent of the area for possible sites of new vent openings, and b) the structures and volcanic features that need to be carefully considered and properly investigated.

While sites of effusive parasitic vents and eruptive fissures activity outside SV caldera can be considered and treated as done in this study, the potential effect of regional/local structures on the distribution of future vent opening locations might also play a significant role. From this perspective, structural data sets for areas outside the caldera appear to be more dependable compared to the ones considered for our maps, as the bulk of structural information outside the SV caldera area, reported by Bruno et al. (1998) and Bruno and Rapolla (1999) for this area (see Section 2.4.5), have been actually interpolated from seismic profiling and not extrapolated like the faults in the “Deep fault” dataset of this study.

3.7 Concluding remarks

This study has produced the first long-term (base-rate) vent opening probability maps for the summit caldera of the SV volcanic complex for the case of the next eruption being Plinian or sub-Plinian. The procedure implemented a structured and quantitative treatment of epistemic and physical uncertainties, and their influences on analyses to determine where the new vent will first open. The vent opening location probability maps, here presented as a mean map and associated uncertainty maps corresponding to 5th and 95th percentile confidence levels, were obtained by linearly combining with appropriate weights nine different volcanological data sets, representing the distribution of past vents for different eruptive categories, together with fault information and a homogeneous location distribution. Weights were defined through a procedure of structured elicitation from a group of experts appositely selected with various degrees of experience and from different fields of expertise. Results from the elicitation were pooled using three different procedures. Outcomes of this study include: a) the definition of continuous probability density functions, obtained through the application of symmetrical Gaussian kernels with appropriate bandwidths, for each individual dataset/variable selected from the data presented in Chapter 2; b) the enumeration of weights to be assigned to alternative vent location probability maps when linearly combined, based on performance-scored expert judgments, and c) the application and inter-comparison of different expert scoring methods, different composition of sub-groups of experts, as well as the consideration of different sets of volcanological data (i.e. maps obtained with and without the contribution of information on deep faults).

Inspection of these probability maps shows that, for a next Plinian/sub-Plinian eruption:

1. the mean probability of vent opening in the area of the present edifice (i.e. the Gran Cono area, assumed circular with a diameter of 1 km). is less than 50%. Uncertainty bounds around this mean value, expressed as 5th and 95th percentiles, correspond to a range between about 36% to 56% probability, when the Classical Model (CM) weights are used;
2. there is a very significant probability, i.e. almost 30% as mean value, that the western portion of the SV caldera (i.e. “Piano delle Ginestre” area) could host the next vent opening. Uncertainty values correspond to a range from about 22% to 37% , again referring to the CM findings;
3. there is a 2.4% mean probability that the caldera will enlarge during the next Plinian/sub-Plinian event.

4. finally, outcomes of these analyses indicate that, despite the past evidence of SV history, there is at least 6% probability that the a high intensity eruption will have its initial vent located outside the present outline of the SV caldera. This situation, and its potentially very significant implications, demands further investigation.

All the findings of the present study appear substantially robust with respect to the adoption of different scoring methods for combining expert judgments, to different sub-sets of the group of experts and to the selection of basic volcanological variables considered in the analysis. Assessing how uncertainty in the potential location of a new vent opening at Somma-Vesuvio could impact on tephra fallout or PDC inundation hazard mapping, if the next future eruption is sub-Plinian or Plinian, cannot be projected simply and directly from the findings reported here. Potential influences of other factors, such as local topography, are many and complex, and thus further detailed investigation and modelling is needed, as has been done, for example, for the nearby Campi Flegrei caldera (e.g. Selva et al. 2010; Neri et al. 2015).

Appendix A: kernel density estimations

The probability density maps associated with each volcanic data set were generated from the application of Gaussian spatial density kernel to the uniform distribution assumed within the uncertainty areas enclosing the volcanic features (Connor and Hill 1995; Connor and Connor 2009).

Kernel density estimation (Silverman 1986) build up a continuous probability density following a number of discrete samplings or a non-continuous density function. The two main phases of the spatial density estimate are the choices of the kernel function and of its bandwidth, or smoothing parameter. The kernel function can be any positive function K that integrates to one (Weller et al. 2006), and in general, given a finite sample $X_i, i=1, \dots, N$, a kernel density estimator can be defined as:

$$f_h(x) = \frac{1}{N} \sum_{i=1}^N K\left(\frac{x - X_i}{h}\right)$$

where h is the bandwidth. In our study K is assumed equal to a two-dimensional radially symmetric Gaussian kernel, as many kernel estimators used in geologic hazard assessments (Gaussian distribution arises in problems of heat and mass transfer, such as those that might be expected in volcanic systems involving diffusion processes; Weller et al. 2006).

The bandwidth h is typically selected using different theoretical and empirical methods developed for optimizing consistency with data (Cappello et al. 2012; Becerril et al. 2013). For instance, in the case of past vents locations, the bandwidth was associated with the spread between each vent and the rest of the dataset. Such distance represents a proxy of the distance at which a next vent will open from the others. Here it is assumed h independent of the spatial location, but depending on the specific features considered (for instance past vents or faults). A characteristic of this study is that the sample of past features locations does not comprise points, but areas of uncertainty of different extent, and each area covers several cells of our computational grid, some of them completely, others only partially. Therefore for each cell it is taken into account the fraction of each area that it contains and then it is applied the kernel convolution to this value. In addition, it is also assumed that the kernel convolution does not spread the probability outside the SV caldera boundary.

An advantage of this approach is that the spatial density estimate will be consistent with the spatial distribution of the past volcanic features. A disadvantage of a symmetrical kernel function is that it does not explicitly allow for local geological and structural boundaries and other specific directional volcanological information. Additional details about this approach can be found in Bevilacqua et al. (2015).

Appendix B: experts' pooling methods

As described in the main text, the procedure of weights assignment to different datasets took advantage of two elicitation sessions. The first plenary session involved multiple presentations and discussion of the topics of concern - i.e. the 'target' questions, and a calibration questionnaire with appropriate 'seed' questions. To facilitate the experts in providing responses to the target items, before the plenary session it was provided to the participants a small compendium that summarized the most important features about single datasets, and also the questionnaire with draft versions of the target questions. These were reviewed when the group convened and, if deemed necessary, modified before individuals then answered them confidentially and independently. During this first session, the calibration seed questions – used for scoring individuals' performances in the Cooke Classical Model SEJ method - were also answered.

These questions were based on carefully researched aspects of SV volcanism, other Italian volcanoes, and about explosive volcanism in general, in relation to which the experts were not expected to know precisely the true values but could be expected to provide meaningful credible ranges to capture them. The overall statistical accuracy and information bandwidth of individual's distribution provided the empirical performance basis for differential weighting of their judgements on the target items.

Immediately after this first session, a document was provided to participants that summarized, anonymously, all their responses to the target items, together with the preliminary vent opening probability maps that stemmed from pooling their judgements with performance weights, and notes about some ambiguities present in the group's responses. Equal weights solutions to target items were also reported, to give context to the pooled findings. Following further group discussion, and in order to generate a final version of weights to be assigned to variables/datasets, a slightly revised questionnaire was prepared and then sent out to participants to complete in a follow-up, remote elicitation. When this second elicitation was completed, the provisional probability maps were amended accordingly.

In order to produce the vent opening probability maps, different data sets, representative of different variables related to the vent opening process, have been linearly combined with different weights, attributed according to estimates of the association that each variable could have with the location of the opening of a new vent. For determining these association weights, performance-based Structured Expert Judgment (SEJ) techniques (Cooke 1991; Aspinall 2006; Bevilacqua et al. 2015; Bevilacqua 2016) were employed, applied through multiple elicitation sessions. In these group elicitations, different experts' opinions were pooled based on a formalized treatment of their judgements on uncertainties in relation to the topic or scientific issue under consideration.

In the performance-based elicitation procedure, statistical accuracy and informativeness scores are derived for each expert (sometimes referred to as calibration) from a set of subject matter 'seed items' (see e.g. Cooke 1991; Aspinall 2006). These seed items comprise factual questions the true values of which an expert is not expected to know precisely, but an expert is expected to be able to provide meaningful credible intervals that capture those values reliably and informatively, by informed reasoning. Each expert's accuracy and information scores are combined to produce a performance-based weight for application to their responses – as one member of the group of experts - to questions

on variables for which estimates are needed, called 'target items'. In these study, it was followed usual practice and elicited individual expert's judgements on 5th percentile, median and 95th percentile values for seed and target questions, in this way obtaining elemental uncertainty distribution markers for each variable. In this form, target item responses are pooled together with the experts' calibration weights to produce a group synthesized uncertainty distribution, often called a Decision Maker (DM) solution.

In this work three alternative expert weighting schemes were applied: the Classical Model (CM; Cooke 1991), the Expected Relative Frequency model (ERF; Flandoli et al. 2011) and the basic Equal Weights (EW) model, and then the different DM results obtained were compared. The general purpose of this approach is to provide robust results by comparing outcomes from selective pooling methods (i.e. the Classical Model DM) with more inclusive methods where more of the experts are combined with modulated weights (as in the ERF method) or all experts are given the same weights (i.e. the equal weights model EW). More specifically, the CM and ERF methods involve adopting different performance scoring rules and different pooling algorithms, depending on whether robust statistical quantification of uncertainty is the goal (in which case, the Classical Model is favored), or accuracy in pointwise (mean) value estimation is desired (for a discussion of these aspects, see Flandoli et al. (2011) and Bevilacqua (2016)). Here, the Classical Model has been used for the computation of the final probabilistic vent opening location maps.

Chapter 4

From field data to numerical modeling: reconstructing key input parameters from eruptive units for model validations

4.1 Introduction

The fundamental starting point for each study aimed at volcanic hazard assessment and volcanic risk reduction lies in a detailed knowledge of the eruptive history of a volcano and in the availability of detailed field data. These are especially useful for constraining numerical modeling of Pyroclastic Density Currents (PDC), which strongly need to be linked to physical parameters derived from field data (Esposti Ongaro et al. 2002; Todesco et al. 2002; Neri et al. 2003; Bursik et al. 2005; Patra et al. 2005; Neri et al. 2007; Esposti Ongaro et al. 2008; Esposti Ongaro et al. 2012; Neri et al. 2015). Key data that need to be carefully evaluated are: a) maximum runout of PDCs; b) total volume; c) Total Grain-Size Distribution (TGSD); d) digital elevation model reproducing a simplified paleotopography before the eruption studied. Similarly, sedimentological interpretation of the deposits aimed at defining the main transport and depositional processes is fundamental for the definition of the type of assumptions that can be reliably made in the physical modeling, and hence of the models to be used.

This Chapter provides new and revised data about PDCs from two different eruptions at Somma-Vesuvio (SV), the overall famous AD 79 “Pompeii” Plinian eruption and the AD 472 “Pollena” sub-Plinian eruption. Quantification of uncertainties and discussion about the implication of the parameters calculated will be extensively discussed in section 4.5. The description of the data in section 4.4 will be anticipated by syntheses of the stratigraphic sequences of the two eruptions (where contribution from different sources are critically summarized) in section 4.2 and by a review of the methodologies employed for different parameter estimations (section 4.3).

4.2 The Pompeii and Pollena eruptions

4.2.1 The AD 79 “Pompeii” eruption

The AD 79 eruption of SV is probably one of the most studied eruption of all time, representing the reference type for Plinian-like volcanic eruptions and surely a good proxy for volcanic hazard assessment from the point of view of PDC inundation area. This eruption in fact resulted in a dramatic change of the surroundings of SV volcano, with PDCs ravaging the highly populated Neapolitan area up to 20 km from the vent area (Gurioli et al. 2010) and causing more than 3,000 casualties (Gurioli et al. 2007) over a territory now house for 1 million people; SV itself suffered from a caldera collapse that deeply modified the present shape of the SV area (Cioni et al. 1999), causing a drastic change on its morphological appearance.

Starting from the early chronicles of Pliny the Younger (Secundus et al. 1980), the eruption itself has been described in details, and numerous field data have been collected (Lirer et al. 1973; Sigurdsson et al. 1985; Carey and Sigurdsson 1987; Barberi et al. 1989; Cioni et al. 1992a; Cioni et al. 1992b; Cioni et al. 1995; Cioni et al. 1999; Gurioli et al. 2002; Gurioli et al. 2005; Cioni et al. 2008; Rolandi et al. 2008; Gurioli et al. 2010). The analysis of such field data allowed Cioni et al. (2008) and Gurioli et al. (2010) to provide a range of values for the eruptive parameters of this eruption, which are listed in Table 4.1.

Type ^a	Fallout Volume (km ³) ^b	PDC Volume (km ³) ^c	Total Volume (km ³) ^d	Peak MDR (kg/s) ^{e, b}	Max runout PDC (km)	Area Invaded Fallout (isopach 10 cm - km ²) ^b	Source(s)	Additional Notes
Plinian	2.6 ⁽¹⁾ 3.9 ⁽²⁾ 2.9 ⁽³⁾	0.35 ⁽⁴⁾ 0.75 ⁽⁵⁾ 0.83 ⁽⁶⁾	2.95 - 4.73	8x10 ⁷ - 1.5x10 ⁸	≈20.5 ⁽⁶⁾	3430 ⁽⁴⁾	⁽¹⁾ Lirer et al. (1973) ⁽²⁾ Sigurdsson et al. (1985) ⁽³⁾ Cioni et al. (2003a) ⁽⁴⁾ Cioni et al. (2008) ⁽⁵⁾ Cioni et al. (1999) ⁽⁶⁾ Gurioli et al. (2010)	^a From Cioni et al. (2008) ^b Method from Fiersten and Nathenson (1992) ^c Method from Favalli and Pareschi (2004) ^d Fallout+PDC (min value-max value) ^e Method from Carey and Sparks (1986)

Table 4.1: range of values for selected parameters of the AD 79 Pompeii eruption calculated by various authors.

The date of the eruption has been historically recognized as August 24-25 based on annotations written on the letters of Pliny the Younger, although some authors suggest, based on recent archaeological findings and seasonal wind pattern analyses, a more probable date of the eruption

between the end of October or the beginning of November (Rolandi et al. 2008). Before this eruption, SV (or “Vesbius” as it was called by the ancient Romans) was dormant with probably no sign of activity since almost three centuries, the last eruption dating back around 216-217 BC (Cioni et al. 2008). The only signs of awakening have been possibly a violent earthquake that shook the area in AD 62 and some minor earthquakes sparsely reported by Pliny the Younger that shortly preceded the eruption (Cioni et al. 2000a). The morphological shape of SV was also quite different with respect to the present one, as clearly evident from Pompeii frescos where the present “Gran Cono” edifice was missing and remnants of the old Mount Somma scarps were clearly visible also to the S (Cioni et al.

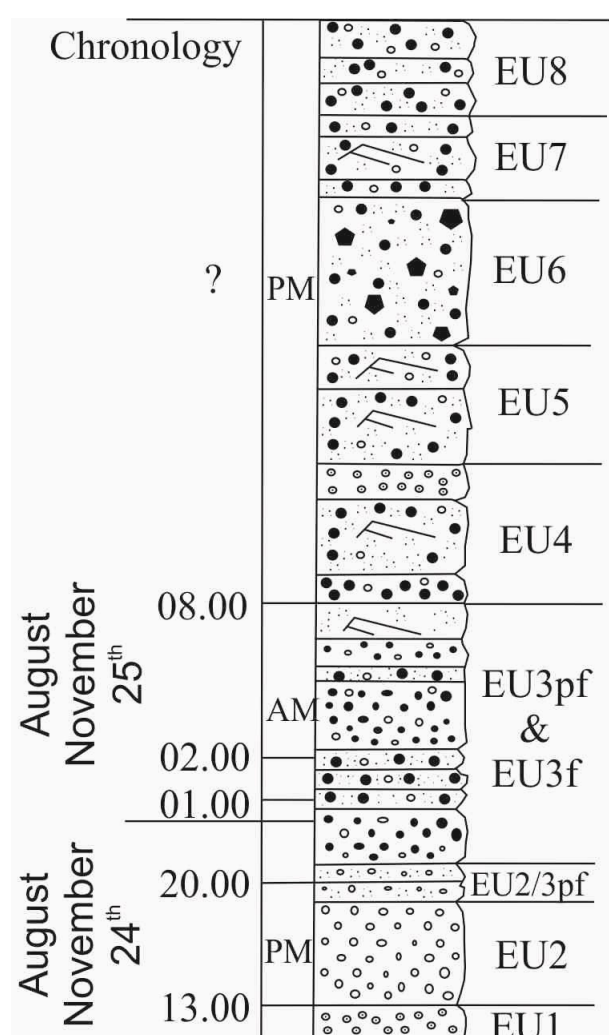


Fig. 4.1: stratigraphic section of the AD 79 Pompeii eruption (redrawn from Gurioli et al. 2005).

1999).

The course of the eruption has been well constrained (Fig 4.1) and subdivided into 8 main Eruptive Units (EU1-EU8) with some minor sub-units (Cioni et al. 1992a; Gurioli et al. 1999; Gurioli et al. 2002; Gurioli et al. 2005).

The overall eruption sequence can be grouped (Gurioli et al. 2005) i) in three phases from the point of view of the predominance of the fragmentation process (an opening phreatomagmatic phase followed by a Plinian magmatic phase and closed by another phreatomagmatic phase) or ii) in two distinct phases from the point of view of the different type of magma erupted (the first phase which produced white-colored phonolitic pumice fragments and the second phase that produced grey tephriphonolitic pumices).

The eruption started probably in late morning-early afternoon of either August (or October) 24 AD 79 with an initial short-lived phreatomagmatic transient phase evidenced by the

thin, accretionary lapilli-bearing, fine ash bed of EU1 unit (Cioni et al. 1992a), which marked probably the opening of the conduit (Sigurdsson et al. 1985; Gurioli et al. 2005). The subsequent EU2-EU3 units are related to a relatively long (around 20 hours) magmatic Plinian phase, which emplaced pumice fall deposits dispersed to the SE and some PDCs that travelled more radially with respect to vent location. Complex changes in eruptive dynamics between EU2/EU3 and EU3/EU4 and within EU3 have been underlined by Gurioli et al. (2005). The initial tapping of the upper phonolitic portion of the stratified magma chamber (EU2) was in fact followed by its progressive mixing with a lower, more mafic portion, producing a tephriphonolitic grey magma represented by denser juvenile clasts (Civetta et al. 1991; Cioni et al. 1995; Marianelli et al. 1995). This first transition, that led to an increase in particle densities due to protracted degassing and crystallization after magma mixing (Gurioli et al. 2005), is probably responsible for the generation of the first, deadly PDC (EU2/3pf) which hit Herculaneum around 8 PM of the first day of the eruption, causing the death of all the inhabitants that had not escaped up to that moment (Sigurdsson et al. 1985; Gurioli et al. 2002). The course of the eruption was subsequently marked (from the night of the first day up to around 8 AM of the second day; Gurioli et al. 2005) by the resumption of a Plinian plume which produced both grey pumice tephra blankets (EU3f) and three thin PDCs (EU3pf1-3) by partial column collapse, that spread radially from the vent area never extending farther than the North reaches of Pompeii. The Plinian phase was then closed by a phase of total column collapse, which produced a PDC that first reached Pompeii in the South, depositing only few centimeters of fine ash (EU3pftot). These PDCs destroyed several farms and villas on the Vesuvius slopes and surroundings. The strong earthquakes and the dark cloud described by Pliny at dawn of the second day of the eruption are probably both related to the beginning of the final (EU4-EU8) phreatomagmatic phase (Gurioli et al. 2005), progressively passing from “dry” at the beginning (EU4-EU5) to mostly “wet” at the end (EU8; Barberi et al. 1989). During this phase, external fluids made their way up to the magma chamber (Barberi et al. 1989; Cioni et al. 1992a; Cioni et al. 1992b), and, consequently, erupted products show a marked increase in both the wall rock/juvenile ratio and the amount of fragments from deep provenance (Cioni et al. 1992b). This late stage (Gurioli et al. 2005) started again with an intermittently sustained Plinian column that produced: i) tephra fallout deposits and highly energetic/widespread PDCs (EU4), which produced the maximum impact, definitively ravaging Pompeii and killing the survivors in the city (Cioni 2000; Gurioli et al. 2005); ii) more valley-confined and proximal PDCs (EU5); iii) very coarse and lithic-rich PDC (the climatic phase of caldera

collapse - EU6); iv) another phase of widespread PDCs (EU7); v) “wet”, accretionary lapilli-bearing, ash-rich PDCs (EU8). Gurioli (1999) reports a lithic-rich unit below EU4, only dispersed on the NW sector of SV. Due to its stratigraphic position and its lithofacies features (massive with lithics>70%), this unit has been interpreted as representative of the final part of the magmatic phase, with PDCs originating from “boiling-over” mechanism capable of overflowing the paleo-Mt. Somma caldera only in its NW part (while in the SE sector the old Mt. Somma caldera could have acted as a barrier).

PDCs deposits from the AD 79 eruption range from stratified to massive (Cioni et al. 2004), representing sedimentation from both fully-dilute PDCs and granular, fluid-based PDCs (Branney and Kokelaar 2002), which sometimes present complex lithofacies associations derived from interaction with substratum morphology.

EU3pf represents the final part of the magmatic Plinian phase of the eruption (Gurioli 1999;

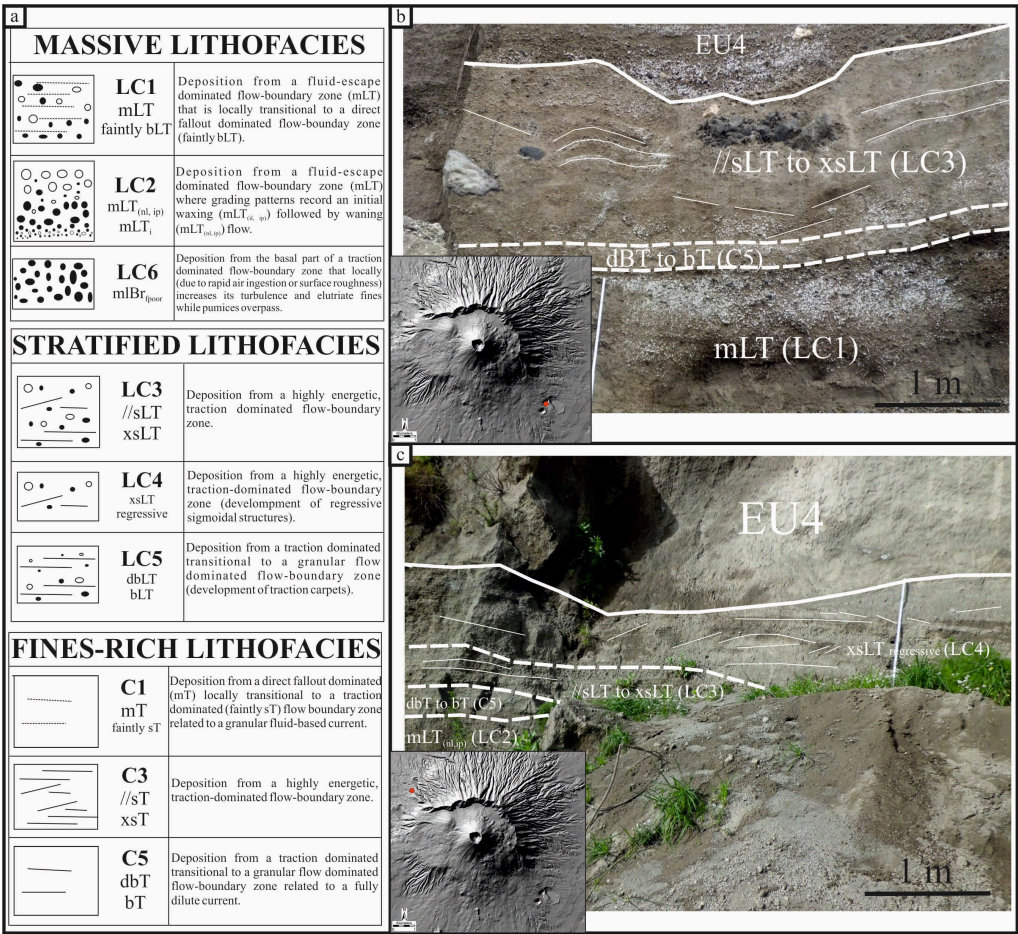


Fig. 4.2: a) lithofacies of the EU3pf unit (Gurioli et al. 1999); b) “Cava Pozzelle (AT)” section (see Fig. 4.7a); c) “Lagno Molaro (AT-c)” section (see Fig. 4.7b).

Gurioli et al. 1999): associated deposits are generally thick (~1 m), radially dispersed (up to 10 km from vent area) and show different types of lithofacies variably associated (Fig. 4.2).

As a general rule, median clast size tends to diminish gradually from proximal to distal sectors and coarser deposits are located

within paleodepressions. It is worth noting, as pointed out by Gurioli et al. (1999), that: i) in the southern part of the SV area the relative smoothness of the paleotopography poorly (only locally) influenced the overall development of the PDC; ii) in eastern sectors of SV, the presence of the remnants of the old Mount Somma scarp caused a general increase of current turbulence, enhancing velocity and air ingestion; iii) in western sectors of SV, the presence of the break in slope of the *Avellino Pumice* caldera increased flow accumulation, producing a depositional fan with thicknesses up to several meters toward sea-facing sectors (like in Herculaneum); iv) in northern sectors of SV, the roughness of paleotopography (with lots of valleys and significative slopes) favored the development within the whole current of a fast-moving, dense underflow confined in the main paleovalleys, with a slower and more dilute portion travelling along morphological highs. EU3pf represents a PDC characterized by marked unsteadiness and non-uniformity, also marked by the presence of several erosional discontinuities not associated with any fallout units (Gurioli et al. 1999). This latter aspect indicates that EU3pf was emplaced by a single PDC collapsing from a Plinian column with time-variable mass discharge rate, as also suggested by numerical simulations from Dobran et al. (1993).

EU4 is related to the onset of the final phreatomagmatic phase, with the massive entering of external water into the feeding system triggered by the caldera collapse (Barberi et al. 1989). This eruptive unit (Fig. 4.3a) presents a simpler stratigraphy with respect to the EU3pf unit, and could be subdivided into three distinct layers (“Basal”, “Intermediate” and “Upper”, Cioni et al. 1992a; “EU4f”, “EU4pf” and “Pisolite-bearing ash bed”, Gurioli et al. 2005): these three sub-units testify, respectively, i) the re-onset of a sustained Plinian convective column (Basal/EU4f fallout layer), ii) the collapse of the column into highly energetic, PDCs depositing a cross-laminated layer (Intermediate/EU4pf layer) and iii) the emplacement of a more “wet”, fines-rich sub-unit (although within the “dry” phase of the phreatomagmatic stage; Upper/Pisolite-bearing ash bed layer), possibly characterized by deposition from a sluggish, laterally transported cloud and, in the more distal outcrops, to delayed fallout sedimentation. For the sake of simplicity, throughout the paper these layers will be named (from bottom to up), level “a”, level “b” and level “c” respectively. It is important to point out that level “c” basically represent at least part of the co-ignimbritic deposit related to level “b” (Gurioli 1999).

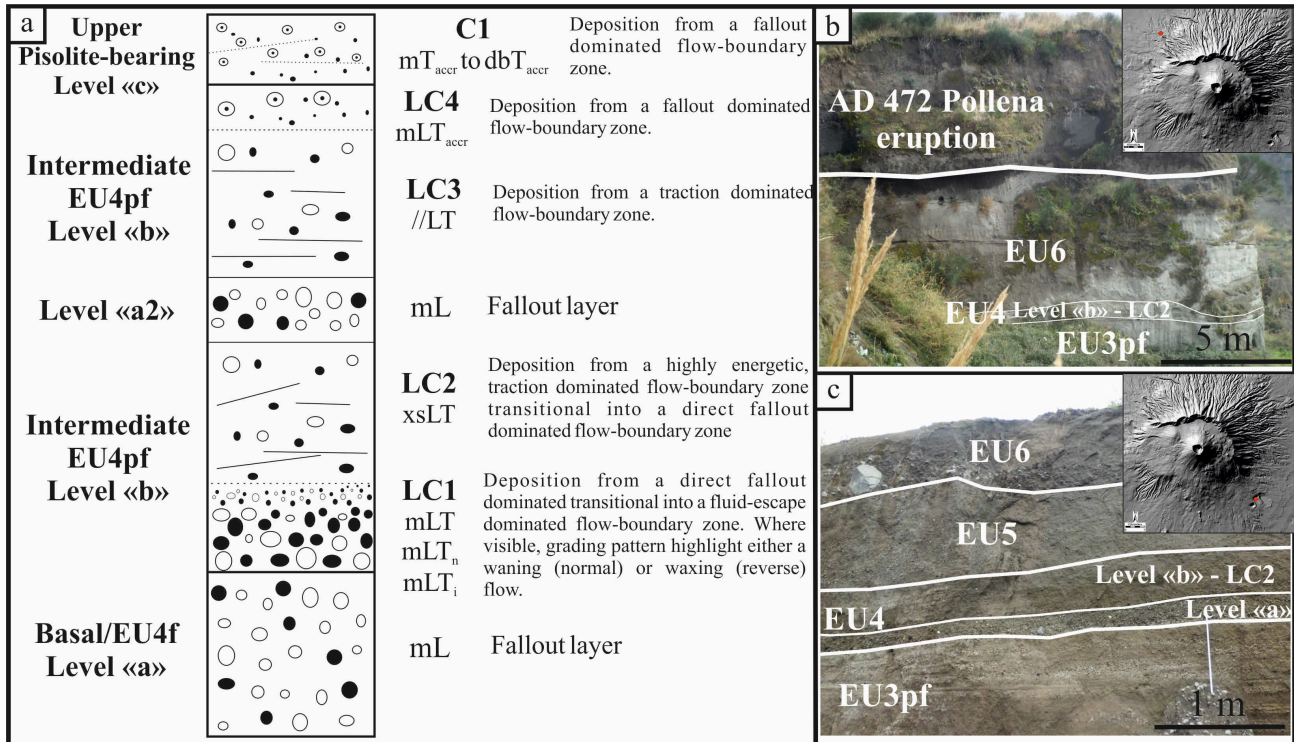


Fig. 4.3: a) stratigraphic section and lithofacies of the EU4 unit (Gurioli 1999); b) “Cava Pollena (AT)” section (see Fig. 4.8b); c) “Cava Pozzelle (AT)” section (see Fig. 4.8f).

PDCs associated with the EU4 unit travelled very far to the S (up to 20 km from vent area; Gurioli et al. 2010) reaching the area presently occupied by the town of Nocera Inferiore (see Fig.1.1). This unit has been extensively studied by Gurioli (1999) which highlighted that: i) the high shear rate exerted by the level “b” is clearly evident by the formation of “traction carpets” with pumices from the underlying level “a”, and to local erosions clearly evident on top of level “b” in very proximal outcrops; ii) in some sections, a second fallout layer (termed level “a2”) has been observed interlayered within level “b”, suggesting a partial, short-lived resumption of a convective plinian column after the first collapse. Volumes were also estimated for the three layers using the methodology by Pyle (1989) for tephra volume estimation ($\log T$ vs $A^{1/2}$), yielding values of 0.08 km³ and 0.32 km³ for levels “a” and “b” respectively, while for level “c” data were insufficient for volume estimations. From a sedimentological point of view, level “b” (which represents on average 60-90% of the thicknesses of the sections where EU4 outcrops) is generally ash-rich, matrix-supported and poorly sorted (Gurioli 1999). Four distinct lithofacies have been observed by Gurioli (1999) for this level (Fig.4.3b), with

various condition of the flow-boundary layer. Lithofacies organization tends to be more complex in areas with higher influence exerted by paleotopography (e.g. the town of Pompeii, built on top of remnants of old buried scoria cones; Gurioli 1999).

4.2.2 The AD 472 “Pollena” eruption

The AD 472 “Pollena” eruption is considered one of the most devastating eruptions of SV during the past nineteen centuries and, according the parameters calculated by various authors (Rosi and Santacroce 1983; Rolandi et al. 2004; Sulpizio et al. 2005, 2007) and listed in Table 4.2, has been catalogued by Cioni et al. (2008) as a sub-Plinian I type eruption.

Type ^(b)	Fallout Volume (km ³) ^(c)	PDC Volume (km ³) ^(d)	Total Volume (km ³) ^(e)	Peak MDR (kg/s) ^{(f)(b)}	Max runout PDC (km)	Area Invaded Fallout (isopach 10 cm - km ²) ^(b)	Source(s)	Additional Notes
sub-Plinian I	0.42 ⁽¹⁾ 1.10 ⁽²⁾ 1.38 ⁽³⁾	0.39 ⁽⁴⁾	0.81 - 1.77	7x10 ⁶ - 3.4x10 ⁷	>8<10 ⁽⁴⁾	1000	⁽¹⁾ Rosi and Santacroce (1983) ⁽²⁾ Rolandi et al. (2004) ⁽³⁾ Sulpizio et al. (2005) ⁽⁴⁾ Gurioli et al. (2010)	^(b) From Cioni et al. (2008) ^(c) Method from Fiersten and Nathenson (1992) ^(d) Method from Favalli and Pareschi (2004) ^(e) Fallout+PDC (min value-max value) ^(f) Method from Carey and Sparks (1986) ^(g) From Gurioli et al. (2010)

Table 4.2: range of values for selected parameters of the AD 472 Pollena eruption calculated by various authors.

As described in Section 1.2.2, these types of eruptions differ mainly from sub-Plinian II type eruptions relative to both physical parameters and sedimentological features of the associated deposits. Important analogies between the two types of eruptions lay in the strong stratification of the fallout products shown by almost all these events, suggesting that magma discharge was dominated by a strong instability (Cioni et al. 2008). The same authors also point out that sub-Plinian I have volumetrically important PDCs. These are generally topographically controlled, with massive to internally stratified, ash- and lithic-rich deposits and only minor, cross-laminated to dune-bedded deposits. Conversely, sub-Plinian II type eruptions are dominated by multiple short-lived phases of convective column, and by only minor (if null) generation of PDC. The AD 472 “Pollena” eruption has been recognized from historical accounts that reported ash fallout occurred in Constantinople in that year but also from sparse and brief local chronicles of that period (De Simone et al. 2012). The relative

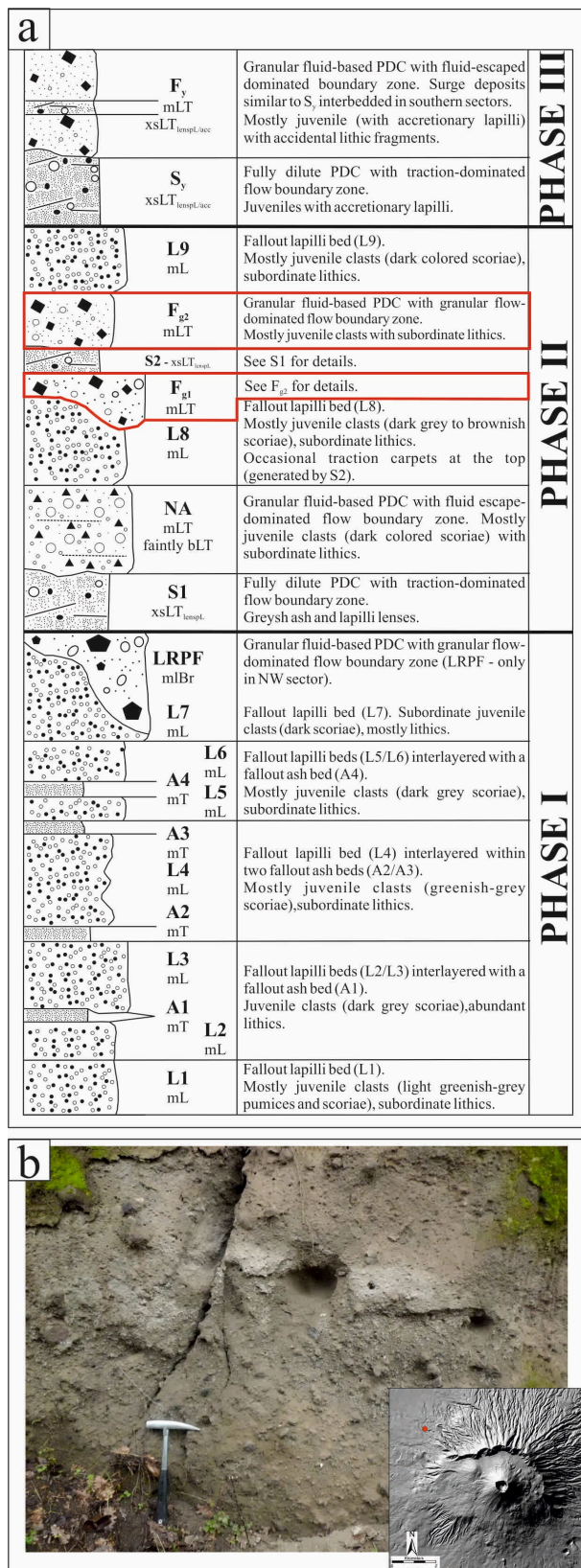


Fig. 4.4: a) stratigraphic section of the AD 472 Pollena eruption (redrawn after Sulpizio et al. 2005, 2007); b) outcrop belonging to the Fg “Cupa Olivella” lobe.

stratigraphic position of the products of this eruption furthermore confirmed its age (Rosi and Santacroce 1983; Sulpizio et al. 2005).

The eruptive sequence summarized in Fig. 4.4 has been extensively treated by Sulpizio et al. (2005) and PDC deposits of this eruption have been studied in more detail by Sulpizio et al. (2007). The above-mentioned authors subdivided the eruption in three main eruptive phases according to changes in the eruptive processes and/or changes in melt composition (Fig. 4.4a). Unlike the Pompeii eruption, the Pollena eruption started with a magmatic opening phase (Phase I; Sulpizio et al. 2005) which led to the formation of a sustained but oscillating sub-Plinian column (units L1-L7 and A1-A4) fed by phono-tephritic to tephri-phonolitic magma. The products erupted during this phase are the most evolved ones, suggesting the presence of a continuous compositional zoning in the magma chamber, unlike in the Pompeii eruption, characterized by two main magma compositions without intermediate products (Sulpizio et al. 2005). The collapse of the convective column that emplaced the L7 bed led to the development of a dense, granular fluid-based PDC which deposited the LRPF level (Sulpizio et al. 2005): the high content of accidental lithics of this level records a probable extensive demolition of the upper conduit system and/or of the volcanic edifice. This structural

failure and consequent reduction of upper crater width might have enhanced the overpressurization of the rising magma: in this view, the first S1 unit (the beginning of Phase II) represents a radial expansion of a pressurized mixture to form a dilute PDC. The following PDC deposits (NA) instead testifies, due to the absence of fall deposits between S1 and NA, an origin by a continuous collapsing fountain (Sulpizio et al. 2005). The subsequent L8 fallout bed records a restoration of a powerful sub-Plinian convective plume, which corresponded to the paroxysmal phase of the eruption (Sulpizio et al. 2005): the presence of deep-seated accidental lithics (marbles and cumulates) within this layer is probably indicative of the deepening of the fragmentation depth. The subsequent S2 (fully dilute PDC with traction-dominated flow boundary layer) and F_{g1-2} (granular fluid-based PDC with fluid-escaped dominated flow boundary zone) units have been indicated instead by the above-mentioned authors as a consequence of the collapsing column that emplaced the L8 fallout bed and partially (for unit F_{g2}) as part of the initial collapse of subsequent unit L9 (Sulpizio et al. 2007). Phase II is capped by another fallout layer (L9) that marks the re-onset of sustained sub-Plinian column. Textural features suggesting phreatomagmatic fragmentation (presence of accretionary lapilli, abundance of fine ash, coarser fragments with a yellowish coat, abundance of loose crystals) characterize instead the final Phase III of the Pollena eruption. This late stage started with the emplacement of a fully-dilute PDC with a traction dominated flow-boundary zone (Sy), which had a dispersal area more restricted toward E and SE sectors (probable influence of Mt. Somma caldera walls; Sulpizio et al. 2005). The Pollena eruption is capped by the Fy unit, a valley-ponded, granular-fluid based PDC with a fluid-escape dominated flow boundary zone; this unit is sometimes interlayered (in S sectors) by a thin layers of more dilute PDCs similar to the Sy unit. Lithology and sedimentological characteristics of Sy and Fy deposits suggest they were emplaced during pulsating, vulcanian-type explosions, without the rising of any sustained, convective column (Sulpizio et al. 2005).

As mentioned above, F_{g1} and F_{g2} units (thicknesses of deposits from few tens of cm up to 7 m: Fig. 4.4b) are subsequent to partial or total collapses of convective columns that deposited fallout units L8 and L9 respectively; similar lithological features of these two units make somewhat difficult their distinction in the field (Sulpizio et al. 2005, 2007). Lithofacies association of F_g units comprises massive, valley-ponded lapilli tuff (mLT) with few examples of crudely stratified deposits at the bottom of mLT lithofacies (Sulpizio et al. 2007). The same authors points out that the general poor sorting combined with the inverse grading of coarser blocks indicate that grain-interaction processes

dominated in the flow boundary zone at the time of deposition (modified grainflows). Furthermore, the absence of ash-rich layers and of any erosive surface indicates rapid aggradation of different pulses.

4.3 Methods

4.3.1 *Maximum runout*

Reconstructed maximum runout for selected PDCs from the two studied eruptions represent the fundamental starting point for model validation, since percentages of matching between model outputs and real inundation area can be easily quantified in this way. They have been reconstructed either for single eruptive units (single episodes of column collapse with progressive or stepwise aggradation of the deposit) or for single PDC lobes (small-volume deposits from short-lived, low mass-flux currents; Branney and Kokelaar 2002) within an eruptive unit. In the study cases, PDC maximum runouts represent the ideal 0 cm isopach, beyond which all the deposits related to that eruptive unit or lobe does not show features typical of lateral transport: in other words, ash-fall deposits from co-ignimbritic plumes are not considered for most of the units, except for the EU4c one which can be considered, at least in part, as derived by fallout from the co-ignimbrite cloud related to level “b”. The approach for maximum runout definition considers different constraints, which are: i) field data related to the thicknesses of the deposit for selected stratigraphic sections; ii) topographic constraints that could have limited PDC dispersal area; iii) areal extent of preserved deposits. Three different outlines of PDC maximum runouts are therefore presented for each unit/lobe, namely “Modal”, “5th percentile” and “95th percentile”. The idea for this specific classification is to provide the best estimation of the maximum runout for the specific unit (represented by the “Modal” outline) with two upper and lower uncertainty bounds (the “5th percentile” and the “95th percentile”) that take into account epistemic uncertainties in the same way as expressed for the vent opening probability maps issue. The procedure for determining reasonable uncertainty bounds starts with the definition of the Modal maximum runout outline, composed by different segments which can be traced with different degrees of confidence (this latter one depending on the number and quality of constraints for that position). In the following figures these segments will be drawn differently (e.g. orange straight lines, dashed lines, etc.) and will be all named “0 cm Modal isopach”. Once defined the number of segments, for each of them the upper (+) and lower (-) uncertainty bounds are evaluated by considering the above-mentioned criteria. For this

study, four different uncertainty bounds have been applied, which are 200 m (low uncertainty), 500 m (moderate uncertainty), 1000 m (moderate-high uncertainty) and 2000 m (high uncertainty). Upper and lower uncertainty values for a single segment of the Modal maximum runout might or might not be the same (e.g. lower bound might be -200 m while the upper might be +1000 m) depending on the amount of constraints available.

4.3.2 Volume estimation

The assessment of tephra volume is a central issue in volcanology, as it represents a critical parameter for volcanic eruption magnitude calculation (Newhall and Self 1982) but also a key input data for numerical modeling for both PDC (Esposti Ongaro et al. 2008; Neri et al. 2015) and fallout (Macedonio et al. 2008; Macedonio et al. 2016) dispersal area definition. The classical approach for the calculation of the volume of volcanic tephra is represented by the method of Pyle (1989) for fallout deposits, which considers plots of $\log_{\text{Thickness}}$ versus isopachs area^{1/2}. This approach is consistent geologically as most of fallout deposits thin exponentially from source and therefore plot as straight lines with these variables (Fierstein and Nathenson 1992); however, as shown by Bonadonna and Houghton (2005), at least three distinct exponential segments can often be defined, and power-law or Weibull functions (Bonadonna and Costa 2012) can provide even better fits in some cases. Further complications are related to the degree of subjectivity introduced by isopaches hand-drawing (Klawonn et al. 2014) and to the lack (due to erosion) of distal, proximal and/or seaward deposits, which can lead to significant underestimations of the real volume of the fallout deposits (Bonadonna and Houghton 2005).

For PDC deposits, although sometimes is easier to define their total inundation areas (i.e. the 0-cm isopach), it is often more complex to determine volumes due to the strong influence that topography exerts on deposit geometry and thicknesses, especially at proximal sites (i.e. no simple decay rules can be envisaged); even when calculated, PDCs volume estimations are affected by significant degrees of uncertainties (Sulpizio et al. 2005; Gurioli et al. 2010). Some of the approaches considered in bibliography for PDC volume estimations include however the usage of the $\log_{\text{Thickness}}$ versus Area^{1/2} rule proposed by Pyle (1989): as mentioned in Section 4.2.1, this method was used for instance by Gurioli (1999) for the estimation of the volume of the *AD 79 Pompeii* EU4 unit. Another method used

by Crandell (1989), although applied for Debris Avalanche deposit volume estimations of Mount Shasta USA, involves the partitioning of the deposit into areas defined according to different homogeneous morphological sectors of the deposit itself. Each of these areas is then assigned a mean value for thickness (applied for the whole area) and the volume of the single area can be easily calculated, as well as the total volume of the unit. Finally, Isaia et al. (2004) estimated the volume of deposits from low-concentration, turbulent PDCs from the Astroni volcano (Campi Flegrei, Italy) with a mixed approach. They extrapolated thickness distribution with distance assuming an exponential decrease, and reconstructed the pristine shape of the deposit by applying a triangular irregular network algorithm on commercial GIS software.

Since there is still not consensus about the best procedure for PDC volume estimations (due to the above-mentioned complexities), in this work different approaches have been compared. In particular, the method from Crandell (1989) was applied for the estimation of the volume of the EU3pf unit. For the EU4 unit, the “trapezoidal rule” approach defined by Fierstein and Nathenson (1992) was considered: it consists of integrating the area under the curve drawn on a Thickness versus Isopach area plot. Each segment defined by two points of the graph identifies a trapezoid made up by a triangle on top of a rectangle. The formula for the volume between isopach T_n of area A_n and isopach T_{n+1} of area A_{n+1} (the area of a single trapezoid) may be written:

$$\Delta V_{n+1} = \frac{1}{2} (T_{n+1} + T_n)(A_{n+1} - A_n) \quad [1]$$

The total volume would then be the sum of the volumes of all the single segments that make up the curve. The above-mentioned authors have shown that this method tend generally to overestimate the actual volume of the deposit, but if there are numerous closely spaced isopachs, the trapezoidal rule is appropriate.

For this project it has also been used the TIN (Triangular Irregulated Network) spatial interpolator available from the ESRI ArcGIS 10® platform for volume estimations of the EU3pf, EU4 and Fg units. A TIN is a vector surface model that consists of a network of triangles that are formed by connecting nodes (input data) according to the Delaunay criterion (Lee and Schachter 1980). In this model, each point on the edge or inside the triangle has a specific value that is calculated through linear interpolation. This approach (although originally implemented for the construction of Digital Elevation Models from elevation data), has the advantage that i) it is easily applicable also for PDC sections

thickness data and ii) it consider a simple linear decaying rule from each point (which is probably more appropriate in this case since no more complex decaying rules can be defined). In the study cases of this project, input data are therefore represented by i) section sites with their value of level thicknesses, ii) reconstructed isopachs (as described in section 4.4.2) and iii) the maximum runout areas of, respectively, the 5th, Modal and 95th percentiles (where thickness is fixed as 0 m).

To summarize, volume estimations for PDC eruptive units/lobes described here (EU3pf and EU4 from the *AD 79 Pompeii* eruption and Fg unit from the *AD 472 Pollena* eruption) have been performed and compared using a) the TIN spatial interpolator for all of the units; b) the method from Crandell (1989) for the EU3pf unit; c) the “trapezoidal rule” (Fierstein and Nathenson 1992) for the EU4 unit. Furthermore, for the EU4 unit, values calculated by Gurioli (1999) using the $\log_{\text{Thickness}}$ versus isopachs area^{1/2} approach are compared with the outcomes of the TIN volume estimation for the EU4 unit itself.

4.3.3 Total Grain Size Distribution (TGSD)

Total Grain Size Distribution (TGSD) represents an important parameter for the inference of fragmentation processes and for numerical models concerning hazard assessment. Several approaches have been proposed for the calculation of this parameter (especially for fallout deposits), mostly regarding the weighted mean of either deposit thickness or mass (Murrow et al. 1980; Walker 1980; Sparks et al. 1981).

The classical approach used to calculate the TGSD was the one that involves the drawing of isomass map. In more detail, for each section the values of mass per unit area (obtained by multiplying the average density of the section times the thickness of the section) is calculated for each grain size class ($\Phi_{M/A}$). Then, isomass maps are drawn for each granulometry and the values of $\ln\Phi_{M/A}$ versus the square root of the area enclosed in each isomass line are plotted for each isomass map. The total mass for each grain size is easily calculated from the above-mentioned plots using the same formula defined by Pyle (1989) for volume estimations. Each mass values is finally divided by the total mass of the unit and multiplied by 100, obtaining the TGSD for the whole unit. This method was applied by Gurioli (1999) in order to calculate the TGSD for the EU4 unit, and this value is compared to the one obtained with the Voronoi tessellation method used in this work and described below.

Bonadonna and Houghton (2005) proposed a method based on the Voronoi tessellation approach, which partitions the study area in as many polygons as the number of data points (expressed as mass per unit area). The tessellation is performed such that each polygon associated with a specific data point contains all spatial locations closer to that point than to any other. The TGSD is obtained by weighting each grain-size analysis of a stratigraphic section using the total mass of the related Voronoi cell. This latter is calculated by multiplying the mass per unit area of the section (the average density of the section times the thickness of the section) with the area of the Voronoi cell. In other words, the TGSD is obtained as the mass per unit area-weighted average of all the Voronoi cells over the whole deposit.

As pointed out by Gurioli (1999), the isomass method (but this is true also for the Voronoi one) is certainly useful for estimating the TGSD of the coarser part of the collapsing column that produce the final PDC deposit, but it represent an underestimation of the finer part of the PDC itself, which is elutriated during the emplacement and deposited in more distal areas.

4.3.4 Reconstruction of paleotopography

As pointed out in Section 4.1, the topography of SV prior to the eruptions studied here (especially for the *AD 79 Pompeii* eruption) was substantially different with respect to the present one. This fact could have a major impact on PDC numerical simulations when trying to validate their outputs with field data, since almost all of the codes used presently are strongly linked with DEM input data (Patra et al. 2005; Esposti Ongaro et al. 2008; Neri et al. 2015; Bevilacqua 2016). A detailed reconstruction of SV paleotopography is quite difficult, especially for older eruptions: for this purpose, necessary information ideally include i) a detailed geological mapping of all the units younger with respect to the eruption under consideration for the whole area of investigation, ii) thickness data at multiple stratigraphic sections and maximum runout outlines of all the units mentioned in the previous point and iii) information about general morphology of the edifice prior to eruptions, possibly from accurate pictures or paintings. For the SV study case, limited amount of data were retrievable with respect to points i) and ii), especially for volcanic units from younger eruptions. Some qualitative information with respect to point iii) were obtained by analyzing frescos from Pompeii excavations, particularly the one reported in Cioni et al. (1999) and by recreating the desired morphological features

described in Section 4.4.7. For what concerns Fg units from the AD 472 Pollena eruption instead, data for points i) and ii) were more abundant. The limited investigation area made in fact easier to retrieve outcrops distribution from the Santacroce and Sbrana (2003) geological map, and the fact that in the investigation area the AD 472 Pollena eruption is the youngest unit allowed use of the stratigraphic sections of this unit to perform a complete “scooping” of the deposit. The procedure of “scooping” consists of the removal of a desired unit from the Digital Elevation Model (DEM) of the study area. It is performed by reconstructing the DEM of the unit itself starting from thickness data from stratigraphic sections and by subtracting this DEM (only where the unit actually outcrops) from the present day DEM of the SV area. All of the two reconstructions have been performed using tools from the ESRI ArcGIS 10.1® platform, and the detailed procedure is described in Section 4.4.8.

4.4 Results

4.4.1 Maximum runout for the EU3pf and EU4 units and for the Fg “Cupa Fontana” lobe

Unit EU3pf, Pompeii eruption

For the EU3pf unit, the procedure for the definition of the maximum runout for PDC invasion (following the description of Section 4.3.1), involved the recognition of three segments of the “Modal” 0-cm isopach, each of them with different uncertainties linked to their position (Fig.4.5a; segments with IDs 1, 2 and 3). The constraints that were mainly used for the positioning of the “Modal” maximum runout segments and for the definition of their uncertainties were the stratigraphic sections of EU3pf outcrops and their related thicknesses. These sections (as it will be described in more details in section 4.4.2) are related to two different field works, the first one carried on by Gurioli (1999) and the second one during this work.

The three segments have been catalogued with different IDs, which are:

- *Modal value ID 1*: PDC toward N, NE and SE; good constraints are represented by the numerous stratigraphic sections where EU3pf is only few cm’s thick, uncertainty is therefore fairly low. 5th percentile –200m; 95th percentile +200m.

- *Modal value ID 2*: inland part toward NW; the only constraint are represented by few stratigraphic sections located NNW, where thicknesses of EU3pf are of the order of few meters; the related uncertainty is moderate-high. 5th percentile –500m; 95th percentile +1000m.

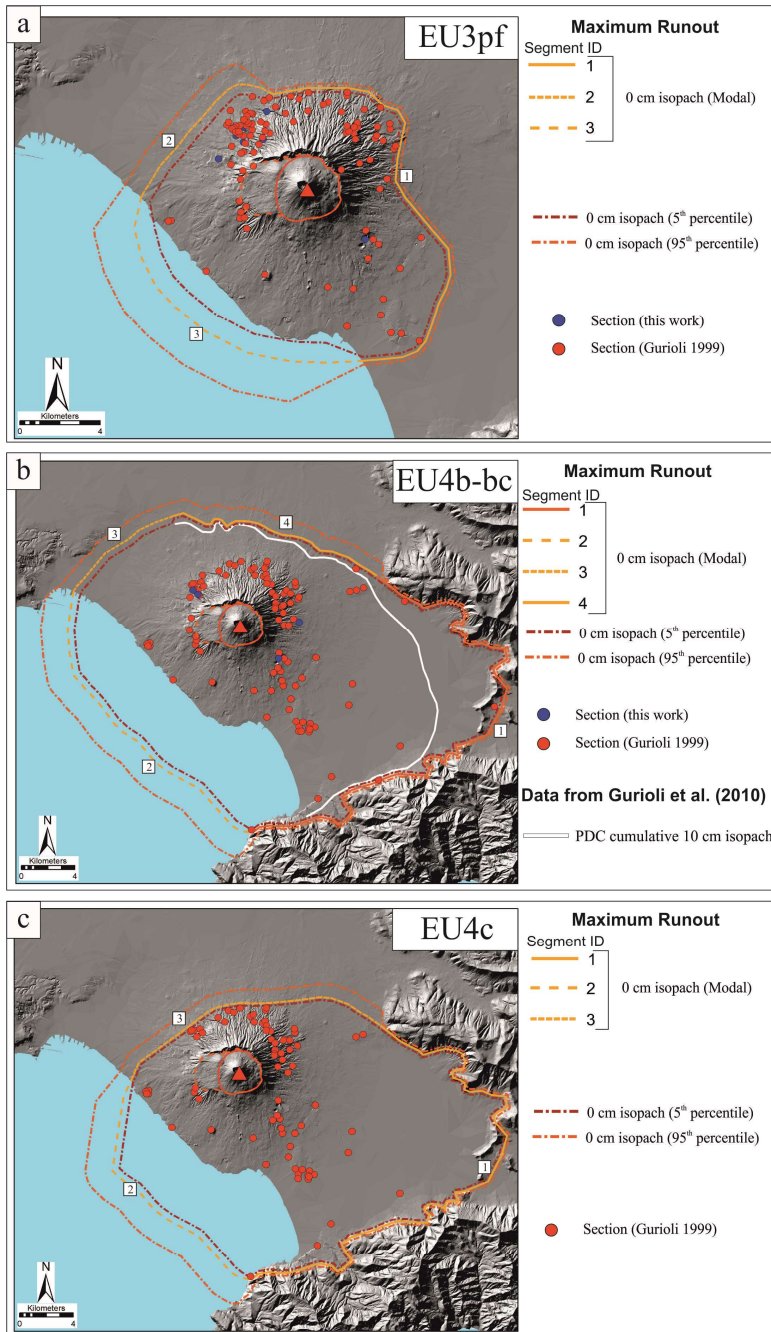


Fig. 4.5: maximum runouts of eruptive units belonging to the AD 79 Pompeii eruption; a) EU3pf; b) EU4b-bc; c) EU4c. Red triangle is the inferred position of vent. Red line is the outline of the uncertainty area of vent position (Section 2.4.2). SV caldera outlined in dark orange dashed line.

- *Modal value ID 3*: seaward part, no useful constraints are available except for few stratigraphic sections near the coastline where thicknesses are of the order of several meters; related uncertainty is therefore high. 5th percentile -1000m; 95th percentile +2000m.

Unit EU4, Pompeii eruption

The definition of the maximum runout for the EU4b unit took advantage (although for a limited part) of the stratigraphic sections that were studied in the above-mentioned field works, but the constraints that were used the most are represented by i) the topography and ii) PDC isopachs defined in Gurioli et al. (2010). With respect to point ii), it is worth pointing out that the isopachs defined in the above-mentioned paper are cumulative isopachs for all the PDC units of the AD 79 “Pompeii” eruption. However, after a consultation with some of the authors, it was assessed that the more

distal isopach of the PDC units of the AD 79 “Pompeii” eruption (the 10 cm isopach reported in Fig.4.5b) is almost entirely referred to the EU4b unit only, and therefore it could be used as a constraint for the definition of the maximum runout outline. For the EU4b unit, four segments were defined (Fig.4.5b; segments with IDs 1, 2, 3 and 4), while for the EU4c three segments were drawn (Fig.4.5c; segments with IDs 1, 2 and 3). In more details, the four segments for the EU4b unit are:

- *Modal value ID 1*: inland part toward E and SE, good constraints are represented by the inclined topography of the northernmost part of the Sorrentina peninsula (to the SE) and of the Apennines (to the E), along with the 10 cm isopach from Gurioli et al. (2010); uncertainty is therefore fairly low. 5th percentile –200m; 95th percentile +200m. This segment is the one that extends the most the maximum runout of the EU4b unit from the vent area: the section of Palazzo Baronale-Còdola (see Fig. 4.8) is located in fact more than 20 km away from the vent area.
- *Modal value ID 2*: seaward part. For this segment (which is the most uncertain one) it is worth mentioning that there are evidences that PDCs travelled at least for 5-7 km after reaching the paleo-coastline at the beginning of the Sorrentina peninsula (S. Maria di Pozzano site, see Fig. 4.8) where thickness of EU4b unit is of the order of some cm’s. For this reason, the “Modal” 0-cm isopach in this segment has been placed 5 km off the coastline. Despite this evidence, uncertainty is however moderately high. 5th percentile –500m; 95th percentile +2000m.
- *Modal value ID 3*: inland part toward W, no strong constraints are present here (the only ones are the 10 cm isopach that ends toward E and the inclined topography that begins toward NW); for these reasons the uncertainty is moderate-high. 5th percentile –500m; 95th percentile +1000m.
- *Modal value ID 4*: inland part toward N, the only good constraint is the 10 cm isopach, and uncertainty is therefore moderate. 5th percentile –200m; 95th percentile +1000m.

Finally, for the EU4c unit, similar constraints with respect to the EU4b unit have been employed, identifying a total of three segments:

- *Modal value ID 1*: inland part toward E and SE, this part has been considered the same as the one defined for the EU4b unit. 5th percentile –200m; 95th percentile +200m.
- *Modal value ID 2*: seaward part. Same considerations as for the EU4b unit. 5th percentile –500m; 95th percentile +2000m.

- *Modal value ID 3*: inland part toward W and NW, the only constraints are represented by stratigraphic sections where thicknesses are of the order of very few cm's; for these reasons the uncertainty is moderate. 5th percentile –200m; 95th percentile +1000m.

A comparative table of the surface of PDC inundation areas for the three units described above is provided in Table 4.3.

EU3pf			EU4b			EU4c		
Area Invaded PDC (km ²)			Area Invaded PDC (km ²)			Area Invaded PDC (km ²)		
5 th	Modal	95 th	5 th	Modal	95 th	5 th	Modal	95 th
143	<u>166</u>	212	492	<u>521</u>	610	405	<u>428</u>	503

Table 4.3. Comparative table of PDC inundation areas for the three units described in text.

Unit Fg, Pollena eruption

For the AD 472 “Pollena” eruption, it has been reconstructed the maximum runout of a PDC lobe from the Fg unit (see section 4.2.2), for which unpublished data about stratigraphic sections (M. Mulas et al.) have been employed. As displayed in Fig. 4.6 some of these stratigraphic sections (14) have been actually mapped in the field. Among these, only for 6 of them there are data about thicknesses. For the remaining sections (21), data about thicknesses have been “interpolated”: in order to do so, the decay rule of thickness among two adjacent “real” sections has been calculated, and by prolonging this decay rule up to the site of the desired “interpolated” section, the thickness value at that site is estimated. Apart from information deriving from stratigraphic sections, the outline of the

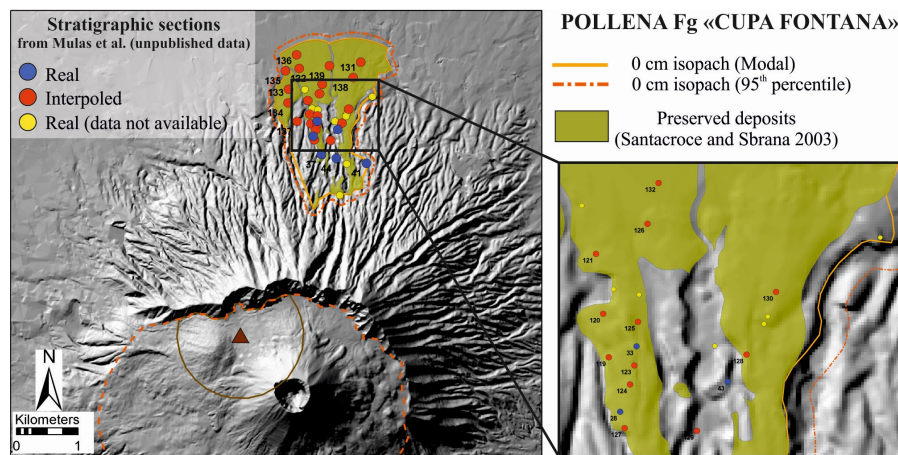


Fig. 4.6: maximum runouts of Fg “Cupa Fontana” PDC lobe belonging to the AD 472 Pollena eruption. Brown triangle is the inferred position of vent. Brown line is the outline of the uncertainty area of vent position (Section 2.4.2). SV caldera outlined in dark orange dashed line.

preserved deposits of PDCs from the geologic map from Santacroce and Sbrana (2003) have been used as well to define the maximum runout of this PDC lobe. Differently with respect to the outlines of the units from the Pompeii eruption, in this case the lower percentile of

uncertainty has not been defined. This is due to the fact that the “Modal” 0-cm isopach outline has been drawn considering the outline of the preserved deposit of the AD 472 “Pollena” PDC units in this area (and the distribution of stratigraphic sections as well). Only one segment of the “Modal” maximum runout has been considered. The choice of putting the modal outline implies that this estimate of the maximum runout is at the same time the best guess and the minimum value of runout. The upper uncertainty bound (95th percentile) has been placed at a constant distance of +200 m with respect to the Modal one, as the thicknesses of the F_g “Cupa Fontana” PDC lobe in the stratigraphic sections close to the Modal outline are of the order of few cm’s (and therefore the PDC could not have travelled too far away). Values of the surface of the PDC inundation areas for these two outlines are reported in Table 4.4.

Area Invaded PDC (km ²)	
5 th /Modal	95 th
<u>4.8</u>	5.7

Table 4.4: PDC inundation areas for the Fg “Cupa Fontana” PDC lobe described in text.

4.4.2 Volume estimation for the EU3pf and EU4 units and for the Fg “Cupa Fontana” lobe Unit EU3pf, Pompeii eruption

As pointed out in section 4.3.2, volume estimations for the EU3pf, EU4b, EU4c units and for the Fg lobe represent critical values for numerical modeling and these estimations, since there are no universally accepted methods for calculating them for PDCs, have been made using different approaches. For all of this calculations, different estimates have been therefore performed considering the two or three outlines of the maximum runouts and, for the EU4b case, also considering maximum and minimum values of different levels measured in each section (see below). With respect to the EU3pf unit, the two methods that have employed here are the TIN interpolation and the sectorialization of the deposit into homogeneous areas (called here PDC fans) according to the procedure described by Crandell (1989). In order to account for a possible influence of the Mt. Somma scarp in partitioning the total erupted volume of material (i.e. the preferred distribution of erupted material toward southern sectors due to the presence of the Mt. Somma barrier), the deposit has been subdivided into two zones (N and S, see green dashed line in Fig.4.7).

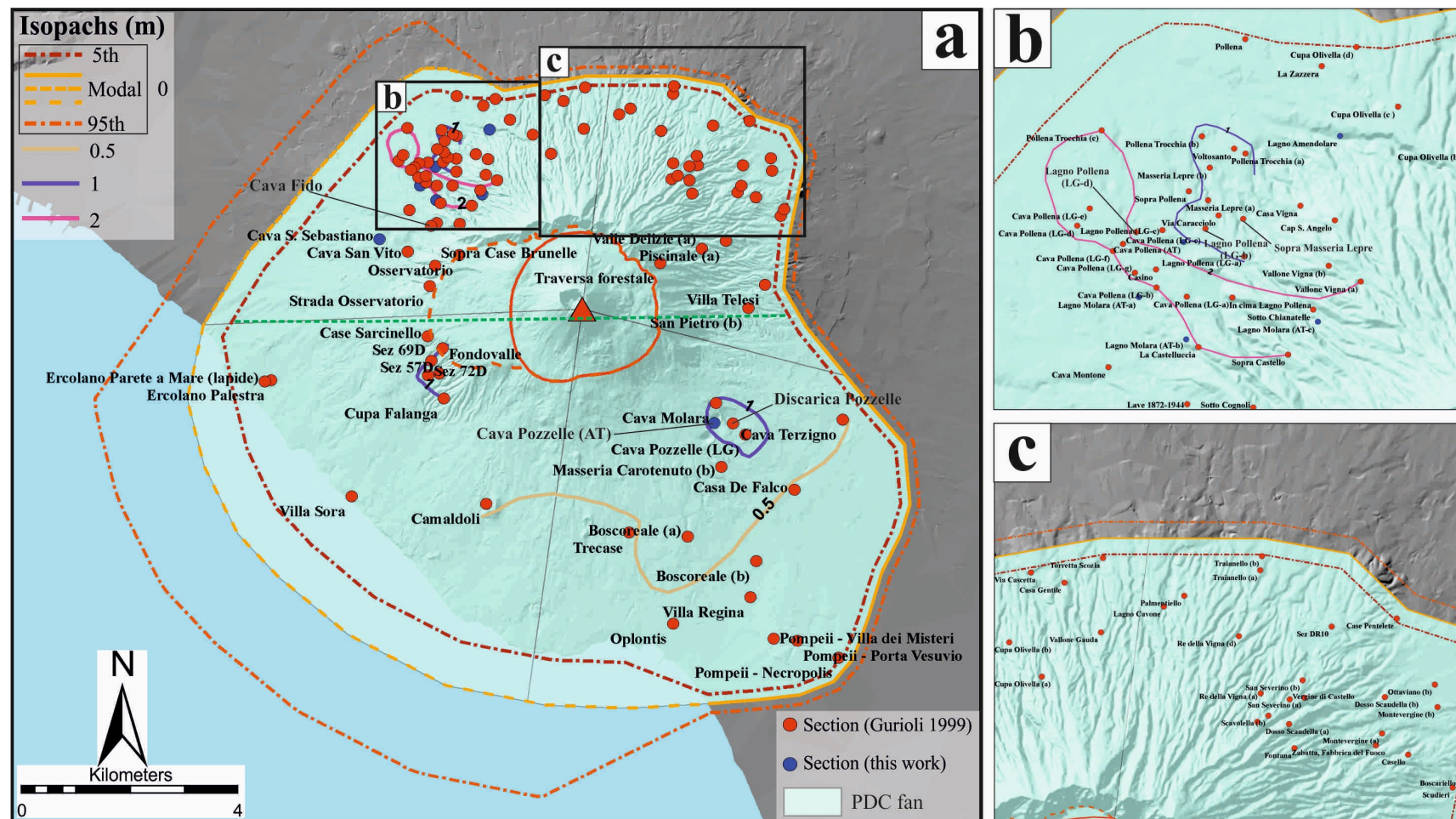


Fig. 4.7: a) stratigraphic sections used for volume estimations of the EU3pf unit. The dark green dashed line subdivides the unit into the northern (N) and southern (S) part as described in text. b) and c) are enlargements of a). Red triangle is the inferred position of vent. Red line is the outline of the uncertainty area of vent position (Section 2.4.2). SV caldera outlined in dark orange dashed line.

The distribution of the stratigraphic sections used for EU3pf volume estimations (along with the reconstructed isopachs and the four PDC fans distribution) is displayed in Fig.4.7. A total of 106 stratigraphic sections (99 from Gurioli 1999 and 7 from this study) have been employed for volume estimations and the complete list of these sections (along with samples collected in each stratigraphic section, see section 4.4.3) is displayed in section 8.4.1. Thicknesses range from 2 cm (“Dosso Scaudella (a)” section) up to 14 m (“In cima Lagno Pollena” section) up to 14 m with a mean value of 1.79 m. The areal coverage of stratigraphic sections is fairly homogeneous but denser in northern sectors: this is due to the higher level of urbanization of the southern sectors and to the rough topography of the northern part of SV, with lots of valleys that allow to describe more stratigraphic sections. Using the values of thicknesses, segments of three different isopachs (i.e. the 0.5 m, the 1 m and the 2 m) have been drawn (Fig. 4.7). For the sectorialization method, four sectors have been drawn, corresponding to the NW, NE, SE and SW part of the EU3pf unit. For each of these “PDC fans”, a mean value of thickness has been calculated starting from the thicknesses of all the sections that fell into that sector, and this mean value has been assigned to the whole sector. The values are 2.53 m (calculated from 52 sections), 0.65 m (calculated from 27 sections), 1.37 m (calculated from 14 sections) and 1.62 m (calculated from 9 sections) for the NW, NE, SE and SW sectors respectively. Due to the low level of reliability of this method (as discussed in section 4.5.2), only the total volume of the EU3pf unit has been calculated with this method. All the values of volume estimations with the TIN and sectorialization methods are displayed in Table 4.5.

TIN						Sectorialization	
NORTH		SOUTH		TOTAL			
Percentile	Volume (km ³)	Percentile	Volume (km ³)	Percentile	Volume (km ³)	Percentile	Volume (km ³)
5 th	0.080	5 th	0.072	5 th	0.152	5 th	0.227
Modal	<u>0.096</u>	Modal	<u>0.092</u>	Modal	<u>0.188</u>	Modal	<u>0.265</u>
95 th	0.113	95 th	0.127	95 th	0.240	95 th	0.345

Table 4.5: volume estimations for the EU3pf unit after the TIN interpolator method and the sectorialization of the deposit (as discussed in text).

From Table 4.5 it is clear how the sectorialization method tend to produce higher estimations for the total volume, although the order of magnitude is the same. With respect to the TIN estimations, it is evident how the two sector (N and S) share substantially the same amount of material in terms of volumetric content.

Unit EU4, Pompeii eruption

For the EU4b and EU4c units instead, a total of, respectively, 102 sections (98 from Gurioli 1999 and 4 from this work) and 77 sections (all from Gurioli 1999) have been employed for volume estimations. The distribution of these sections is reported in Figs. 4.8 and 4.9 respectively.

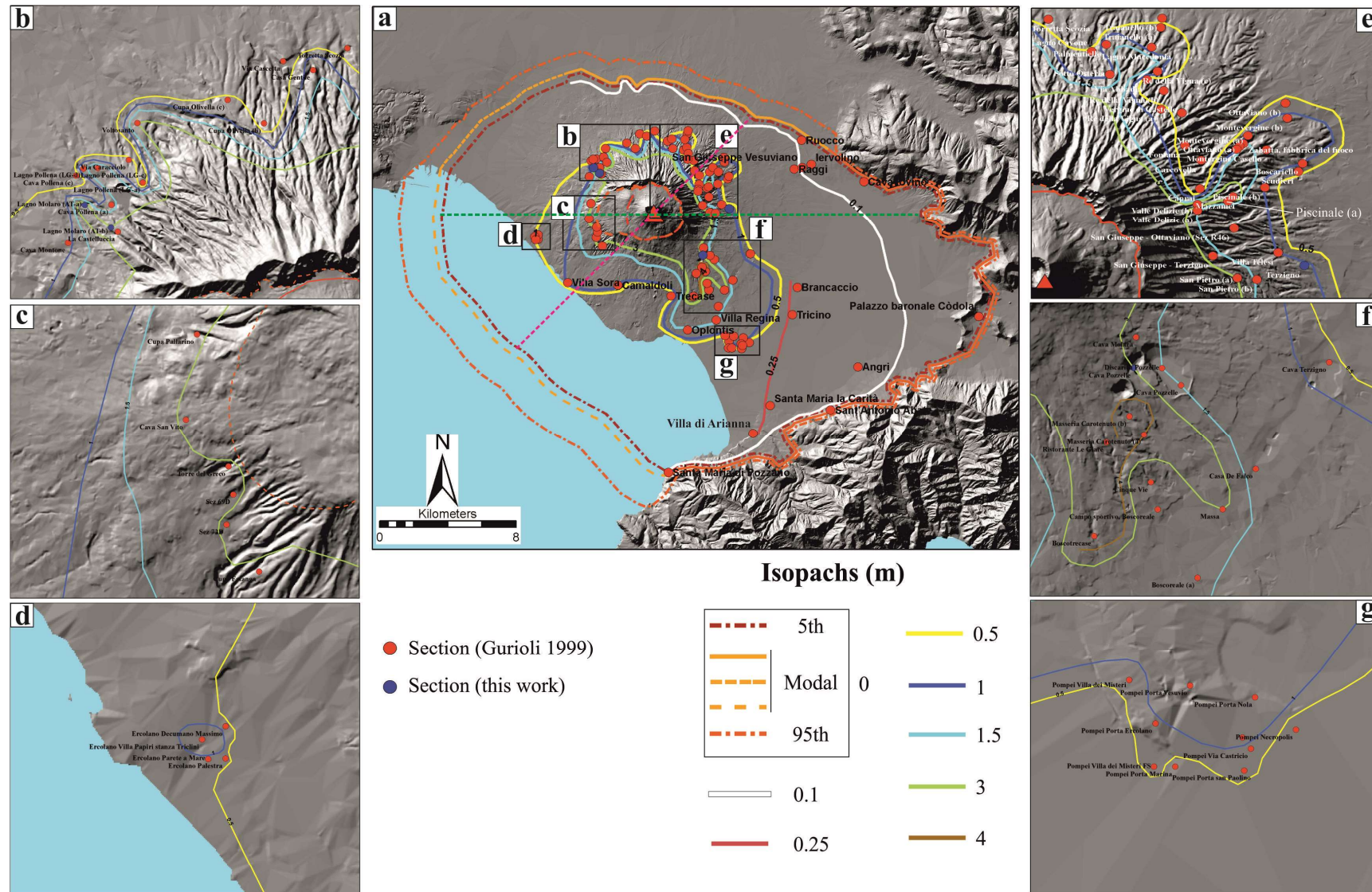
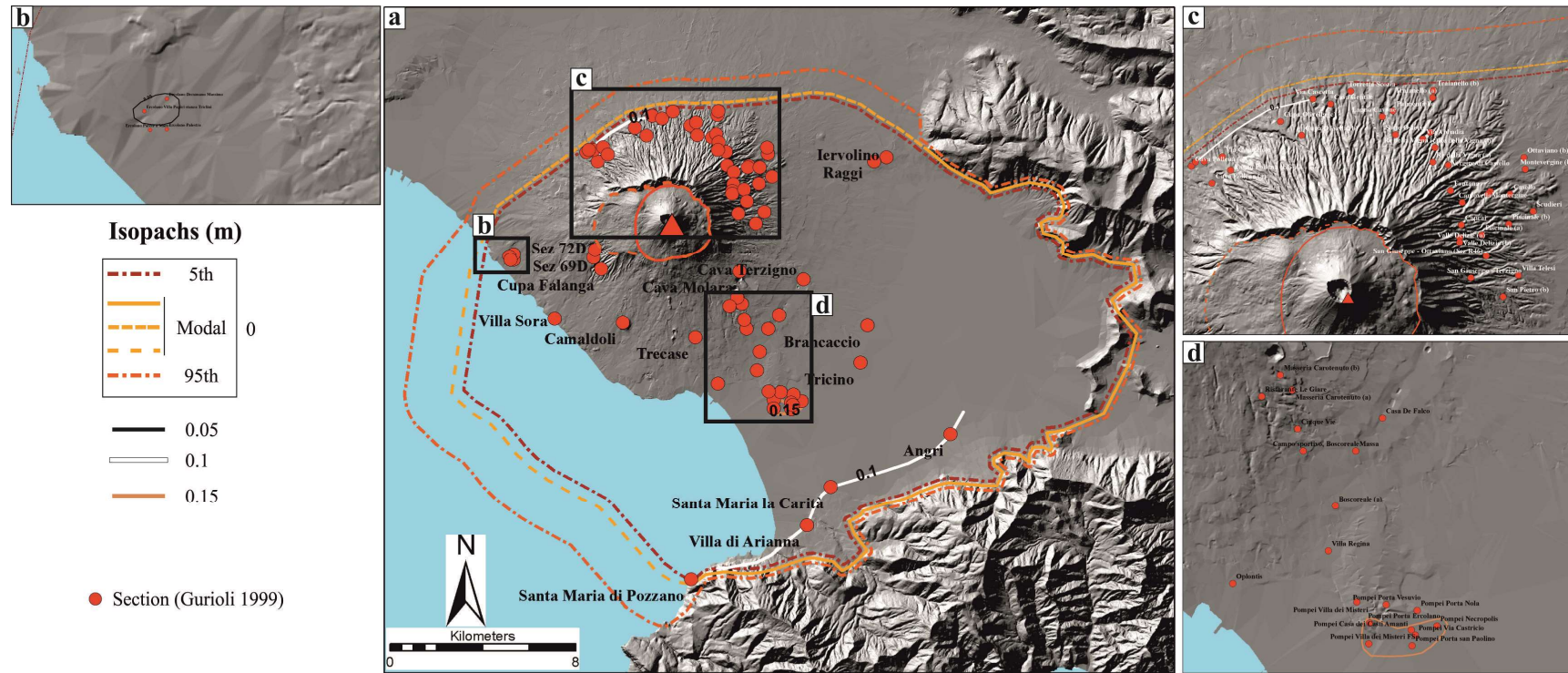


Fig. 4.8: a) stratigraphic sections used for volume estimations of the EU4b unit; b) - g) enlargements of a). The dark green and the purple dashed lines in a) identifies the N/S and E/W sectors as described in text. Red triangle is the inferred position of vent. Red dashed line is the outline of the uncertainty area of vent position (Section 2.4.2). SV caldera outlined in dark orange dashed line.



Total thickness values for the EU4b and c units (considered together) range from 2 cm (“Palazzo Baronale-Còdola” section) up to 8 m (“Ercolano Villa dei Papiri stanza dei Triclini” section – see Fig. 4.8). Original data for the EU4 unit as a whole were in some cases inhomogeneous with respect to the information available: a complete list of these sections (where thicknesses and samples for both EU4b and EU4c units are stored) is available in section 8.4.2. A problem for what concerns the information available for the EU4 unit as a whole was related to the fact that only for 57 sections out of 102 there were information on both the total thickness of the section and on partial thicknesses of the three levels of EU4 (a, b and c). For the remaining sections, only total thicknesses were reported, and therefore the values of thickness of a, b and c levels was estimated starting from the relative ratios of a, b and c thicknesses at some key sections. These values underline how the cumulative thickness of b and c levels accounts, on average, for the 80% of the total thickness of the sections. Moreover, level “a” has not been found to be thicker than 70 cm and, as shown by Gurioli (1999), the dispersal axis of level “a” is directed toward SE. With respect to levels b and c, the thickness of c made up, on average, 7% of the cumulative thickness of b and c. With these information, partial thicknesses of levels a, b and c were extrapolated for 26 sections (highlighted in orange color in Table 8.4 from section 8.4.2), while for the remaining 19 sections (mainly in the northern sector) the total thickness was considered representative of levels b and c solely and calculated accordingly. A further element of inhomogeneity is related to the fact that for 34 sections out of the 57 for which partial thicknesses were originally present, for some of the three levels two values of thickness are reported, which indicate a maximum and a minimum value of thickness. For this latter point, although the values of volume estimations have been calculated using either the minimum or the maximum values, a mean value of volume estimations has been calculated as well. With the information available, it was possible (for the EU4b unit) to draw entirely or partially a total of 7 isopachs, namely the 0.1 m (same as drawn by Gurioli et al. 2010), the 0.25 m, the 0.5 m, the 1 m, the 1.5, the 3 m and the 4 m ones. For the EU4c instead, it was possible to draw only parts of the 0.05 m, the 0.1 m and the 0.15 m isopaches. Volume has been estimated also considering levels b and c together (EU4b/c). The TIN interpolation method has been employed for the calculation of the volume of EU4b, EU4c and EU4b/c, while the trapezoidal rule has been used to calculate the volume of EU4b and EU4b/c only (due to the fact that for the few isopachs of the EU4c only few discontinuous segments were drawn). With respect to this latter method, the intercept (T_0) within the graph Thickness versus Area has been calculated by prolonging the segment of the two thickest isopachs up to the y axis (zero distance). Equation [1] from section 4.3.2 have been therefore applied to 5 segments for both EU4b and EU4b/c units.

EU4 - b					
TOTAL					
Percentile		Volume km ³		Volume km ³ (MEAN)	
5 th		0.290 - 0.293		0.292	
Modal		0.294 - 0.297		0.295	
95th		0.311 - 0.314		0.313	
NORTH			EAST		
Percentile	Volume km ³	Volume km ³ (MEAN)	Percentile	Volume km ³	Volume km ³ (MEAN)
5 th	0.105 - 0.106	0.106	5 th	0.172 - 0.174	0.173
Modal	0.106 - 0.106	0.106	Modal	0.173 - 0.176	0.175
95 th	0.111 - 0.111	0.111	95 th	0.178 - 0.181	0.179
SOUTHEAST			NORTHWEST		
Percentile	Volume km ³	Volume km ³ (MEAN)	Percentile	Volume km ³	Volume km ³ (MEAN)
5 th	0.184 - 0.187	0.186	5 th	0.119 - 0.119	0.119
Modal	0.187 - 0.190	0.189	Modal	0.120 - 0.121	0.120
95 th	0.201 - 0.203	0.202	95 th	0.133 - 0.133	0.133
EU4 - c					
TOTAL					
Percentile		V km ³		V km ³ (MEAN)	
5 th		0.032 - 0.033		0.033	
Modal		0.034 - 0.035		0.034	
95 th		0.041 - 0.042		0.041	
NORTH			EAST		
Percentile	Volume km ³	Volume km ³ (MEAN)	Percentile	Volume km ³	Volume km ³ (MEAN)
5 th	0.003 - 0.003	0.003	5 th	0.026 - 0.029	0.027
Modal	0.003 - 0.003	0.003	Modal	0.030 - 0.030	0.030
95 th	0.004 - 0.004	0.004	95 th	0.035 - 0.036	0.035
SOUTHEAST			NORTHWEST		
Percentile	Volume km ³	Volume km ³ (MEAN)	Percentile	Volume km ³	Volume km ³ (MEAN)
5 th	0.029 - 0.029	0.029	5 th	0.004 - 0.004	0.004
Modal	0.030 - 0.031	0.031	Modal	0.004 - 0.004	0.004
95 th	0.037 - 0.038	0.037	95 th	0.006 - 0.006	0.006
EU4 - b/c					
TOTAL					
Percentile		Volume km ³		Volume km ³ (MEAN)	
5 th		0.301 - 0.304		0.303	
Modal		0.305 - 0.308		0.306	
95 th		0.324 - 0.327		0.325	
NORTH			EAST		
Percentile	Volume km ³	Volume km ³ (MEAN)	Percentile	Volume km ³	Volume km ³ (MEAN)
5 th	0.106 - 0.106	0.106	5 th	0.182 - 0.184	0.183
Modal	0.107 - 0.107	0.107	Modal	0.184 - 0.186	0.185
95 th	0.112 - 0.112	0.112	95 th	0.190 - 0.192	0.191
SOUTHEAST			NORTHWEST		
Percentile	Volume km ³	Volume km ³ (MEAN)	Percentile	Volume km ³	Volume km ³ (MEAN)
5 th	0.195 - 0.198	0.196	5 th	0.119 - 0.120	0.120
Modal	0.198 - 0.200	0.199	Modal	0.121 - 0.121	0.121
95 th	0.212 - 0.214	0.213	95 th	0.133 - 0.134	0.134

Table 4.6: volume estimations for the EU4 unit (levels b, c and b/c – see text) using the TIN interpolator method.

EU4 - b		EU4 - b/c	
Percentile	Volume (km ³)	Percentile	Volume (km ³)
5 th	0.357	5 th	0.362
Modal	<u>0.364</u>	Modal	<u>0.370</u>
95 th	0.386	95 th	0.392

Table 4.7: volume estimations for the EU4 unit (levels b and b/c – see text for details) using the trapezoidal rule.

Results of the TIN and trapezoidal methods are displayed in Table 4.6 and 4.7 respectively. Values calculated using the trapezoidal rule for the EU4b and EU4b/c units tend to be slightly higher with respect to the values calculated using the TIN method. If compared to the values calculated by Gurioli (1999) for the EU4b unit using the $\log_{\text{thickness}}$ versus $A^{1/2}$ (which is 0.32 km³) it can be easily seen how the mean value calculated with the TIN method (0.295 km³) but also the one calculated using the trapezoidal rule (0.364 km³) are in full agreement with it, and the differences might be considered within an acceptable margin of error. Similarly to what has been done for the EU3pf unit, also in this case the effect of Mt. Somma in partitioning the total erupted volume has been evaluated, again by subdividing the deposit outline in two distinct sectors (North and South) with a straight line (dark green dashed line in Fig. 4.8). In this case, because of the strong asymmetry of the EU4 unit, the deposit itself has been subdivided into two distinct areas, named “NorthEast” and “SouthWest”. These partitions have been defined by drawing a straight line (purple dashed line in Fig. 4.8) perpendicular with respect to the axis of maximum elongation of the deposit (which is oriented roughly NW-SE). The above-mentioned calculations have been done for the EU4b, EU4c and EU4b/c units and are displayed in Table 4.6. The North versus South partitioning is more pronounced in this case for all the three units, with more material falling into the S sector. With respect to the SE-NW partitioning instead, most of the erupted material (from a volumetric point of view) falls into the SE sector for all the three units.

Unit Fg, Pollena eruption

As mentioned before, volume estimations for the “Cupa Fontana” PDC lobe from the AD 472 “Pollena” eruption were performed using the TIN interpolator only and considering the 5th/Modal percentiles and the 95th percentile outlines as discussed in section 4.4.2.

A total of 27 stratigraphic sections (6 real and 21 interpolated) have been used, with thickness values ranging between 1 cm (section 130 – see Fig. 4.6) and 4.8 m (section 124 – see Fig. 4.6). The

complete list of the stratigraphic sections (M. Mulas et al., unpublished) is available in Table 8.6 from section 8.4.3. With this information it was possible to estimate the values for the volume of this PDC lobe, which are listed in Table 4.8.

Percentile	Volume (km ³)
5 th /Modal	<u>0.0026</u>
95 th	0.0029

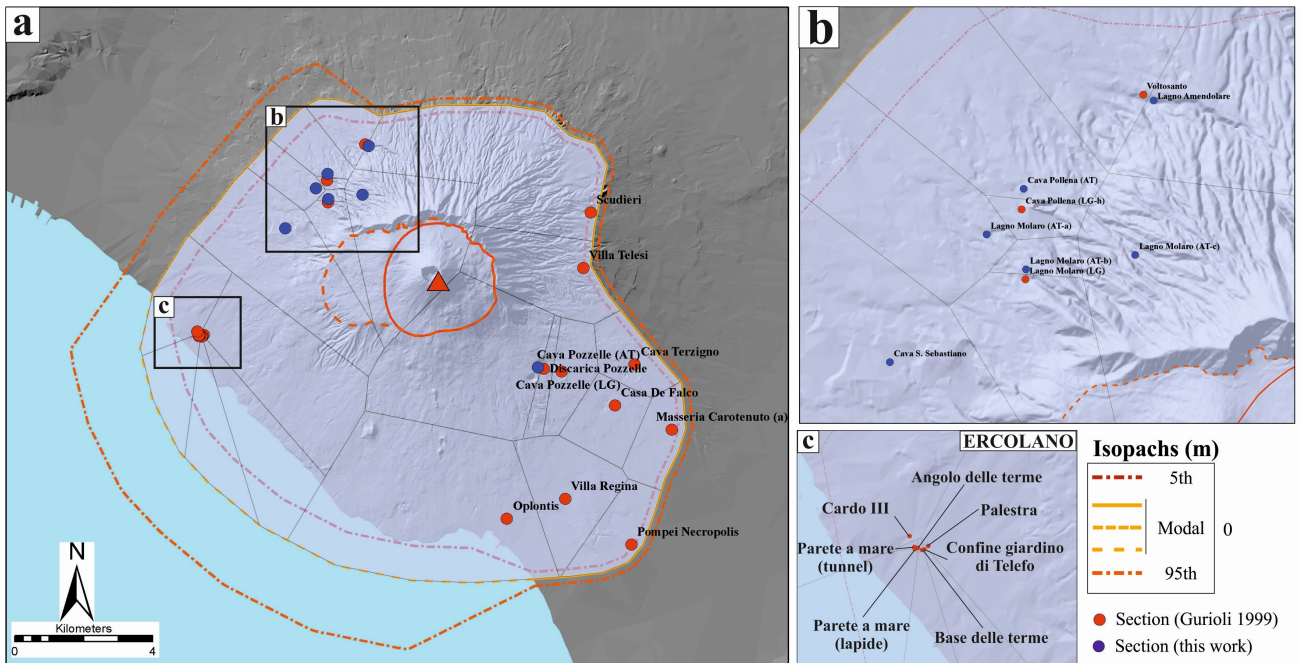
Table 4.8: volume estimations for the “Cupa Fontana” PDC lobe of the Fg unit using the TIN interpolator.

4.4.3 TGSD for the EU3pf and EU4 units and for the Fg “Cupa Fontana” lobe

Grain size analysis have been performed in the interval -4Φ - 5Φ at a 1Φ interval. For sections with more than one sample, the average grain size of the section has been calculated by obtaining the arithmetic mean of all the sample grain size analyses from that section. Integration of these data over the whole dispersal area was performed through the Voronoi tessellation method, according to the procedure described in section 4.3.3. Voronoi polygons have been extended up to the “Modal” maximum runout outline for each unit. Density values for the deposit of the EU3pf, EU4b and EU4c have been calculated from sample analyses (17 samples for EU3pf, 18 for EU4b and 2 for EU4c). For each sample the density value was obtained after a measurement of the volume and of the mass of the sample itself. The average density values used for TGSD calculations were 1120 kg/m^3 (for the EU3pf unit), 1305 kg/m^3 (for the EU4b unit) and 1335 kg/m^3 (for the EU4c unit). For the EU4b/c unit, density values for sections with samples from both level b and c were calculated as the weighted mean (with respect to the thickness of b or c relative to the total section thickness) of the densities of levels b and c.

Unit EU3pf, Pompeii eruption

For the EU3pf unit, a total of 98 samples (13 from this work and 85 from Gurioli 1999) have been collected from 27 stratigraphic sections (6 from this work and 21 from Gurioli 1999). The distribution of the stratigraphic sections is displayed in Fig. 4.10, while all the grain size analyses for each sample are stored in Table 8.7 from section 8.5.1. A synthetic description of the lithofacies and the position within the stratigraphic sections where samples were collected is available in Table 8.4 from section 8.4.1.



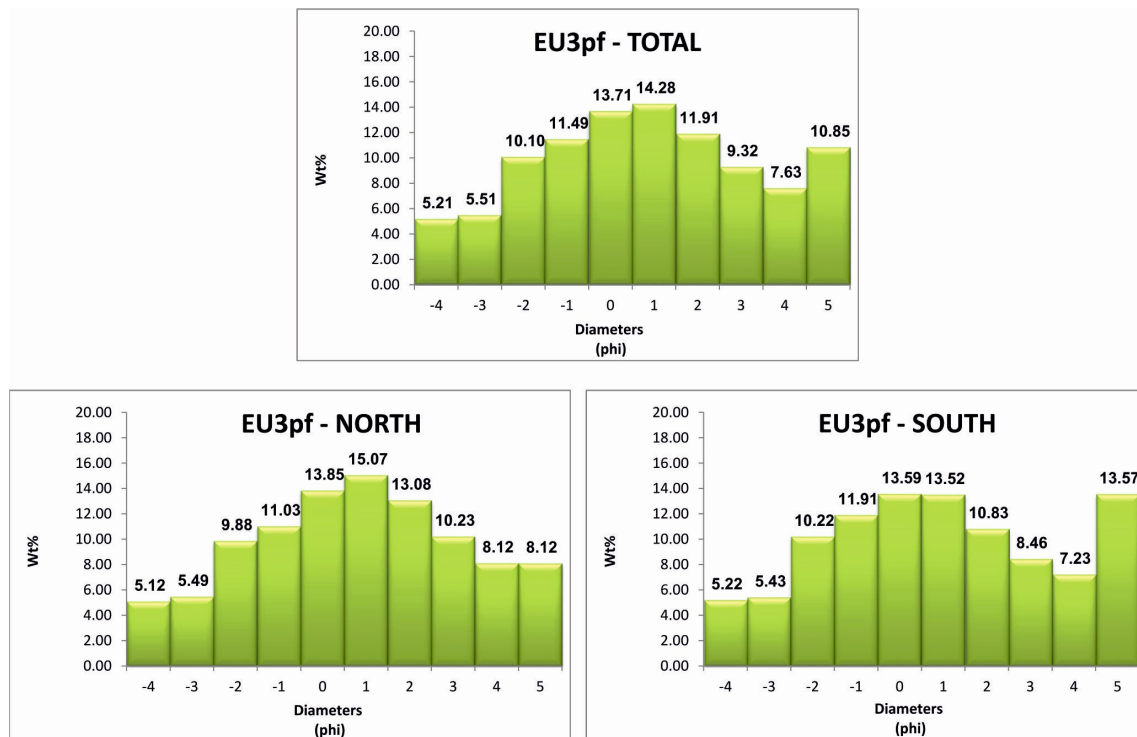


Fig. 4.11: Total-grain size distributions for the EU3pf unit.

The Total-Grain Size Distribution for the whole EU3pf eruption is shown in Fig. 4.11, along with TGSD for the N and S sectors as defined in section 4.4.2. For these two latter cases, the Voronoi tessellation drawn for the whole areal extent of the EU3pf has been cut in two parts: in this way all the polygons (or parts of polygons) that fell into one or the other sector have been used for the separate calculations of the TGSD for the N and S sectors. The TGSD for the whole EU3pf unit is a mesokurtic and quasi-normal distribution (with an enrichment in fine particles), with $F1=39.71\%$ and $Md\Phi=0.27$. The N ($F1=39.56\%$, $Md\Phi=0.30$) and S ($F1=40.10\%$, $Md\Phi=0.26$) sectors share very similar TGSD with respect to the one for the whole EU3pf unit, but it is clearly evident how the S sector is much richer in fine-grained particles with respect both to the N one and to the Total one.

Unit EU4, Pompeii eruption

TGSD estimations for the EU4 unit have been performed for both the EU4b, the EU4c and the EU4b/c units. For the EU4b unit, a total of 68 samples (5 from this study and 63 from Gurioli 1999) have been collected from 31 sections (4 from this study and 27 from Gurioli 1999). For the EU4c unit,

8 samples have been collected from 8 sections (all from Gurioli 1999). For the EU4b/c TGSD estimations, the average grain size for sections with both EU4b and EU4c samples (the 8 above-mentioned sections) have been calculated with the weighted mean of each grain size analysis for each sample (weighted with respect to the thickness of either level b or c with respect to the total thickness of the section). The distribution of the sections used for the TGSD estimations for EU4b and EU4c are displayed in Fig. 4.12a and Fig. 4.12b respectively. A list of all the samples used for the TGSD calculation is available in Table 8.8 from section 8.5.2 (for EU4b) and Table 8.9 from section 8.5.3 (for EU4c). Table 8.5 from section 8.4.2 reports instead (where possible) the lithofacies and the position within the stratigraphic section where each sample was collected.

The TGSD analyses for the EU4b/c unit are reported in Fig. 4.13: calculations have been performed for the whole EU4b/c unit and for the four sectors (N versus S, SE versus NW) defined previously. TGSD analyses for the EU4b and EU4c units separately are displayed instead in Fig. 4.14, with same differentiation in sectors as done for unit EU4b/c. Table 4.9 instead collects all the main parameters calculated for the different EU4 units.

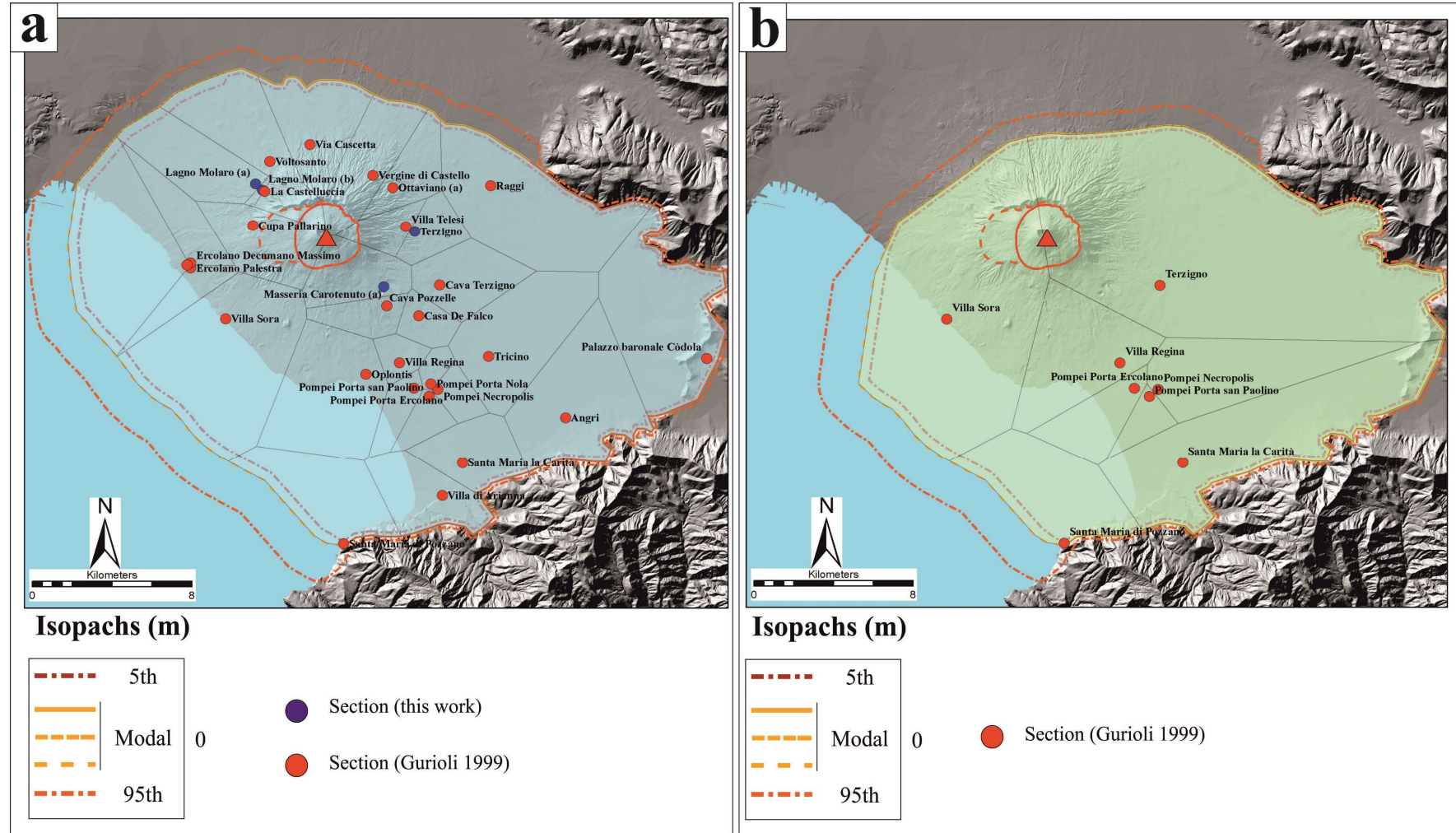


Fig. 4.12: a) sections where samples for TGSD calculation for the EU4b unit were collected. Voronoi tessellation is defined by the light blue polygons; b) sections where samples for TGSD calculation for the EU4c unit were collected. Voronoi tessellation is defined by the light green polygons. Red triangle is the inferred position of vent. Red line is the outline of the uncertainty area of vent position (Section 2.4.2). SV caldera outlined in dark orange dashed line.

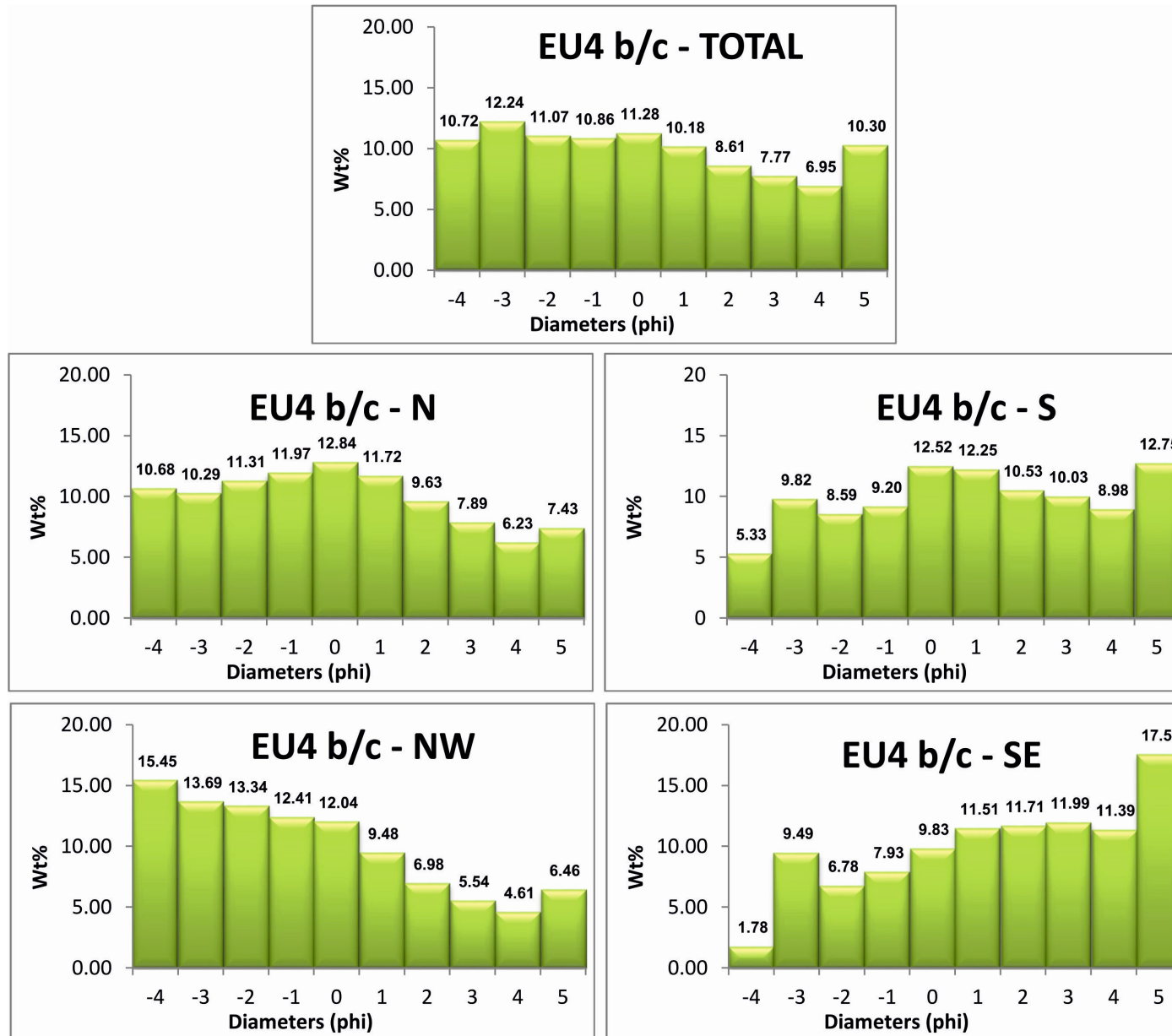


Fig. 4.13: Total-Grain Size Distributions for the EU4 unit (levels b and c together).

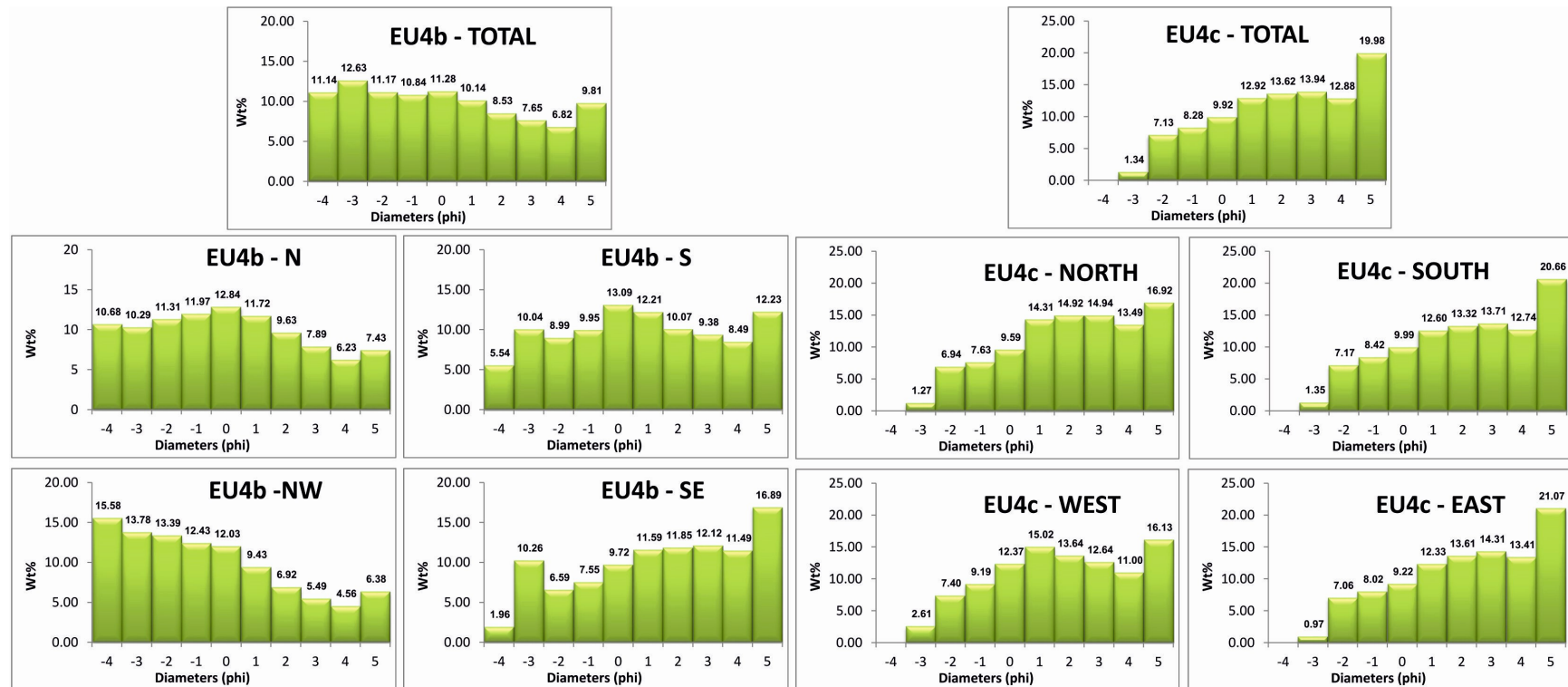


Fig. 4.14: Total-Grain Size Distributions for the EU4 unit (levels b and c separately).

Unit	Sector	Parameter	Value	Unit	Sector	Parameter	Value	Unit	Sector	Parameter	Value
EU4b	Total	MdΦ	-0.62	EU4c	Total	MdΦ	1.76	EU4b/c	Total	MdΦ	-0.54
		F1	32.80			F1	60.42			F1	33.64
		Skewness	Positive (fine)			Skewness	Negative (fine)			Skewness	Positive (fine)
		Kurtosis	Platykurtic			Kurtosis	Platykurtic			Kurtosis	Platykurtic
	North	MdΦ	-0.55		North	MdΦ	1.68		North	MdΦ	-0.55
		F1	31.18			F1	60.27			F1	31.18
		Skewness	Nearly symm.			Skewness	Nearly symm.			Skewness	Nearly symm.
		Kurtosis	Platykurtic			Kurtosis	Platykurtic			Kurtosis	Platykurtic
	South	MdΦ	0.19		South	MdΦ	1.78		South	MdΦ	0.30
		F1	40.17			F1	60.45			F1	42.29
		Skewness	Nearly symm.			Skewness	Negative (fine)			Skewness	Nearly symm.
		Kurtosis	Platykurtic			Kurtosis	Platykurtic			Kurtosis	Platykurtic
	SE	MdΦ	1.19		SE	MdΦ	1.91		SE	MdΦ	1.22
		F1	52.34			F1	62.40			F1	52.66
		Skewness	Negative (fine).			Skewness	Negative (fine)			Skewness	Negative (fine)
		Kurtosis	Platykurtic			Kurtosis	Platykurtic			Kurtosis	Platykurtic
	NW	MdΦ	-1.41		NW	MdΦ	1.24		NW	MdΦ	-1.39
		F1	23.35			F1	53.41			F1	23.59
		Skewness	Positive (fine)			Skewness	Nearly symm.			Skewness	Positive (fine)
		Kurtosis	Platykurtic			Kurtosis	Platykurtic			Kurtosis	Platykurtic

Table 4.9: list of parameters calculated from the TGSD analyses for the EU4b, EU4c and EU4b/c units.

With respect to TGSD analyses for the units, it can be easily assessed that: i) unit EU4c represents the more fines-rich unit; ii) TGSD are similar for the N and S sectors for all the units; iii) large difference exists for the TGSD of SE versus NW, with the SE sector being much more fines-rich and coarse-poor. A further comparison could be done (for the EU4b unit) with the TGSD estimation performed by Gurioli (1999) using the isomass maps method. Comparing the TGSD diagram (Fig. 7.33 from Gurioli 1999) it is clear how the modal value of the distribution is in this case the 2Φ class (differently with respect to Fig. 4.14, where the modal value of the total EU4b is -1Φ), with a marked enrichment in fines particles (5Φ).

Finally, with the information related to the density and thickness of each stratigraphic section, it was possible to calculate the total mass for all the units: this was done by calculating a) the mass per unit area, b) the mass of each Voronoi cell and finally c) by summing all the mass values from all the Voronoi cells. The total mass values for each units (and for each sector) are displayed in Table 4.10.

Unit	Sector	TOT mass (kg)
EU3pf	Total	<u>3.2×10^9</u>
	North	1.6×10^9
	South	1.6×10^9
EU4b	Total	<u>9.5×10^{11}</u>
	North	4.1×10^{11}
	South	5.3×10^{11}
	SE	3.1×10^{11}
	NW	6.4×10^{11}
EU4c	Total	<u>1.0×10^{12}</u>
	North	0.2×10^{11}
	South	0.8×10^{11}
	SE	0.8×10^{11}
	NW	0.2×10^{11}
EU4b/c	Total	<u>9.8×10^{11}</u>
	North	4.1×10^{11}
	South	5.7×10^{11}
	SE	3.4×10^{11}
	NW	6.4×10^{11}

Table 4.10: total mass values for the four units discussed in this section.

Unit Fg, Pollena eruption

TGSD analysis for the “Cupa Fontana” PDC lobe was calculated on the basis of 4 samples from 4 stratigraphic sections collected by M. Mulas et al (see Table 8.10 from section 8.5.4 for the complete list of samples). Mean value of density calculated for this TGSD analysis was performed on the basis of 27 density analyses made at 27 stratigraphic sections. In this case, the mean value of density was obtained by applying the Voronoi tessellation to the density values, with the same procedure described for the TGSD estimation. This latter one was performed by M. Mulas and yields values displayed in Fig. 4.15. From this TGSD analysis it is evident how the “Cupa Fontana” PDC lobe is fines-poor, with a distribution skewed toward coarse-grained particles although quasi normal. The distribution is also mesokurtic, with $Md\Phi = -0.96$ and $F1 = 22.60\%$.

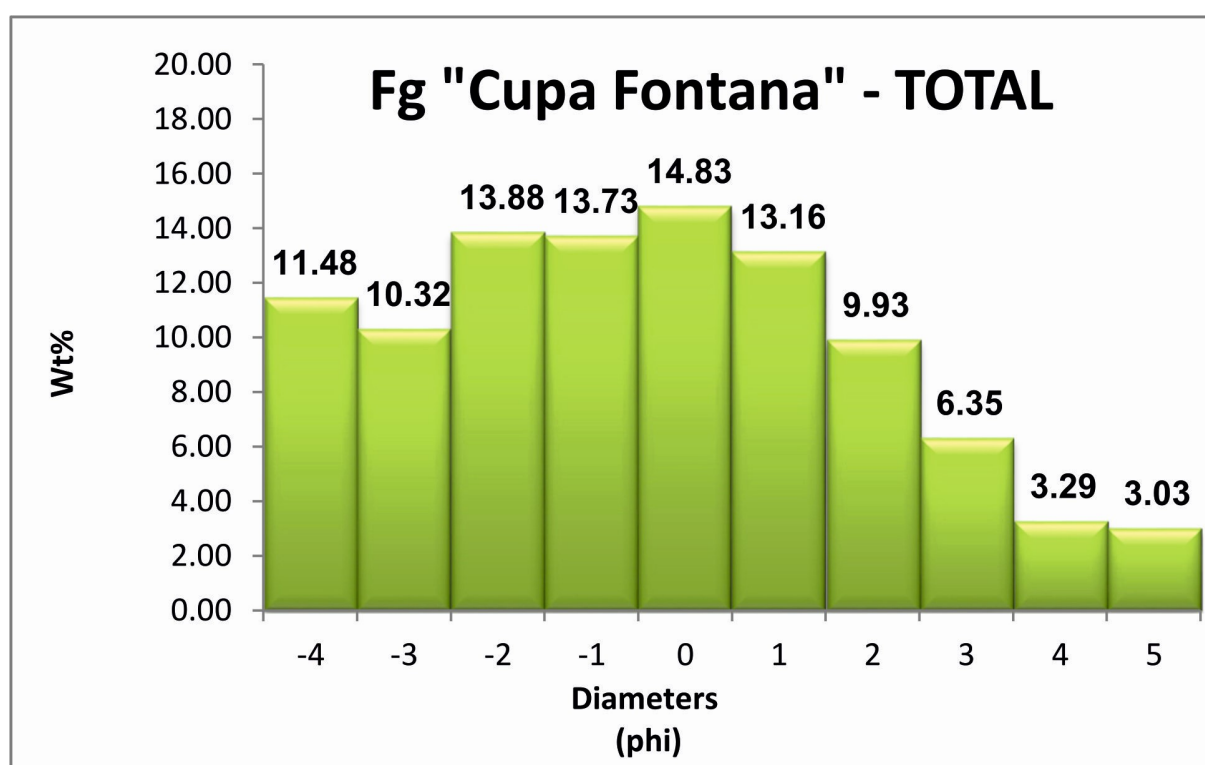


Fig. 4.15: Total-Grain Size Distributions for the “Cupa Fontana” PDC lobe of the Fg unit from the AD 472 “Pollena” eruption.

4.4.4 Paleotopography before the AD 79 “Pompeii” eruption and before the AD 472 “Pollena” eruption

The reconstruction of the paleotopography before the AD 79 eruption was performed, as described in section 4.3.4, mostly on the basis of a fresco from the Pompeii excavations where the SV morphological outline (probably seen from the Pompeii town) is displayed (Fig. 4.16b). From this fresco it is possible to note that the present Gran Cono was missing and there was a S-facing ridge with a big notch, probably a remnant of the old Mt. Somma slopes to the S.

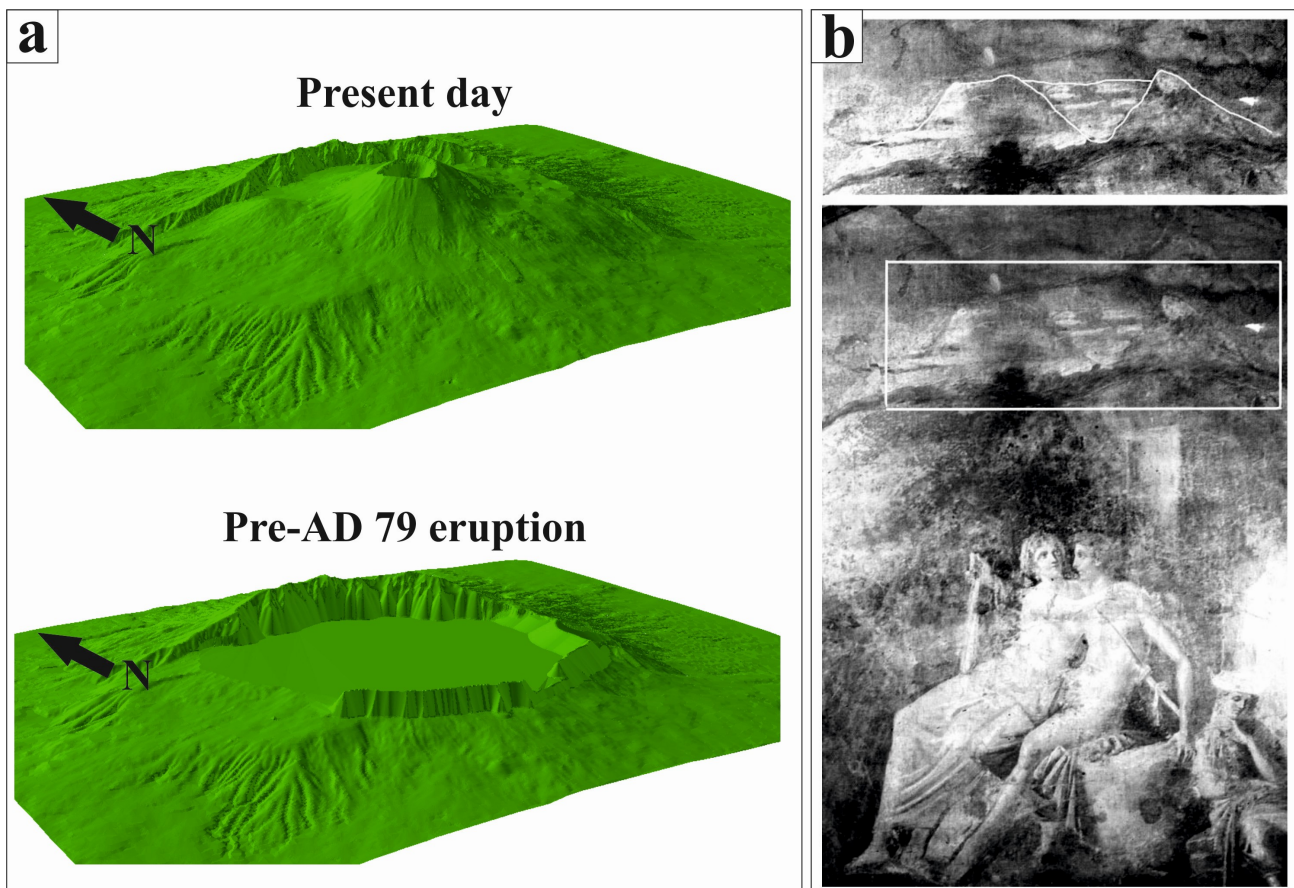


Fig. 4.16: a) the Somma-Vesuvius volcanic complex presently (above) and its possible appearance before the AD 79 Pompeii eruption (below); b) the “Amore di Enea e Didone” fresco from the “Casa del Citarista” at Pompeii (now at the “Museo Archeologico di Napoli”). Modified from Cioni et al. (1999).

The procedure for the reconstruction of the paleotopography was made on the basis of the 10-m resolution DEM implemented by Tarquini et al. (2007) and involved basically two steps: i) the elimination of the Gran Cono and ii) the creation of the ridge. At this stage a “scooping” of all the

geologic units postdating the AD 79 Pompeii eruption has not been performed due to the lack of detailed data.

With respect to point i), it has been firstly chosen a contour line (from the 10-m resolution DEM) within the SV caldera that could have served as a starting point for the flat area that would have had to replace the Gran Cono. The contour line used was the 657 m one, chosen because above it (in the original DEM) the slope angle started to increase (identifying therefore the roots of the Gran Cono edifice). Once chosen this contour line, a GRID file was created, using (to the S and W) the outline of the 657 m contour line and (to the N and E) the outline of the SV caldera: this latter choice has been done in order to preserve the morphology of the Mt. Somma scarp to the N and (partially) to the E, which has been considered substantially similar to the one at the time of the AD 79 eruption. The resulting GRID file was therefore composed of a regularly spaced 10-m resolution grid, where all the cells were attributed the value of 657 m: this file was then mosaicked with the original DEM, replacing therefore the Gran Cono with a flat area at the altitude of 657 m. An adjustment was made in order to provide a more reliable appearance of the S-facing Mt. Somma scarp to the N and the W-facing scarp to the E. The replacement of the flat area in fact produced a vertical cliff that was almost 200 m high in some parts: this was due to the fact the feet of the Mt. Somma scarp (in the original DEM) were lying at an altitude that in some cases reached the height of almost 850 m. A more gradual decreasing of the SV scarp has been therefore realized. Technically, this operation has been done using the “Buffer Wizard” tool which created outlines (converted into contour lines) at a constant distance. A lower slope angle (35°) has been used for the E part of the Mt. Somma scarp.

With respect to step ii), it has been initially chosen the top height value of the ridge, which was set to 800 m. Such a value has been chosen so that the representation of SV from the Pompeii fresco (Fig. 4.16b) was the most similar possible. Once chosen this value, the top contour line of the ridge was drawn, and subsequent contour lines (down to the value of 657 m) were drawn using the same procedure adopted for the prolongation of the Mt. Somma scarp. The final result of the paleotography reconstruction before the AD 79 “Pompeii” eruption is displayed in Fig. 4.16a.

The reconstruction of the paleotopography before the AD 472 “Pollena” eruption instead, presented less complexities with respect to the above-described one because i) the smaller area of investigation (for the Fg “Cupa Fontana” PDC lobe) and ii) the fact that this unit is the youngest one in the area, with all the remaining ones being older with respect to the eruption itself. A simple

“scooping” of the deposit has therefore been done. In order to do this, a 10-m resolution DEM of the “Cupa Fontana” PDC lobe has been initially obtained from the TIN used for the volume calculation of this lobe (see section 4.4.3). Then, this DEM has been subtracted from the original 10-m DEM of the SV area (Tarquini et al. 2007) only from areas where the “Cupa Fontana” lobe actually outcrops (PDC deposits from the geological map from Santacroce and Sbrana 2003, see Fig. 4.6). The final result is a slightly modified DEM where areas presently occupied by the “Cupa Fontana” lobe have been deleted.

4.5 Discussion

4.5.1 *Maximum runouts*

Several considerations can be made with respect to the maximum runout outlines. Firstly, it has to be pointed out that as a general rule it was preferred, while evaluating uncertainties, not to overestimate the reliability of the available constraints, and therefore to adopt a conservative approach. The most reliable constraint for PDC maximum runout considered here is the case where the topography might have played a significant role in limiting PDC dispersal area, since it is here made the reasonable assumption that the topography of the reliefs, at a broad scale, has not changed significantly over the last 2000 years. On the contrary, areas subjected to the highest degree of uncertainty are those located seaward. For these zones it is somewhat difficult to provide extremely reliable maximum runouts, also because the processes acting when PDCs travel within large water bodies (seas, oceans,...) are still poorly constrained. Recently, Freundt (2003) described the processes acting when a hot PDC enters into water in a small-scale analogue experiment. Results show that i) at the moment of the entrance into water, a water wave is generated and rapidly travels away from the shore; ii) two portions of the PDC can be described after the entrance into water, a more dilute, fine ash-cloud that travels above water and a denser turbulent mixing zone that travels below water as long as the pyroclastic flow is maintained; iii) pumices float to the surface as raft; iv) mixing across the water surface over some distance from shore generates steam explosions forming fountains of wet and dry ash and convectively rising fine-ash plumes; v) the ash fountains could feed small-scale pyroclastic surges, that travels at high speed along the surface. Eyewitness of PDC entering in the sea are rare (Carey et al. 1996; Cole et al. 1998): in some cases (e.g. Krakatau eruption in 1883, see Carey et al. 1996) PDC have been claimed to travel for almost 80 km from the source area. For the SV case,

Sigurdsson et al. (1982) have discussed the chronicles of Pliny the Younger that describe the effects of the eruption at his location (Capo Miseno, 30 km to the NW with respect to the vent area). According to Pliny reports, in the morning of the second day of the eruption (i.e. 24 August/November) there was some ash which began to fall. This was light at first then so heavy that he describes it as "night". Furthermore, in his report Pliny declares that this event hit also the island of Capri (~30 km to SW of the vent area). The temporal frame of this event is coherent with the emplacement of the EU4 unit, and the above-mentioned authors (along with Carey et al. 1996) claim that this could be representative of pyroclastic surge. Although Pliny talks about "ash fall", it is not impossible that a pyroclastic surge could have travelled along such a distance (e.g. Krakatau, 1883) but at the moment there are no stratigraphic sections nearby the area of Capo Miseno that could prove to be part of the EU4b unit and deposited after direct lateral transport. It is certainly true that this "ash fall" could not be linked to the emplacement of the EU4a fallout unit: as shown by Gurioli (1999), in fact, the dispersal axis of this unit is toward SE, following the prevailing wind directions. Alternative possible interpretations for this event could be: i) the emplacement of fine ash from the co-ignimbritic plume that formed from the EU4b PDC or ii) the deposition after a small scale pyroclastic surge that originated from the collapse of an ash plume formed after steam explosions (Freundt 2003). However at the moment, without any other field data, it is too speculative to attribute this event to a PDC (which in this case would have travelled as far as 30 km from the vent area), and the maximum runout outlines proposed in section 4.4.1 (based on field evidences) appears to be more robust. It is also worth pointing out that other PDC entrances into the sea have been observed at SV during the AD 1631 sub-Plinian eruption (Rosi et al. 1993). Although in this case PDCs appeared to be denser with respect to the AD 79 eruption ones (Sulpizio et al. 2005), numerous paintings (e.g. Giovan Battista Passeri, "Vero disegno dell'incendio del mons Vesuvii 1631") show that all the PDCs stopped few hundred meters after entering the sea (see also section 8.3.3).

A clear feature of the EU4b maximum runout outline (and partly also of the EU4c one), is the marked asymmetry of the deposit with respect to the vent area, a feature that is much less pronounced for the EU3pf unit, which is more radially dispersed. Several explanations for this peculiar aspect (including the effect of for volume partitioning or fine versus coarse material partitioning) are discussed more deeply in section 4.5.3.

A final consideration with respect to maximum runout outlines is related to the surface of the total invasion areas. With the exclusion of the small Pollena “Cupa Fontana” PDC lobe, the other PDC inundation areas from the AD 79 eruption could be put in correlation with the extent of the present Red Zone area defined very recently (DPC 2014), which is the one considered to be almost surely invaded by PDC in the case of an eruptive event similar to the AD 1631 sub-Plinian eruption. The total extent of this area is 295 km², a value that is very close to the upper uncertainty bound of the EU3pf maximum runout outline (212 km²).

4.5.2 Volume estimations

Some considerations can be made also respect to different estimations of the volume of the deposits. First of all, the general agreement between different estimates for all the units considered here made with different methods point toward a robustness of the data. Among all the procedure employed, the TIN one appears however to be the most reliable at the moment. This is due to the fact that the other methods have several caveats: a) the sectorialization method tends probably to overestimate too much the volume, since the mean values of thicknesses attributed to each sectors are too much skewed toward higher values; b) the trapezoidal rule in this case has been done without considering enough isopachs outlines, providing values that are possibly an overestimations of the true volume of the deposit. The TIN method instead, at this stage of knowledge where no clear decay rule for PDC deposit thicknesses with distance can be envisaged, appear to provide more robust estimates, since it assumes the simplest decay rule (i.e. a linear one).

Another possible overestimations of EU4 and EU3pf volumes could derive from the fact that with the TIN interpolation, the integration area that has been considered correspond to the whole maximum runout outlines. It has however been observed in PDC deposits at SV (e.g. the PDCs from the AD 472 “Pollena” eruption, see Sulpizio et al. 2005; 2007) that the more proximal areas (along the upper part of SV slopes) are often sites of “non-deposition”. In order to evaluate the effect of this possible “non-deposition”, another integration of PDC volume has been made for the EU4b unit without considering the more proximal sites, which correspond basically to the SV caldera outline slightly elongated to the N (Fig. 4.17).

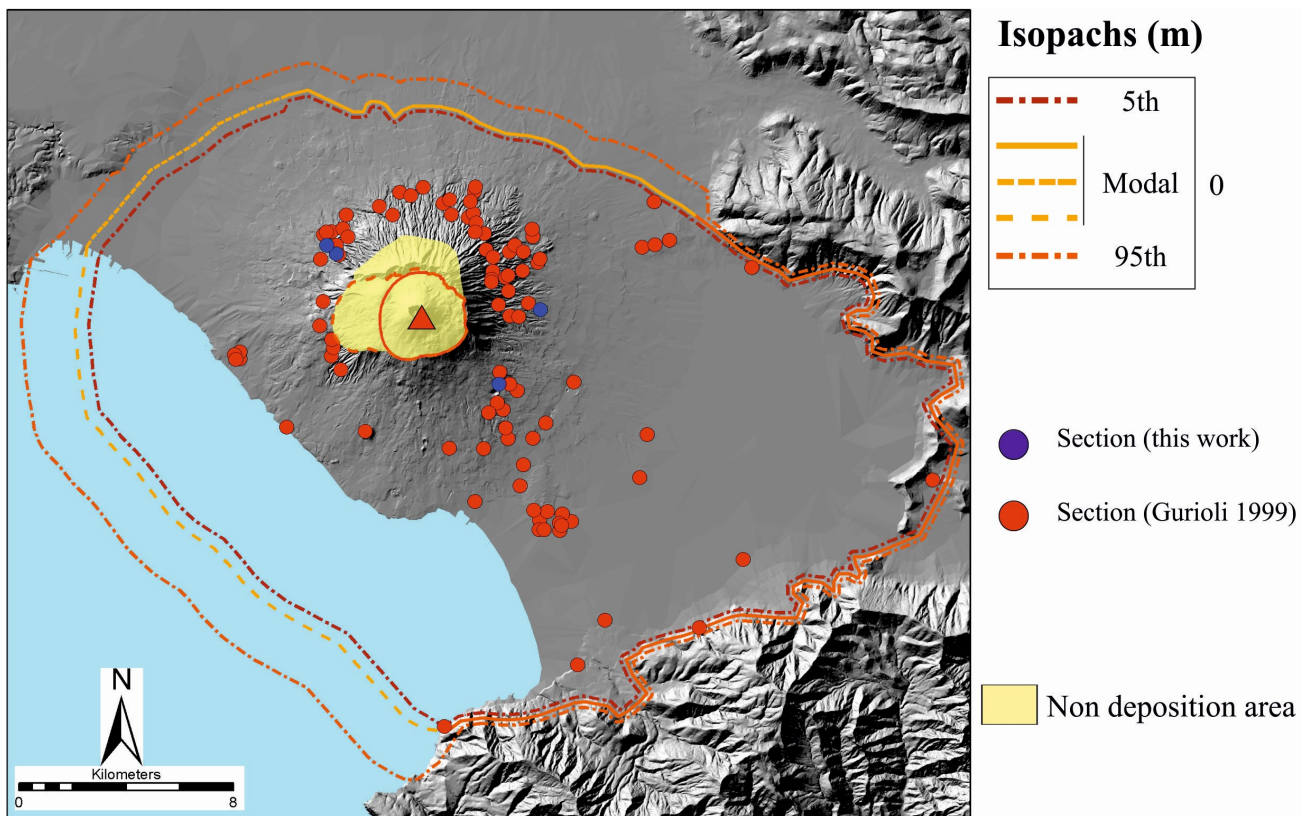


Fig. 4.17: the “Non deposition area” discussed in text. Red triangle is the inferred position of vent. Red line is the outline of the uncertainty area of vent position (Section 2.4.2). SV caldera outlined in dark orange dashed line.

In order to do so, with the TIN interpolator it has been imposed that the thickness value is zero at the limits of the yellow area of Fig. 4.17, so that the deposit thickness decay linearly to zero up to that limit. Values of EU4b volume calculated without considering this area are 0.221-0.224 km³ using the “Modal” maximum runout outline. Differences with the volume estimations calculated for the whole area for the EU4b unit with the “Modal” maximum runout outline (0.295-0.297 km³) are within uncertainty limits: no further calculations have therefore been done, and the values of Table 4.6 have been kept as the reference ones.

A final consideration could be done with respect to the volume partitioning into the 4 sectors of Fig. 4.8 (N versus S and SE versus NW). For the EU3pf unit it is clearly evident from Table 4.5 that the volumetric content of the two sectors is quite the same, with the N one with a slightly higher amount of material. When compared to the areal extent of the two sectors (54 km² the N one and 111 km² the S one) it is however evident as well how N sector, despite a smaller area, contains

proportionally more material with respect to the S sector, which is bigger from the point of view of the areal extent. This situation is exactly the opposite as the expected one (where the effect of Mt. Somma should have favored the partition of material toward S sectors), and three alternative explanation can be proposed at the moment: a) the maximum runout in the N part is underestimated; b) the rugged topography of N sectors favor the concentration of solid particles; c) wind plays a role in the partitioning. With respect to this latter point the explanation might be counter intuitive, and first of all it has to be pointed out that, as shown by Gurioli (1999) and Gurioli et al. (2005), at the time of the eruption high-altitude winds were blowing toward SE (due to the maximum dispersal axis of fallout units). Wind might favor the partitioning of more fine-grained particles toward the direction of wind blowing: as clearly evident from Fig. 4.11, this situation is particularly evident also for the S sector, which shows a marked richness in fine-grained particles with respect to the N one. A possible effect of fine particles partitioning could be related to the increased mobility of fines-rich PDCs (more developed to the S) with respect to fines-poor PDCs (more developed to the N): in other words, with this wind effect the same amount of material is spread over a larger area in the S sector. This effect will be discussed more deeply in section 4.5.3.

The effect of volume partitioning is evident also for the EU4 units: for such units in fact the values of volume estimations are consistently lower for sectors with a minor areal extent (the N and the W ones) with respect to the other (the S and the E ones), particularly for the EU4c unit. This is consistent with the fact that in this case the maximum runout outlines are much less developed toward N and W with respect to S and E, and volume estimations are therefore lower.

4.5.3 TGSD estimations

Considerations about TGSD outcomes from all the units are extremely interesting from the point of view of PDC mobility. First of all, a consideration should be done with respect to the amount of data available: for the EU3pf unit, despite many samples have been collected and analyzed, there are still several areas (i.e. in between Ercolano sites and the Oplontis site and in between the NW sections and the NE sections, see Fig. 4.10) where no samples have been collected (due to the scarcity of outcrops), and therefore the TGSD analysis with the Voronoi tessellation attributed Grain Size values that belong to stratigraphic sections far away from that site. Incrementing the number of samples from

these areas will certainly improve the TGSD estimations. The same consideration can be done for the EU4c unit, while the EU4b unit features a better areal coverage of samples collected (see Fig. 4.12). The “Cupa Fontana” PDC lobe instead, despite few samples were collected, due to its limited extension has provided a reliable TGSD estimations.

With respect to the TGSD estimation made by Gurioli (1999) for the EU4b unit, the TGSD estimation made with Voronoi tessellation tends to shift the $Md\Phi$ toward a coarser grain-size. It should be however noted how a) the isomass method (Gurioli 1999) was performed considering a fewer amount of samples and b) in the same method the isomass lines for some grain-size classes (especially the finer ones) have been extended to the SE much more with respect to the maximum runout outline used for this work, resulting in a higher wt% of finer grained particles in the TGSD.

As already mentioned in section 4.5.2, the asymmetry of PDC deposits (much pronounced for the EU4b and c units, less evident for the EU3pf one) has been put possibly in correlation with a wind effect (high-altitude winds at the time of the eruption were blowing toward SE; Gurioli 1999). In this section this possibility will be discussed more deeply, along with possible influences of vent geometry on the different TGSD observed in different PDC deposit sectors.

Carey and Bursik (2000) discussed over the effect of wind on the shape of volcanic plumes, considering two end-members: a) “strong plumes”, where the ratio between crosswind speed and upward plume speed is <1 , which develop the classical umbrella cloud; b) “weak plumes”, where the above-mentioned ratio is >1 , which develop a characteristic “bent-over” shape. Carey and Bursik (2015) furthermore linked plume vertical speed to magma discharge rate (MDR), highlighting how weak plumes are generally produced by MDR as low as 10^4 kg/s, while strong plumes can be produced with MDR up to 10^7 - 10^8 kg/s. The well-known description of Pliny the Younger on the shape of the AD 79 eruption plume, along with the calculated MDR of the eruption (see Table 4.1), points toward a classical strong plume shape, indicating that upward plume velocity overcame the crosswind speed. Nevertheless, due to the strong asymmetry of the AD 79 fallout deposits to the SE (Gurioli 1999; Gurioli et al. 2005), it has however been assessed how wind speed in the umbrella region was substantially high, influencing the deposition of the finest part of the eruptive column. This effect could also be extended to the development of the PDCs related to the collapse of the eruptive columns (EU3pf and EU4). Despite it is true that high wind speeds promote air ingestion (especially in the upwind part) and therefore plume stability (Degruyter and Bonadonna 2013), it has been also proved by

Graf et al. (1999) how strong winds could affect the partitioning of fine particles in the upwind/downwind regions: particularly, it has been assessed how the horizontal distribution of ash in a rising plume with strong wind conditions is more tilted toward the downwind part, while there is only a minor transport of ash in the upwind region. Recently, Cerminara et al. (2016) have shown that both in the case of a strong and weak plume, coarse particles (>1 mm), due to larger settling velocities (with respect to fine particles) and different coupling regimes with the gas phase, are more prone to proximal fallout from the plume margins and reduced transport by the umbrella region. It is therefore reasonable to infer that the distribution of coarse particles in PDC deposits derived from column collapse should be radially homogeneous with respect to vent area, while more fine-grained particles could be forced toward the downwind sector of the collapsing column, enhancing PDC mobility and therefore extending maximum runout outline. This latter aspect has been extensively described both by analogue experiments (Phillips et al. 2006) and numerical modeling (Neri et al. 2003).

The situation described can be easily applicable to the EU3pf unit. According to the TGSD of Fig. 4.11, the maximum runout outlines of Fig. 4.5a, the volume estimations of Table 4.5, the mass calculations of Table 4.10 and the parameters described in section 4.4.3 it can be assessed that: i) EU3pf unit has a slightly asymmetrical maximum runout outline to the S-SE (area of S sector is double of the area of the N sector); ii) the total erupted volume is almost the same in the N and S part, and the total erupted mass is exactly the same in the two sectors; iii) TGSD analyses indicate that in the N and S sectors the coarse part of the unit has the same wt%, while the finer part is sensibly higher in the S sector with respect to N sector (particularly the 5Φ class, whose wt% is almost the double in the S sector). All of these elements point toward a situation where: a) the development of a strong plume eventually resulted in a column collapse; b) PDCs deriving from column collapse spread uniformly toward all directions; c) the presence of wind that were blowing toward the southern portion of the collapsing column; d) PDC mobility and maximum runouts were enhanced toward S-SE. At the moment, Mt. Somma scarp to the N apparently did not act as a barrier to the N propagation of PDCs.

A different situation can be instead envisaged for the EU4 unit. In this case in fact the TGSD of Fig. 4.12 and 4.13, the maximum runout outlines of Fig. 4.5b-c, the volume estimations of Table 4.6, the mass calculations of Table 4.10 and the parameters of Table 4.9, show that: i) the asymmetry of PDC deposits with respect to the maximum runout elongation axis (SE) is much more pronounced for both the EU4b and EU4c units with respect to the EU3pf one; ii) volumetric content and total mass

stored in the two sectors toward the maximum runout elongation axis (the S and SE sectors) are higher with respect to the other two sectors; iii) the TGSD of the EU4b and EU4b/c units for the E and W sectors are almost symmetrical (SE versus NW), with the SE sectors featuring a TGSD substantially skewed toward more finer-grained particles and the NW sectors strongly skewed toward coarse-grained particles. N versus S sectors instead share very similar TGSD, while TGSD for the EU4c unit are all strongly skewed toward finer-grained particles. These data can be discussed on the basis of two possible explanations: a) the orientation of the rising plume might have been slightly tilted toward the upwind direction, a situation that could have favored the accumulation of the more coarse-grained particles toward this direction; b) the wind blowing toward the SE might have favored the accumulation of fine-grained particles toward the downwind part, enhancing PDC mobility and maximum runout.

With respect to point i), several arguments can be added. First of all, if the total mass of the coarser particles (i.e. in the interval $-4\Phi-0\Phi$) is calculated for the NW (upwind) and SE (downwind) sectors for the EU4b/c unit, it can be assessed how these values are 4.31×10^{11} kg and 1.22×10^{11} kg for the NW and SE sectors respectively. These values show the same ratios also for the EU4b and EU4c units. As a reference, the total inundation areas of the NW and SE sectors are, respectively, 169 km² and 352 km²: this implies that over the NW sector (which is half of the surface of the SE one) coarser grained material have been deposited (as an absolute value of total mass). A situation like this could hardly been explained by the effect of wind alone, as coarse-grained particles are poorly influenced by that. A more reasonable explanation could be linked to the geometry of the near-vent area, which might have enhanced the emission of erupted materials more to the NW with respect to the SE. With respect to this latter point it should be noted how the EU4 unit marks the transition to the final phreatomagmatic phase of the AD 79 eruption, when the massive entrance of water into the magma chamber triggered the caldera collapse.

With respect to point ii), it should be also noted how the contemporaneous blowing of the wind toward SE might have created a situation where fine and coarse particles were decoupled, the first ones being pushed more toward SE (enhancing PDC mobility and runouts) while the second ones more concentrated to the NW.

The Fg “Cupa Fontana” PDC lobe, due to the TGSD analysis of Fig. 4.15 and the lithofacies that describe all the outcrops of this unit (mLT; see Sulpizio et al. 2005), can be placed at the

“Granular-fluid based” end of PDC spectra (Branney and Kokelaar 2002), while the EU4 unit can be placed more appropriately in the “Fully dilute” PDC end-member. EU3pf instead, due to its intermediate TGSD and lithofacies association features can be seen as an intermediate member in between the two “Cupa Fontana” and EU4 end-members.

A final consideration is related to a probable underestimation of the fine-grained portion of these TGSD estimations with respect to the initial collapsing column, which is due to the fact the most of the fine particles are elutriated while PDC is moving. This considerable amount of material (produced partly after clasts abrasion and breakage) is transferred into the co-ignimbritic plume and deposited elsewhere, out of the maximum runout outline described in this Chapter. As shown by Dufek and Manga (2008), the fraction of pumice comminuted to ash can be as high as 10–20% of the volume of pumice. Recent research projects (Mundula et al. 2014) are focused on the quantification of clast shape parameters from known eruptions at SV in order to get an estimation of the total amount of material lost from PDC due to its transfer into the co-ignimbritic plume.

4.6 Conclusions

Data presented in this chapter are the result of a research that involved the usage of different data sets aimed at reconstructing some key parameters that could be employed as input data for numerical modeling of Pyroclastic Density Currents (PDC). Two eruptive units (from the AD 79 “Pompeii” eruption of Somma-Vesuvio; units EU3pf and EU4) and one PDC lobe (from the AD 472 “Pollena” eruption of Somma-Vesuvio; Fg “Cupa Fontana” lobe) have been analyzed, and four main parameters have been calculated or reconstructed: a) the maximum runouts of PDC units (with upper and lower uncertainty bounds); b) the total volume of the erupted materials (with estimations performed with different methods); c) the Total-Grain Size Distribution of the units/lobe; d) the paleotopography predating the two eruptions. The research included also a synthesis of the stratigraphic features of the different PDC deposits from the two eruptions described in different sources.

Main conclusions achieved include also some interpretations about the mobility of PDCs with respect to the volcanic plume collapse: i) the EU3pf unit (at the end of the magmatic phase of the AD 79 “Pompeii” eruption) was probably emplaced after an axisymmetrical collapse, but the strong wind at the time of the eruption partitioned the finer-grained particles toward the direction of wind blowing,

enhancing PDC mobility and maximum runout toward that direction; ii) the EU4 unit (at the beginning of the final phreatomagmatic phase of the AD 79 “Pompeii” eruption) featured instead a probable asymmetrical collapse of the eruptive column, which caused the more coarse grained particles to be partitioned toward the N and NW. Finer-grained particles of the EU4 unit were instead forced toward the direction of wind blowing, with the same implications described for the EU3pf unit; iii) the effect of the pre-existing Mt. Somma scarp to the N does not seem to have influenced the partitioning of fine/coarse particles.

Results described in this Chapter will be employed in the next Chapter as input parameters for numerical model validations with field data.

Chapter 5

Application of numerical models using field data

5.1 Introduction

The increased availability of numerical models capable of reproducing (in a simplified way) the dynamics of mass flows has provided geoscientists and civil authorities new potentially valuable tools for hazard assessments. Particularly, with respect to Pyroclastic Density Currents, several numerical codes have been developed over the past years, from early simplified kinetic models (Sheridan and Malin 1983; Dade and Huppert 1995) up to more complex, depth-averaged (Patra et al. 2005) or even multiphase approaches (Neri et al. 2003; Esposti Ongaro et al. 2007). The purpose of these efforts is twofold, since on one side intends to investigate more deeply the complex dynamic of PDCs, while on the other side it aims at providing fast computing but reliable tools for PDC hazard assessment. In general, although complex multiphase approaches for PDC numerical modeling provides more accurate results (useful to investigate the dynamics of PDCs), their high computational times (on the order of days or weeks for a single simulation) do not make the related codes useful for producing a probabilistic PDC invasion map. It is therefore important at the moment to rely on simplified and fast numerical codes that reproduce as close as possible the emplacement of PDCs at specified locations. In this context, model validations (i.e. the evaluation of the degree of overlapping between model outputs and actual field data) assume the important task of providing numerical values about the degree of uncertainty associated with a model output.

In this Chapter, values calculated and discussed in the previous Chapter 4 have been used as input parameters for two well-established codes, the Box-Model and TITAN2D. The procedure of validation of such models involves the calculation of the degree of overlapping between model and field data from the point of view of areal invasion, thickness profile and mass fractions of different granulometry classes with respect to distance. To the knowledge of the author, this type of approach has been partially adopted by few authors (Dade and Huppert 1996; Kelfoun 2011; Charbonnier et al. 2015) and more substantially by Tierz et al. (2016). Validation analyses are preceded by a section that deals with the review of numerical modeling of PDCs, the Box-Model and TITAN2D codes and numerical simulations of PDCs at SV.

5.2 Numerical modeling of PDCs

PDCs, as all the gravity currents, results whenever a fluid of one density is injected horizontally into a fluid of different density (Roche et al. 2013). The dynamics of PDCs moving through time (both in the case of a finite volume instant release or in the case of a continuous feeding from a sustained source), are controlled i) by the release conditions and the geometry of the source area (at the beginning of their motion), ii) by the balance between inertial and buoyancy forces (during flow movement) and iii) by the balance between buoyancy and resisting forces (when PDCs are about to stop), as pointed out by Roche et al. (2013).

In the context of volcanic hazard assessment, numerical simulations of PDCs simulate mathematical equations that cannot be analytically solved (Sulpizio et al. 2014). The basic concept of numerical simulations of PDCs is to solve conservation equations (called “governing equations”) of mass (density and/or thickness), momentum and energy (sometimes enthalpy). These quantities are described, among others, by the Navier–Stokes equations, for which exact solutions are generally impossible: the standard methodology is therefore to discretize equations in space and/or time (Roche et al. 2013). To close the system of governing equations, data about initial conditions, boundary conditions and constitutive equations (e.g. relating stress and velocity, for granular-like media or fluid-like media) need to be provided as well.

According to Sulpizio et al. (2014), the fully-dilute part of PDC spectra can be described using the laws of fluid dynamics (Huppert 2006), whereas the granular fluid-based ones more properly obeys the laws of granular materials (Bursik et al. 2005). The discretization of equations in space and/or time has been obtained with different approaches (Fig. 5.1), but all of them tend to obtain approximated solutions at the nodes of a discretized space (Roche et al. 2013).

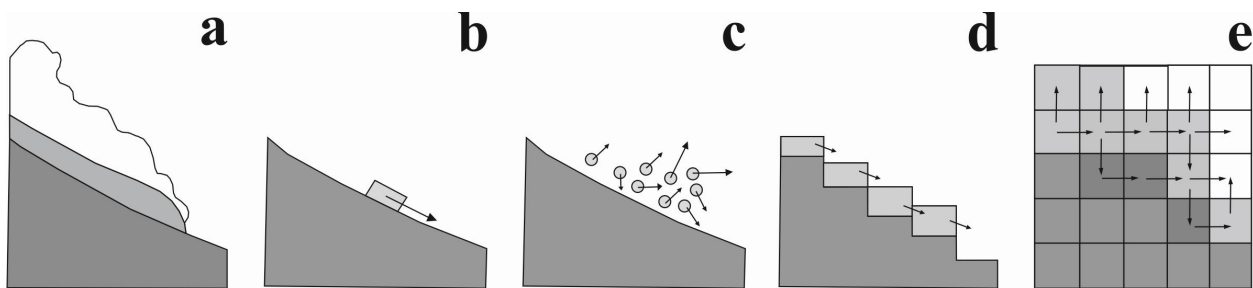


Fig. 5.1: a) natural PDC composed of a dense basal flow and the ash-cloud surge; b) kinetic approach; c) discrete element approach; d) depth-averaged approach; e) multiphase model. Modified from Roche et al. (2013).

Early simulations were made using the kinetic approach (Fig. 5.1b), which simulates trajectories only for the flow front, and considers the flow as a rigid block (Roche et al. 2013). Within this approach it is included the energy line concept (Malin and Sheridan 1982; Sheridan and Malin 1983), which basically calculates the flow runout distance starting from the height of volcanic column collapse generating the flow. The principle is that of the conversion of potential energy (through height) into kinetic energy (through distance): in three dimensions the energy line delineates a cone with height/distance ratio as slope, and the intersection of the energy line with the topography gives the maximum runout distance of the simulated flow (Sulpizio et al. 2014). Several limits of these early versions of the kinetic approach for PDC numerical modeling have been underlined by Roche et al. (2013), which point out that they cannot take into account density variations, sedimentation and air ingestion: for these reasons the above-mentioned authors considers this approach too simplistic for fully-dilute PDCs simulations. Nevertheless, results from this approach are generated very rapidly and recent extensions and development of this concept made possible its application for the simulation of the dilute part of PDCs. A code for this latter aspect has in fact been recently designed by Neri et al. (2015) and Bevilacqua (2016) for PDC hazard assessment at Campi Flegrei. It is based on early studies carried on by Von Karman (1940) and has been termed “Box-Model” by Huppert and Simpson (1980), Dade and Huppert (1995) and by Dade and Huppert (1996), who used it for model validations using data from the Taupo ignimbrite. Details about this code, including the latest development from Bevilacqua (2016), are provided in section 5.2.1 and Appendix 2.

A more rigorous approach is adopted for PDC modeling with the discrete element approach (Fig. 5.1c), where the equation of motion are solved for every particle in the flow and the motion of each constituent grain is simulated (Roche et al. 2013). However, due to the huge number of particles that are required to obtain meaningful statistics, this method can hardly be adopted to simulate natural PDCs on real topography, unless combined with methods that consider the continuum hypothesis (Roche et al. 2013).

Another way to solve this situation is to discretize the space into a mesh and averaging the physical properties of each particle on each mesh node. This is implemented by depth-averaged methods (Fig. 5.1d), which translate meshes into columns where all the properties are vertically averaged and their related equations are vertically integrated (Roche et al. 2013). All of this considerations work under the assumption that the flow length is much greater than its depth, so that

vertical displacements are negligible. As pointed out by Roche et al. (2013), depth-averaged methods are very efficient if flow density can be assumed constant in time and space, and their application is more suitable for the simulation of granular fluid-based PDCs rather than fully-dilute ones. A key issue of these approaches is represented however by the choice of the rheology of viscous stresses, for which numerous possibilities exist (Roche et al. 2013). A depth-averaged approach is at the basis of the TITAN2D code developed by Patra et al. (2005) which has been used in this project and it will be discussed more deeply in section 5.2.2 and Appendix 3.

Finally, in order to account for both temporal and spatial variations of PDCs, multiphase approaches (Fig. 5.1e) have been developed (Roche et al. 2013). In order to produce more realistic 3D simulations, the calculation domain is divided into a horizontal and vertical grid where particles and gas are distinguished and treated separately. All phases present (different clast size of particles, gases of various compositions) share however the same mesh and interact with each other (Roche et al. 2013). Despite the fact that outputs of numerical simulations from this approach still suffer from the incomplete understanding of the physics of PDCs, still some complex behaviors (e.g. vertical density stratifications) have been underlined (Roche et al. 2013). Recent implementation of the multiphase approach into a code (named PDAC) have been performed by Esposti Ongaro et al. (2007). Neri et al. (2007) and Esposti Ongaro et al. (2008), moreover, have performed transient 3D and 4D numerical simulations of PDCs at SV using the PDAC code: the most important outcomes of these simulations are reported in section 5.2.3.

5.2.1 The Box-model code

In the case of a gravity current where a finite volume is instantly released (i.e. dam-break configuration), a possible assumption for simplifying a natural case is to approximate mass conservation through equal area geometrical elements (rectangles for 2D problems –see Fig. 5.2b- and cylinder for 3D). This configuration represents the basis of the so-called “Box-Model” originally designed by Huppert and Simpson (1980).

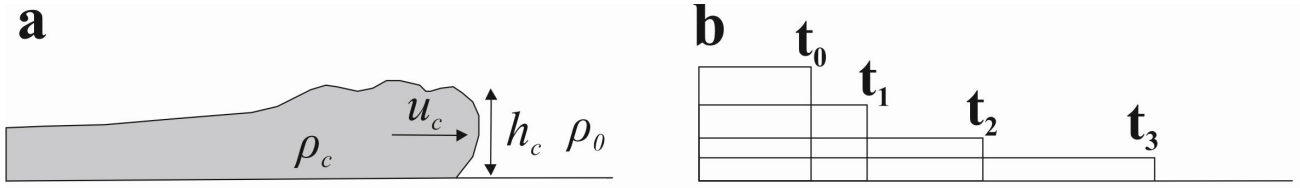


Fig. 5.2: a) schematic diagram of an inertial gravity current with a depth h_c , flow front velocity u_c and density ρ_c in an ambient fluid of density ρ_0 ; b) schematic diagram of mass conservation in a box model at times t_0 to t_3 . Modified from Roche et al. (2013).

The box does not rotate or shear, but changes in aspect ratio (i.e. stretches out) as the flow progresses (Bevilacqua 2016): with this configuration it is possible to predict the position of the front of a turbulent current (in which inertial effects dominate over viscous forces and particle-particle interactions) as a function of time. In a similar way to the energy-cone approach, Bevilacqua (2016) computed the front average kinetic energy and compared it to the potential energy associated to an obstacle of height H through a function (which replaces the straight line of the energy line approach). A description of the equations associated with the development of the Box-Model are presented in Appendix 2. Neri et al. (2015) and Bevilacqua (2016) implemented a code where: i) it is assumed a single particle size representative of the mean Sauter diameter (i.e. the diameter of a sphere with the same volume of the particle) of the grain-size distribution of the mixture; ii) the propagation of the PDC has been assumed axisymmetrical; iii) PDC invasion model has been applied in an inverse mode, i.e. starting from the invasion area (obtained from density functions of past PDC dispersal areas) and then computing the maximum runout associated with such propagation, given a specific vent location and surrounding topography. The above-mentioned code simplify the dynamics of the problem in a way that a) the forces controlling the flow are not directly considered but only their effects and b) entrainment of ambient fluid is assumed negligible. In this code, key input parameters that influences PDC maximum runout and deposition of particles are represented by: a) the total collapsing volume (expressed in term of the dimension of the initial cylinder with height= h_0 and radius= l_0); b) the initial concentration of solid particles (ϕ_0); c) density of granulometry classes (ρ_{si}); d) settling velocities (w_s) for each granulometry class; e) ambient air density ($\rho_g=1.12 \text{ kg/m}^3$); f) Froude number ($Fr=1.18$); g) gravity acceleration ($g=9.81 \text{ m/s}^2$). With respect to points b), c) and d), more details are provided in section 5.3.1.

In the case study of this project, different versions of this code have been compared and validated, including i) a polydisperse version of the code where a ‘direct’ approach is considered; ii) a

monodisperse version of the code where a ‘direct’ approach is considered; iii) a monodisperse version of the code where the ‘inverse’ approach is considered (i.e. the same code used by Neri et al. 2015 and Bevilacqua et al. 2016). For the polydisperse version of the code, both axisymmetrical and asymmetrical simulations have been performed. In this latter case the resulting simulations are derived from two separate simulations where the initial volume and the TGSD of the deposit corresponding to two different sectors are forced to collapse separately in the corresponding sector.

5.2.2 The TITAN2D code

The TITAN2D code solves the incompressible Navier–Stokes equations, assuming that velocity does not vary with flow height (Pitman et al. 2003; Patra et al. 2005; Pitman and Le 2005). This procedure of shallow water model for PDCs works with the assumption that basal flow is relatively thin with respect to the whole current, but it may be very fast, as from theoretical models and field observations (Sulpizio et al. 2014). The governing equations (provided in Appendix 3) are the result of early studies by Savage and Hutter (1989) and subsequent modifications by Iverson and Denlinger (2001) and Denlinger and Iverson (2004); the code has been instead developed by the Geophysical Mass Flow Modeling Group at the University at Buffalo (Patra et al. 2005).

The granular material is assumed to be an incompressible continuum satisfying a Mohr Coulomb law, which states that slip planes appear inside the bulk and at its base as soon as the state of stress overpasses the Coulomb criteria of failure, $\tau/\sigma=\tan\varphi$, where σ and τ are the normal and shear stresses acting on a granular material, and φ is the friction angle of the medium (Charbonnier et al. 2015). This latter one can assume different values if it is representing the internal failure of the medium (φ_{int}) or its movement with respect to the plane on which the medium is sliding (φ_{bed}), as

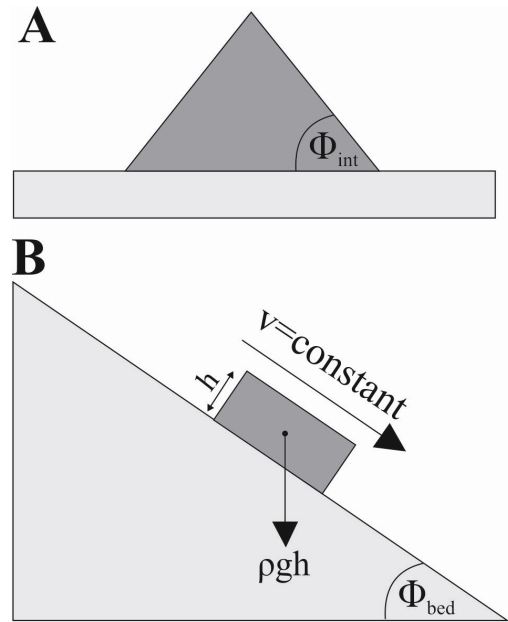


Fig. 5.3: Sketch of a finite mass of granular material on a plane. a) the internal friction angle ϕ_{int} , is the steepest angle that the upper surface of a conical pile of dry sand can make with respect to the horizontal plane it is resting on; b) the bed (also known as basal) friction angle, ϕ_{bed} , is the angle that a plane needs to be inclined so that a block of material will slide downslope at a constant speed. Modified from Charbonnier et al. (2015).

represented in Fig. 5.3. The Coulomb friction relates the shear stress τ to both the normal stress at the base of the flow and the friction angle φ_{bed} between the flow and the ground (Kelfoun 2011).

The code developed by Patra et al. (2005) combines numerical simulations of a flow with digital elevation data of natural terrain supported by a Geographical Information System (GIS) interface. Topographical data are imported into a regular grid/mesh structure that define a two-dimensional spatial box in which the simulation will occur (Charbonnier et al. 2015): in order to increase simulation accuracy, a system of mesh refinement (i.e. the splitting of the computational domain in smaller cells) is adopted only where the simulation actually take place (“AMR”, Adaptive Mesh Refinement). The version used for the simulations in this project was released in June 2016 and is freely available on the VHub website (Palma et al. 2014). This version is furthermore integrated by three supplementary constitutive laws designed for different type of materials: i) a version of the Coulombian rheology which takes into account the presence of interstitial fluid (Pitman and Le 2005); ii) a version that adds to the Coulomb friction a stress which depends on the square of the velocity, incorporating a coefficient which is used to represent the effect of turbulence and/or collisions (Christen et al. 2010; Fischer et al. 2012); iii) a friction law based on empirical parameters that need to be calculated for different materials (Pouliquen and Forterre 2002). For this project the simple Coulombian friction law was employed, whose major inputs which parametrize a flow include (Dalbey 2009):

- A Digital Elevation Model (DEM) of terrain, supported in GRASS GIS format. As of October 2016, the online version of TITAN2D on VHub provides a tool for DEM conversion from other formats, which provides as output a 20-m resolution DEM;
- One or more sources of volume (and therefore mass); TITAN2D can use a combination of any number of the following two types of mass sources
 - A pile of material with specified volume (defined by major/minor axes length and initial height), position, geometry (cylindrical/paraboloid, perpendicular/inclined with respect to topography), and direction toward which the mass is eventually accelerated (defined by initial velocity and initial direction);
 - A flux source, which adds mass over a specified time period and area at a specified rate (extrusion velocity, m/s) with the external shape of a paraboloid. As with a pile, the necessary descriptions include total volume (defined by major/minor axes length,

extrusion velocity and total time of extrusion), position, geometry, and direction toward which the mass is eventually accelerated (defined by initial velocity and initial direction);

- Two material properties (ϕ_{int} and ϕ_{bed} ; Fig. 5.3).
- Computational parameters (simulation time and order method). Under the first order method, the values for pile height, momentum etc. that are calculated by the model are approximated as constant across the entire cell while under the second order method, the values of the parameters are assumed to vary linearly across the cell.
- Scaling parameters H and L, which are the cube root of the total volume from all piles and flux sources (the former) and the maximum expected runout of the simulated flow (the second).

As of October 2016, TITAN2D has been used for numerical modeling of volcanic-related geophysical mass flows, mostly block-and-ash flows from dome collapses, where the pile geometry and Coulomb-like friction models have been chosen (Hidayat et al. 2007; Charbonnier and Gertisser 2009; Procter et al. 2010; Capra et al. 2011; Charbonnier and Gertisser 2012; Charbonnier et al. 2015). Very few attempts have been put forward in order to reproduce PDCs from collapsing columns, always using a pile geometry (Murcia et al. 2010). In this project it is intended to explore the numerical modeling of this latter type of PDCs using the flux source feeding system (more realistically representing a continuous feeding from a collapsing column) using the version of TITAN2D available on the VHub website.

5.2.3 Numerical modeling of PDCs at Somma-Vesuvio

Due to the long history of data collection and geological interpretations and due to the already discussed volcanic hazard of the Neapolitan area, SV has been long the topic of several studies aimed at reproducing PDC dispersal areas through numerical modeling.

Early studies were made by Sheridan and Malin (1983), which adopted the energy line/cone approach based on parameters from the AD 472 “Pollena” eruption. Results of this first approach (referred to the occurrence of dilute PDCs) described a quasi-circular invasion area of PDCs, assuming

the limit of invasion area to be in Naples and the vent to be at the western rim of the present caldera. The same approach was also employed by Rossano et al. (1998).

Extensive PDC modeling at SV was performed by Dobran et al. (1994), who benefited from the multiphase code developed by Dobran et al. (1993): in this latter one, two phases were separately modeled, the gas one (involving water vapor and air) and the solid one (involving one particle size class of 100 μm). Input parameters for the numerical simulations of Dobran et al. (1994) were derived from field data of the AD 79 “Pompeii” eruption (Papale and Dobran 1993) and allowed to determine several key parameters such as Mass Discharge rate, pyroclasts velocity at the vent and particle volumetric fraction at the vent. Main important results of these simulations were referred especially to the times at which PDCs emitted from the present Gran Cono are able to reach different locations on the SV surroundings.

More recently, Todesco et al. (2002) and Esposti Ongaro et al. (2002) performed several simulations using the multiphase code PDAC2D (Neri et al. 2003) for a selected topographic profile along the N sector of SV. For those simulations, the magmatic system and the vent conditions corresponding to different possible eruptive scenarios were defined on the basis of petrological studies and magma ascent modeling; moreover, the natural obstacle of Mt. Somma in these simulations is not capable of halting the flow, at least for the greatest eruption intensities considered (in between sub-Plinian I and Plinian).

Finally, Neri et al. (2007) and Esposti Ongaro et al. (2008) performed transient 3D numerical simulation at SV using the PDAC code (Esposti Ongaro et al. 2007): in this code pyroclasts sedimentation and elutriation, as well as the air entrainment and heating, are explicitly computed through the solution of the non-equilibrium multiphase flow equations. In the simulations presented the authors have chosen: i) a sub-Plinian I reference scenario for eruptive parameters (Cioni et al. 2008); ii) a two-sized particle formulation (assuming equal amount of 30 and 500 μm particles) resulting from field data about the AD 1631 and AD 472 “Pollena” eruptions (Rosi et al. 1993; Sulpizio et al. 2005). These two particle sizes were assumed to be representative of the finest and median size of the mixture whereas the coarsest particle component of some mm size was neglected; iii) vent diameters of 125-175 m and exit velocities of 100-250 m/s (Papale and Longo 2008). Particularly, Esposti Ongaro et al. (2008) focused in detail two simulations (SIM3 and SIM4, Fig. 5.4) describing a situation of partial collapse from an eruptive column (with an inlet radius of the vent of 125 m – SIM3) and a “boiling-

over” condition of total collapse (with an inlet radius of the vent of 175 m –SIM4). For each of these two setting of parameters, Esposti Ongaro et al. (2008) performed different simulations changing the vent location from the present Gran Cono edifice to the “Valle del Gigante” area, trying to reproduce the locations of volcanic vents for the AD 1631 and the AD 472 “Pollena” eruptions respectively. Results of these simulations are displayed in Fig. 5.4 and clearly indicate how the effect of the Mt. Somma topographic barrier is particularly evident using this set of input parameters, particularly in the possibility for PDCs to propagate toward N sectors.

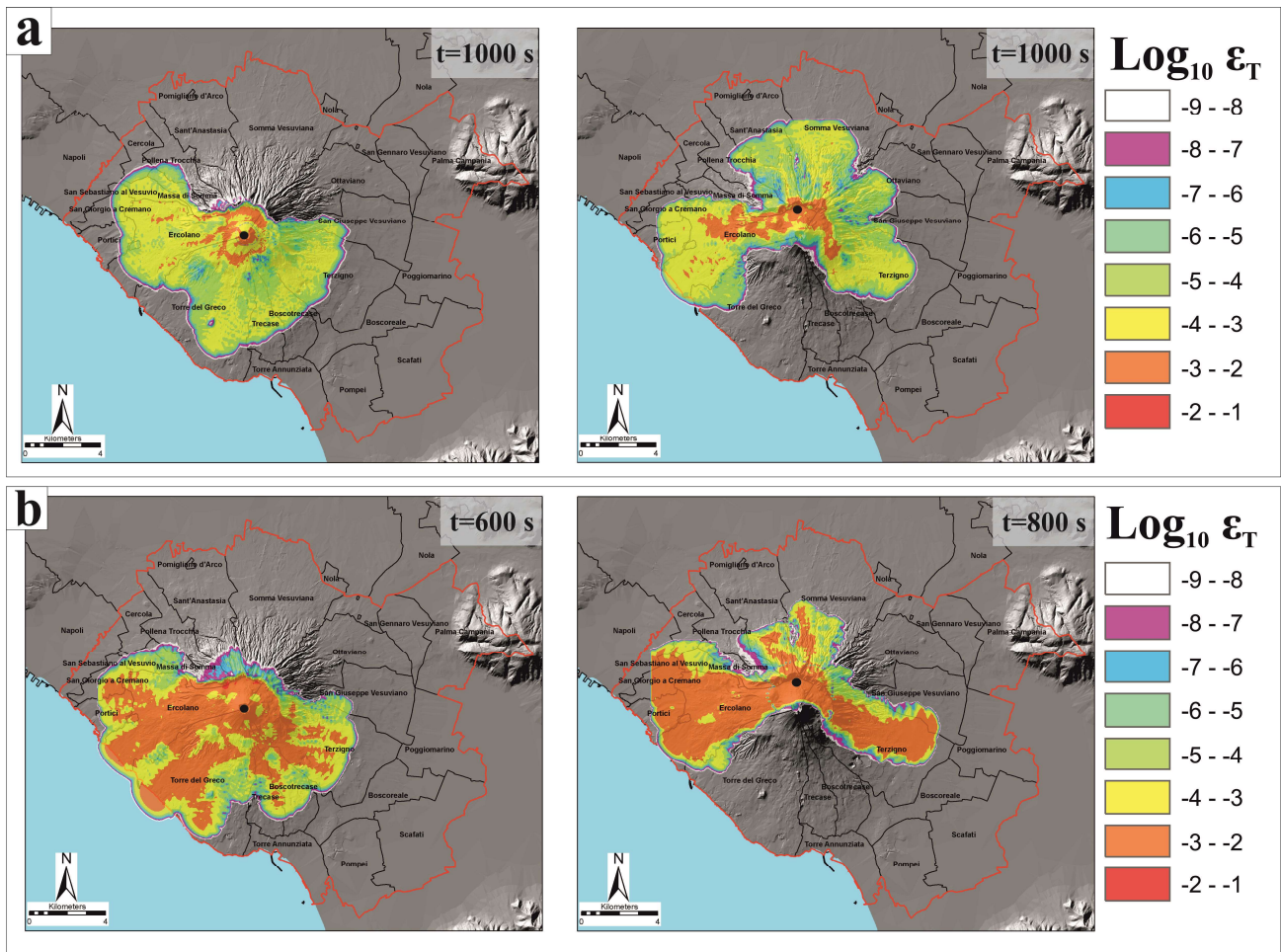


Fig. 5.4: a) maps of the base-10 logarithm of the total volume particle fraction at 10 m above ground for two simulations representing a partial collapse of an eruptive column (SIM3 from Esposti Ongaro et al. 2008) after 600 s from the beginning of the collapse. Different vent locations are represented by the black dots; b) maps of the base-10 logarithm of the total volume particle fraction at 10 m above ground for two simulations representing a total collapse of an eruptive column (SIM4 from Esposti Ongaro et al. 2008) after 600 and 800 s from the beginning of the collapse. Different vent locations are represented by the black dots. Red Zone from the latest emergency plan (DPC 2014) and municipality boundaries are represented as well.

5.2.4 Model validations with field data

For this project two main types of validation (or sensitivity analyses) have been performed comparing numerical model outputs with field data (described in Chapter 4): validations with respect to thickness and with respect to inundation areas. A third type of validation has been performed for the outcomes of the Box-Model with respect to mass fractions of different clast sizes in correspondence of selected stratigraphic sections.

The validation of numerical model outputs with respect to thickness has been performed differently for the Box-Model and TITAN2D: a) for the first one, selected profiles have been chosen from a raster derived from the TIN of the modal outline of the PDC deposit. The thicknesses of the deposit along these profiles have been therefore compared with the thickness of the Box-Model simulation outputs (calculated in absence of topography); b) for the TITAN2D simulations instead, thicknesses of the deposit of all the stratigraphic sections of the dataset have been compared with the thickness value of the model output in that location.

From the point of view of the inundation area instead, the methodology adopted for model validations rely on the approach described by Fawcett (2006) and implemented by Cepeda et al. (2010) for landslide deposit back-analyses. This method is based on the quantification of the degree of matching between true class instances (deposit) and hypothesized class instances (simulation), which are compared using a classification model (Fig. 5.5). In this classification, it can be easily quantified

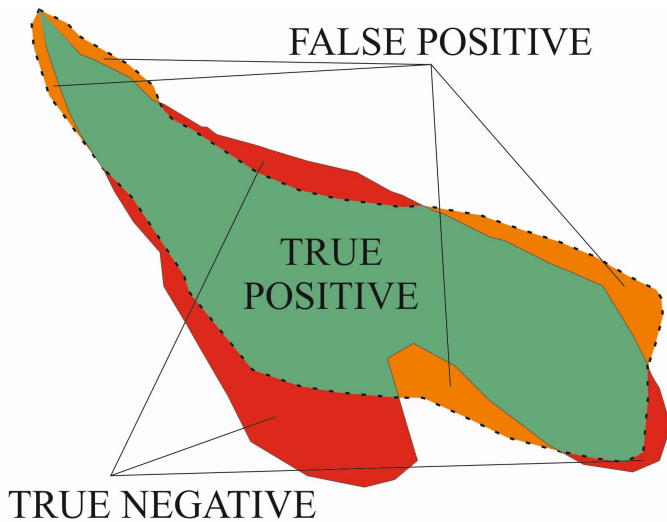


Fig. 5.5: sketch representing the three areas used for the validation procedure (the model output outline is represented in dashed black line).

the percentage of model overlapping on the actual deposit $\left[TRUE POSITIVE = \left(\frac{Area Sim \cap Area Dep}{Area Sim \cup Area Dep} \right) \cdot 100 \right]$, the percentage of model overestimation with respect to the actual inundation area given by the deposit $\left[FALSE POSITIVE = \left(\frac{Area only Sim}{Area Sim \cup Area Dep} \right) \cdot 100 \right]$ and the percentage of model underestimation with respect to the actual inundation area given by the deposit

$\left[TRUE\ NEGATIVE = \left(\frac{Area\ only\ Deposit}{Area\ Sim \cup Area\ Dep} \right) \cdot 100 \right]$. The False Negative case (no deposit nor simulation) has not been obviously calculated.

5.3 Numerical simulations and validations

5.3.1 Choice of input parameters

For the simulations displayed in this section, input parameters from field data discussed in Chapter 4 have been employed. Particularly, the EU3pf and EU4 units from the AD 79 “Pompeii” eruption have been reproduced using the Box-Model code, while the Fg “Cupa Fontana” PDC lobe has been modeled using the TITAN2D code. For the case of the EU4 unit it has been chosen to consider parameters from the EU4b and EU4c sub-units together (EU4b/c), since at the beginning of the collapse of the eruptive column they constituted a single unit. Several parameters have been however modified from the ones described in Chapter 4 or have been added.

- *Volume*: volume estimations are input parameters for both the Box-Model and the TITAN2D code. For the second case, the volume of the deposit (corresponding to the “5th/Modal” runout percentile) of the Fg “Cupa Fontana” PDC lobe from Table 4.8 (which includes the volume of the porosity) has been employed. For the Box-Model simulations instead, the volume of the deposit without porosity has been calculated starting from values of porosity from equivalent mediums. In order to do so, values of porosity of gravel, sand, silt/clay have been firstly retrieved from Wolff (1982): these values are 34%, 40% and 44% respectively. Secondly, different weight percent of granulometry classes comparable in size with gravel, sand and silt/clay from the EU3pf and EU4b/c TGSD estimations (Figs. 4.11 and 4.13) have been calculated, and a value of porosity has been estimated considering the weighted mean (with respect to wt%) of the porosities of gravel, sand and silt/clay. These calculations yielded values of 37% of porosity for the EU4b/c unit and 38% for the EU3pf unit: volume of the deposits without porosity have been calculated accordingly for simulations. The porosity has been added again to the thickness values of the outputs of the Box-Model when validating them with the actual deposit. Volume estimations from which the porosity has been subtracted correspond to

the calculations performed considering the “Modal” outline of the PDC maximum runouts (see Tables 4.7 and 4.8 for EU3pf and EU4b/c respectively). Moreover, for some simulations the volumes calculated in Chapter 4 have been added “artificially” a certain amount of volume (of the order of 7.5%-15% more) in order to account for the loss of the finest particles in the co-ignimbritic plume (see Section 5.3.2). Volume estimates for different sectors of the deposit the EU3pf unit (i.e. sectors N and S in Fig. 4.7) have been employed as well. For the EU4b/c unit, sectors NW and SE from Fig. 4.8 have been slightly modified and volumes for these two new NW and SE sectors have been calculated accordingly.

- *TGSD*: the TGSD estimations have been employed for simulations using the Box-Model and therefore the calculations for the EU3pf (Fig. 4.11, both the Total, the N and S) and for the EU4b/c (Fig. 4.13, both the Total, the NW and the SE) have been considered. As mentioned before, in some simulations the TGSD values have been artificially corrected in order to add more fine-grained particles (i.e. the two finest classes, 4ϕ and 5ϕ) for taking into account the mass loss due to the co-ignimbritic plume. Weight percent added to these two granulometry classes account for values of 15% or 7.5%, which have been divided by the two classes and subtracted homogeneously from the remaining 7 granulometry classes. For simulations with a monodisperse code, the value of $Md\phi$ has been employed. As a reference, in a very recent work Macedonio et al. (2016) have used a TGSD derived from field data from the AD 79 eruption for fallout hazard assessment: those values are fully comparable with the TGSD from the EU3pf unit described here, although richer in finer particles (5ϕ).
- *Density*: for the Box-Model code it is necessary to provide values of the densities for each granulometry class that is employed. In order to provide values of this value linked to field data, parameters retrieved from Gurioli (1999) have been employed. Particularly, different wt% of the components (juvenile, lithics and crystals) for the list of samples of Table 8.4 (for EU3pf) and Tables 8.5 and 8.6 (for EU4b/c) have been considered, and density values calculated by Barberi et al. (1989) have been associated to each component. From the values reported in

Table 5.1, the weighted mean (with respect to wt%) has been easily calculated for both EU3pf and EU4b/c.

EU3pf		Φ									
		-4	-3	-2	-1	0	1	2	3	4	5
Juveniles	Mean Density (kg/m ³)	810	805	955	860	970	1600	2350	2550	2550	2600
	Mean wt%	51.73	66.68	63.26	55.21	45.93	41.33	37.37	100.00	100.00	100.00
Lithics	Mean Density (kg/m ³)	2614	2614	2614	2614	2614	2614	2614	2614	2614	2614
	Mean wt%	48.27	33.32	36.49	42.29	45.08	41.27	36.59	0.00	0.00	0.00
Crystals	Mean Density (kg/m ³)	2800	2800	2800	2800	2800	2800	2800	2800	2800	2800
	Mean wt%	0.00	0.00	0.25	2.50	8.98	17.40	26.05	0.00	0.00	0.00
WEIGHTED MEAN DENSITY (kg/m³)		1681	1408	1565	1650	1874	2160	2541	2550	2550	2600
EU4b/c		Φ									
		-4	-3	-2	-1	0	1	2	3	4	5
Juveniles	Mean Density (kg/m ³)	810	805	955	860	970	1600	2350	2550	2550	2600
	Mean wt%	42.05	59.81	48.86	43.53	47.48	49.30	41.22	47.55	55.47	100.00
Lithics	Mean Density (kg/m ³)	2614	2614	2614	2614	2614	2614	2614	2614	2614	2614
	Mean wt%	57.95	40.19	50.69	56.02	49.56	46.89	51.13	47.85	38.54	0.00
Crystals	Mean Density (kg/m ³)	2800	2800	2800	2800	2800	2800	2800	2800	2800	2800
	Mean wt%	0.00	0.00	0.46	0.45	2.96	3.81	7.65	4.59	5.99	0.00
WEIGHTED MEAN DENSITY (kg/m³)		1855	1532	1804	1851	1839	2103	2519	2495	2590	2600

Table 5.1: calculated mean densities for each granulometry classes for both the EU3pf and EU4b/c units.

- *Settling velocities* (w_s): this parameter need to be defined for each granulometry class for the Box-Model code. Settling (or terminal or vertical) velocity has been defined variously by several authors and has been given different values according to the flow regime of a current which could be more turbulent (with Reynolds number $Re \geq 1000$) or more laminar (with $Re < 1000$). For this project, settling velocities for each of the i-esimal particle class with dimension d_i have been calculated using the formulas defined by Doyle et al. (2010) and by Esposti Ongaro et al. (2016) which are, respectively

$$w_{s,i} = \left(\frac{4 \cdot (\rho_{s,i} - \rho_g) g d_i}{3 C_d \rho_g} \right) \quad [\text{Doyle et al. 2010}]$$

$$w_{s,i} = g \cdot \frac{\varphi_i \rho_{s,i}}{D_{s,g}} \quad [\text{Esposti Ongaro et al. 2016}]$$

where C_d is the drag coefficient, φ_i is the volumetric or mass fraction of the i-esimal particle

class and $D_{s,g}$ is the gas-particle drag coefficient, a function that depends on C_d among other parameters. Esposti Ongaro et al. (2016) propose that $C_d=0.44$ if $Re \geq 1000$ and $C_d > 1.4$ if $Re < 1000$, while Doyle et al. (2010) propose that $C_d=1$ basing on values calculated by Woods and Bursik (1991). Since the formula from Doyle et al. (2010) works better with particles of higher dimensions and under more laminar flow regimes while fine-grained particles obey in a better way to the second formula (T. Esposti Ongaro, personal communication), in this project two alternative combinations for settling velocities have been considered for the granulometry classes, the first one where all the classes have been attributed velocities according to the formula by Doyle et al. (2010), while the second one where the settling velocities of the 5 coarsest classes ($-4\phi/0\phi$) are always derived from the formula by Doyle et al. (2010), while the 5 finest ($1\phi/5\phi$) are derived from Esposti Ongaro et al. (2016). For some of the simulations where the monodisperse version was used, in order to better fit the outline of the deposit the settling velocity was assigned an empirical value derived after several attempts. This situations, although a case limit, can be partially explained with the effect given by fluidization. Settling velocity values employed in this project are listed in Table 5.2.

EU3pf -Polydisperse										
ϕ	-4	-3	-2	-1	0	1	2	3	4	5
w_s (Doyle et al. 2010) m/s	17.72	11.46	8.55	6.21	4.68	3.55	2.72	1.95	1.38	0.99
EU3pf -Monodisperse										
Md ϕ	TOT=0.27									
w_s (Doyle et al. 2010) m/s	4.34									

EU4b/c - Polydisperse										
ϕ	-4	-3	-2	-1	0	1	2	3	4	5
w_s (Doyle et al. 2010) m/s	18.61	11.96	9.18	6.57	4.63	3.50	2.71	1.91	1.38	0.99
w_s (Esposti Ongaro et al. 2016) m/s	-	-	-	-	-	2.05	0.97	0.43	0.16	0.03
EU4b/c -Monodisperse										
Md ϕ	TOT=-0.54		TOT+7.5% fines=-0.19		SE=1.22		SE+15% fines=2.39		NW=-1.39	
w_s (Doyle et al. 2010) m/s	5.75		5.09		3.12		-		7.72	
w_s (Esposti Ongaro et al. 2016) m/s	-		-		1.73		0.71		-	
w_s (empirical value) m/s	-		1.63		-		0.1		0.5	

Table 5.2: settling velocities calculated for the EU3pf and EU4b/c units. Values for “TOT Md ϕ ” refer to the values described in Section 4.4.3 for the whole eruptive unit considered (for details see text).

5.3.2 Box-Model simulations

For the Box-Model code, a total of 11 simulations (4 for the EU3pf unit and 7 for the EU4b/c unit) are discussed here, whose main parameters are displayed in Table 5.3.

BOX-MODEL							
Unit	Sim_Code	Parameters					
		Code	Collapse	ϕ_0	Granulometry	w_s	Others
EU3pf	SBM1	P - D	AX	3%	TGSD	Doyle et al. (2010)	-
	SBM2	M - D	AX	3%	Md ϕ	Doyle et al. (2010)	-
	SBM3	P - D	AS	N-4% S-2%	TGSD-N TGSD-S	Doyle et al. (2010)	-
	SBM4	M - I	AX	2.24%	Md ϕ	Doyle et al. (2010)	-
EU4b/c	SBM5	P - D	AS	NW-5% SE-1%	TGSD-NW TGSD-SE	Doyle et al. (2010)	2/3 of the total volume
	SBM6	M - D	AS	NW-5% SE-1%	Md ϕ	Doyle et al. (2010)	2/3 of the total volume
	SBM7	P - D	AS	NW-0.75% SE-0.5%	TGSD-NW TGSD+15% fines-SE	Doyle et al. (2010) - -4 ϕ /0 ϕ Esposti Ongaro et al. (2016) - 1 ϕ /5 ϕ	1/3 of the total volume +15%
	SBM8	M - D	AS	NW-0.75% SE-0.5%	Md ϕ - NW Md ϕ +15% fines - SE	Empirical value (0.5) - NW Empirical value (0.1) - SE	1/3 of the total volume +15%
	SBM9	P - D	AX	1%	TGSD+7.5% fines	Doyle et al. (2010)	Total volume +7.5%
	SBM10	M - D	AX	1%	Md ϕ +7.5% fines	Empirical value (1.63)	Total volume +7.5%
	SBM11	M - I	AX	1.18%	Md ϕ +7.5% fines	Empirical value (1.63)	Total volume +7.5%

Table 5.3: list of simulations performed using the Box-Model code. Symbols key: P – D “Polydisperse-Direct”; M – D “Monodisperse-Direct; M – I “Monodisperse-Inverse”; AX “Axisymmetrical; AS “Asymmetrical.

For both the EU3pf and EU4b/c units, it has been performed both axisymmetrical and asymmetrical simulations, despite the fact that (especially for the EU4b/c unit) the strong asymmetry of the deposit suggests a more probable asymmetrical collapse. Axisymmetrical simulations were performed in order to test if the Box-Model code was capable to capture at least the order of magnitude of the invaded area. Particularly, simulations for the EU3pf unit are displayed in Fig. 5.6 (along with validations with respect to the inundation area) and their validations with respect to thickness and mass fractions of different granulometry classes can be appreciated in Fig. 5.7. For the EU4b/c unit instead, asymmetrical simulations are displayed in Figs. 5.8 and 5.9, where the validations with respect to inundation are and thicknesses/mass fractions can be respectively appreciated. Axisymmetrical simulations are instead displayed in Fig. 5.10, and a final comparison between polydisperse and monodisperse simulations is instead available in Fig. 5.11.

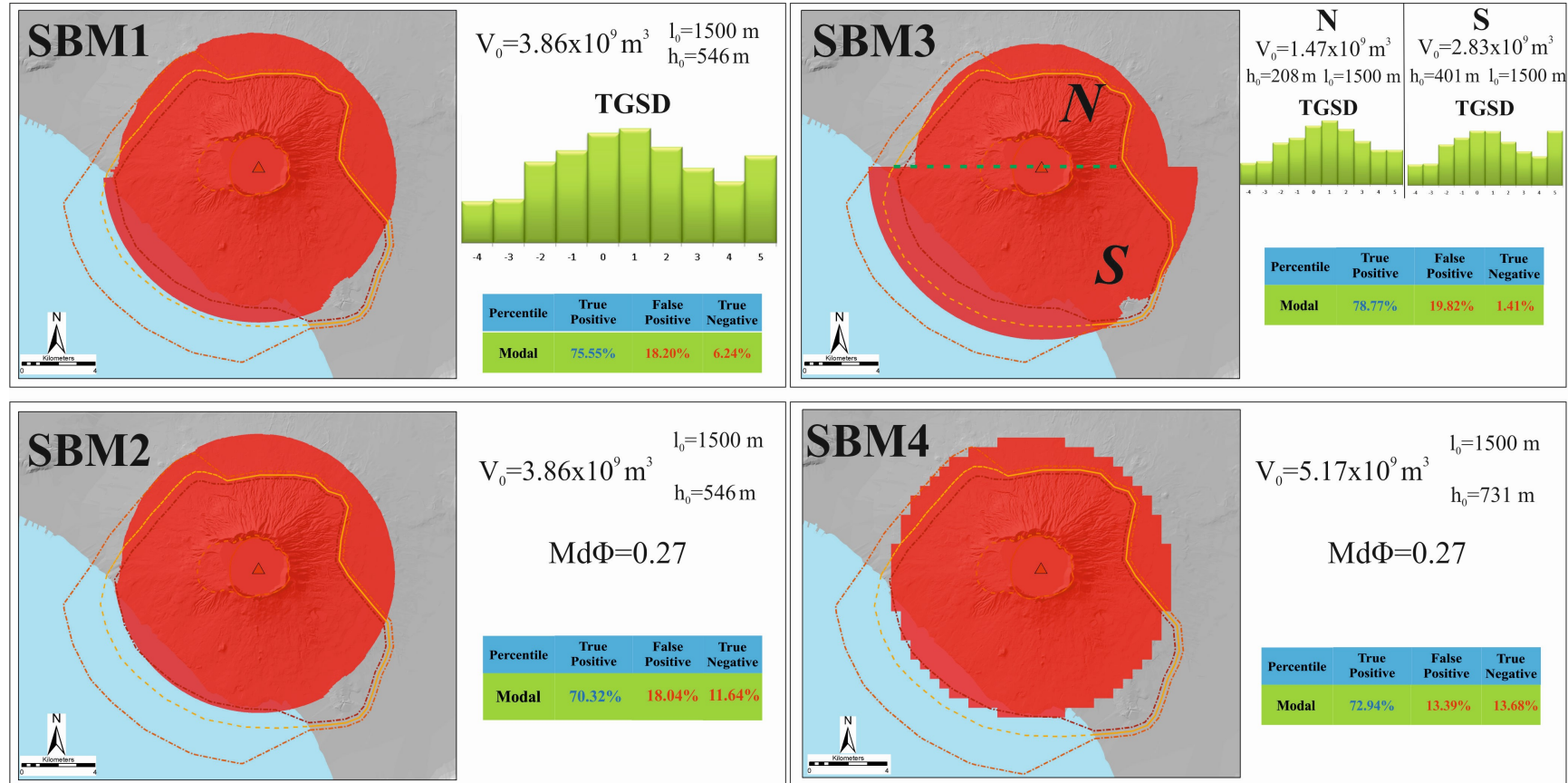


Fig. 5.6: simulations with the Box-Model code with the indication of the initial volume (V_0), the radius (l_0), height (h_0) and TGSD/ $\text{Md}\Phi$ of the collapsing cylinder and the areal validations for each simulation. The green dashed line from simulation SBM3 indicates the N-S sectors of the asymmetrical simulation. SBM1 and SBM2 simulations with $\phi_0=3\%$, SBM3 simulation with $\phi_0(\text{S})=2\%$ and $\phi_0(\text{N})=4\%$, SBM4 simulation with $\phi_0=2.24\%$. Red triangle is the inferred position of vent. Red line is the outline of the uncertainty area of vent position (Section 2.4.2). SV caldera outlined in dark orange dashed line.

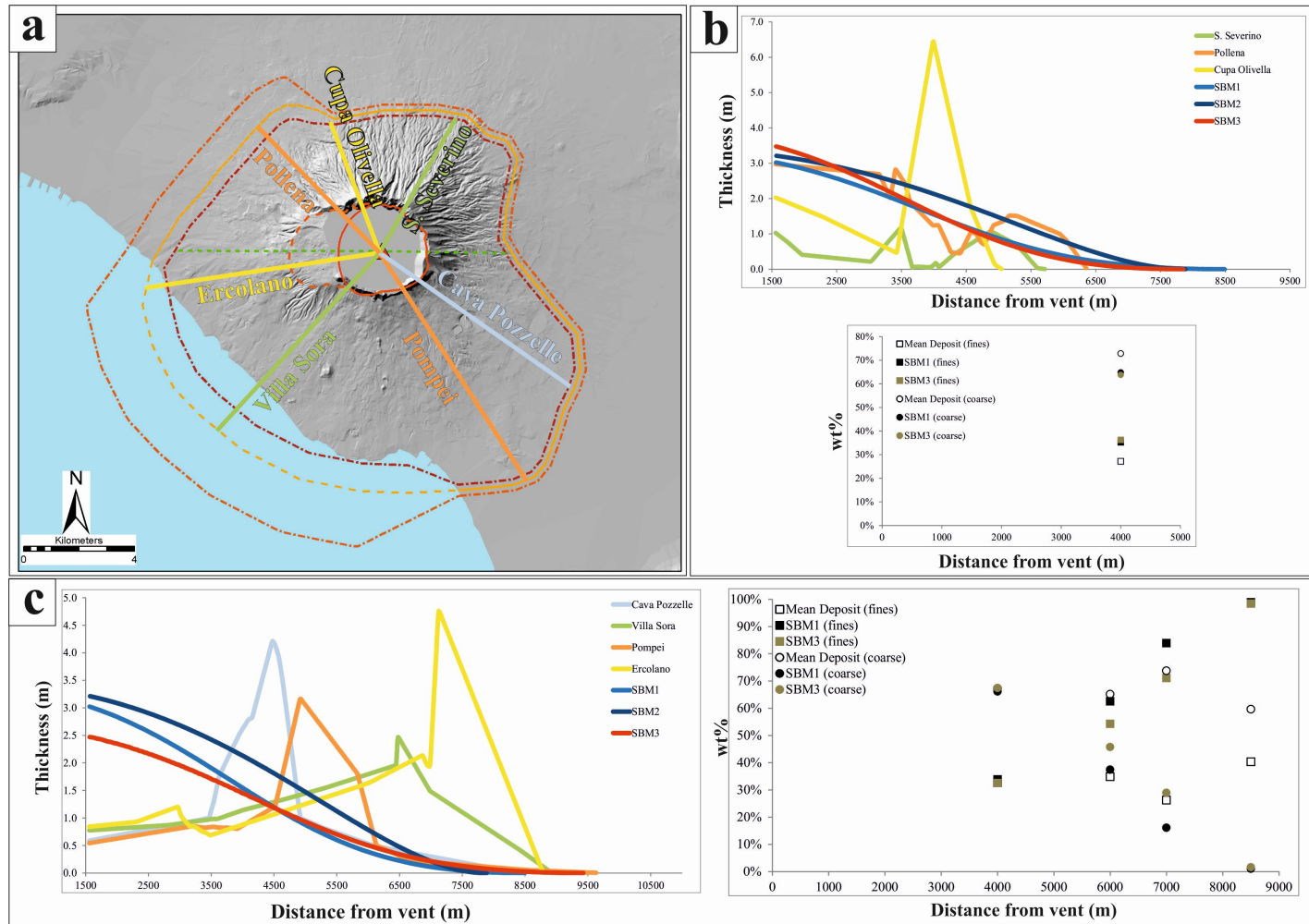


Fig. 5.7: thicknesses profiles of selected transects along the EU3pf deposit compared with the thicknesses of the Box-Model outputs along with diagrams of fines ($3\phi/5\phi$) vs. coarse ($-4\phi/2\phi$) particles for selected stratigraphic sections compared with outputs of the Box-Model code; a) location of transects; b) diagrams for N sector; c) diagrams for S sector. Green dashed lines identify the two collapse sectors (NW and SE). Red triangle is the inferred position of vent. Red line is the outline of the uncertainty area of vent position (Section 2.4.2). SV caldera outlined in dark orange dashed line.

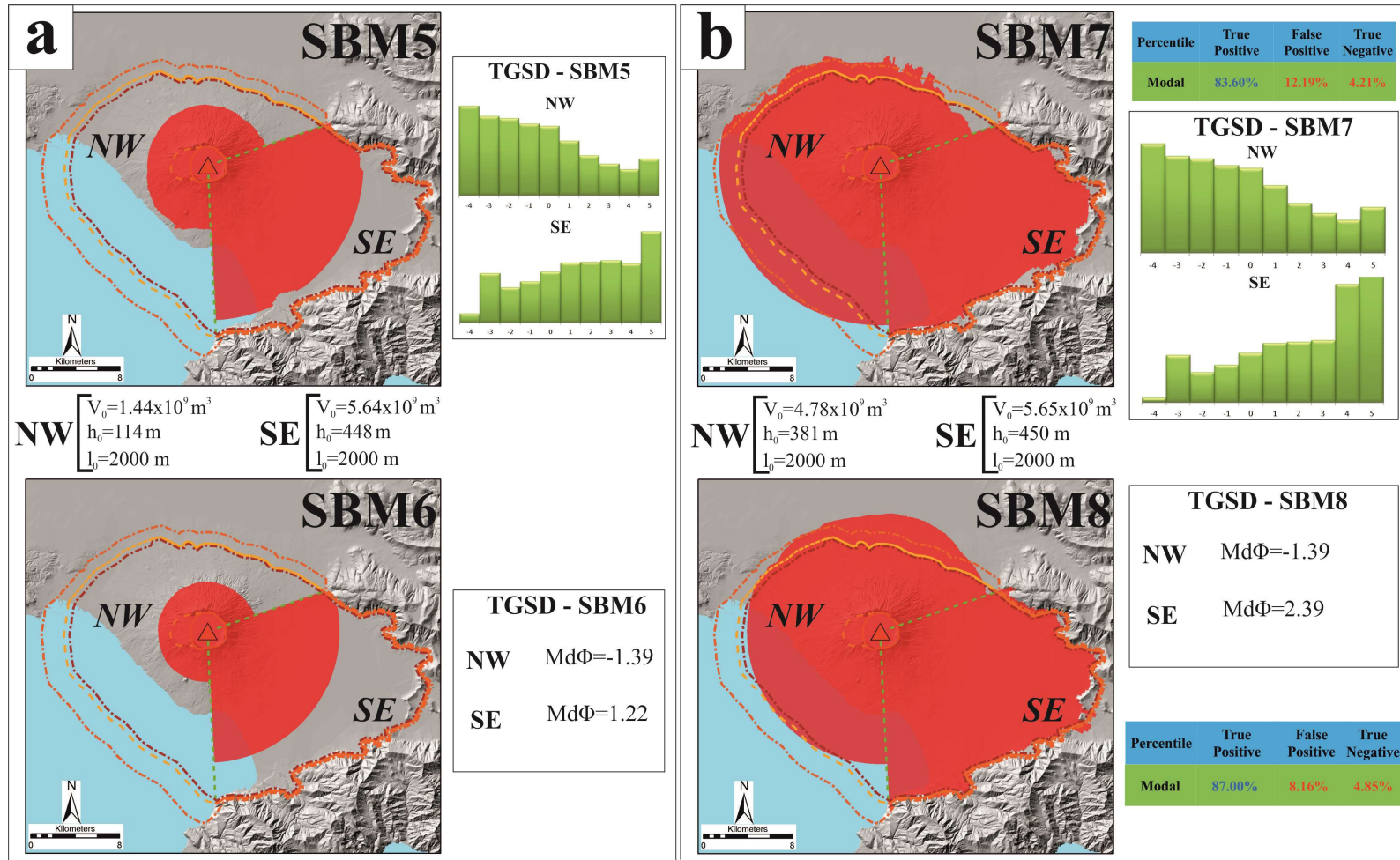


Fig. 5.8: asymmetrical simulations for the EU4b/c unit with the indication of the initial volume (V_0), the radius (l_0), height (h_0) and TGSD/Md Φ of the collapsing cylinder and the areal validations (for the SBM7 and SBM8 simulation); a) SBM5 (polydisperse) and SBM6 (monodisperse) simulations ($\phi_0(\text{NW})=5\%$; $\phi_0(\text{SE})=1\%$); b) SBM7 (polydisperse) and SBM8 (monodisperse) simulations ($\phi_0(\text{NW})=0.75\%$; $\phi_0(\text{SE})=0.5\%$). Green dashed lines identify the two collapse sectors (NW and SE). Red triangle is the inferred position of vent. Red line is the outline of the uncertainty area of vent position (Section 2.4.2). SV caldera outlined in dark orange dashed line.

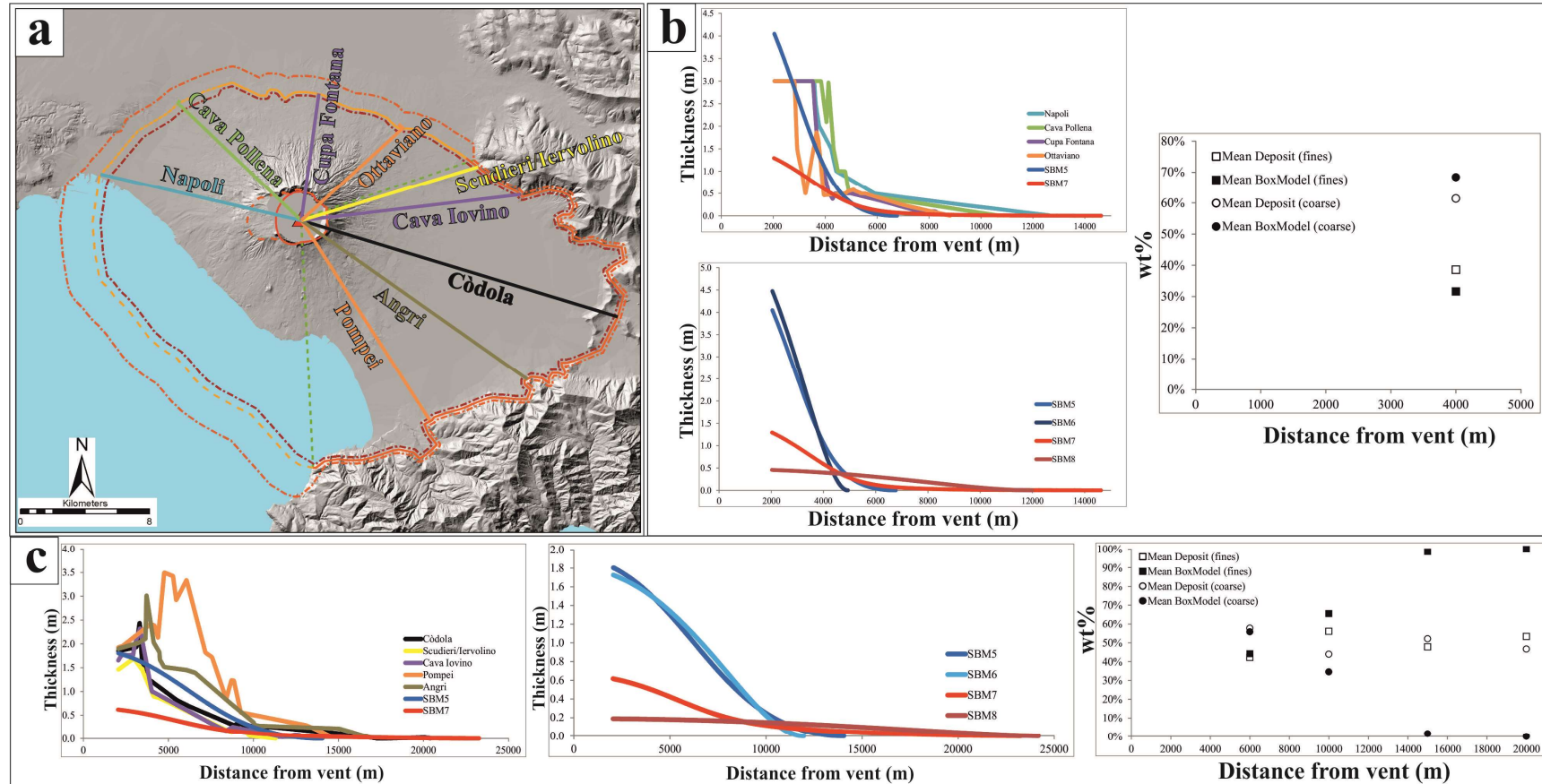


Fig. 5.9: thicknesses profiles of selected transects along the EU4b/c deposit compared with the thicknesses of the Box-Model outputs along with diagrams of fines ($3\phi/5\phi$) vs. coarse ($-4\phi/2\phi$) particles for selected stratigraphic sections compared with outputs of the Box-Model code; a) location of transects; b) diagrams for NW sector; c) diagrams for SE sector. Green dashed lines identify the two collapse sectors (NW and SE). Red triangle is the inferred position of vent. Red line is the outline of the uncertainty area of vent position (Section 2.4.2). SV caldera outlined in dark orange dashed line.

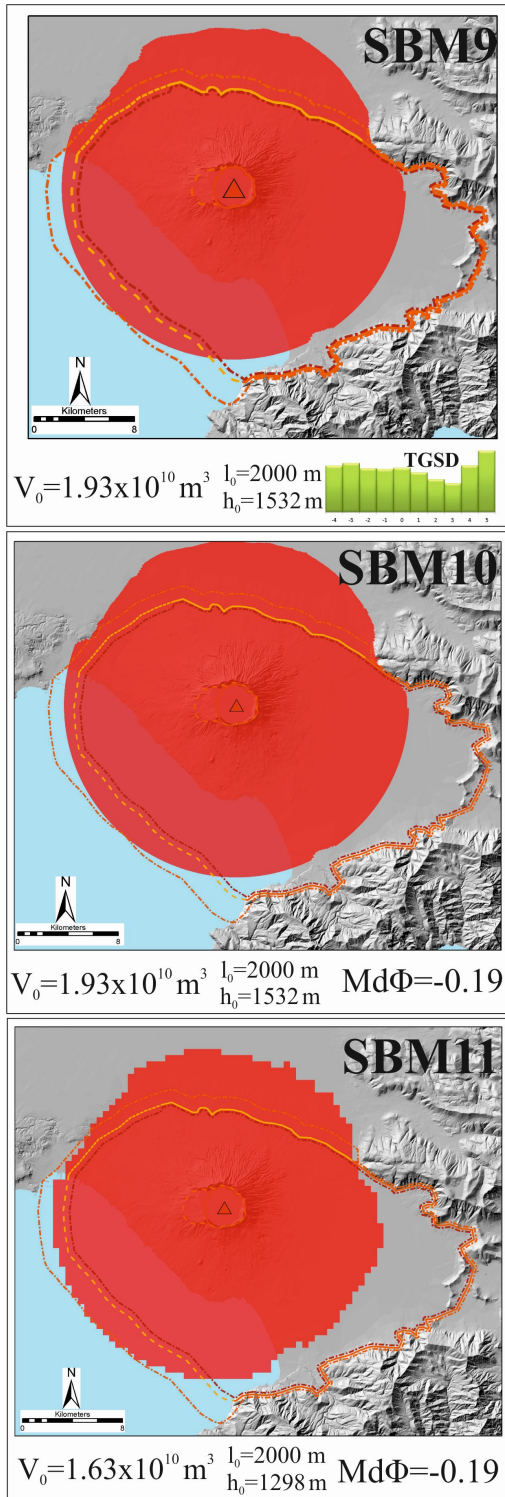


Fig. 5.10: simulations with the Box-Model code with the indication of the initial volume (V_0), the radius (l_0), height (h_0) and TGSD/ $Md\Phi$ of the collapsing cylinder. SBM9 and SBM10 simulations have $\phi_0=1\%$, SBM11 has $\phi_0=1.18\%$. Red triangle is the inferred position of vent. Red line is the outline of the uncertainty area of vent position (Section 2.4.2). SV caldera outlined in dark orange dashed line.

The parameters displayed in Table 5.3 are the result of empirical calibrations of the Box-Model code with field data: particularly in the case of the EU4b/c unit for the monodisperse cases (SBM8, SBM10 and SBM11 simulations), values for the settling velocities and ϕ_0 have been attributed in order to best fit at least the invasion area of the correspondent polydisperse simulation. Simulations SBM5/SBM7 and SBM6/SBM8 represent instead an attempt for better reproducing the dynamic of the EU4 collapse. According to Gurioli (1999) in fact, the tripartite EU4 unit (levels “a”, “b” and “c”, see section 4.2.1 and Fig. 4.3) present two fallout units, the basal “a” level and a thinner level “a2” interlayered within level “b”: this level outcrops discontinuously toward S sectors and only in distal sections, while in the N counterpart is represented by a level enriched in ballistic blocks. Level “a2” divides level “b” in two parts, which are approximately 2/3 (the lower one) and 1/3 (the upper one) of the total thickness of level “b” (Gurioli 1999). For this reason, two separate asymmetrical simulations have been performed by considering that only 2/3 (simulations SBM5 and SBM6) and 1/3 (simulations SBM7 and SBM8) of the total EU4b/c volume collapsed. For these two alternative set of simulations, different values of ϕ_0 were considered as well (Table 5.3). From the point of view of the validation with respect to thicknesses, the transects of the deposits have been selected in order to cover as much as possible the inundation area, but trying to avoid portions of the deposit (especially for the EU4b/c unit) that were affected by a high degree of uncertainty: this is particularly true for the seaward part of the deposit, for which stratigraphic sections are completely lacking. With respect

to the values of mass fractions for the deposit (indicated as “Mean Deposit (fines)” or “Mean Deposit (coarse)” in Figs. 5.7 and 5.9), they are the results of an average of the mass fraction values of all the stratigraphic sections at a similar distance. More precisely:

- for the values of EU3pf in the N sector at 4 km, the sections of Voltosanto, Scudieri, Villa Telesi, Cava Pollena (LG – A) and Lagno Molaro (LG) have been employed (see Fig. 4.10);
- for the values of EU3pf in the S sector have been employed (Fig. 4.10): at 4 km the sections of Cava Pozzelle (LG) and Discarica Pozzelle; at 6 km the sections of Casa de Falco and Cava Terzigno; at 7 km all the five sections of Ercolano and the sections of Villa Regina and Oplontis; at 8-9 km the sections of Masseria Carotenuto (a) and Pompei Necropolis;
- for the values of EU4b/c in the NW at 4 km, the sections of Via Cascetta, Voltosanto, Lagno Molaro (a), Vergine di Castello and Ottaviano (a) have been employed (see Fig. 4.12a);
- for the values of EU4b/c in the SE sector have been employed (Fig. 4.12a): at 6-7 km the sections of Cava Terzigno, Casa de Falco, Villa Regina and Oplontis; at 9-10 km all four sections of Pompei and the section of Tricino; at 13-15 km the sections of Angri, Santa Maria la Carità, Villa di Arianna and Santa Maria di Pozzano; at 20 km the section of Palazzo Baronale-Còdola.

For the mass fractions of the EU4b/c simulations, the “Mean Box-Model” values (Fig. 5.9b,c), are the result of a weighted mean of the mass fractions values of the SBM5 and SBM7 simulations, where it has been assigned 2/3 of weight to SBM5 simulation and 1/3 of weight to the SBM7 simulation (reflecting the total volume involved in the two simulations).

Areal validations have been performed only for simulations for which it is visually intuitive that a comparison is meaningful, that is the inundation area are similar. The lack of stratigraphic sections in the N sector (for the EU3pf unit) and the NW sector (for the EU4b/c unit) limited the availability of comparisons with respect to mass fractions, which are limited to sections at 4 km of distance with respect to the vent area. In the case of the simulations concerning the EU4b/c unit, an amount of 15% more volume was added to the initial collapsing mixture for the SE sector in the case of the asymmetrical simulations (SBM7 and SBM8). This amount of material was considered to be representative of the 4 ϕ and 5 ϕ grain sizes solely and was added in order to increase the mobility of the PDC and therefore justify the long runout toward SE. Such values do not include the coarser grain sizes since they are already included in level “c”, which (as discussed in Chapter 4) can be seen as part of the

co-ignimbritic deposit of unit EU4b. The values described here are in agreement with values calculated by Engwell et al. (2014) for the Campanian Ignimbrite. When considering simulations with axisymmetrical collapses (SBM9, SBM10 and SBM11) a total of 7.5% of volume composed of the 4ϕ and 5ϕ grain sizes was added. This value is due to the fact that the volume collapsed in the SE sector is exactly half of the total collapsing volume.

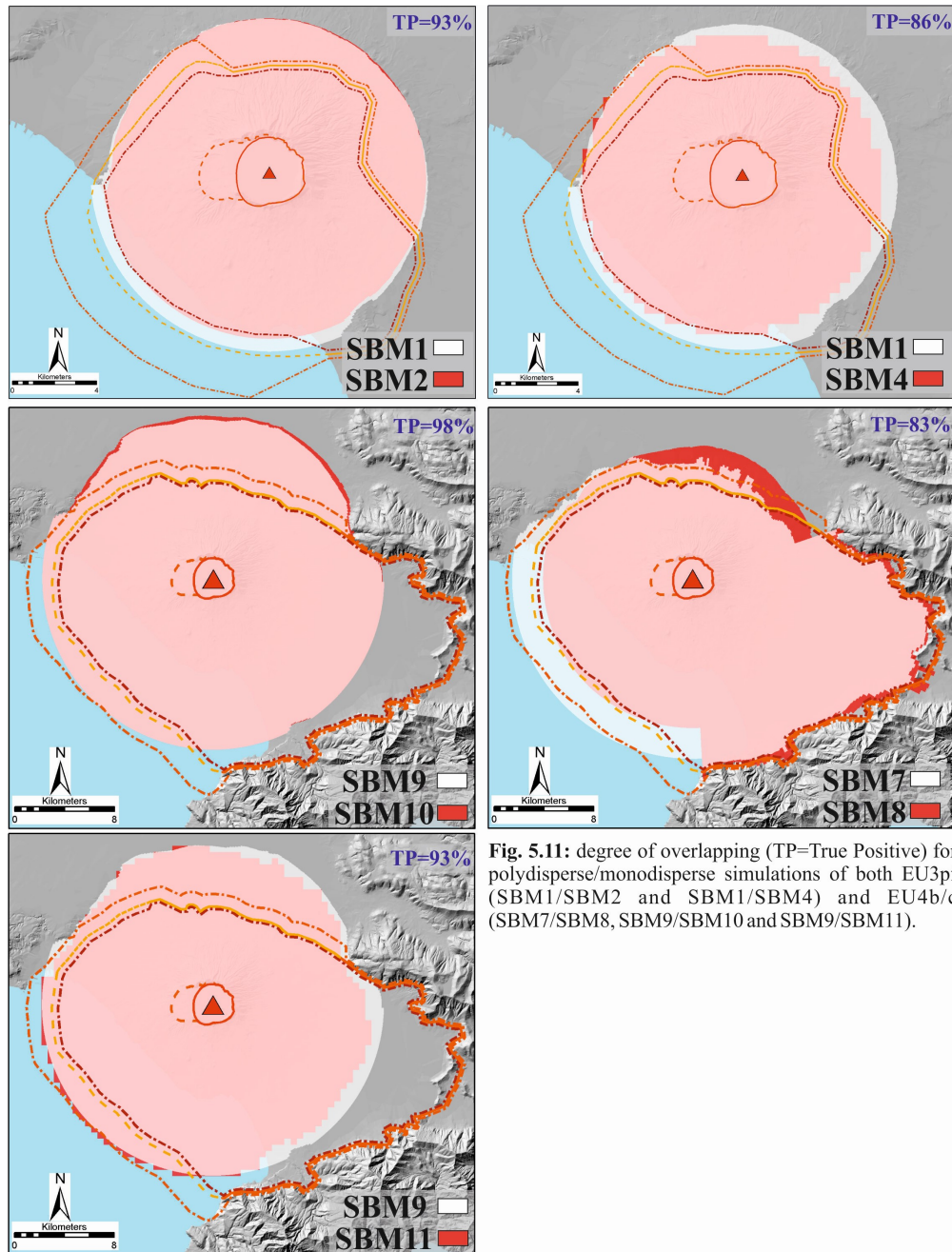


Fig. 5.11: degree of overlapping (TP= True Positive) for polydisperse/monodisperse simulations of both EU3pf (SBM1/SBM2 and SBM1/SBM4) and EU4b/c (SBM7/SBM8, SBM9/SBM10 and SBM9/SBM11).

5.3.3 TITAN2D simulations

For the TITAN2D code, a total of 12 simulations are listed in Table 5.4.

TITAN2D								
Sim_Code	Parameters							
	Major/minor axes (m)	$\varphi_{\text{int}} (^{\circ})$	$\varphi_{\text{bed}} (^{\circ})$	Extrusion vel. (m/s)	Initial speed (m/s)	Time extr. (s)	Initial dir. ($^{\circ}$)	Or. angle ($^{\circ}$)
ST1	25	30	13	43.65	43.65	120	79	0
ST2	25	30	13	17.46	17.46	300	79	0
ST3	25	30	13	8.73	8.73	600	79	0
ST4	25	30	15	43.65	43.65	120	79	0
ST5	25	30	15	17.46	17.46	300	79	0
ST6	25	30	15	8.73	8.73	600	79	0
ST7	25	30	17.5	43.65	43.65	120	79	0
ST8	25	30	17.5	17.46	17.46	300	79	0
ST9	25	30	17.5	8.73	8.73	600	79	0
ST10	25	30	20	43.65	43.65	120	79	0
ST11	25	30	20	17.46	17.46	300	79	0
ST12	25	30	20	8.73	8.73	600	79	0

Table 5.4: list of simulations performed using the TITAN2D code.

For all of them four parameters have been kept fixed, which are:

- the major and minor axes of the flux source, which have been put equal identifying a circular flux source (the value of 25 m corresponds to the radius of the valley where the flux source has been placed);
- the value of the internal friction angle $\varphi_{\text{int}}=30^{\circ}$ (this value, which does not affect significantly the overall behavior of the flow, is normally adopted for simulations performed with the TITAN2D code, such as in Charbonnier et al. (2015));
- the initial direction (in degree with respect to E) toward which the material is accelerated (the value of 79° correspond to the direction of the segment which joins the flux source and the beginning of the deposit along the valley axis);
- the orientation angle, which indicates whether the major axis of the flux source is tilted or not with respect to the E (the value of 0° corresponds to a situation where the material is not tilted);

The flux source has been positioned at the beginning of the valley which ends up in the “Cupa Fontana” PDC deposit, as close as possible to the top of the Mt. Somma caldera rim, in a position where the accidental fall of material backward into the SV caldera is avoided. Differently with respect to the Box-Model simulations, in the TITAN2D simulations the initial collapsing volume was considered equal to the volume of deposit without any subtractions of porosity. The choice of the

extrusion times has been put in relation with the values of peak MDR calculated by Sulpizio et al. (2005), which are in between 7×10^6 kg/s and 3.4×10^7 kg/s. With extrusion times of 120, 300 and 600 s and the values of total mass of the “Cupa Fontana” PDC lobe it can be easily calculated the corresponding theoretical MDR, which are 3.57×10^7 kg/s, 1.43×10^7 kg/s and 7.14×10^6 kg/s respectively. These values in total agreement with respect to the values calculated by the above-mentioned authors. Total simulated time for each simulation was 1800 s (30 min). Among all the simulations of Table 5.4, it has been chosen two simulations which visually best fitted the deposit (ST3 in Fig. 5.12 and ST6 in Fig. 5.13). In order to take into account the uncertainty related to the fact that TITAN2D simulations never completely stops, two alternative validations have been proposed, considering two snapshots, one at the end of the simulation (1800 s) and another one after 660 s (11 min), that is (for both simulations) 60 s after the end of the extrusion of material. Due to their extreme unreliability, thickness values < 0.01 m have not been considered for model validations.

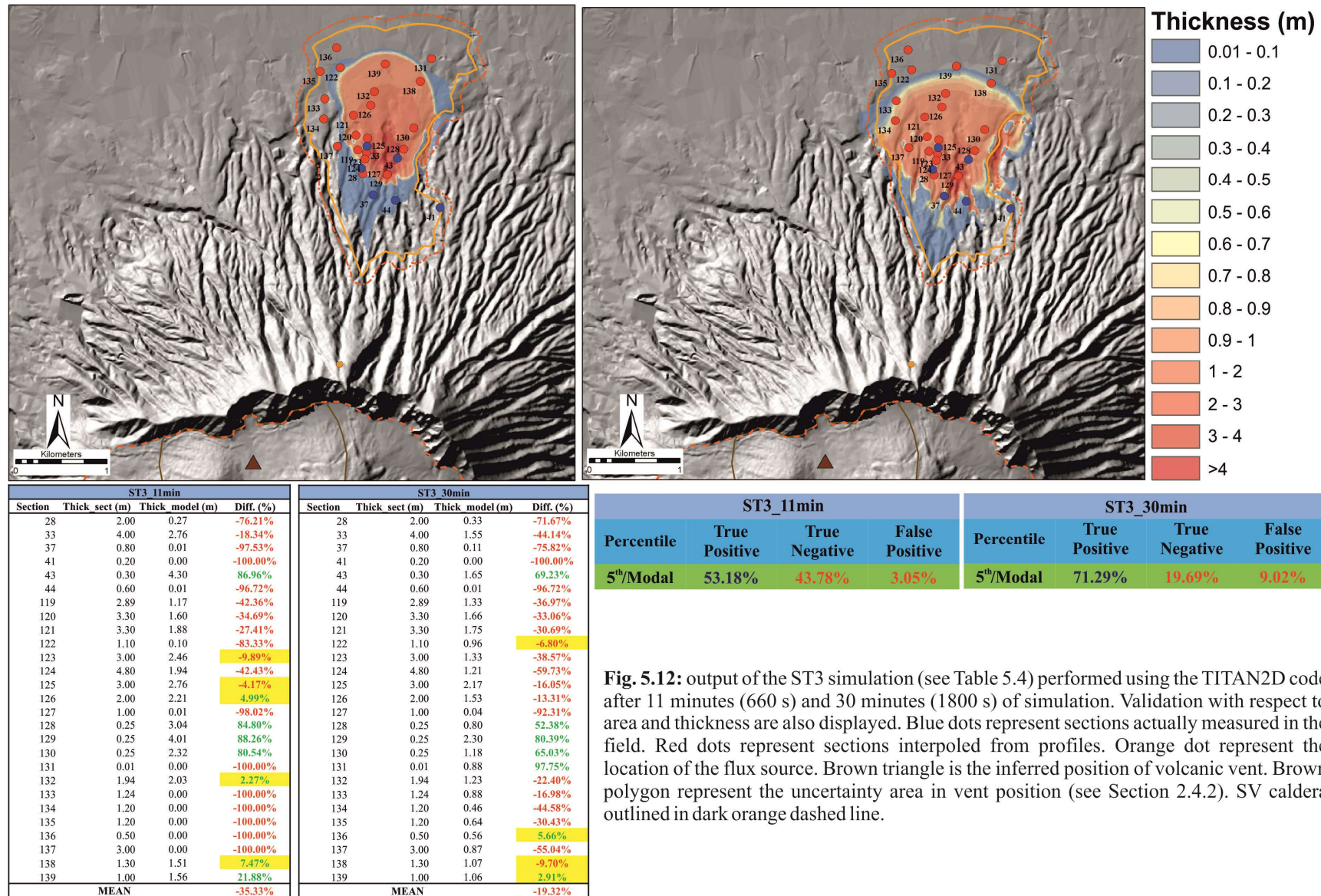


Fig. 5.12: output of the ST3 simulation (see Table 5.4) performed using the TITAN2D code after 11 minutes (660 s) and 30 minutes (1800 s) of simulation. Validation with respect to area and thickness are also displayed. Blue dots represent sections actually measured in the field. Red dots represent sections interpolated from profiles. Orange dot represent the location of the flux source. Brown triangle is the inferred position of volcanic vent. Brown polygon represent the uncertainty area in vent position (see Section 2.4.2). SV caldera outlined in dark orange dashed line.

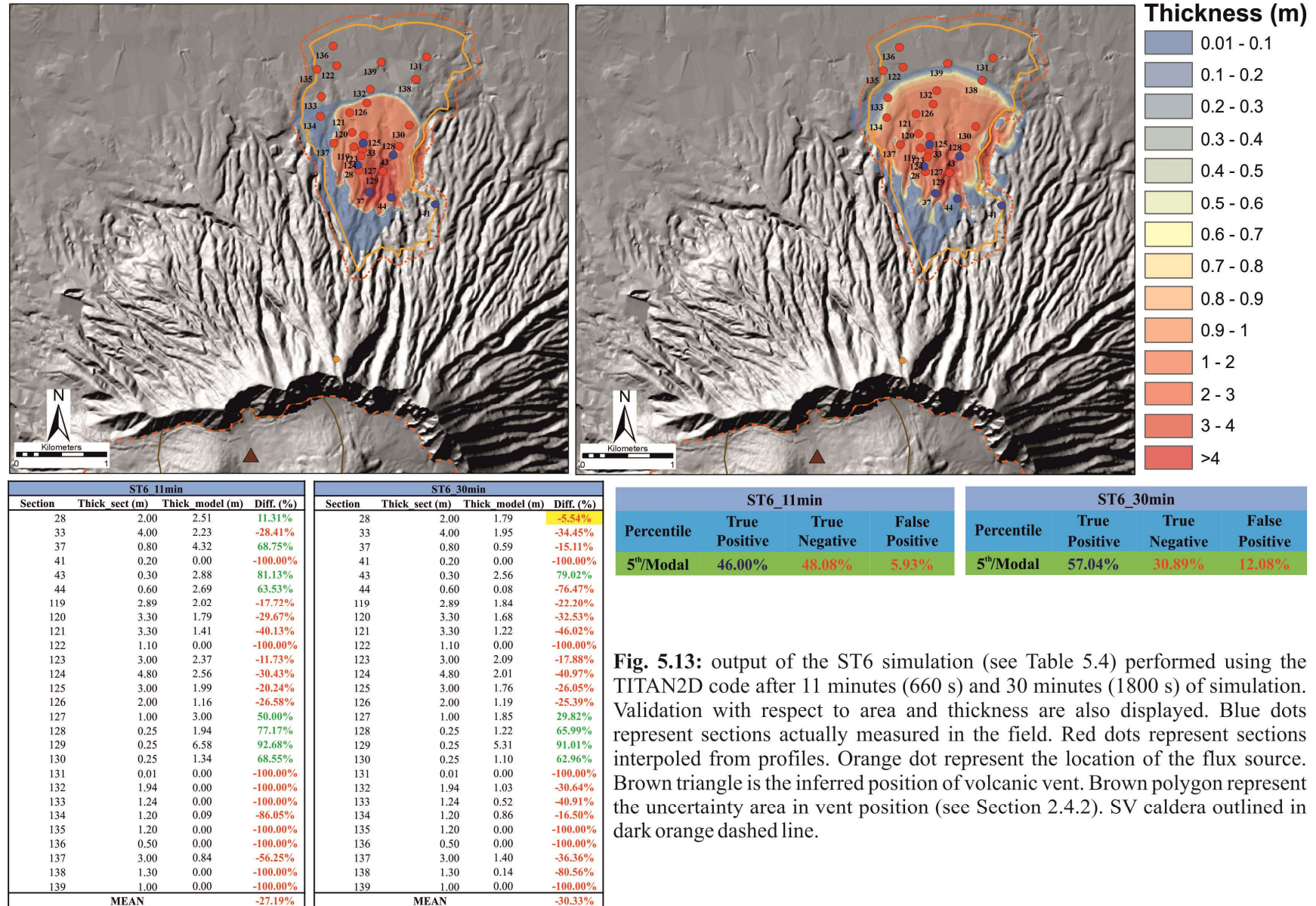


Fig. 5.13: output of the ST6 simulation (see Table 5.4) performed using the TITAN2D code after 11 minutes (660 s) and 30 minutes (1800 s) of simulation. Validation with respect to area and thickness are also displayed. Blue dots represent sections actually measured in the field. Red dots represent sections interpolated from profiles. Orange dot represent the location of the flux source. Brown triangle is the inferred position of volcanic vent. Brown polygon represent the uncertainty area in vent position (see Section 2.4.2). SV caldera outlined in dark orange dashed line.

5.4 Discussion

5.4.1 Box-Model simulations

The procedure for model validation for the outputs of the Box-Model code was aimed at three main objectives for both the EU3pf and EU4b/c units: i) quantifying the degree of reliability of the model while trying to reproduce the deposit (from the point of view of invasion areas, thickness from source area to maximum runout and mass fractions of different granulometry classes at selected distances), ii) testing the sensitivity of the model when varying the most uncertain parameters (i.e. φ_0 and w_s) and iii) evaluating the reliability of the code when considering simpler assumptions (i.e. polydisperse vs. monodisperse situations). Point i) will be discussed further on separately for EU3pf and EU4b/c simulations.

As a general consideration, it should be noted that the procedure through which the Box-Model code produces the invasion map involves a) the calculation of the maximum runout in the case of absence of topography and b) the truncation of the maximum runout wherever the kinetic energy of the flow at a certain point is lower than the potential energy associated to a topographic obstacle. In this way, however, the material that lies beyond the truncation is neither redistributed nor considered in the rest of the simulation. It should however be pointed out that this amount of material is quite limited. As an example, the simulation SBM7 (Fig. 5.8), in its SE part, has several truncations due to the intersection of the decay function of kinetic energy with several topographic barriers, i.e. the Apennines to the ENE and the mounts of the Sorrentina Peninsula to the SE (see Figs. 1.1 and 5.8). To the ENE in some sites the maximum runout of the model is in the order of 11-12 km out of a maximum runout (in absence of topography) computed that is 23 km. At the distance of 11 km the total thickness of the deposit given by the Box-Model is 7 cm (composed for more than 80% in weight by the three finest granulometry classes), which drops down to 1 cm at 17 km and is less than 1 cm at 19 km. Furthermore, if it is considered that most of the runout of the flow given by the model is within 15-17 km, it can be easily understood that the amount of material not deposited is minimal. However, further development of the code might consider this non-deposited material.

Another general consideration is related about the fact that the direct version and the inverse version of the Box-Model code have two different computational resolutions: the direct code has in fact a “radial accuracy” (i.e. the minimal distance at which the comparison between topography profiles and the decay of kinetic energy are performed) of 25 m, while for the inverse one is 500 m. This sensible difference is due to the fact that the inverse code has been designed in order to optimize the accuracy

and the computational efficiency while producing PDC probabilistic invasion maps (see Chapter 6). This difference produces obviously some discrepancies as highlighted from Fig. 5.11: it is however clear that a degree of overlapping (True Positive – TP) of 86% (for the SBM1 and SBM4 simulations for the EU3pf) and 93% (for the SBM9 and SBM11 simulations of the EU4b/c) can be considered within an acceptable uncertainty margin, especially for the EU4b/c unit.

For the EU3pf simulations (SBM1, SBM2, SBM3 and SBM4) the initial attempts were aimed at reproducing the inundation area of the real deposit using an axisymmetrical collapse: however, due to the slight asymmetry of the deposit to the S (see Chapter 4), an asymmetrical collapse has been considered as well. Considerations about the degree of overlapping between the model output area and the deposit maximum runout (True Positive - TP) have to be discussed in conjunction with the actual quantification of the degree of model overestimation (False Positive - FP) and underestimation (True Negative - TN): these calculations (described in section 5.2.4) have been done only with respect to the modal invasion area outline of the deposit, since the initial collapsing volume considered was the one corresponding to this outline. The results presented in Fig. 5.6 show how the TP values for the four simulations are in the interval 70%-78%, while TN values range from 1% and 13% and FP values range from 13% and 19%. This situation indicates that, while the degree of overlapping between model and deposit (for the modal outline) is at an acceptable value and the percentage of model underestimation is below 15%, the model still tend to overestimate too much the modal outline of the deposit. As an example, simulation SBM3 shares at the same time the best TP and TN values (78% and 1% respectively) and the worst FP value (19%). With respect to this latter point it should however be noted that the FP value for the SBM3 simulation calculated considering the maximum runout of the 95th percentile is less than 10%. Similarly, the TN value calculated considering the 5th percentile is 0.7%. These two values indicate that the percentage of areal overestimation and underestimation which do not coincide neither with the maximum runout upper or lower uncertainty bounds is at an acceptable degree, with a higher tendency for overestimation. It is also worth pointing out that in the monodisperse case with the inverse code (SBM4 – invasion area equal to the modal one of the deposit), the TP value is fairly similar with respect to the SBM3 simulation (72%), while the percentages of model overestimation/underestimation are equal (13%). With respect to the comparison (for the simulations SBM1, SBM2 and SBM3) of the thicknesses of the real deposit versus the Box-Model ones (Fig. 5.7b,c) in both the two sectors (N and S) along which the comparisons have been made, the Box-Model

is not able to reproduce in a satisfactory way the trend with the distance of the real deposit. This can be explained partially by the fact that the EU3pf unit (see Chapter 4 and Gurioli 1999) was emplaced a) to the N atop an extremely rough topography (similar to the present one), where the interaction of the current with the surface produced extremely variable lithofacies and b) to the S atop a gentler topography, with however a topographic high on which the town of Pompeii was built on. This latter aspect is also evident from Vogel and Märker (2010), who reconstructed the pre-AD79 paleotopography of the Sarno river plain (to the SE of the SV edifice). From this work it is possible to appreciate how the modeled depth of the pre-AD79 surface (with respect to the present surface) is 0-1 m in correspondence of the present town of Pompei and the ancient Pompeii excavations, while it is up to 6-7 m deep to the NW of these sites. Due to its simplified formulation and the fact that a complete version of the pre-AD79 paleotopography is not available at the moment, the Box-Model fails to reproduce this aspect of the validation at an acceptable degree. With respect to the comparison between the mass fraction of the granulometry classes of actual deposit versus the Box-Model ones, the situation presented in Fig. 5.7b,c indicate that (for both the N and S sectors) the Box-Model has a good agreement with the values of the actual deposit up to the distance of 4 km and (to the S) up to the distance of 7 km. Beyond this limit (to the S), the Box-Model, since it is not able to account for fluidization effects, fails to transport up to those sites the same amount of coarse materials found in the deposit.

For the EU4b/c simulations (SBM5, SBM6, SBM7, SBM8, SBM9, SBM10 and SBM11) the initial strategy chosen in order to better reproduce the real inundation area was to consider an asymmetrical collapse (simulations SBM5-SBM8), due to the strong asymmetry of the deposit to the SE (see Chapter 4). However, axisymmetrical collapses have been considered as well (simulations SBM9-SBM11): this was aimed at calibrating the two most uncertain parameters (i.e. ϕ_0 and w_s) in order to obtain, for the Box-Model output, at least the same value (in km²) of areal extent of the actual deposit. Particularly, for the two simulations where the direct code has been applied (SBM9 and SBM10) the inundation area surfaces are 549 km² and 563 km², which are fully in agreement with the value of the modal inundation area of the deposit (521 km²). As for the EU3pf simulations, also in this case the validation with respect to inundation area, thickness and mass fractions of different granulometry classes have been done considering the modal inundation area of the actual deposit, although it has been estimated whether the Box-Model outputs at least were included into the two

upper and lower uncertainty bounds. Simulations SBM5-SBM7 and SBM6-SBM8 (Fig. 5.8) represent instead, as previously stated, an attempt to account for the complexity of the EU4b/c unit using a polydisperse (SBM5-SBM7) and a monodisperse (SBM6-SBM8) approach respectively. For the SBM5 and SBM6 simulations, validations with respect to areal invasion have not been computed since it was clearly impossible to obtain a good fit. Nevertheless, validations with respect to thickness (Fig. 5.9b,c) show that (especially in SE sector, Fig. 5.9c) the thickness of the Box-Model output lies in between the thicknesses of the real deposit for the selected transects. Thicknesses of the outputs for the polydisperse (SBM5) and monodisperse (SBM7) simulations overlap almost perfectly for the SE sector (Fig. 5.9c). For the NW sector (Fig. 5.9b) the agreement between the model and the deposit seems to be less evident, probably due to the fact that also in this case the rugged topography of this sector influenced sensibly the emplacement of the current. An opposite situation is evident in the case of the simulations SBM6 (polydisperse) and SBM8 (monodisperse). In this case in fact the areal matching between the model and the real deposit (TP) is between the range 83%-87%, higher with respect to EU3pf simulations. Moreover, values of area overestimation (FP) and underestimation (TN) are sensibly lower with respect to simulations for the EU3pf case, with values of 8%-12% and 4.2%-4.8% respectively. For what concerns the mass fractions of the different granulometry classes, also for the EU4b/c unit (for all the simulations) the model seems to approximate in a satisfactory way the trend of the deposit up to the distance of 10 km, while beyond this point the values of the model and of the real deposit do not coincide (Fig. 5.9b,c). Interestingly, mass fractions of the granulometry classes for the real deposit (especially in the SE sector, Fig. 5.9c) seem to be constant with the distance, with an almost equal subdivision between fine particles and coarse particles.

Two considerations can be made with respect to points ii) and iii) respectively (see the beginning of the paragraph). Firstly, the values assigned to ϕ_0 (0.5%-5%) and w_s (obtained with the two formulas describe in previous paragraphs) have been proved to reproduce in a satisfactory way at least the areal extent of the PDC units tested. Secondarily, in a monodisperse versus polydisperse cases, the value for $Md\phi$ and w_s attributed in the monodisperse cases have reproduced almost perfectly the areal extent given by the polydisperse case in all the cases (Fig. 5.11). However, especially with respect to w_s , some issues were raised. More precisely, for the EU3pf unit the value of the w_s for the monodisperse simulations has been calculated using the formula by Doyle et al. (2010), while for the EU4b/c monodisperse simulations the value calculated with the same formula did not produce

acceptable results: as a consequence its value has been empirically lowered. These two different results might be explained by the TGSD of the two units, which is more symmetrical around the $Md\phi$ value for the EU3pf unit and more skewed toward coarse-grained classes for the EU4b/c unit. As a consequence, the $Md\phi$ value used for the simulations of the EU3pf unit might be more representative of the overall behavior of the unit. A consideration can be finally made on the basis of the comparison between the outputs of the polydisperse code versus the ones of the monodisperse ones (Fig. 5.11). This step has been performed in order to evaluate if the simpler formulation of the Box-Model code (monodisperse) with the inverse approach (which has been applied by Bevilacqua (2016) for producing the PDC invasion map of the Campi Flegrei area) is capable of approximating at least the areal inundation of the more dilute part of a PDC. It is certainly true that future developments would have to implement the polydisperse direct code approach for the production of PDC invasion maps, since in this way the only empirical calibration on the most uncertain parameters has only to be done for the ϕ_0 value, while for the w_s it is possible to use more physically related values. However, as demonstrated in Fig. 5.11, by a reasonable calibration of ϕ_0 and w_s using the output of the polydisperse approach, it is possible to obtain acceptable degree of overlapping (TP values) between the polydisperse and monodisperse approaches (values between 83% and 98%). The TP values in this way can be seen as a degree of accuracy of the final results of an hypothetical PDC invasion map.

5.4.2 TITAN2D simulations

The major aim of the validation of the outputs of the TITAN2D code with real PDC deposits of SV was related to the fact that denser PDCs with more laminar flows (constituting both single eruptive units or part of them) cannot be realistically reproduced using the Box-Model code. The procedure of model validation (also in this case) involved the definition of the TP, TN and FP values (see section 5.2.4) for what concern inundation area validations, while the comparison between thickness values has been done comparing the thickness value of each stratigraphic section with the value of the TITAN2D output at that location.

Before discussing the validation outputs, two general consideration have to be done. Firstly, the importance of Digital Elevation Model (DEM) resolutions on TITAN2D model outputs has been recognized to have a certain effect, especially for DEM with resolutions such as 50 m or 90 m (Capra et

al. 2011; Stefanescu et al. 2012; Charbonnier et al. 2015). The DEM used for the simulations of this project derived from the 10 m resolution ones of Tarquini et al. (2007), scaled down to 20 m resolution in order to be uploaded in the online version of TITAN2D on Vhub. Such a resolution has been observed by Capra et al. (2011) to have a minor effect on numerical model outputs when compared to the outputs derived using a higher resolution DEM (i.e. 5 m resolution). However, the availability of extremely high resolution DEMs derived from LiDAR data (1 m resolutions) for the SV area might represent a future development for TITAN2D model outputs refinement, using an offline version of the TITAN2D code which allows to use higher resolution DEMs. A flaw of the TITAN2D outputs is related to the “thin-layer” problem (which is common to all the depth-averaged codes), that is the incapacity of the code to completely stops the flow. This happens, as discussed by Dalbey (2009), because velocity is typically computed as momentum (hu , hv ; see Appendix C) divided by flow depth h : numerical error in an already small h can therefore result in overly large velocities. As the already too fast flow moves into empty cells, the procedure of averaging further reduces flow depth and increases flow speed, cumulating in an “infinitely” fast, infinitesimally thin layer of material coating the domain. The thin-layer problem is not limited to the thinnest cells of the computational domains, since a flow of material at the limits of the computational domains affect also the adjacent cells: this is particularly evident in Figs. 5.12 and 5.13 and it will be discussed further on. This problem has been tentatively faced by introducing into the TITAN2D code a “Stopping criteria”, capable of setting at a certain point all the velocities to zero. This has been done by enabling a “Drag-based” stopping criteria, which evaluates whether the gravitational forces in the X and Y directions are lower than the sum of two other drag forces (the drag due to internal friction and the drag due to bed friction) or not. If so, TITAN2D assumes that the flow should physically stop by setting the velocities in the X and Y directions to zero. The “Drag-based” stopping criteria has been enabled for the simulations presented in Table 5.4, but the resulting outputs are identical with the outputs of the same simulations where this stopping criteria has been disabled. In this way, the end of the simulation (i.e. when the flow is completely at rest) is totally defined by the user, who has to set the total simulation time and calibrate it empirically. In order to illustrate the discrepancies within a single simulation at different timings, two snapshots for each of the two simulations which visually best fitted the real deposit (simulations ST3 and ST6, Figs. 5.12 and 5.13 and Table 5.4) have been chosen. Each of the two simulations have total

extrusion times of 600 s (10 min), and the two snapshots have been chosen at 11 min (1 min after the end of the extrusion) and 30 min (20 min after the end of the extrusion).

The two simulations which, at the end of the simulation time of 1800 s (30 min) better overlap with the actual deposit are the ST3 and ST6 ones (Table 5.4): the main difference between them is related to the value of the basal friction angle, which is 13° for ST3 and 15° for ST6. The value of the former is slightly lower with respect to the average value (15°) used from many authors for simulating PDCs (e.g. Capra et al. 2011; Kelfoun 2011). With respect to this latter point it should be noted that, although the Fg “Cupa Fontana” PDC lobe is certainly primarily a dense PDC with more laminar flow, it is true that at some locations lithofacies typical of a more dilute-like flow can be seen. Assuming a lower basal friction angle can be therefore explained as an effect due to a slight fluidization of the flow. Simulation ST3 (Fig. 5.12) at the end of the 30 minutes of the simulation shows the best TP value (71%) and a good FP value (overestimation - 9%), but the TN value (model underestimation) is moderately high (19%). After 11 minutes however the situation is sensibly different, with a lower TP value (53%) and an higher TN value (43%). Validation with respect to model and deposit thickness (in order to highlight discrepancies) has yielded contrasting results. As a general feature, simulation ST3 seems, on an average, to underestimate the thickness values of all the stratigraphic sections with a mean value of -35% percent (after 11 minutes) and -19% (after 30 minutes), with only 5 (after 11 minutes) or 4 (after 30 minutes) stratigraphic sections where the difference between the real deposit and the model output is less than +/- 10% (highlighted in yellow in Fig. 5.12). If we consider however only the more proximal sections (within a distance of less than 1.5 km, i.e. the stratigraphic sections where the densest and coarsest part of the flow deposited) or the more distal ones (where the finest and more turbulent-like part of the flow deposited), the situation is slightly different. The proximal sections involved are 16 (sections 28, 33, 37, 41, 43, 44, 119, 120, 123-125, 127-130, 137; see Fig. 5.12) and the distal ones are 7 (sections 121, 122, 126, 131-136, 138, 139; see Fig. 5.12). For the more proximal sections the mean difference between the model and the real deposit (after 30 minutes) is -28%, while after 11 minutes is -33%. At the more distal sections instead, the situation is much better (at least after 30 minutes), since the difference is -6%. Simulation ST6 instead (Fig. 5.13), shows slightly worse degree of overlapping (TP values) between the model output and the deposit, both after 11 minutes (46%) and after 30 minutes (57%). In the 11 minutes case moreover, the TN value (48%) is even higher with respect to the TN one. This latter one is sensibly high (30%) also after 30 minutes, while for both cases the FP values

are lower (5% after 11 minutes and 12% after 30 minutes). As for the ST3 simulation, also for the ST6 one the indicate a tendency of the model for the underestimation of the thicknesses of the stratigraphic sections (-27% and -30% for the 11 minutes and the 30 minutes snapshots respectively). Differences with respect to proximal and distal sections (the same employed for the ST3 simulation) describes an opposite situation with respect to the ST3 simulation: in this case in fact the discrepancy between model output and real deposit is sensibly low for proximal sections (+1% and -4% after 11 minutes and 30 minutes respectively), while it is higher for more distal ones (-60% and -67% after 11 minutes and 30 minutes respectively). Sections where the differences between the model and the true deposit are less than +/- 10% are only 1 (after 30 minutes), while none of them are found after 11 minutes. Therefore, simulation ST3 produce a better areal coverage of the deposit (better TP value) at least after 30 minutes of simulation, but simulation ST6 is more able to reproduce the same thicknesses of the deposit for the more proximal sections, which are representative of the densest and more laminar-like part of the flow.

As a conclusion for what concerns the TITAN2D code, the simulations performed have highlighted that in some instances at least the areal coverage of the deposit has been reproduced in a satisfactory way, although some uncertainties affect the final results. Particularly, better results are obtained when: a) basal friction angle is lower (13°) with respect to the normal range of value used in literature; b) the total simulated time is high (30 minutes), probably too high for the emplacement of a single PDC lobe. More studies are therefore needed to better constrain the range of values for basal friction angle (possibly considering some fluidization effects which are important even for denser PDCs) and implement new stopping criteria which does not force the user to arbitrarily define a total simulation time.

5.5 Conclusions

This Chapter aimed at providing reliable tools for evaluating the performances of numerical models while trying to reproduce actual PDCs from known eruptive units at SV (i.e. the EU3pf and EU4b/c unit from the AD 79 Pompeii eruption and the Fg “Cupa Fontana” PDC lobe from the AD 472 Pollena eruption). For this purpose two codes have been employed, in the attempt of reproducing the two main end members of the complex spectrum of PDCs, the dilute ones (with solid particle

concentrations φ_0 in the range 0.5%-5%) and the denser ones (with solid particle concentrations φ_0 greater than 10%). The former PDCs have been modeled using the Box-Model code, while the latter ones using the TITAN2D code. Performances of the PDC numerical models have been evaluated with their validation (in comparison of the parameters of the real deposits described in Chapter 4) with respect to the dispersal area, the thickness values and (for the Box-Model code only) the mass fractions of different grain sizes at different distances with respect to the eruptive vent location.

Simulations using the Box-Model code have been performed considering a polydisperse mixture with 10 grain sizes (the TGSD calculated in Chapter 4) and a monodisperse case where the $Md\phi$ value of the above-mentioned TGSD has been considered. Two different versions of the code have been employed, the first one which considers a direct approach (i.e. the collapsing mixture is released and the invasion area is computed accordingly) and an inverse version of the code (where the initial collapsing mixture is forced to invade an initially defined area). Different simulations have been done considering either axisymmetrical collapses or asymmetrical collapses, where the values of φ_0 (for all the simulations) and settling velocities (w_s – for the monodisperse simulations only) have been empirically calibrated. Results indicate that the best performances (i.e. the better validation values) have been obtained for the EU4b/c unit. The acceptable degree of matching (True Positive – TP value) between the output of the polydisperse simulation with a direct approach and the monodisperse one with the inverse approach (TP=93%) suggests the employment of the parameters of this eruptive unit for the development of PDC probabilistic map in the case of an axisymmetrical collapse after a Plinian eruption.

For the TITAN2D code simulations, results indicate that: a) best results for the simulations discussed (ST3 and ST6) indicate that the values of the basal friction angle is within the interval 13-15°; b) the absence of a reliable stopping criteria provides results subjected to a certain degree of uncertainty, since the timing of the simulation when the flow actually stops is obscure. At the moment, the employment of the TITAN2D code for the PDC hazard assessment for what concerns more dense-like PDCs has not been performed at SV.

Appendix A: derivation of Shallow water equations from Navier-Stokes equations

Let us consider the Navier-Stokes equation relative to the conservation of mass [1] and momentum [2]

$$\begin{cases} \frac{\partial}{\partial t} \rho + \nabla \cdot (\rho \vec{u}) = 0 \\ \frac{\partial}{\partial t} (\rho \vec{u}) + \nabla \cdot (\rho \vec{u} \otimes \vec{u} + PI - \vec{\tau}) - \rho \vec{g} = 0 \end{cases} \quad [1]$$

$$[2]$$

where $\vec{u} = \begin{pmatrix} u \\ v \\ w \end{pmatrix}$ velocity (m/s)

ρ = density of the fluid (kg/m³)

P = pressure (Pa)

$$I = \begin{bmatrix} 1 & 0 & 0 \\ 0 & 1 & 0 \\ 0 & 0 & 1 \end{bmatrix} \text{ Identity matrix}$$

$$\vec{\tau} = \begin{bmatrix} \tau_{xx} & \tau_{xy} & \tau_{xz} \\ \tau_{yx} & \tau_{yy} & \tau_{yz} \\ \tau_{zx} & \tau_{zy} & \tau_{zz} \end{bmatrix} \text{ stress tensor (Pa/m}^2\text{)}$$

\vec{g} = gravity acceleration (m/s²)

We introduce the approximation for incompressible fluids and $\vec{\tau} = 0$ (the second one is the condition for non-viscous fluid).

With these conditions equations [1] and [2] become

$$\begin{cases} \nabla \cdot \vec{u} = 0 \\ \frac{\partial}{\partial t} \vec{u} + \nabla \cdot \left(\vec{u} \otimes \vec{u} + \frac{1}{\rho} PI \right) - \vec{g} = 0 \end{cases} \quad [3]$$

$$[4]$$

which can be written into the scalar form

$$\begin{cases} \frac{\partial u}{\partial x} + \frac{\partial v}{\partial y} + \frac{\partial w}{\partial z} = 0 \end{cases} \quad [5]$$

$$\begin{cases} \frac{\partial u}{\partial t} + u \frac{\partial u}{\partial x} + v \frac{\partial u}{\partial y} + w \frac{\partial u}{\partial z} + \frac{1}{\rho} \frac{\partial P}{\partial x} = 0 \end{cases} \quad [6]$$

$$\begin{cases} \frac{\partial v}{\partial t} + u \frac{\partial v}{\partial x} + v \frac{\partial v}{\partial y} + w \frac{\partial v}{\partial z} + \frac{1}{\rho} \frac{\partial P}{\partial y} = 0 \end{cases} \quad [7]$$

$$\begin{cases} \frac{\partial w}{\partial t} + u \frac{\partial w}{\partial x} + v \frac{\partial w}{\partial y} + w \frac{\partial w}{\partial z} + \frac{1}{\rho} \frac{\partial P}{\partial z} = g \end{cases} \quad [8]$$

Let us consider now a PDC propagating on a substrate which is at an elevation b with respect to sea level, a thickness h and with a free upper surface $S=b+h$ (Fig. 5.14).

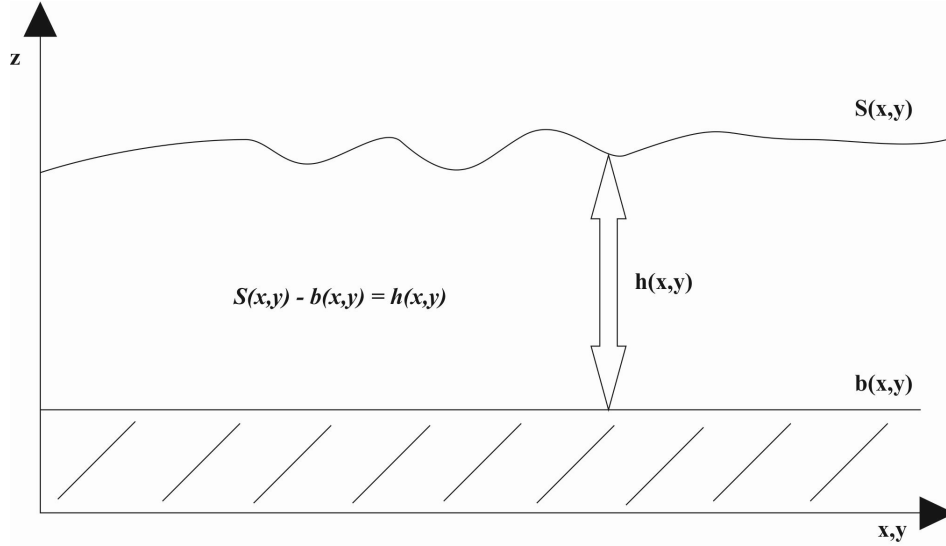


Fig. 5.14: schematic representation of a PDC in a 2D view.

Let us now consider boundary conditions for shallow water equations, for which no flux of mass occur across the basal surface and vertical acceleration at the two surfaces are zero:

Bottom: $\vec{v}_b \cdot \hat{n} = 0 \rightarrow u_b \frac{\partial b}{\partial x} + v_b \frac{\partial b}{\partial y} - w_b = 0$ [9]

Free upper surface: $\vec{v}_s = \frac{ds(x,y)}{dt} = \frac{\partial s(x,y)}{\partial t} + \frac{\partial s}{\partial x} \frac{\partial x}{\partial t} + \frac{\partial s}{\partial y} \frac{\partial y}{\partial t} = \frac{\partial s(x,y)}{\partial t} + \frac{\partial s}{\partial x} u_s + \frac{\partial s}{\partial y} v_s$ [10]

$\frac{\partial h}{\partial t} = w_s - \frac{\partial s}{\partial x} u_s - \frac{\partial s}{\partial y} v_s$ [11]

where \vec{v}_s and \vec{v}_b are velocities at the free surface and at the bottom of the flow respectively and \hat{n} is the versor normal to the lower boundary.

We furthermore introduce that vertical acceleration of different particles are negligible (hydrostatic pressure):

$$\frac{\partial w}{\partial t} = 0 \rightarrow P(z) = \rho g(b + h - z) + P_{atm}(b + h) \cong \rho g(s - z) \quad [12]$$

where we have considered variations in $P_{atm} = 0$.

Considering a flow in two dimensions (so we are not considering equation [8]) and by applying equation [12] to equations [6] and [7] we obtain

$$\left\{ \begin{array}{l} \frac{\partial u}{\partial x} + \frac{\partial v}{\partial y} + \frac{\partial w}{\partial z} = 0 \end{array} \right. \quad [13]$$

$$\left\{ \begin{array}{l} \frac{\partial u}{\partial t} + u \frac{\partial u}{\partial x} + v \frac{\partial u}{\partial y} + w \frac{\partial u}{\partial z} = -g \frac{\partial s}{\partial x} \end{array} \right. \quad [14]$$

$$\left\{ \begin{array}{l} \frac{\partial v}{\partial t} + u \frac{\partial v}{\partial x} + v \frac{\partial v}{\partial y} + w \frac{\partial v}{\partial z} = -g \frac{\partial s}{\partial y} \end{array} \right. \quad [15]$$

We now integrate all the above-reported equations along the z axis starting from equation [13]:

$$\int_b^s \left(\frac{\partial u}{\partial x} + \frac{\partial v}{\partial y} + \frac{\partial w}{\partial z} \right) dz = \int_b^s \frac{\partial u}{\partial x} dz + \int_b^s \frac{\partial v}{\partial y} dz + \int_b^s \frac{\partial w}{\partial z} dz \quad [16]$$

In order to solve this equation we first recall the Leibniz's formula for the differentiation under the integral sign

$$\frac{d}{dx} \int_\alpha^\beta f(x, y) dy = \int_\alpha^\beta \frac{\partial}{\partial x} f(x, y) dy + \frac{\partial \beta}{\partial x} f(\beta(x), x) - \frac{\partial \alpha}{\partial x} f(\alpha(x), x) \quad [17]$$

which is then applied to first and second term of equation [16], while the third term of the equation is simply $w_s - w_b$

$$\int_b^s \frac{\partial}{\partial x} u dz + u|_s \frac{\partial s}{\partial x} - u|_b \frac{\partial b}{\partial x} + \int_b^s \frac{\partial}{\partial y} v dz + v|_s \frac{\partial s}{\partial y} - v|_b \frac{\partial b}{\partial y} + w_s - w_b = 0 \quad [18]$$

Equation [18] can be rearranged (depth-averaging procedure) by considering that $\int_b^s u dz$ and $\int_b^s v dz$ are the average of u and v velocities along the thickness of the flow h ($h\bar{u}$ and $h\bar{v}$ respectively)

$$w_s - u|_s \frac{\partial s}{\partial x} - v|_s \frac{\partial s}{\partial y} + u|_b \frac{\partial b}{\partial x} + v|_b \frac{\partial b}{\partial y} - w_b + \frac{\partial h\bar{u}}{\partial x} + \frac{\partial h\bar{v}}{\partial y} = 0 \quad [19]$$

which, if we consider boundary conditions [9] and [11], can be finally written as

$$\frac{\partial h}{\partial t} + \frac{\partial h\bar{u}}{\partial x} + \frac{\partial h\bar{v}}{\partial y} = 0 \quad [20]$$

that represent the continuity equation.

Derivations of equations [14] and [15] are identical, so we will limit to the elements of equation [14]

$$\int_b^{b+h} \frac{\partial u}{\partial t} dz = \frac{\partial}{\partial t} \int_b^{b+h} u dz + u|_{b+h} \frac{\partial h}{\partial t} - u|_b \frac{\partial b}{\partial t} \quad [21]$$

$$\int_b^{b+h} u \frac{\partial u}{\partial x} dz = \int_b^{b+h} \frac{\partial}{\partial x} (u^2) dz = \frac{\partial}{\partial x} (h\bar{u}^2) + u^2|_{b+h} \frac{\partial(b+h)}{\partial x} - u^2|_b \frac{\partial b}{\partial x} \quad [22]$$

$$\int_b^{b+h} v \frac{\partial u}{\partial y} dz = \frac{\partial}{\partial y} (h\bar{u}\bar{v}) + uv|_{b+h} \frac{\partial(b+h)}{\partial y} - uv|_b \frac{\partial b}{\partial y} \quad [23]$$

$$\int_b^{b+h} w \frac{\partial u}{\partial z} dz = (uw)|_{(b+h)} - (uw)|_b \quad [24]$$

$$\int_b^{b+h} -g \frac{\partial(b+h)}{\partial x} dz = -g \frac{\partial(b+h)}{\partial x} h = -gh \frac{\partial h}{\partial x} - gh \frac{\partial b}{\partial x} = -g \frac{\partial}{\partial x} \left(\frac{h^2}{2} \right) - gh \frac{\partial b}{\partial x} \quad [25]$$

We can delete the third term of eq. [21] by recalling the boundary conditions.

Combining equations [21] through [25], equation [14] (which can be simply called MOM_x , that is equation for momentum conservation along the x axis) integrated along the z axis becomes

$$\begin{aligned} \int_b^{b+h} \{MOM_x\} dz = & \frac{\partial}{\partial t} (h\bar{u}) + u|_{b+h} \frac{\partial(b+h)}{\partial t} + \frac{\partial}{\partial x} (h\bar{u}^2) + u^2|_{b+h} \frac{\partial(b+h)}{\partial x} - u^2|_b \frac{\partial b}{\partial x} + \frac{\partial}{\partial y} (h\bar{u}\bar{v}) + \\ & \bar{u}\bar{v}|_{b+h} \frac{\partial(b+h)}{\partial y} - \bar{u}\bar{v}|_b \frac{\partial b}{\partial y} + uw|_{b+h} - uw|_b = -g \frac{\partial}{\partial x} \left(\frac{h^2}{2} \right) - gh \frac{\partial b}{\partial x} \end{aligned} \quad [26]$$

which can be simplified by considering that the 2°, 4°, 7° and 9° terms on the left hand-side of the equation are equal to zero, and that the 5°, 8° and 10° terms always on the left hand-side of the equation are equal to zero too (these elements grouped together represent the boundary conditions of equations [9] and [10]).

Equation [15] can be integrated in the same way, leading to the definition of the three shallow water equations for 2D incompressible and non-viscous fluids

$$\left\{ \begin{array}{l} \frac{\partial h}{\partial t} + \frac{\partial h\bar{u}}{\partial x} + \frac{\partial h\bar{v}}{\partial y} = 0 \end{array} \right. \quad [27]$$

$$\left\{ \begin{array}{l} \frac{\partial(h\bar{u})}{\partial t} + \frac{\partial(h\bar{u}^2)}{\partial x} + \frac{\partial(h\bar{u}\bar{v})}{\partial y} = -g \frac{\partial}{\partial x} \left(\frac{h^2}{2} \right) - gh \frac{\partial b}{\partial x} \end{array} \right. \quad [28]$$

$$\left\{ \begin{array}{l} \frac{\partial(h\bar{v})}{\partial t} + \frac{\partial(h\bar{u}\bar{v})}{\partial y} + \frac{\partial(h\bar{v}^2)}{\partial x} = -g \frac{\partial}{\partial y} \left(\frac{h^2}{2} \right) - gh \frac{\partial b}{\partial y} \end{array} \right. \quad [29]$$

Appendix B: the Box-Model equations

The equations at the basis of the Box-Model code requires that it is considered a) the conservation of momentum, b) the conservation of mass and c) an equation representing the particle sedimentation. These three equations can be summarized, in the case of a polydisperse mixture of n classes of particles, as

$$\left\{ \begin{array}{l} u = \frac{dl}{dt} = Fr(g_p \phi h)^{1/2} \end{array} \right. \quad [1]$$

$$\left\{ \begin{array}{l} l^2 h = V \end{array} \right. \quad [2]$$

$$\left\{ \begin{array}{l} \frac{d\Phi}{dt} = - \sum_{i=1}^n \frac{w_{si} \Phi_i}{h} \end{array} \right. \quad [3]$$

where Fr is the Froude number, g_p the reduced gravity, ϕ the volume fraction of all the particles in the flow, V the volume of collapsing mixture divided by π , w_{si} the settling velocity of the i -esimal particle class and ϕ_i the volume fraction of the i -esimal particle class.

Equation [1] represent a simplified form of the conservation of momentum equation, with the ratio between the inertial forces (represented by u) and the buoyancy forces (represented by $(g_p \phi h)^{1/2}$) that equals the value of the Froude number (Fr). Roche et al. (2013) reminds that for a current flowing into deep surroundings ($h \ll$ height of the surroundings), Fr is a constant with a theoretical value of $\sqrt{2}$ (Von Karman 1940). The reduced gravity g_p for a current of density ρ_c is instead presented in the form

$$g_p = g \frac{\rho_c - \rho_0}{\rho_{ref}} \quad [4]$$

where g is the acceleration due to gravity, ρ_0 is the density of the surrounding fluids and ρ_{ref} is a reference density. When the density of the current and the density of the surroundings are not very different in magnitude (i.e. in fully-dilute PDCs), $\rho_{ref} = \rho_0$ (Roche et al. 2013).

Equation [2] represents a simplified version of the conservation of mass equation while equation [3] represents the particle sedimentation. Bevilacqua (2016) has shown how the equations [1] through [3] can be solved in the case of a monodisperse mixture, and in the case of a polydisperse one it can be proved that

$$l(t) = \left[\tanh \left(\frac{2t}{Fr^{-1}(g_p \Phi_0 V)^{-1/2}} \right) \right]^{1/2} l_{max} \quad [5]$$

where Φ_0 is the initial volume concentration of all the particles in the mixture, and l_{max} is the maximum distance reached by the flow (i.e. the PDC run-out). This latter parameter, always following Bevilacqua (2016), for a polydisperse case with n classes of particles can be calculated through the equation

$$l_{max} = \left(8 \cdot \sum_{i=1}^n \frac{\Phi_{0i}^{1/2}}{w_{si}} \cdot g_p^{1/2} \cdot V^{2/3} \cdot Fr \right)^{1/4} \quad [6]$$

As shown by Bevilacqua (2016), the ‘box model’ approximation permits a first approximation of the kinetic energy of the front of the flow as a function of the distance l ; the comparison of the kinetic energy with the potential energy associated to overcoming topographical barriers (neglecting hydraulic effects associated with flow-obstacle interactions) is therefore

$$\frac{1}{2} u^2 = gH \quad [7]$$

where H is the height of the obstacle and u the velocity of the flow front.

By applying equation [5] to equation [7], it is possible to derive an expression for $u(l)$ and therefore the expression for H for a polydisperse case with n classes of particles

$$H = \frac{1}{2g} \left[\frac{\left(\frac{(Fr^2 \sum_{i=1}^n (w_{si} \Phi_i) g_p l_{max}^{1/3})^{1/3}}{2} \right)^2}{\frac{l}{l_{max}} \cosh^2 \arctanh \left(\frac{l}{l_{max}} \right)^2} \right]^2 \quad [8]$$

From equation [8] it is possible to derive the function named “C” by Bevilacqua (2016) used for the comparison with the potential energy, which is (for a monodisperse case but easily extendible for a polydisperse one):

$$C = \frac{(Fr^2 w_s \phi_0 g_p)^{1/3}}{2} \quad [9]$$

Appendix C: the TITAN2D equations

With respect to the shallow water equations derived in Appendix 1, the governing equations for the TITAN2D code are applied in the case where viscous stresses are considered (i.e. $\vec{\tau} \neq 0$). The original code considers boundary conditions for the stresses which are stress-free condition at the free surface and a Coulomb-like friction law imposed at the interface between the granular flow and the basal surface (Patra et al. 2005). With respect to equations [27] through [29] from Appendix 1, the new equations (which consider also the viscous stress with the boundary conditions described above) can be extended and written as:

$$\begin{cases} \frac{\partial h}{\partial t} + \frac{\partial h\bar{u}}{\partial x} + \frac{\partial h\bar{v}}{\partial y} = 0 \end{cases} \quad [1]$$

$$\begin{cases} \frac{\partial(h\bar{u})}{\partial t} + \frac{\partial(h\bar{u}^2)}{\partial x} + \frac{\partial(h\bar{u}\bar{v})}{\partial y} = - \left[\frac{\partial\tau_{xx}}{\partial x} + \frac{\partial\tau_{yx}}{\partial y} + \frac{\partial\tau_{zx}}{\partial z} \right] - g \frac{\partial}{\partial x} \left(\frac{h^2}{2} \right) - gh \frac{\partial b}{\partial x} \end{cases} \quad [2]$$

$$\begin{cases} \frac{\partial(h\bar{v})}{\partial t} + \frac{\partial(h\bar{u}\bar{v})}{\partial y} + \frac{\partial(h\bar{v}^2)}{\partial x} = - \left[\frac{\partial\tau_{yy}}{\partial y} + \frac{\partial\tau_{xy}}{\partial x} + \frac{\partial\tau_{zy}}{\partial z} \right] - g \frac{\partial}{\partial y} \left(\frac{h^2}{2} \right) - gh \frac{\partial b}{\partial y} \end{cases} \quad [3]$$

Following Patra et al. (2005), the constitutive models for the stress tensor assume (using the Mohr-Coulomb theory) that the normal stresses τ_{xx} and τ_{yy} can be related to the normal stress τ_{zz} (which in turn is $\tau_{zz}=(\rho g_z h)/2$) by using a lateral stress coefficient k_{ap} so that:

$$\tau_{xx} = \tau_{yy} = k_{ap} \tau_{zz}$$

The subscript “ap” from the k_{ap} coefficient (sometimes referred as “earth pressure coefficient”; Kelfoun 2011) stands for “active/passive” and identifies two situations when the material is under elongation (active) or compression (passive). Savage and Hutter (1989) and Iverson and Denlinger (2001) have shown (using the Mohr diagram) that the earth pressure coefficient is related to the internal (ϕ_{int}) and bed (ϕ_{bed}) friction angles through the relation

$$k_{ap} = 2 \cdot \frac{1 \pm [1 - \cos^2 \varphi_{int} (1 + \tan^2 \varphi_{bed})]^{1/2}}{\cos^2 \varphi_{int}} \quad [4]$$

in which “-“ stands for the active state and “+” for the passive case.

Patra et al. (2005) also provide the relations for the other components of the stress tensor, which are:

$$\begin{cases} \tau_{xy} = \tau_{yx} = -sgn \frac{\partial \bar{u}}{\partial y} \times \frac{1}{2} k_{ap} \rho g_z h \sin \varphi_{int} \end{cases} \quad [5]$$

$$\begin{cases} \tau_{zx} = -\frac{\bar{u}}{\sqrt{\bar{u}^2 + \bar{v}^2}} \left[\rho g_z h \left(1 + \frac{\bar{u}}{r_x g_z} \right) \right] \times \tan \varphi_{bed} \end{cases} \quad [6]$$

$$\begin{cases} \tau_{zy} = -\frac{\bar{v}}{\sqrt{\bar{u}^2 + \bar{v}^2}} \left[\rho g_z h \left(1 + \frac{\bar{v}}{r_y g_z} \right) \right] \times \tan \varphi_{bed} \end{cases} \quad [7]$$

where r_x and r_y are the radii of local bed curvature along the x and y axes respectively.

By substituting equations [4] to [7] into equations [2] and [3] it is possible to obtain the governing equations used by the TITAN2D code, which (including equation [1]) assumes the vector form (Denlinger and Iverson 2004):

$$\frac{\partial}{\partial t} (\vec{U}) + \frac{\partial}{\partial x} (\vec{F}(\vec{U})) + \frac{\partial}{\partial y} (\vec{G}(\vec{U})) = \vec{S}(\vec{U}) \quad [8]$$

The terms of equation [8] are, respectively:

$$\vec{U} = \begin{bmatrix} h \\ hu \\ hv \end{bmatrix}$$

which represents the vector of conserved variables (h is the flow depth, hu and hv are the momentums in the x and y directions respectively);

$$\vec{F}(\vec{U}) = \begin{bmatrix} hu \\ hu^2 + \frac{1}{2} k_{ap} g_z h^2 \\ huv \end{bmatrix}$$

which represents the vector of mass and momentum fluxes in the x direction (hu is the mass flux, $hu^2 + \frac{1}{2} k_{ap} g_z h^2$ is the x-momentum flux in the x direction and huv is the y-momentum flux in the x direction);

$$\vec{G}(\vec{U}) = \begin{bmatrix} hv \\ huv \\ hv^2 + \frac{1}{2} k_{ap} g_z h^2 \end{bmatrix}$$

which represents the vector of mass and momentum fluxes in the y direction (hv is the mass flux, huv is the x-momentum flux in the y direction and $hv^2 + \frac{1}{2}k_{ap}g_z h^2$ is the y-momentum flux in the y direction);

$$\vec{S}(\vec{U}) = \begin{bmatrix} 0 \\ g_x h - hk_{ap} \operatorname{sgn}\left(\frac{\partial u}{\partial y}\right) \frac{\partial}{\partial y}(g_z h) \sin \varphi_{int} - \frac{u}{\sqrt{u^2 + v^2}} \max\left(g_z + \frac{u^2}{r_x}, 0\right) h \tan \varphi_{bed} \\ g_y h - hk_{ap} \operatorname{sgn}\left(\frac{\partial v}{\partial x}\right) \frac{\partial}{\partial x}(g_z h) \sin \varphi_{int} - \frac{v}{\sqrt{u^2 + v^2}} \max\left(g_z + \frac{v^2}{r_y}, 0\right) h \tan \varphi_{bed} \end{bmatrix}$$

which represents the vector of dissipative forces ($g_x h$ is the driving gravitational force in the x direction, $-hk_{ap} \operatorname{sgn}\left(\frac{\partial u}{\partial y}\right) \frac{\partial}{\partial y}(g_z h) \sin \varphi_{int}$ is the dissipative internal frictional force in the x direction and $-\frac{u}{\sqrt{u^2 + v^2}} \max\left(g_z + \frac{u^2}{r_x}, 0\right) h \tan \varphi_{bed}$ is the dissipative basal frictional force in the x direction; same meanings for the terms of the third equation along the y direction).

Chapter 6

Pyroclastic Density Currents invasion maps

6.1 Introduction

PDC hazard assessment needs to rely on the most updated possible scenarios (leading to different propagation paths for PDCs), which at SV, as discussed in Chapter 4, depends on, among other factors, the geometry of the collapse area, the interaction with the topography and the partition of fines/coarse particles due to the effect of wind. Moreover, variable vent opening positions (Chapter 3) and approximations of numerical model when reproducing PDCs (Chapter 5) add more complexity and uncertainty to this task. Despite these limits, the high number of people directly threatened and the considerable amount of elements at risk in the Red Zone area (Zuccaro and De Gregorio 2013) claim for a deep investigation of the problem. To the author's knowledge, the only effort so far aimed at producing a first PDC probabilistic invasion map for SV has been put forward by Tierz et al. (2016): in their approach, the Energy Cone model has been adopted. The outputs of this simple model have been validated (with respect to maximum runouts and inundation areas) using field data of PDC deposits from Gurioli et al. (2010) and Probability Density Functions (representing the aleatoric uncertainty of the system) have been defined for the two parameters of the energy cone model, the collapse height and the angle of the energy line. Main result of this first map is the identification of an area with high PDC-arrival frequencies over an ~8-km radius from the present crater area at SV.

This final Chapter aims at constituting a first PDC probabilistic invasion map for the SV area, that combines all the achievements described in previous Chapters and quantifies the degree of uncertainty and unknown variables, which might affect the reliability of the final product. Due to the complexities of PDC phenomena and the poorly reproduced dynamics of some aspects of PDC (e.g. the interaction with proximal topography), the preliminary map presented here is referred to a specific scenario, represented by an axisymmetrical collapse of an eruptive column on the order of magnitude of a Plinian eruption. According to the values defined by Neri et al. (2008) about the different probabilities about the type of the next eruption at SV, Plinian eruptions represent only the 4% of probability of occurrence. The maps presented here thus accounts only for a limited scenario at SV, and

moreover the complex effects related to asymmetrical collapses or wind effects are not considered here. This attempt represents however one of the first attempt at SV, and possibly a starting point for more complex and more inclusive studies that aim at providing a tool for better evaluating the PDC hazard and quantify the risk for the SV area. In this Chapter the approach adopted by Neri et al. (2015) and Bevilacqua (2016) for PDC hazard assessment at the Campi Flegrei area (with whom this project is strongly linked) is described and applied at the SV case. Due to the sensitivity of this topic, it should be pointed out that the maps or considerations proposed here does not necessarily represent official views and policies of the Dipartimento della Protezione Civile or local authorities.

6.2 Methods

The approach adopted by Neri et al. (2015) and Bevilacqua (2016) and here applied to the SV case integrates i) field data about PDC runout outlines related to the AD 79 Pompeii Plinian eruption, ii) information on the distribution of the spatial probability of vent opening (Chapter 3) and iii) the results from a simplified PDC flow invasion model (i.e. the Box-Model code, see Chapter 5). As for the vent opening probability maps (Chapter 3), the procedure creates maps of PDC invasion in terms of a mean value and of representative percentiles with respect to the uncertainty sources considered (5th and 95th). With the location of the eruptive vent determined and the value of the area to be invaded by the flow defined, the simulation of a single PDC propagation event associates a value of 1 to those zones reached by the flow, and 0 otherwise. Therefore, by repeating the simulation of a single PDC, a large number of times randomly changing vent location and inundation area, and then aggregating the zone 0/1 values obtained to estimate their means, it is possible to approximate, by the law of large numbers, the probability that each location of the map is reached by a PDC conditional on the occurrence of an explosive eruption (Bevilacqua 2016).

6.3 Results and Discussion

6.3.1 Input parameters

With respect to the aleatoric uncertainty defined by different past PDC inundation areas, for the SV case the amount of Plinian and sub-Plinian eruptions for which considerable PDCs occurred (see

section 8.3) is quite limited. On the other side for each of the 7 Plinian and sub-Plinian I eruptions at SV, a triplet of PDC inundation areas (the 5th, Modal and 95th percentiles) is provided: for the preliminary maps, the values of PDC inundation areas defined by the EU4b unit of the AD 79 Pompeii eruption have been adopted. The Monte Carlo sampling therefore was run for 1000 times, and for each sampling it was chosen a site for the volcanic vent (from the triplet of vent opening probability maps with caldera enlargement from Fig. 3.10, see Chapter 3) and a value of inundation area from the triplet of Table 4.3 (values of the EU4b unit). The version of the Box-Model code employed is the monodisperse inverse one described in Chapter 5, with the values of $Md\phi$ and w_s stored in Table 5.3. This version has been shown to reproduce the inundation area of its polydisperse direct counterpart with a degree of accuracy (i.e. the True Positive value between the two outputs) of 93%. As a comparison, a PDC probabilistic invasion map has also been produced considering a fixed position of the vent correspondent the centroid of the crater of the present edifice.

6.3.2 PDC invasion map

The two above-mentioned set of PDC probability maps are displayed in Fig. 6.1, with the set of maps where both the vent position and the inundation area varies (Fig. 6.1a) and the one where only the latter one vary (Fig. 6.1b). Both the two versions have been superimposed on the present outline of the Red Zone (DPC 2014) and the municipality boundaries of the circum-vesuvian area.

These maps allow to discuss some preliminary considerations. First of all, one of the main evidence of the maps is the fact that the variation of vent position does not seem to affect significantly the PDC dispersal area in this specific case. Differences between the position of contour lines from Fig. 6.1a (i.e. lines that enclose cells with higher percentages) are in fact minimal. The comparison with the PDC invasion maps where vent position is coincident with the centroid of the present edifice (Fig. 6.1b) furthermore confirms this trend. With respect to this latter triplets of maps it should be noted how different probabilities of invasion are (for the 5th and 95th percentile maps) only either 0% or 100%, while for the mean map the values are more smoothed at the limits of the inundation area. With respect to these latter triplets of maps it should be noted how different probabilities of invasion are (for the 5th and 95th percentile maps) only either 0% or 100%, while for the mean map the values are more smoothed at the limits of the inundation area. This is due to the fact that in this much simplified case,

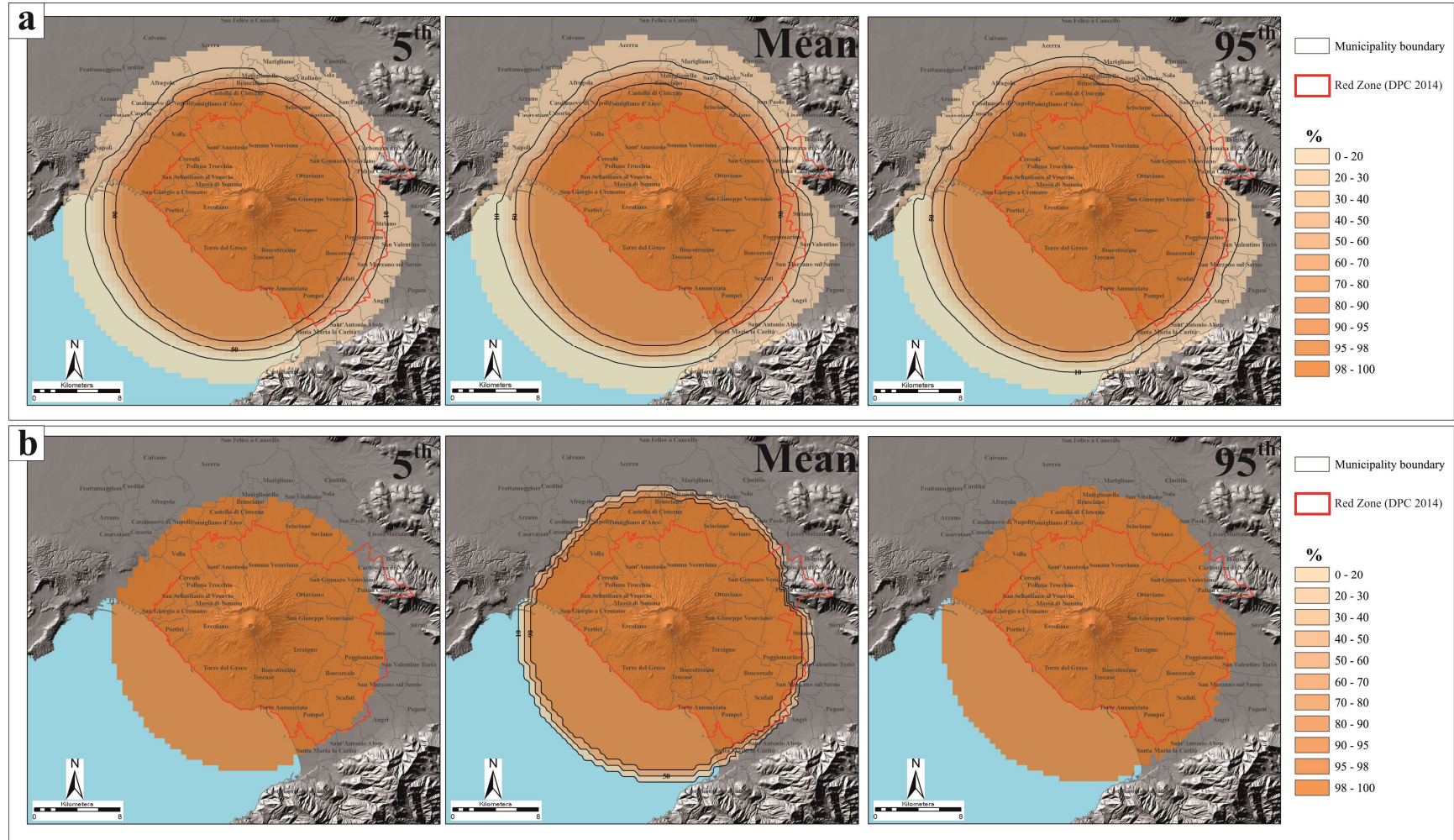


Fig. 6.1: a) PDC probability invasion maps computed by considering the Vent Opening probability maps of Fig. 3.10a (Chapter 3) and the three values of invasion areas relative to the EU4b unit (see Table 4.3 from Chapter 4); b) PDC probability invasion maps computed by considering the vent location fixed in the centroid of the present crater of the Gran Cono edifice, with varying invasion areas corresponding to the values of the unit EU4b from Table 4.3 (Chapter 4).

the map of vent opening location is 100% concentrated in one cell – so none the percentile maps can include intermediate values.

A general consideration with respect to invasion areas is the fact that, if no other sources of interference with PDC dispersal is considered (i.e. wind effects or asymmetrical collapse), a total of 63 municipalities would be involved (partially or totally) with PDC invasion in the case of a Plinian eruption (considering all the three maps of Fig. 6.1a). Among these municipalities, the ones which would be totally invaded (probabilities, in the mean map, greater than 98%) are 17. With respect to the Red Zone outline it should be noted how (despite the fact that this latter one has been targeted to a sub-Plinian I event), there are still some areas that hardly can be invaded even in the case of a Plinian eruption: these correspond to the NE tip of the Palma Campana municipality (located within a small valley). All the remaining municipalities within the Red Zone could be affected by PDC with various probabilities. Notably, the portion of the municipality of Napoli affected by PDCs in this specific case would be greater with respect to the part enclosed by the Red Zone outline.

As specified before, these preliminary maps account only for a very specific case of PDC development, and they could not be taken as reference scenario for a PDC probabilistic invasion map that consider all the possibilities of PDC propagation after both a Plinian or sub-Plinian I eruption (like the vent opening probability maps described in Chapter 3). However, as it has been shown throughout all this thesis for similar issues (i.e. the vent opening probability maps), two approaches can be envisaged for the future developments of PDC probabilistic invasion maps.

The first one involves the calculation of a probability density function for values the invasion areas described for the 7 major Plinian and sub-Plinian I eruptions: the Montecarlo sampling would then be related to this latter function when calculating the PDC probabilistic invasion map.

The second approach instead considers a linear combination of different PDC probability invasion maps, each of them targeted to a specific scenario. In this case, possible scenarios for column collapses (leading to PDC formation and propagation) that have been so far considered (see Chapter 4) include: a) an axisymmetrical collapse, b) an asymmetrical collapse (for instance, due to differential caldera collapses), c) an axisymmetrical collapse where proximal topography plays a role in PDC dispersal area (in the case of sub-Plinian I eruptions where vent position is located far from the Mount Somma scarp to the N), d) an axisymmetrical/asymmetrical collapse where wind plays a role in partitioning fine-grained particles (therefore enhancing PDC mobility toward downwind sectors). If the Box-Model code would be employed for these future developments, first of all it would be more desirable (as shown in Chapter 5) to employ the polydisperse direct version of the code, as the

calibration of the more uncertain parameters is less subjective. Secondly, variations to the outputs of the Box-Model code should be applied if the above-mentioned scenarios would be considered. For the case of scenarios b) and d) a possible solution might be represented by the application of a “stretching” coefficient to the output of an axisymmetrical collapse simulation. The stretching is basically a geometrical element which stretches the whole simulation output toward a certain direction at a certain degree. For the case where wind might play a role in PDCs dispersal (case d), the direction of stretching and its degree might be sampled (with a Montecarlo approach) from, respectively, wind directions and speeds defined by Macedonio et al. (2016). For the case where an asymmetrical collapse due to differential caldera collapse is considered (case b), it is instead more difficult to estimate these parameters: the simplest assumption is to consider the direction of asymmetrical collapse (and therefore stretching) uniformly distributed toward all the directions, while the degree of stretching might be considered equal toward all the directions with a fixed empirical value. Finally, for the case where the proximal topography of the N Mount Somma scarp might influence PDC dispersal area (case c), a possibility might be to impose (during the Montecarlo sampling from the vent opening probability maps from Chapter 3) that: i) if the vent position is sampled close to the Mount Somma scarp (e.g. from Sector B from Fig. 1.2b) then all the collapsing volume is spread axisymmetrically; ii) if the vent is sampled somewhere else within the SV caldera then all the collapsing volume is forced to collapse only toward S (reproducing in this way the shielding toward N sector exerted by the Mount Somma scarp). The final, critical step of this procedure would be the definition of the relative probability of occurrences of these different scenarios, in order to define proper weights to be assigned for linear combination. A final elicitation session could be a possibility for this extremely difficult task, where the possibility that other scenarios not considered so far might be raised as well.

6.4 Conclusions

This Chapter briefly describe a possible output of a PDC hazard assessment at SV through the development of a preliminary PDC probabilistic invasion map (targeted to a Plinian eruption with an axisymmetrical eruptive column collapse) with variable vent position (according to the vent opening probability maps described in Chapter 3) and variable values of PDC inundation areas (defined by maximum runout outlines described in Chapter 4). Input parameters have been derived using volumes,

maximum runout outlines and Total-Grain Size Distributions from the EU4b/c unit from the AD 79 “Pompeii” Plinian eruption: these parameters and the Box-Model monodisperse code with the inverse formulation have been tested in Chapter 5, providing a degree of accuracy with its polydisperse counterpart (i.e. the percentage of overlapping between the outputs of the two codes) of 93%.

The set of maps presented here (although not representing any official views of civil protection authorities) allowed to draw some considerations about municipalities possibly involved by PDC inundation and allowed a comparison with respect to the Red Zone outline (i.e. the area subjected to PDC invasion according to the latest emergency plan of SV area). Finally, some ideas have been proposed in order to obtain a PDC probabilistic invasion maps that considers other possible scenarios that could lead to PDC formation and propagation.

Chapter 7

Conclusions

7.1 Main conclusions and achievements

This 3-years long project led to the development of three important products aimed at volcanic hazard assessment in the Somma-Vesuvio area, which are:

- a geo-database including the distribution of past volcanic activity and main structural features;
- a set of vent opening probability maps;
- a preliminary PDC probabilistic invasion map;

In general, this project provided methodology procedures that could be extended to other volcanological case studies. In particular it is here presented: a) a methodology for the development of a probabilistic vent map for a caldera-forming volcano; b) the development and application of methods for volume and total grain size distribution from PDC deposits; c) an integrated use of dense and dilute PDC models and validation against field data. This study provides moreover a contribution to the volcanic hazard assessment from the point of view of PDC inundation areas by identifying different types of column collapse scenarios and possible developments of PDC probabilistic invasion maps that take into account such scenarios.

More precisely, the main objectives achieved include:

- The datasets which compose the geo-database quantify the spatial uncertainty (which encompass their positional imprecision) through the use of uncertainty areas drawn around the variables. This feature reflects quantitatively the intrinsic uncertainty due, on one side, to a lack of complete, detailed knowledge of past events (i.e. epistemic uncertainty) and, on the other, to the unpredictable variability of the dynamics of the system (i.e. aleatoric or physical variability).
- The first long-term vent opening probability maps for the summit caldera of the Somma-Vesuvio (SV) volcanic complex related to the case that next eruption will be Plinian or sub-

Plinian. Main results include: a) the realization of continuous probability density functions based on symmetrical Gaussian kernels, for each single dataset/variable selected from data displayed in Chapter 2, with the definition of appropriate bandwidths for each kernel; b) the definition of weights to be assigned to alternative probability maps when linearly combined, based on performance based expert judgment techniques aimed at uncertainty quantification on the final vent opening maps probability density values; c) the comparison of different experts' scoring methods, different sub-groups of experts with different backgrounds and expertise and sub-groups of volcanological features (i.e. maps without deep faults contribution). Quantitative outcomes of the work indicate that there is at least 6% of probability that next Plinian/sub-Plinian eruption will have its initial vent located outside the present outline of the caldera. Secondly, considering different caldera sectors, there is less than 50% of probability that next eruption will start in the area of the present edifice (Gran Cono), while there is a significant probability (almost 30%) that the western portion of the SV caldera ("Piano delle Ginestre" area) will host the next vent opening of a Plinian/sub-Plinian eruption. Caldera enlargement probability due to a Plinian eruption has been evaluated as well, and results indicate that, considering a 9.5% mean probability that next eruption will be a Plinian one, there is 2.4% mean probability that SV will enlarge, mostly concentrated toward N/NE (1.0%).

- Regarding the definition of input parameters derived from eruptive units and PDC lobes, besides the definition of the maximum runouts, volume and Total Grain Size distributions for the EU3pf, EU4 and Fg "Cupa Fontana" lobe, some interpretations about the mobility of PDCs with respect to the volcanic plume collapse have been done. Particularly: i) the EU3pf unit was probably emplaced after an axisymmetrical collapse, but the strong wind at the time of the eruption partitioned the finer-grained particles toward the direction of wind blowing, enhancing PDC mobility and maximum runout toward that direction; ii) the EU4 unit featured instead a probable asymmetrical collapse of the eruptive column, which caused the more coarse grained particles to be partitioned toward the N and NW. Finer-grained particles of the EU4 unit were instead forced toward the direction of wind blowing, with the same implications described for the EU3pf unit; iii) the effect of the pre-existing Mt. Somma scarp to the N does not seem to have influenced the partitioning of fine/coarse particles.

- Numerical simulations using the Box-Model code have been performed considering a polydisperse mixture with 10 grain sizes (the TGSD calculated in Chapter 4) and a monodisperse case where the $Md\phi$ value of the above-mentioned TGSD has been considered. Two different versions of the code have been employed, the first one which considers a direct approach (i.e. the collapsing mixture is released and the invasion area is computed accordingly) and an inverse version of the code (where the initial collapsing mixture is forced to invade an initially defined area). Different simulations have been done considering either axisymmetrical collapses or asymmetrical collapses, where the values of ϕ_0 (for all the simulations) and settling velocities (w_s – for the monodisperse simulations only) have been empirically calibrated. Results indicate that the best performances (i.e. the better validation values) have been obtained for the EU4b/c unit, which suggests the employment of the parameters of this eruptive unit for the development of PDC probabilistic map in the case of an axisymmetrical collapse after a Plinian eruption. For the TITAN2D code simulations, results indicate that the code is capable of capturing the general trend of the deposits (inundation areas and thicknesses), although at this stage no PDC hazard assessments have been done at SV for these type of flows using this code.
- Finally, this thesis presents a preliminary PDC probabilistic invasion map (targeted to a Plinian eruption with an axisymmetrical eruptive column collapse) with variable vent position (according to the vent opening probability maps described in Chapter 3) and variable values of PDC inundation areas (defined by maximum runout outlines described in Chapter 4). The set of maps presented here (although not representing any official views of civil protection authorities) allowed to draw some considerations about municipalities possibly involved by PDC inundation and allowed a comparison with respect to the Red Zone outline (i.e. the area subjected to PDC invasion according to the latest emergency plan of SV area).

7.2 Open questions and future perspectives

This PhD project has brought new perspectives and important results from the point of view of PDC hazard assessments, along with many possible future developments of key aspects of this complex

issue. More in detail, divided by different research topics, this project has indicated as possible developments:

- The SV geodatabase has several possible developments toward the definition of a comprehensive geo-database of all the related aspects of SV which would include: a) the datasets of Chapter 2; b) the isopaches of PDCs described in Chapters 4 and 8 along with some isopaches described in Gurioli et al. (2010); c) the isopaches of fallout deposits from different eruptions at SV, retrievable from the vast bibliography on that topic; d) the remaining datasets described in Chapter 8 (dikes, subsurface structures, seismic activity, CO₂ emissions).
- The vent opening probability maps issue has highlighted that, according to the experts' opinion, the probability of initial vent openings outside the present outline of the SV caldera is not negligible, on the order of 6-10% of probability. This future research topic is surely challenging, and some possible developments have been proposed (closed conduit and open conduit conditions).
- Field data have highlighted how the present amount of sample analyses for both the EU3pf and the EU4 units, in some cases might have led to some underestimations, especially with respect to TGSD estimations. Particularly, for the EU3pf unit some samples are missing for some parts of the N and of the S sectors, while for the EU4 unit some more distal samples in the NW sector might help in confirming the tendency of this sector to feature more coarse-grained particles. It should however be pointed out that, with respect to this latter unit, the high urbanization of the NW sector might prevent sample collection.
- Numerical model outputs have shown how, with respect to the Box-Model code, more precise estimations with respect to the amount of material that is not deposited in the final output due to truncations might help in quantifying this source of uncertainty. With respect to the TITAN2D code instead, it has been highlighted how the employment of DEMs of higher resolutions might slightly improve the final outputs of the simulations, although the main research topic regarding this code is the need for the implementation of more reliable stopping criteria.

- Possibilities for the development of a comprehensive PDC probabilistic invasion map have been proposed. These include i) the identification of different scenarios that could lead to different PDC dispersal areas (asymmetrical collapses, wind effects, proximal topographic barriers); ii) the implementation of a probability density function that takes into account the uncertainty in PDC dispersal area of known eruptions at SV.

Chapter 8

Supporting information

8.1 Accessory datasets for SV geo-database

8.1.1 Dikes or tabular intrusions

At SV, dikes (Fig. 8.1) are presently exposed in limited sectors of the area, namely along the south-facing wall of the northern Mount Somma scarp.

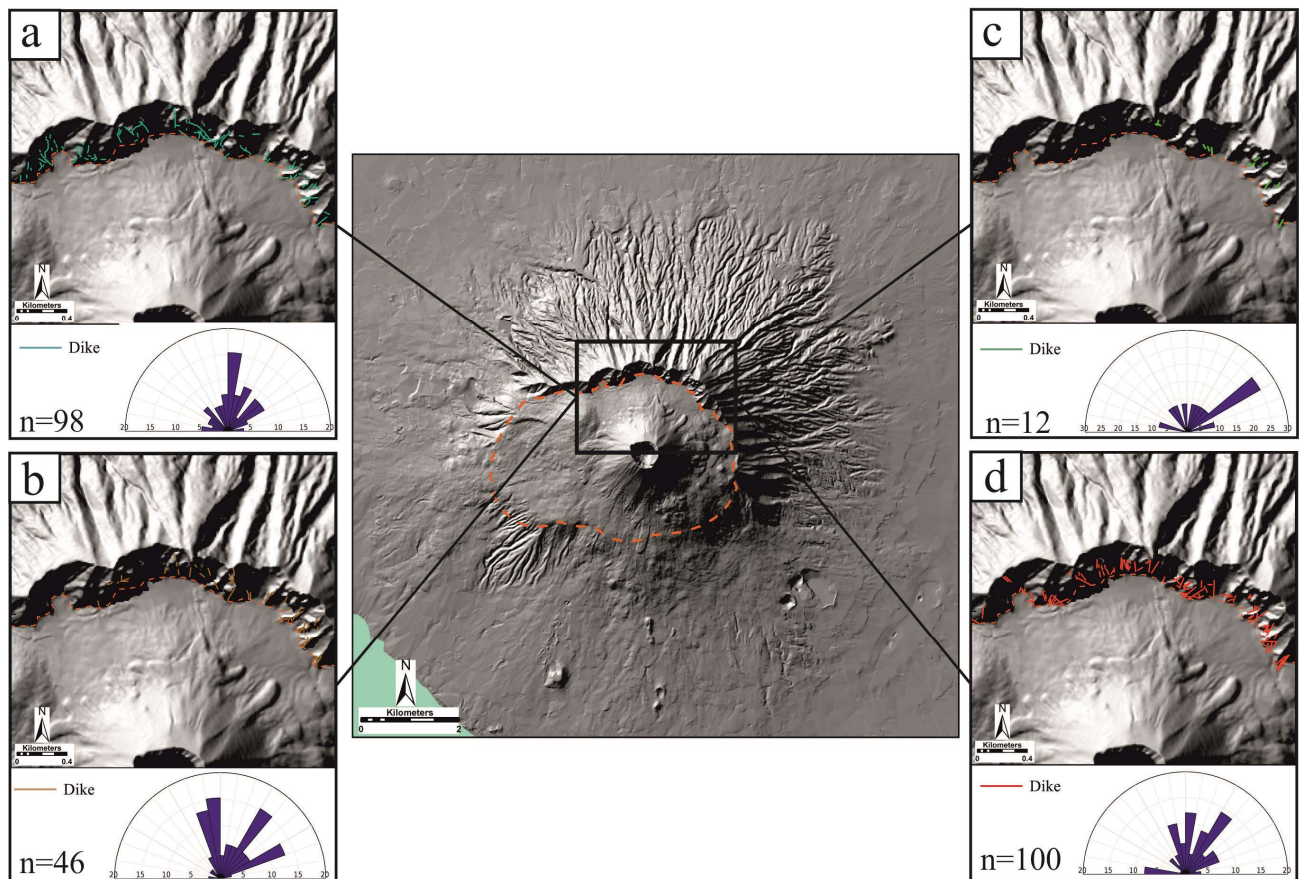


Fig. 8.1: dikes dataset compiled from different bibliographic sources. SV caldera outlined in dark orange dashed line. Petal size of related rose diagrams is 10°. a) Marinoni (2001); b) Santacroce and Sbrana (2003); c) Ventura et al. (2005); d) Porreca et al. (2006).

For this reason, all of the dikes that compose this dataset refer either to the activity of the Mount Somma (before the Pomici di Base eruption of 22 ka BP) or to the activity of SV before the Mercato

eruption of 8.8 ka BP; furthermore, their surface exposure is located outside the SV caldera as defined in the present paper, although their centroid might be located within the caldera itself. The dataset itself is composed of four different linear feature classes, each of them referring to a different bibliographic source that deals with locations of Mount Somma dikes (Marinoni 2001; Santacroce and Sbrana 2003; Ventura et al. 2005; Porreca et al. 2006). The reason for this differentiation lies in the uncertainty of discriminating between different dikes when comparing all the bibliographic sources, with the high possibility of excluding some data. On the other hand, it is likely that in some cases two dikes recorded by two different sources might represent the same dike, leading to data duplication: for this reason, field work with data comparison is needed to account for this possibility. The highest number of dikes (Fig. 8.1) is reported respectively by Porreca et al. (2006) (100 dikes) and Marinoni (2001) (98 dikes), while Santacroce and Sbrana (2003) and Ventura et al. (2005) report 46 and 12 dikes respectively. Dikes vary in lengths between 6 m (reported by Ventura et al. 2005) and 203 m (reported by Marinoni 2001) with a mean value of 52 m and 77% of the data between 10 and 70 m. With respect to the orientations, all the dikes from different sources confirm one preferential orientation along the NE-SW direction (Fig. 8.1). With the exception of Ventura et al. (2005), where dykes exhibit only one preferential orientation possibly due to the limited dataset studied (Fig. 8.1c), the other three sources display at least two preferential orientation along the N-S and NNE-SSW orientations (Fig. 8.1a,b,d). Porreca et al. (2006) record that approximately 57% of the dikes are radial to the older Somma cone, ~27% are oblique and ~16% tangential; among the latter two groups, ~32% are outward dipping and ~11% inward dipping. The authors also calculated the sense of propagation for 19 dikes and 13 of them display a vertical one. A moderate percentage (32%) of the radial dikes is oriented NE-SW and (less frequently) NW-SE (Fig. 8.1d), consistently with the orientation of main regional fault systems. Porreca (2006) reports also dike thicknesses, that range between 0.15 m to 3.17 m (mean value is 1.17 m) with 75% of the data between 0.15 m and 1.5 m.

Dikes dataset has been compiled integrating informations coming from several georeferenced raster images (Marinoni 2001; Santacroce and Sbrana 2003; Porreca et al. 2006; RMSE are less than 1 meter) or existing databases (Ventura et al. 2005). However, due to the small scale of such structures and the fact that for the bulk of the data (Marinoni 2001 and Porreca et al. 2006) the digitalization was performed after the georeferencing of sketches with few cartographic reference points, a buffer area is suggested to be taken into consideration for these structures. A possible reasonable value of buffer area

radius is 5 meters, corresponding to 1/10 of the mean length of all the dikes of the four feature classes (50 meters), with the bulk of the data having lengths between 10 and 30 meters.

Within each feature class of the dikes dataset, all the data are catalogued according to a univocal code, their strike and their length.

8.1.2 Subsurface faults/lineaments

The “Subsurface faults/lineaments” sub-dataset (Fig. 8.2) is composed of 84 elements grouped

in a linear feature class that comprises lineaments with a structural meaning identified after geological field data (21 faults; Bruno et al. 1998), DTM analysis and field checks (18 faults and 3 fractures; Ventura and Vilardo 1999a) and DTM analysis alone (21 buried scarps and 21 fractures; Ventura and Vilardo 1999a).

Data from Ventura and Vilardo (1999a) have been extracted by the authors after a critical analysis of a 20-m cellsize DTM of the Vesuvian area, and have been interpreted as faults when the dip direction was determined, and as fractures otherwise. Furthermore, lineaments without field evidences have been interpreted as buried scarps that, according to Oakey (1994) may reflect the surface expression of buried fault scarps. As the reactivation of superficial structures of SV have been reported in historical accounts before and during

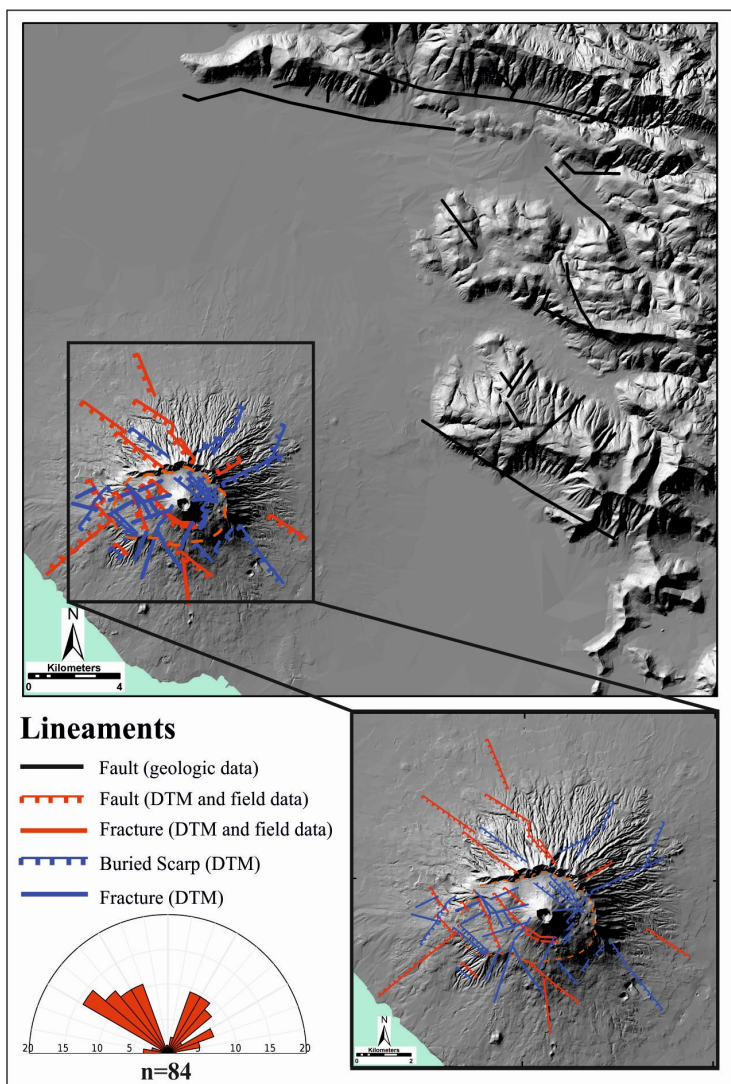


Fig. 8.2: subsurface lineaments dataset (see text for details). SV caldera is outlined in dark orange dashed line. Petal size of related rose diagrams is 10°.

eruptions, and these reactivations are possibly related to increasing pore pressure of aquifers and hydrothermal system, Ventura and Vilardo (1999a) also performed a slip-tendency analysis of the above-mentioned structures using hydraulic parameters of SV superficial deposits (Ventura and Vilardo 1999b). Results show that for intermediate values of fluid pore pressure, faults that are more likely to be reactivated (i.e. with higher slip tendency rates) follow a prevailing NW-SE trend, consistently with the orientation of deep regional structures (Bianco et al. 1998) and the prevailing orientation of inferred eruptive fissures. Among the 84 recognized features, 32 of them cross the SV caldera, being 6 faults/3 fractures from combined DTM-field analyses and 8 buried scarps/24 fractures from DTM analysis alone. Microfaults with surface exposure (totaling 59 structures) related to regional structures have been reported by Bianco et al. (1998) in the NE and NW part of SV caldera (Sector B of Fig. 1.2B) and outside SV caldera, both on northern and southern flanks (17 microfaults). Other 207 faults whose orientation are consistent with the regional stress field have been reported by Marinoni (1996) along the northern, south-facing Mount Somma scarp.

For subsuperficial faults/fractures sub-dataset, a possible value for buffer area width relies on the methodology through which most of the data have been acquired. According to Ventura and Vilardo (1999a) in fact, the first approach for lineament positions determination derive from a detailed 20-m cellsize DTM analysis enhanced by the application of appropriate filters elaborations. A value of 20 m for buffer area width should account for imprecision in feature recognition; this value is equally reasonable also for superficial faults derived from geological field data.

Similarly to the “deep faults” sub-dataset, elements in this sub-dataset are classified according to a univocal code, how the fault has been located (geological data, DTM, field checks or both), the presence/absence of a downthrown block, the azimuth, the length expressed in meters and the source from which it has been retrieved.

8.1.3 Seismic activity

Seismic activity dataset of SV (Fig. 8.3) has been compiled after the integration of four different available databases about seismicity in Italy and within the Vesuvian area.

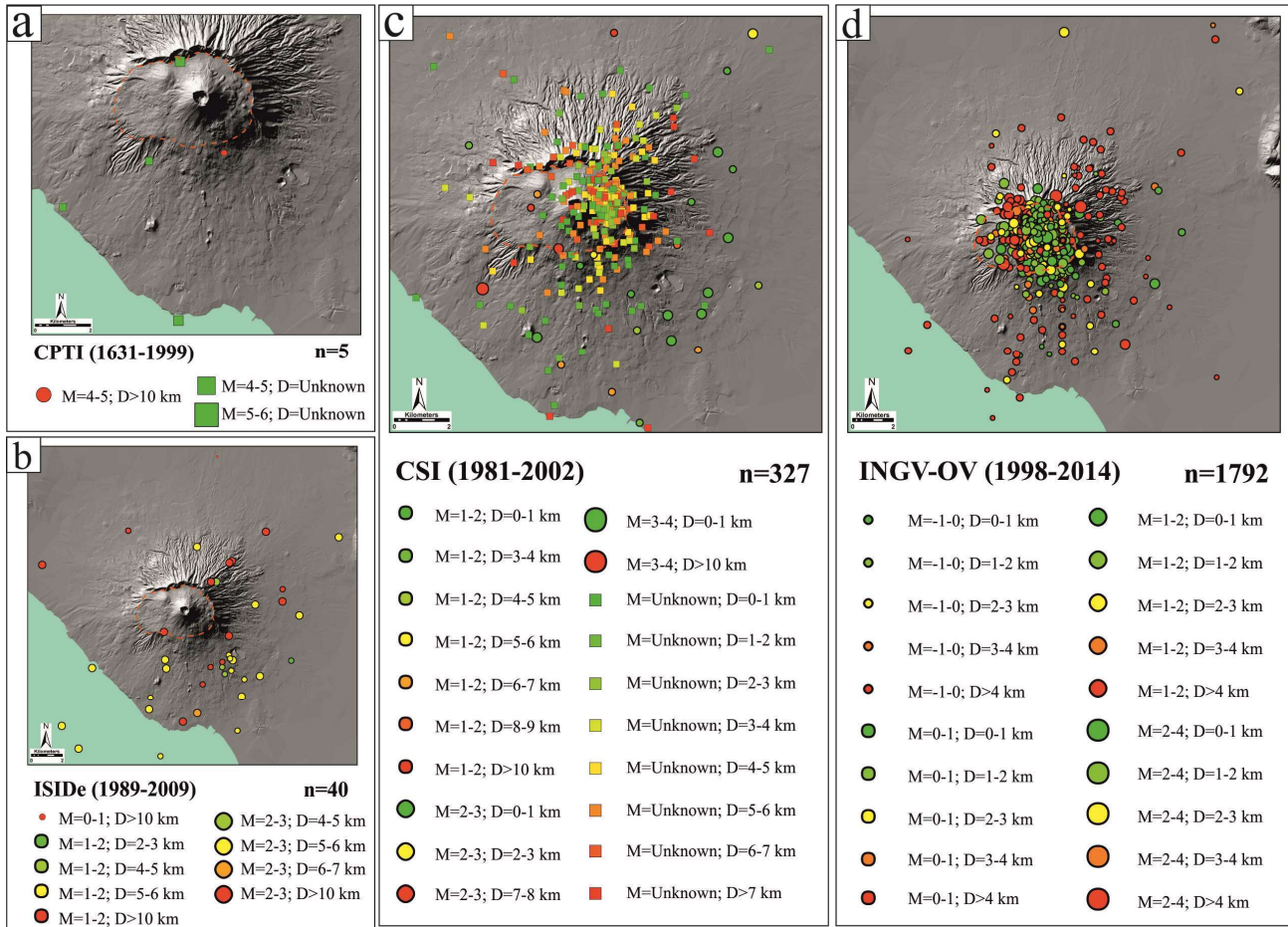


Fig. 8.3: seismic activity dataset compiled after integration of different catalogues: a) Catalogo Parametrico dei Terremoti Italiani (CPTI); b) Italian Seismological Instrumental and Parametric Database (ISIDe); c) Catalogo della Sismicità Italiana (CSI); d) Database sismologico dei vulcani della Campania – Osservatorio Vesuviano (INGV-OV). M=magnitude; D=depth. SV caldera outlined in dark orange dashed line.

All the seismic events are related to tectonic or volcano-tectonic activity, excluding all the earthquakes related to other sources. Data presented here have been stored in four different point feature classes, each one referring to a different database from which the data have been retrieved and catalogued according to a univocal code, x and y coordinate of the event, its magnitude and its depth. Data about magnitudes rely on macroseismic data (CPTI11, Rovida et al. 2011), instrumental data (ISIDe 2010; INGV-OV 2014) or have been evaluated when possible from other parameters (CSI1.1, Castello et al. 2006). A summary of the events from the four different catalogues are reported in Table 8.1.

Database	Period	Type of data	n° events	Inside caldera	Magnitude					Depth (km)						
					-1-1	1-3	3-5	>5	Unkn.	0-2	2-4	4-6	6-8	8-10	>10	Unkn.
CPTI11	1631-1999	Macroseismic	5	1	0	0	3	2	0	0	0	0	0	0	1	4
CSI 1.1	1981-2002	Other	327	153	0	27	1	0	299	91	72	105	40	12	7	0
ISIDe	1988-2009	Instrumental	40	1	1	39	0	0	0	1	0	23	1	12	3	0
INGV-OV	1998-2014	Instrumental	1792	1612	1042	748	2	0	0	1168	596	22	3	2	1	0
TOT	1631-2014		2164	1767	1043	814	6	2	299	1260	668	150	44	26	12	4

Table 8.1: summary of different databases used for the “Seismic data” dataset (see text for more details).

A total of 2164 earthquakes compose the dataset, the bulk of them being stored in the INGV-OV feature class (1792 events). 1767 out of 2194 events are located within the SV caldera as defined in the present paper, while from the point of view of magnitude and depth, the bulk of the data lie, respectively, between -1/1 (1043 events) and 0-2 km (1168 events). A significative amount of events (299) reported in the CSI 1.1 database have not been attributed a magnitude due to incompleteness of the data. It is worth noting that Vilardo et al. (1996) point out that seismic activity at Vesuvius is clustered around the present crater axis, at depths that rarely exceeds 5-6 km from the top of the volcanic cone (1200 m).

8.1.4 CO₂ emissions

CO₂ emissions at SV (Fig. 8.4) are presently most likely surface manifestation of the deep intrusion of alkali-basaltic magma into the sedimentary carbonate basement, accompanied by sidewall assimilation and CO₂ volatilization (Iacono-Marziano et al. 2009). The dataset have been composed after the integration of three different type of data, two of them about CO₂ emissions in the area of the Gran Cono measured in the years 2000 and 2006 (Fronadini et al. 2004; Granieri et al. 2013) and the third one about CO₂ emissions in the apron and calderic area of SV (Aiuppa et al. 2004) measured in the year 2000.

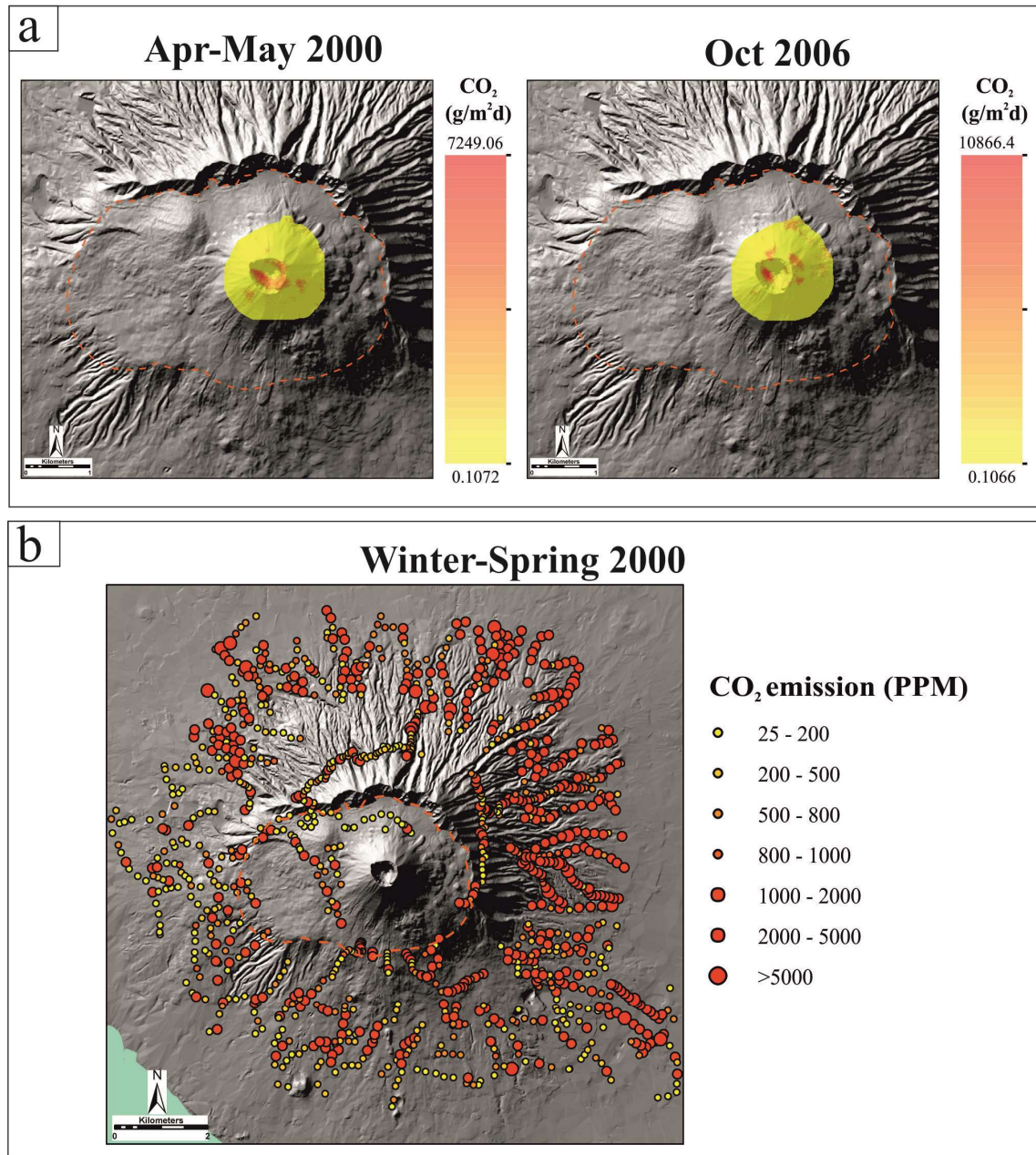


Fig. 8.4: CO₂ emission dataset compiled after a) Granieri et al. (2013) for the years 2000 (on the left) and 2006 (on the right) and b) Aiuppa et al. (2004) for the year 2000. SV caldera outlined in dark orange dashed line.

Data from Frondini et al. (2004) and Granieri et al. (2013) consist of two point feature classes that record CO₂ emissions from the area of Gran Cono expressed in terms of $\text{g}/(\text{m}^2)(\text{d})^{-1}$ related to two different periods, April-May 2000 (Frondini et al. 2004) and October 2006 (Granieri et al. 2013). These

data have been converted into point feature class (Fig. 8.4a) from GRID data and consist of 12,780 (year 2000) and 12,764 (year 2006) emission points respectively catalogued according to X and Y UTM coordinates and CO₂ emission. Values range from 0.1 and 7,249 for the year 2000 and from 0.1 and 10,866 for the year 2006 and allowed Granieri et al. (2013) to point out that a) a value between 120 and 140 t/day of CO₂ is representative of the total CO₂ discharged by diffuse degassing from the summit area of Vesuvius and b) the highly emissive area of the present crater is well correlated with a NW-SE active fault that leak deep gas from the bottom of the crater; this latter conclusion is coherent with the trend of deep faults dissecting SV caldera (Fig. 2.6) as discussed in section 3.6.1. Data from Aiuppa et al. (2004) consist of a point feature class with 1110 records (Fig. 8.4b) catalogued according to X and Y UTM coordinates and CO₂ emission in terms of parts per million (PPM). Values of CO₂ emissions vary between 25 and 10,500 PPM and with respect to point locations, 74 out of 1110 are located within SV caldera as defined in the present paper. These data have been used by the authors in order to constrain possible pathways responsible of carbon dioxide diffuse degassing taking place during the present state of quiescence of the volcano. Results highlight that a) main degassing lineaments are oriented according to the NE-SW and NW-SE trends and b) a main degassing area is located on the southern and eastern parts of SV, reflecting the shallow depth of the carbonate basement (500 m) in this area.

8.2. Expert elicitation

This section reports additional information about the technical outcomes of the elicitation sessions or some complementary results.

Complementary results listed in this addendum and cited in the main text comprise all the information and changes produced after the first elicitation session and alternative maps built in order to provide more robustness to the final results considering different scoring methods (Fig.8.5), different subgroups of experts (Fig.8.6), different subgroups of datasets (Fig.8.7) or alternative assumptions for caldera enlargements (Fig.8.8).

Notably, throughout all this documents one could notice that the Uncertainty area of Small Explosive eruptions that occurred before the Avellino Plinian eruption is extended along all the SV caldera and not along the uncertainty area that reflects the extension of the SV caldera before the Avellino eruption, as correctly cited throughout Chapters 2-3. This is due to the fact that offline after the second elicitation session, some participants raised the question about the correct extent of the uncertainty area that should account for missing VS to AE eruptions before the Avellino eruption, and it was decided that the extent considered so far (the whole present extent of the SV caldera) had to be reduced.

8.2.1 First questionnaire: outcomes and preliminary maps

TARGET QUESTIONS

In the questionnaire we have reported (IN RED) the results obtained with the Cooke Classical Method (CM), those obtained with Expected Relative Frequency (ERF) method (IN BLUE) and the results obtained with the Equal Weights (EW – i.e. all experts are equally weighted) method (IN GREEN). At the end of the questionnaire you will find different vent opening probability maps obtained by using weights calculated with the three above-mentioned methods. For each of the method you will find maps corresponding to the 5th percentile, the mean map and the map corresponding to the 95th percentile.

The first two questions would like to assess the probability that the vent of a future medium-large scale explosive eruption at SV (i.e. Plinian, Sub-Plinian I and Sub-Plinian II), could be located Q2 outside the caldera region, differently from our Q1 basic assumption (inside the caldera).

	5%ile value	50%ile value	95%ile value
Q1: how much probability do you assign to the possibility that the next medium-large scale explosive eruption of SV will have its eruptive center within the caldera outline reported in the above figures? (%)	82 (68) (45)	98 (85) (85)	99.9 (94) (99.4)
Q2: how much probability do you assign to the possibility that the next medium-large explosive eruption of SV will have its eruptive center outside the caldera outline defined so far? (%)	10⁻² (4) (0.3)	1 (14) (13)	17 (27) (61)

For defining the background (base rate) spatial probability of vent opening, what relative weights do you give to three alternative ‘information models’: Q3 the seven variables related to past vents/eruptive fissures distributions (considered jointly as a single factor); Q4 structural information coming from the deep faults dataset; Q5 other unknown or neglected influences not considered here (such as other spatial distributions, e.g. geochemical or geophysical factors) but represented here as a simple spatially-uniform distribution?

	5%ile value	50%ile value	95%ile value
Q3: how much weight do you assign to the information provided jointly by the distributions of the seven variables related to past vents/eruptive fissures distribution considered here? (%)	49 (44) (24)	74 (65) (65)	94 (83) (92)
Q4: how much weight would you give to the distribution of the structural data provided (deep faults)? (%)	1 (8) (2)	5 (18) (20)	30 (39) (66)
Q5: how much weight should be given to a spatially uniform distribution inside the SV caldera? (%)	9 (7) (2)	20 (16) (14)	35 (34) (53)

For defining the positional background (base rate) probability of a new vent opening related to a medium-large scale explosive eruption of SV, what weights would you assign to the three datasets of “Past vents/fissures” we are considering, i.e. Q6 the Plinian/Subplinian I-II eruptions dataset; Q7 the Violent Strombolian to Continuous Ash emission dataset; Q8 the effusive eruption dataset?

	5%ile value	50%ile value	95%ile value
Q6: how much weight would you give to the Plinian/Subplinian I-II eruptions dataset as a whole (10 vents recognized in the last 22 ka)? (%)	30 (39) (16)	59 (56) (58)	89 (80) (91)
Q7: how much weight would you give to the Violent Strombolian to Continuous Ash emission eruptions dataset as a whole (32 eruptions recognized in the last 4.3 ka)? (%)	10 (19) (7)	30 (35) (34)	51 (56) (82)
Q8: how much weight would you give to the effusive eruptions dataset as a whole (from AD 1631 to AD 1944)? (%)	4 (9) (1)	9 (16) (11)	22 (31) (77)

The following questions address specifically the relative importance that should be given to: Q9 Plinian, and Q10 Sub-Plinian (I and II) eruptions within the medium-large scale explosive eruptions dataset:

	5%ile value	50%ile value	95%ile value
Q9: how much weight would you give to the Plinian eruptions (large scale) map as a whole (4 vents recognized)? (%)	20 (29) (17)	39 (46) (45)	61 (63) (82)
Q10: how much weight would you give to the Sub-Plinian eruptions (medium scale including both Sub-Plinian I and II) map as a whole (6 vents recognized)? (%)	38 (40) (30)	60 (57) (57)	79 (62) (86)

The following questions address specifically the relative importance that should be given to the maps representing the uncertainty areas of the vent position of the Violent Strombolian to Continuous Ash emission eruptions dataset: Q11 that occurred in the period before 4.3 ka; Q12 in the period 4.3 ka BP – 1631 AD; Q13 in the period 1631 AD – 1944 AD (entire SV caldera, Gran Cono uncertainty area and 1944 Crater rim uncertainty area, respectively).

	5%ile value	50%ile value	95%ile value
Q11: how much weight would you give to an homogeneous map representing the vent locations of small scale explosive events occurred before 4.3 ka BP (period before 4.3 ka)? (%)	10 (20) (10)	39 (37) (37)	69 (57) (76)
Q12: how much weight would you give to the map representing the vent locations of the small scale explosive events occurred in the Gran Cono uncertainty area (period 4.3 ka BP – 1631 AD; 22 eruptions recognized)? (%)	10 (20) (12)	30 (35) (35)	53 (56) (71)
Q13: how much weight would you give to the map representing the vent locations of the small scale explosive events occurred within the 1944 crater rim uncertainty area (period 1631 AD – 1944 AD; 10 eruptions recognized)? (%)	9 (13) (5)	29 (26) (23)	51 (49) (75)

The following questions would like to assess how much weight should be given to the two maps representing: Q14 the distribution of the effusive (parasitic) vents; Q15 eruptive fissures of the effusive eruptions dataset.

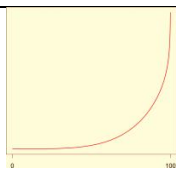
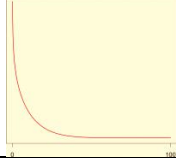
	5%ile value	50%ile value	95%ile value
Q14: how much weight would you give to the map representing the locations of the effusive vents (46 vents mapped/buried, 47 “lost”)? (%)	20 (31) (16)	49 (55) (54)	79 (74) (84)
Q15: how much weight would you give to the map representing the locations of the eruptive fissures on the Gran Cono (24 fissures recognized)? (%)	20 (24) (14)	49 (44) (44)	79 (65) (79)

8.2.2 Second questionnaire: outcomes and definitive results

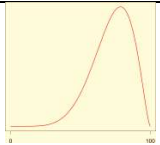
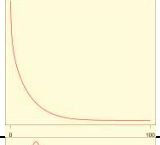
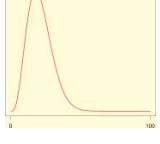
TARGET QUESTIONS

In the questionnaire we have reported IN RED the results obtained with the Cooke Classical Method (CM), IN BLUE those obtained with the Expected Relative Frequency (ERF) method and IN GREEN the results obtained with the Equal Weights (EW) method. Next to each question is reported the graph of the Beta distribution associated with the CM.

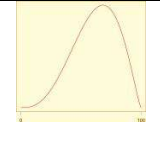
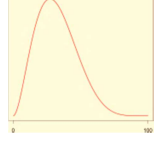
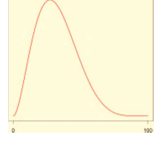
The first two questions would like to assess the probability that the INITIAL VENT (i.e. the centroid of the vent area) of a future medium-large scale explosive eruption at SV (i.e. Plinian, Sub-Plinian I and Sub-Plinian II), could be located within (Q1) or outside (Q2) the caldera region.

	5%ile value	50%ile value	95%ile value	Beta distribution
Q1: how much probability do you assign to the possibility that the next medium-large scale explosive eruption of SV will have its eruptive center within the caldera outline reported in the above figures? (%)	58 (73) (58)	93 (90) (89)	99 (97) (99)	
Q2: how much probability do you assign to the possibility that the next medium-large explosive eruption of SV will have its eruptive center outside the caldera outline defined so far? (%)	0.5 (2.4) (0.7)	6.1 (10) (9.5)	28 (21) (32)	

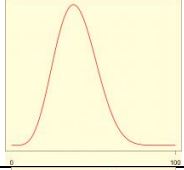
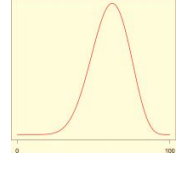
For defining the background (base rate) spatial probability of vent opening, what relative weights do you give to three alternative ‘information models’: Q3 the seven variables related to past vents/eruptive fissures distributions (considered jointly as a single factor); Q4 structural information coming from the deep faults dataset; Q5 other unknown or neglected influences not considered here (such as other spatial distributions, e.g. geochemical or geophysical factors) but represented here as a simple spatially-uniform distribution.

	5%ile value	50%ile value	95%ile value	Beta distribution
Q3: how much weight do you assign to the information provided jointly by the distributions of the seven variables related to past vents/eruptive fissures distribution considered here? (%)	47 (54) (45)	72 (72) (71)	95 (89) (95)	
Q4: how much weight would you give to the distribution of the structural data provided (deep faults)? (%)	0.6 (3.4) (1.2)	6.3 (9.9) (9.1)	32 (20) (32)	
Q5: how much weight should be given to a spatially uniform distribution inside the SV caldera? (%)	6.4 (7.9) (4.4)	21 (18) (18)	37 (30) (37)	

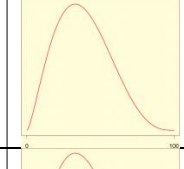
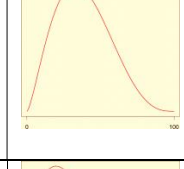
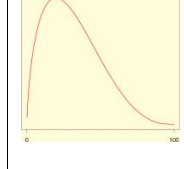
For defining the positional background (base rate) probability of a new vent opening related to a medium-large scale explosive eruption of SV, what weights would you assign to the three datasets of “Past vents/fissures” we are considering, i.e. Q6 the Plinian/Subplinian I-II eruptions dataset; Q7 the Violent Strombolian to Continuous Ash emission dataset; Q8 the effusive eruption dataset?

	5%ile value	50%ile value	95%ile value	Beta distribution
Q6: how much weight would you give to the Plinian/Subplinian I-II eruptions dataset as a whole (10 vents recognized in the last 22 ka)? (%)	30 (40) (21)	60 (57) (60)	90 (82) (93)	
Q7: how much weight would you give to the Violent Strombolian to Continuous Ash emission eruptions dataset as a whole (32 eruptions recognized in the last 4.3 ka)? (%)	10 (15) (6.8)	31 (30) (29)	59 (52) (72)	
Q8: how much weight would you give to the effusive eruptions dataset as a whole (from AD 1631 to AD 1944)? (%)	0.8 (5.7) (1.1)	8.6 (12) (9.2)	22 (26) (48)	

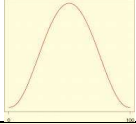

The following questions address specifically the relative importance that should be given to: Q9 Plinian, and Q10 Sub-Plinian (I and II) eruptions within the medium-large scale explosive eruptions dataset:

	5%ile value	50%ile value	95%ile value	Beta distribution
Q9: how much weight would you give to the Plinian eruptions (large scale) map as a whole (4 vents recognized)? (%)	20 (29) (23)	39 (46) (46)	60 (62) (70)	
Q10: how much weight would you give to the Sub-Plinian eruptions (medium scale including both Sub-Plinian I and II) map as a whole (6 vents recognized)? (%)	40 (38) (30)	64 (55) (55)	80 (71) (77)	

The following questions address specifically the relative importance that should be given to the maps representing the uncertainty areas of the vent position of the Violent Strombolian to Continuous Ash emission eruptions dataset: Q11 that occurred in the period before 4.3 ka; Q12 in the period 4.3 ka BP – 1631 AD; Q13 in the period 1631 AD – 1944 AD (entire SV caldera, Gran Cono uncertainty area and 1944 Crater rim uncertainty area, respectively).

	5%ile value	50%ile value	95%ile value	Beta distribution
Q11: how much weight would you give to an homogeneous map representing the vent locations of small scale explosive events occurred before 4.3 ka BP (period before 4.3 ka)? (%)	11 (21) (11)	37 (38) (40)	69 (58) (78)	
Q12: how much weight would you give to the map representing the vent locations of the small scale explosive events occurred in the Gran Cono uncertainty area (period 4.3 ka BP – 1631 AD; 22 eruptions recognized)? (%)	11 (22) (13)	34 (38) (36)	59 (59) (79)	
Q13: how much weight would you give to the map representing the vent locations of the small scale explosive events occurred within the 1944 crater rim uncertainty area (period 1631 AD – 1944 AD; 10 eruptions recognized)? (%)	7.3 (13) (5.1)	29 (25) (19)	65 (46) (69)	

The following questions would like to assess how much weight should be given to the two maps representing: Q14 the distribution of the effusive (parasitic) vents; Q15 eruptive fissures of the effusive eruptions dataset.

	5%ile value	50%ile value	95%ile value	Beta distribution
Q14: how much weight would you give to the map representing the locations of the effusive vents (46 vents mapped/buried, 47 “lost”)? (%)	20 (32) (22)	47 (56) (57)	79 (74) (85)	
Q15: how much weight would you give to the map representing the locations of the eruptive fissures on the Gran Cono (24 fissures recognized)? (%)	20 (23) (14)	60 (44) (42)	79 (65) (72)	

8.2.3 Maps obtained with different scoring methods (CM, ERF and EW methods)

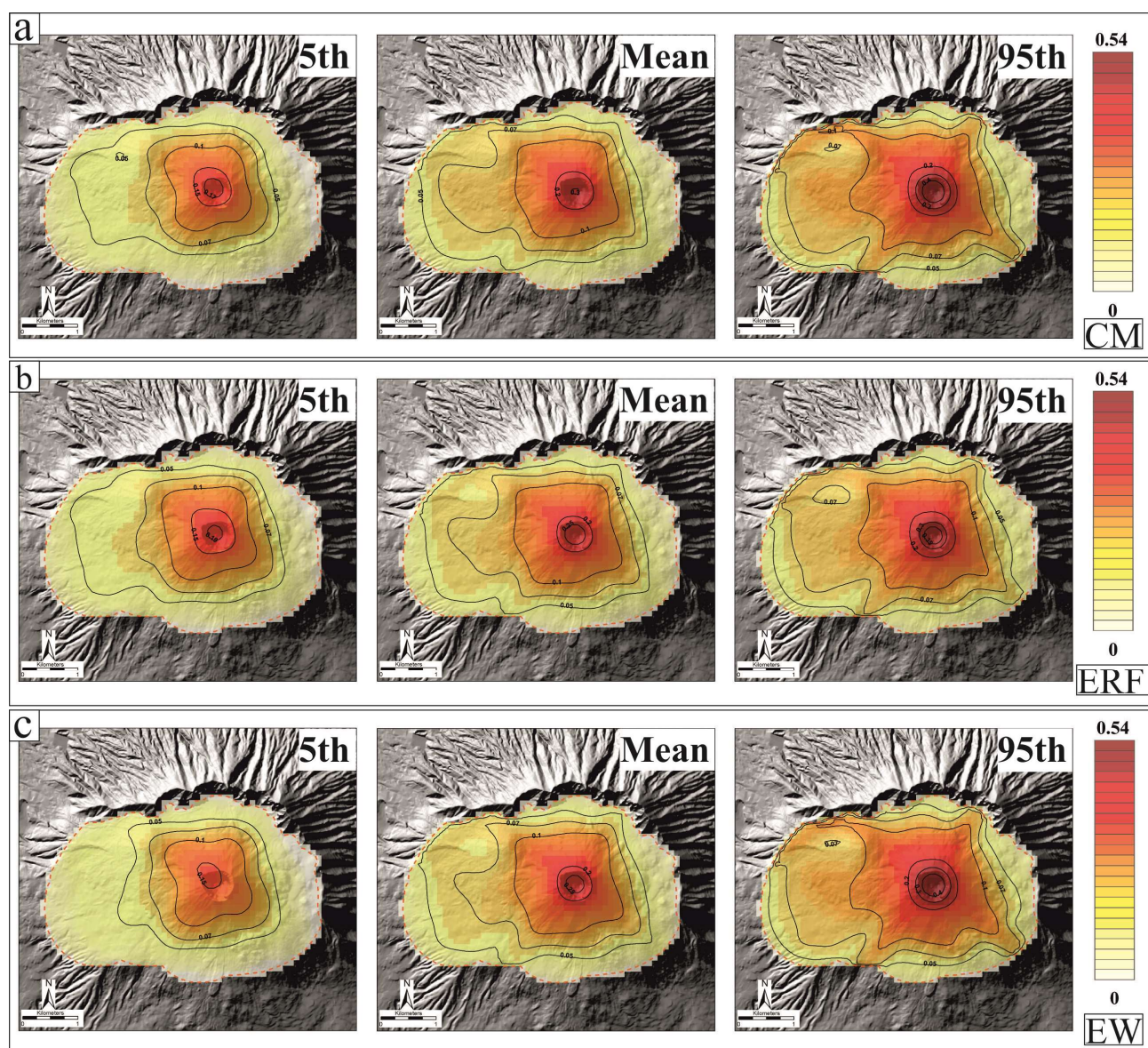


Fig. 8.5: a) maps of the 5th, mean and 95th percentiles obtained after the Classical Model (CM) expert pooling technique; b) maps of the 5th, mean and 95th percentiles obtained after the Expected Relative Frequency (ERF) expert pooling technique; c) maps of the 5th, mean and 95th percentiles obtained after the Equal Weight (EW) expert pooling technique. Cellsize is 100 m; values are probability percentages per cell; contour lines enclose areas where cell values are higher than the value of the line itself.

8.2.4 Sub-groups of experts (CM and EW methods): elicited values

Dataset/Variable	% - 5 th /Median/95 th														
	CM														
	All			A1 (Seniors)			A2 (Juniors)			B1 (Geologists)			B2 (Modelers)		
<i>INSIDE</i> <i>CALDERA</i> <i>(initial vent)</i>	57.7	<u>93</u>	98.9	79.5	<u>95</u>	99	50	<u>90</u>	95.6	42.3	<u>87</u>	97.6	59.6	<u>93</u>	98.9
<i>OUTSIDE</i> <i>CALDERA</i> <i>(initial vent)</i>	0.4	<u>6.1</u>	27.6	1	<u>5.1</u>	18.3	10 ⁻²	<u>9.9</u>	30	1.2	<u>12</u>	43.3	0.4	<u>6</u>	26.3
Dataset/Variable	% - 5 th /Median/95 th														
	EW														
	All			A1 (Seniors)			A2 (Juniors)			B1 (Geologists)			B2 (Modelers)		
<i>INSIDE</i> <i>CALDERA</i> <i>(initial vent)</i>	58.1	<u>89.3</u>	98.9	59.5	<u>89.4</u>	98.9	58.2	<u>88.9</u>	98.9	58.0	<u>87.3</u>	98.9	59.9	<u>92.7</u>	98.9
<i>OUTSIDE</i> <i>CALDERA</i> <i>(initial vent)</i>	0.7	<u>9.5</u>	31.8	0.6	<u>9.2</u>	32.8	1.0	<u>10.1</u>	30.4	1.1	<u>11.0</u>	32.2	0.2	<u>6.8</u>	30.3

Table 8.2: elicited values from sub-group of experts for the two questions Inside versus Outside caldera (see text for more details) for the CM and EW scoring methods.

Dataset/Variable	Weight (%) - 5 th /Mean/95 th)												Weight (%) - 5 th /Mean/95 th)											
	CM												EW											
	A1 (Seniors)			A2 (Juniors)			B1 (Geologists)			B2 (Modelers)			A1 (Seniors)			A2 (Juniors)			B1 (Geologists)			B2 (Modelers)		
Uniform Map	10.7	<u>22.0</u>	34.9	7.1	<u>18.2</u>	32.1	2.9	<u>15.5</u>	32.4	8.6	<u>20.1</u>	33.7	5.7	<u>18.1</u>	33.5	7.1	<u>18.2</u>	32.2	4.6	<u>17.5</u>	33.6	7.7	<u>19.5</u>	33.9
Deep Faults	1.3	<u>6.6</u>	14.7	0.5	<u>12.0</u>	31.8	2.3	<u>12.0</u>	26.1	0.4	<u>9.4</u>	26.0	1.9	<u>10.3</u>	22.7	0.5	<u>11.9</u>	31.8	2.0	<u>10.3</u>	22.7	1.0	<u>12.4</u>	30.3
Plinian Eruptions	8.0	<u>16.1</u>	25.6	10.6	<u>17.4</u>	24.9	6.8	<u>17.7</u>	32.0	8.0	<u>16.2</u>	26.0	6.6	<u>18.0</u>	31.8	10.6	<u>17.4</u>	25.0	8.8	<u>20.4</u>	35.1	5.5	<u>15.1</u>	26.8
Subplinian Eruptions	14.8	<u>25.8</u>	38.1	16.0	<u>25.2</u>	35.4	7.6	<u>19.2</u>	34.3	14.5	<u>25.8</u>	38.7	8.0	<u>20.9</u>	36.3	16.1	<u>25.3</u>	35.3	10.0	<u>22.5</u>	38.1	7.9	<u>20.1</u>	34.1
Violent Strombolian to Ash Emission Eruptions – 1944 Crater	1.4	<u>5.7</u>	12.4	3.0	<u>7.8</u>	14.1	0.9	<u>7.2</u>	17.8	1.3	<u>6.6</u>	14.5	0.2	<u>4.9</u>	14.1	3.0	<u>7.8</u>	14.1	0.2	<u>4.3</u>	13.0	0.8	<u>6.4</u>	15.7
Violent Strombolian to Ash Emission Eruptions – Gran Cono	1.9	<u>6.7</u>	13.8	4.2	<u>9.0</u>	15.2	1.4	<u>8.8</u>	20.5	2.0	<u>7.4</u>	15.4	1.1	<u>8.2</u>	19.9	4.1	<u>9.0</u>	15.3	0.7	<u>7.5</u>	18.6	1.9	<u>8.4</u>	18.9
Violent Strombolian to Ash Emission Eruptions – Caldera	2.5	<u>8.6</u>	16.9	3.2	<u>7.1</u>	12.1	1.0	<u>8.3</u>	19.9	2.1	<u>8.1</u>	16.7	1.2	<u>8.5</u>	20.5	3.2	<u>7.0</u>	12.1	0.9	<u>8.3</u>	20.2	1.5	<u>7.9</u>	18.1
Effusive Eruptions – Parasitic Vents	1.1	<u>4.3</u>	9.3	0.3	<u>1.5</u>	3.7	0.2	<u>7.1</u>	20.0	0.5	<u>3.1</u>	7.7	0.2	<u>6.3</u>	18.0	0.3	<u>1.5</u>	3.7	0.1	<u>5.2</u>	15.7	0.1	<u>5.7</u>	17.2
Effusive Eruptions – Eruptive Fissures	1.0	<u>4.2</u>	9.2	0.3	<u>1.7</u>	4.1	0.1	<u>4.3</u>	12.8	0.5	<u>3.2</u>	8.0	0.2	<u>4.9</u>	14.5	0.3	<u>1.7</u>	4.1	0.1	<u>3.9</u>	12.0	0.1	<u>4.5</u>	14.0

Table 8.3. elicited values from sub-group of experts for the remaining questions (see text for more details) for the CM and EW scoring methods.

8.2.5 Sub-groups of experts (CM method): different maps

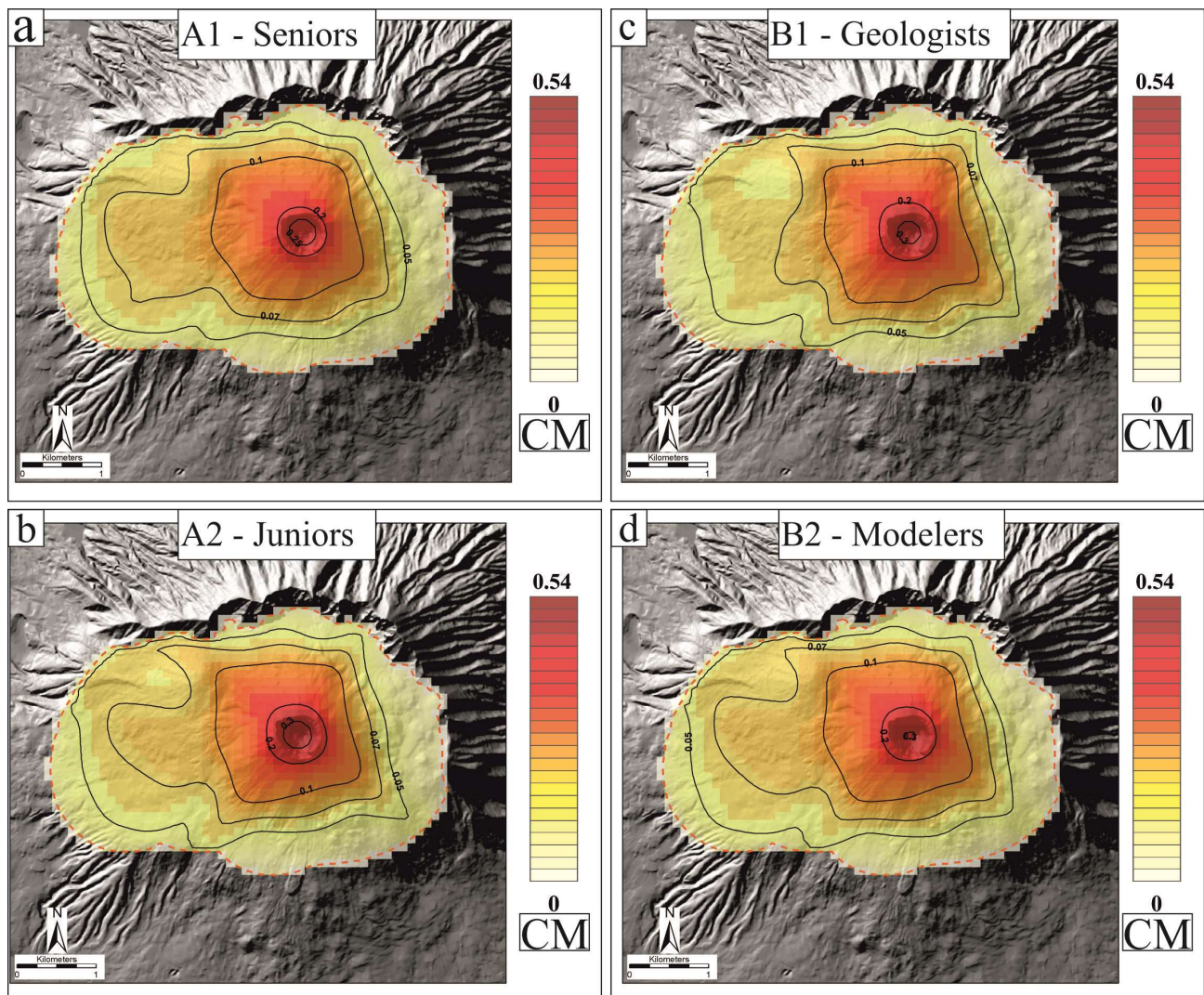


Fig. 8.6: a) mean map produced using weights from the A1 sub-group (Seniors) pooled with the Classical Model (CM) method; b) mean map produced using weights from the A2 sub-group (Juniors) pooled with the Classical Model (CM) method; c) mean map produced using weights from the B1 sub-group (Geologists) pooled with the Classical Model (CM) method; d) mean map produced using weights from the B2 sub-group (Modelers) pooled with the Classical Model (CM) method. Cellsize is 100m; values are probability percentages per cell; contour lines enclose areas where cell values are higher than the value of the line itself.

8.2.6 Maps obtained without the “Deep faults” dataset (CM and EW methods)

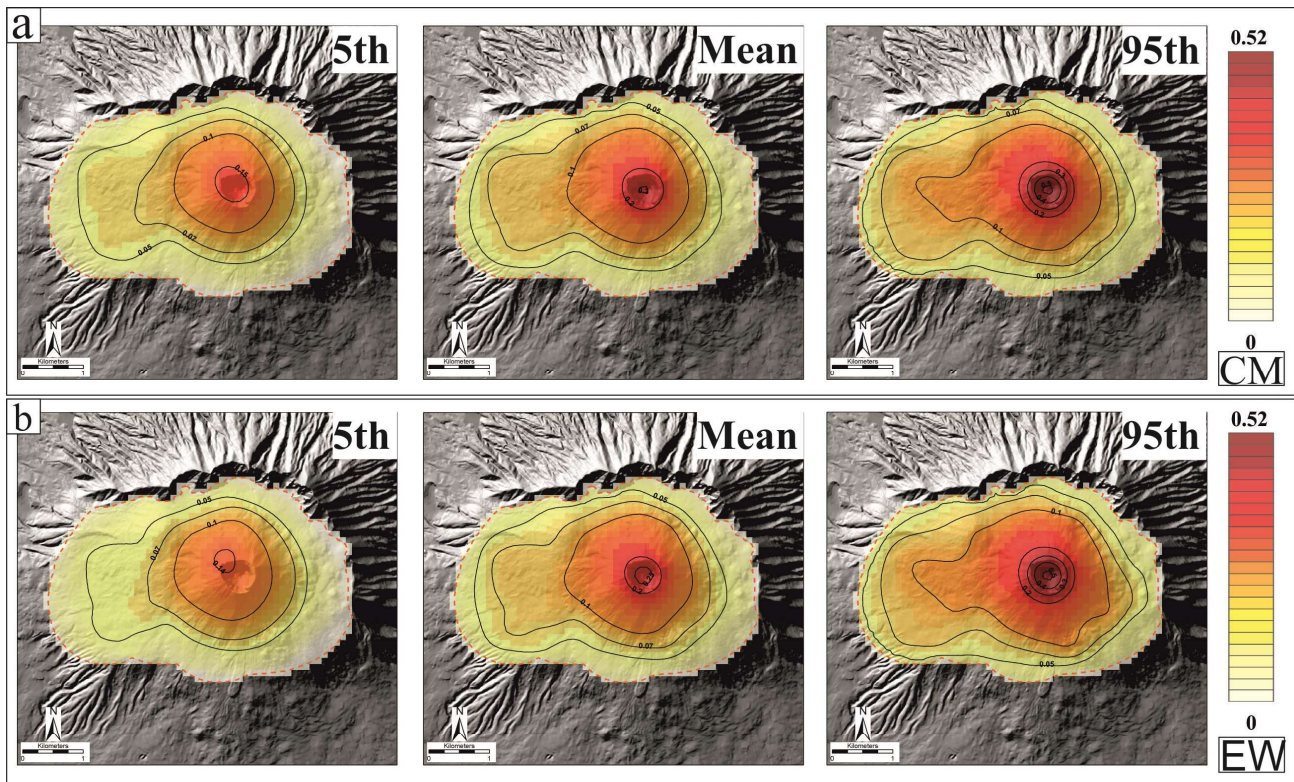


Fig. 8.7: a) maps of the 5th, mean and 95th percentiles obtained after the Classical Model (CM) expert pooling technique without the “Deep Faults” dataset; b) maps of the 5th, mean and 95th percentiles obtained after the Equal Weight (EW) expert pooling technique without the “Deep Faults” dataset. Cellsize is 100 m; values are probability percentages per cell; contour lines enclose areas where cell values are higher than the value of the line itself.

8.2.7 Maps obtained considering caldera enlargements in case of a Plinian eruption only

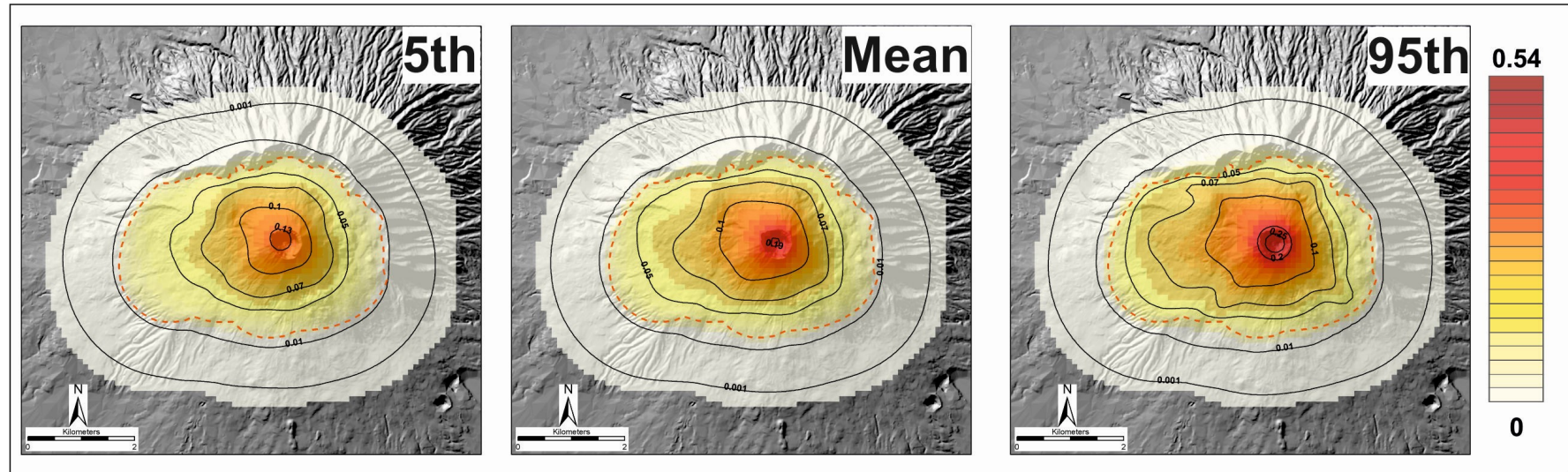


Fig. 8.8: Vent opening location probability maps with caldera enlargement effects included. Maps are the 5th, mean and 95th percentile probability values derived from the reference Classical Model (CM) weights for a Plinian eruption alone. Cell size is 100 m; values are probability percentages per cell; contour lines enclose areas where cell probabilities exceed the contour value.

8.3 Maximum runout for PDCs from the Avellino eruption, the AD 472 Pollena eruption and the AD 1631 eruption

This section groups additional analyses that have been performed in order to define maximum runouts and related invasion areas for PDCs from 3 different eruptions at SV, namely the Avellino, the AD 472 “Pollena” and the AD 1631 eruptions. Particularly, these outlines are related to either a single PDC lobe (for the AD 472 “Pollena” Fg “Cupa Olivella”), to the cumulative PDCs from a single eruption (for the AD 472 “Pollena” and for the AD 1631 eruptions) or to both a single eruptive unit and to the whole PDCs from that eruption (for the Avellino eruption).

The approach used for the definition of these outlines is the same as the one described in Section 4.3.1

8.3.1 Avellino

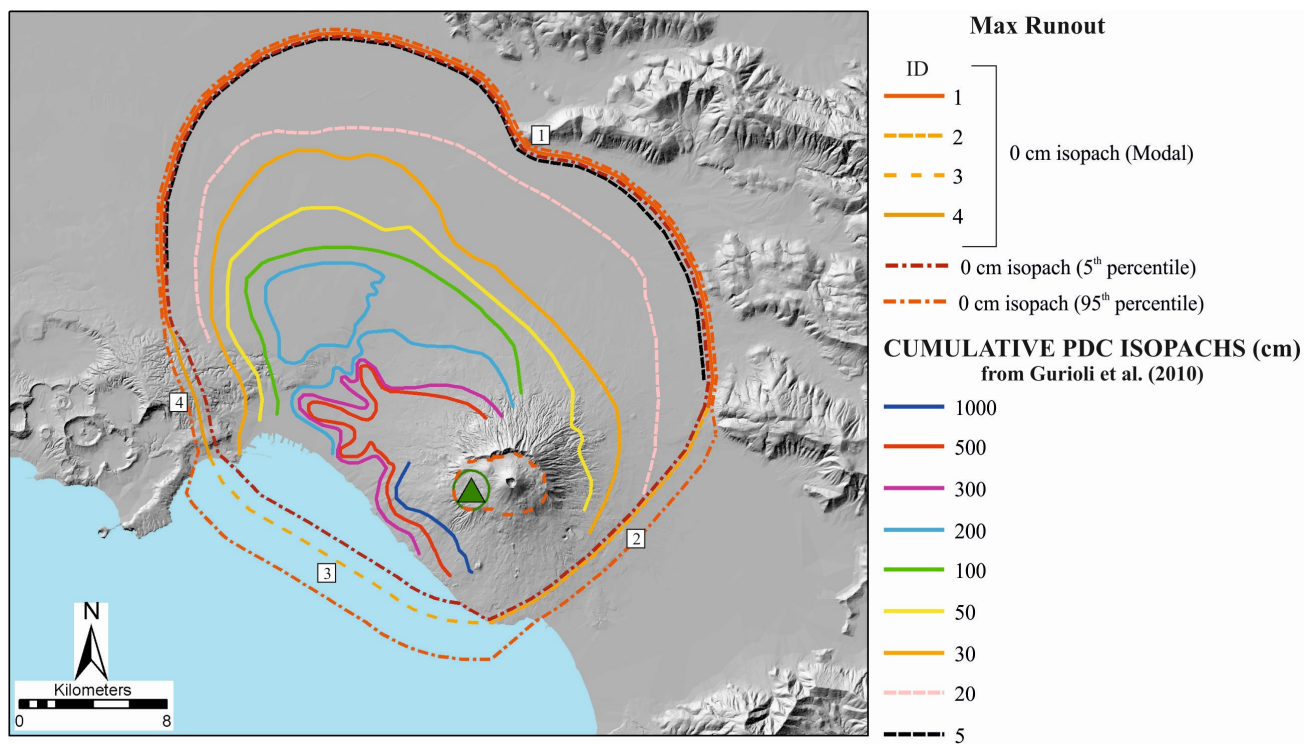


Fig. 8.9: maximum runouts of cumulative PDCs belonging to the Avellino eruption.

0 cm isopach

Modal value ID 1: inland part starting from WNW to ENE, good constraints are represented by the relief and the 5 cm isopach (Gurioli et al. 2010), uncertainty fairly low. 5th percentile –200m; 95th percentile +200m.

Modal value ID 2: inland part toward SE, the only constraints are the 20, 30 and 5 cm isopachs, uncertainty is moderate. 5th percentile –200m; 95th percentile +1000m.

Modal value ID 3: seaward part, uncertainty is moderate-high. 5th percentile -1000m; 95th percentile +2000m.

Modal value ID 4: inland part toward SW, the only constraint is the relief, uncertainty is moderate. 5th percentile -500m; 95th percentile +500m

8.3.2 Pollena

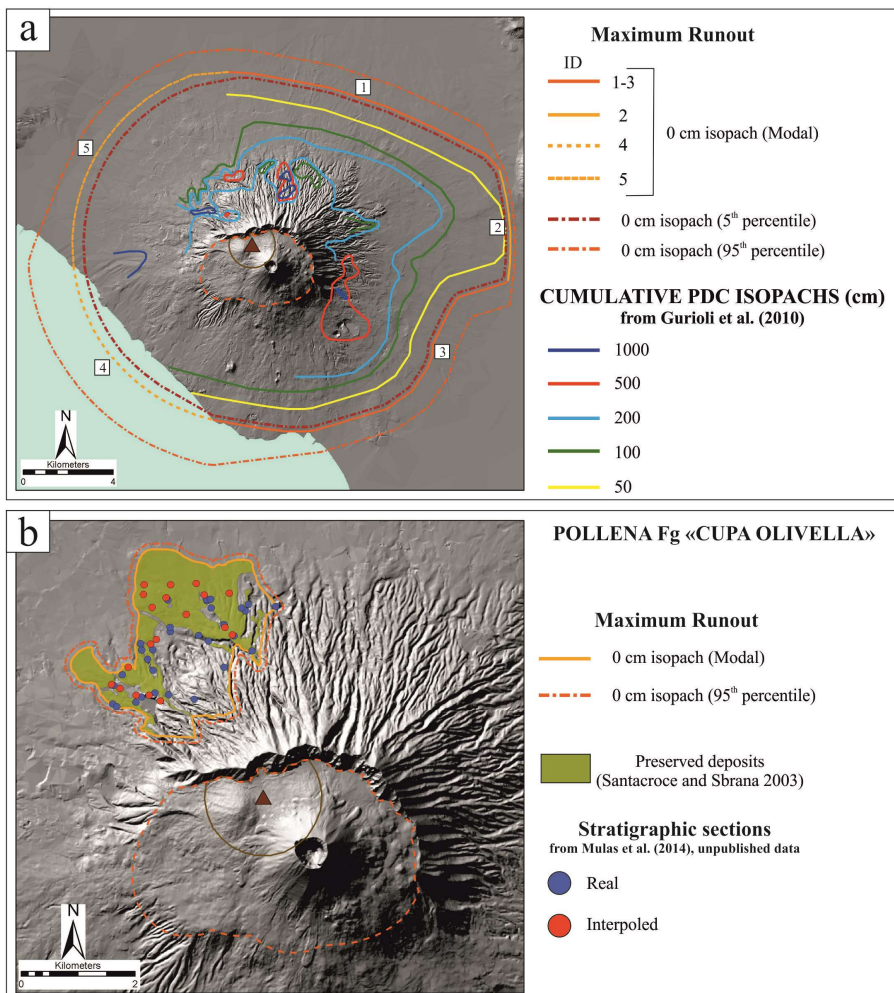


Fig. 8.10: a) maximum runouts of cumulative PDCs belonging to the AD 472 Pollena eruption; b) maximum runout of the Fg “Cupa Olivella” PDC lobe belonging to the AD 472 Pollena eruption.

0 cm isopach (whole eruption)

Modal value ID 1 and 3: two inland part toward SE and NE respectively, the only constraint is the 50 cm isopach, uncertainty is moderate. 5th percentile –200m; 95th percentile +1000m.

Modal value ID 2: small inland part toward E, good constraints are the 50 cm isopach and the maximum runout value of 11.5 km (Gurioli et al. 2010), uncertainty is fairly low. 5th percentile – 200m; 95th percentile – 200m.

Modal value ID 4: seaward part, uncertainty is moderate. 5th percentile –500m; 95th percentile +2000m.

Modal value ID 5: inland part toward W, the only constraint is the 50 cm isopach (prolonged toward S and SW), uncertainty is moderate-high. 5th percentile –500m; 95th percentile +1000m.

0 cm isopach (Fg “Cupa Olivella” PDC lobe)

Similarly to the “Cupa Fontana” PDC lobe (see section 4.5.1), also for the “Cupa Olivella” PDC lobe, only one segment was defined for the whole “Modal” outline, and it was drawn mostly considering the outline of the preserved deposits of PDC units belonging to the AD 472 eruption displayed in the Santacroce and Sbrana (2003) geological map. The upper 95th percentile uncertainty bound was place at a fixed distance of +200 m with respect to the “Modal” maximum runout outline.

8.3.3 AD1631

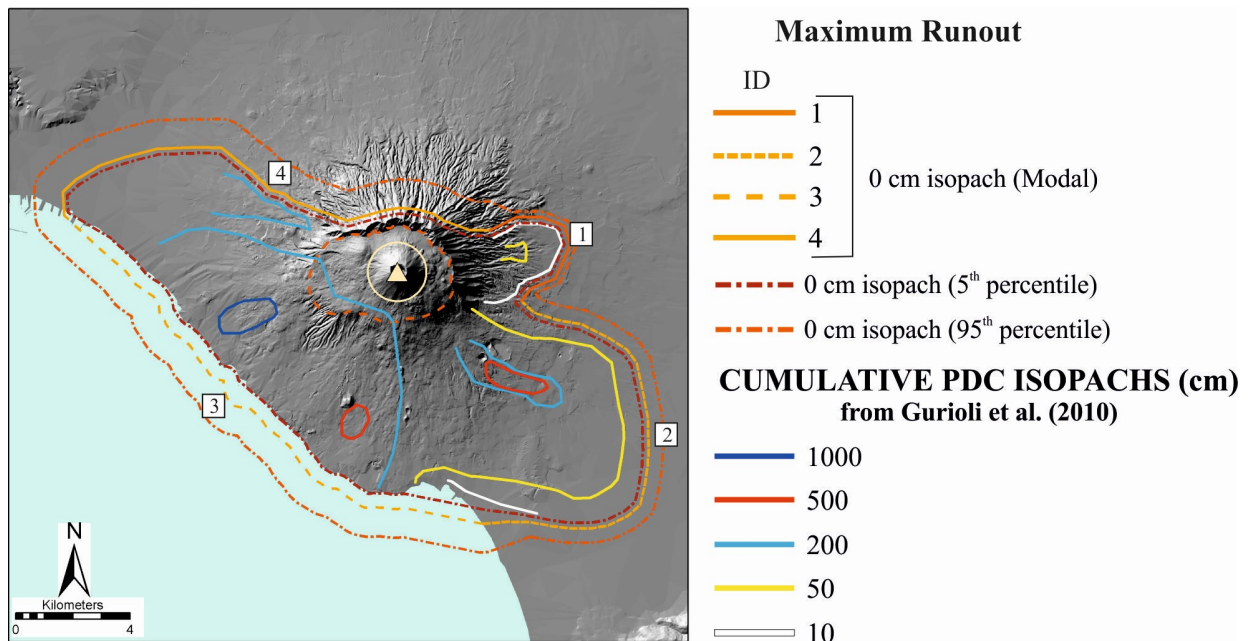


Fig. 8.11: maximum runouts of cumulative PDCs belonging to the AD 1631 eruption.

0 cm isopach

Modal value ID 1: PDC toward NE, good constraints are the 10 cm isopach and the maximum runout value of 10 km (Gurioli et al. 2010), uncertainty fairly low. 5th percentile –200m; 95th percentile +200m.

Modal value ID 2: inland part toward E, the only constraint are the 50 cm and the 10 cm isopachs, uncertainty is moderate-low. 5th percentile –200m; 95th percentile +500m.

Modal value ID 3: seaward part, uncertainty is moderate. In this case uncertainty is lower (with respect to other eruptions) since historical chronicles and paintings show clearly how PDCs stop in correspondence of the coastline. 5th percentile -500m; 95th percentile +1000m.

Modal value ID 4: inland part toward WNW, the only constraint is the 200 cm isopach, uncertainty is moderate. 5^o percentile –200m; 95^o percentile +1000m.

8.4 Sections used for volume and TGSD estimations

8.4.1 EU3pf

Site	Section Name	X UTM coordinate (m)	Y UTM coordinate (m)	Unit	Facies	Sample	Sample location	Section Thickness (cm)
Boscariello	Sez24_EU3pf_LG	456202.168	4521097.160	EU3pf	-	-	-	8
Boscoreale (a)	Sez110a_EU3pf_LG	455591.596	4513406.080	EU3pf	-	-	-	22
Boscoreale (b)	Sez110b_EU3pf_LG	454091.856	4513941.220	EU3pf	-	-	-	500
Camaldoli	Sez83_EU3pf_LG	449693.780	4514655.170	EU3pf	-	-	-	55
Cap. S. Angelo	Sez116_EU3pf_LG	449733.504	4522191.840	EU3pf	-	-	-	250
Casa De Falco	Sez60_EU3pf_LG	456905.518	4515313.531	EU3pf	-	VS98-595	-	40
				EU3pf	-	VS99-700	Morphological high	
				EU3pf	-	VS99-701a	Morphological high	
				EU3pf	-	VS99-701b	Morphological high	
				EU3pf	lensL	VS99-702	Lens on top of the section in a topographic low	
Casa Gentile	Sez89_EU3pf_LG	451383.932	4523461.640	EU3pf	-	-	-	350
Casa Vigna	Sez117_EU3pf_LG	449472.369	4522302.370	EU3pf	-	-	-	30
Case Pentelete	Sez118_EU3pf_LG	455442.269	4523023.660	EU3pf	-	-	-	4
Case Sarcinello	Sez119_EU3pf_LG	448420.505	4518322.440	EU3pf	-	-	-	60
Casello	Sez108_EU3pf_LG	455584.018	4521354.870	EU3pf	-	-	-	13
Casino	Sez120_EU3pf_LG	448378.784	4521818.390	EU3pf	-	-	-	220
Cava Fido	Sez121_EU3pf_LG	448491.801	4520730.300	EU3pf	-	-	-	800
Cava Molara	Sez06_EU3pf_LG	454711.468	4516858.770	EU3pf	-	-	-	150
Cava Montone	Sez57_EU3pf_LG	448019.799	4521078.940	EU3pf	-	-	-	570
Cava Pollena (AT)	Sez06_EU3pf_AT	448586.737	4522026.195	EU3pf - LC3	//sLT to xsLT	PPM19	Pumice-rich level	98
				EU3pf - LC3	//sLT to xsLT	PPM20	Ash-rich level	
Cava Pollena (LG - a)	Sez54a_EU3pf_LG	448612.743	4521612.600	EU3pf	-	-	-	610
Cava Pollena (LG - b)	Sez54b_EU3pf_LG	448382.501	4521682.750	EU3pf	-	-	-	200

Cava Pollena (LG - c)	Sez54c_EU3pf_LG	448129.045	4522012.200	EU3pf	-	-	-	500
Cava Pollena (LG - d)	Sez54d_EU3pf_LG	447783.384	4522151.170	EU3pf	-	-	-	250
Cava Pollena (LG - e)	Sez54e_EU3pf_LG	447878.714	4522281.090	EU3pf	-	-	-	260
Cava Pollena (LG - f)	Sez54f_EU3pf_LG	448053.942	4521957.980	EU3pf	-	-	-	200
Cava Pollena (LG - g)	Sez54g_EU3pf_LG	448219.155	4521793.870	EU3pf	-	-	-	250
Cava Pollena (LG - h)	Sez54h_EU3pf_LG	448567.319	4521837.963	EU3pf	mlBr	VS98-574	Lithic-rich unit atop a morphological high	-
				EU3pf	mlBr	VS98-575	Lithic-rich unit in a topographic low	
				EU3pf - LC5	dbLT to bLT	VS99-679	-	
				EU3pf - LC5	dbLT to bLT	VS99-680	-	
				EU3pf - LC5	dbLT to bLT	VS99-681	-	
				EU3pf - LC5	dbLT to bLT	VS99-682	Top of the section	
				EU3pf - LC1	mLT to faintly bLT	VS99-714	Topographic low	
				EU3pf	-	VS99-715	Fines-rich level on top of the section	
				EU3pf - LC5	dbLT to bLT	VS99-716	Morphological high	
Cava Pozzelle (AT)	Sez02_EU3pf_AT	454678.884	4516418.636	EU3pf	-	VS99-717	-	250
				EU3pf - C3	//sT to xsT	PPM5	Bottom of section	
				EU3pf - LC1	mLT to faintly bLT	PPM6	Intermediate part of section	
				EU3pf - LC3	//sLT to xsLT	PPM7	Top of section (pumice-rich)	

				EU3pf - LC3	//sLT to xsLT	PPM8	Top of section (ash-rich)	
				EU3pf - C3	//sT to xsT	VS98-603	Bottom of section	
				EU3pf	-	VS98-604	Intermediate part of the section	
Cava Pozzelle (LG)	Sez08b_EU3pf_LG	455362.424	4516296.142	EU3pf	-	VS98-605	Intermediate part of the section	486
				EU3pf	-	VS98-606	Top of section	
				EU3pf	-	VS99-636	Dune on top of section	
Cava S. Sebastiano	Sez05_EU3pf_AT	447366.037	4520443.239	EU3pf - LC1	mLT to faintly bLT	PPM17	Bottom of section	500
				EU3pf - LC5	dbLT to bLT	PPM18	Top of section	
Cava S. Vito	Sez56_EU3pf_LG	447985.482	4520167.740	EU3pf	-	-	-	400
Cava Terzigno	Sez07_EU3pf_LG	457476.599	4516499.850	EU3pf	-	VS91-75	-	55
Cupa Falanga	Sez51_EU3pf_LG	448773.213	4516960.730	EU3pf	-	-	-	100
Cupa Olivella (a)	Sez87a_EU3pf_LG	451107.025	4522310.390	EU3pf	-	-	-	6
Cupa Olivella (b)	Sez87b_EU3pf_LG	450709.138	4522729.500	EU3pf	-	-	-	650
Cupa Olivella (c)	Sez88a_EU3pf_LG	450210.892	4523052.770	EU3pf	-	-	-	290
Cupa Olivella (d)	Sez88b_EU3pf_LG	449896.300	4523504.650	EU3pf	-	-	-	60
				EU3pf - LC1	mLT to faintly bLT	VS98-598	Morphological high	
Discarica Pozzelle	Sez08a_EU3pf_LG	454842.034	4516376.680	EU3pf - LC1	mLT to faintly bLT	VS98-599	Basal part of a topographic low	300
				EU3pf - LC2	mLT _(nl,ip)	VS98-600	Intermediate part of a topographic low	

				EU3pf - LC2	mLT _(nl,ip)	VS98-601	Top part of a topographic low	
				EU3pf - LC1	mLT to faintly bLT	VS98-602	Basal part of a topographic low	
				EU3pf - LC5	dbLT to bLT	VS98-603a	Intermediate part of a topographic low	
				EU3pf	-	VS99-649	-	
Dosso Scaudella (a)	Sez122a_EU3pf_LG	454128.097	4521729.090	EU3pf	-	-	-	2
Dosso Scaudella (b)	Sez122b_EU3pf_LG	455298.574	4522059.090	EU3pf	-	-	-	4
Ercolano - Angolo terme	Sez70_EU3pf_LG	444937.181	4517317.065	EU3pf - LC6	mIBr _{fpoor}	ER 96-7	-	-
Ercolano - Base delle terme	Sez69_EU3pf_LG	444894.524	4517338.006	EU3pf - LC1	mLT to faintly bLT	ER 96-6	-	-
Ercolano - Cardo III	Sez67_EU3pf_LG	444814.549	4517454.11	EU3pf - LC2	mLT _(nl,ip)	ER 96-38	Bottom of section	-
Ercolano - Palestra	Sez66_EU3pf_LG	444998.294	4517358.826	EU3pf - LC2	mLT _(nl,ip)	ER 96-16	-	200
				EU3pf - LC2	mLT _(nl,ip)	ER 97-65	Bottom of section	
				EU3pf - LC2	mLT _(nl,ip)	ER 97-66	Intermediate part of the section	
				EU3pf - LC2	mLT _(nl,ip)	ER 97-67	Top of section	
Ercolano - Parete a mare (lapide)	Sez72_EU3pf_LG	444864.423	4517326.498	EU3pf - LC2	mLT _(nl,ip)	ER 96-12	-	500
Ercolano - Parete a mare (tunnel)	Sez71_EU3pf_LG	444860.776	4517348.18	EU3pf - LC6	mIBr _{fpoor}	ER 96-10	-	-
				EU3pf - LC6	mIBr _{fpoor}	ER 97-64	-	-
Ercolano -	Sez73_EU3pf_LG	444957.333	4517323.191	EU3pf - LC2	mLT _(nl,ip)	ER 97-68	-	-

Confine giardino di Telefo				EU3pf - LC2	mLT _(nl,ip)	ER 97-69	-	
				EU3pf - LC2	mLT _(nl,ip)	ER 97-70	-	
Fondovalle	Sez123_EU3pf_LG	448747.58	4518057.22	EU3pf	-	-	-	140
Fontana	Sez98_EU3pf_LG	454193.563	4521435.060	EU3pf	-	-	-	230
In cima Lagno Pollena	Sez124_EU3pf_LG	448957.210	4521606.750	EU3pf	-	-	-	1400
La Castelluccia	Sez49_EU3pf_LG	448701.509	4521230.870	EU3pf	-	-	-	200
La Zazzera	Sez125_EU3pf_LG	449633.775	4523360.310	EU3pf	-	-	-	70
Lagno Amendolare	Sez04_EU3pf_AT	449772.124	4522831.704	EU3pf - LC5	dbLT to bLT	PPM13	Bottom of section	800
				EU3pf - LC1	mLT to faintly bLT	PPM14	Top of section	
Lagno Cavone	Sez91_EU3pf_LG	452595.737	4523167.660	EU3pf	-	-	-	200
Lagno Molaro (AT - a)	Sez01a_EU3pf_AT	448249.236	4521608.801	EU3pf - C1	mT to faintly sT	PPM1	Bottom of section	400
				EU3pf - LC1	mLT to faintly bLT	PPM2	Top of section	
Lagno Molaro (AT - b)	Sez01b_EU3pf_AT	448607.940	4521289.789	EU3pf - LC5	dbLT to bLT	PPM11	-	150
Lagno Molaro (AT - c)	Sez01c_EU3pf_AT	449603.978	4521422.687	EU3pf - LC5	dbLT to bLT	PPM21	Bottom of section	199
				EU3pf - LC1	mLT to faintly bLT	PPM22	Intermediate part (47 cm thick)	
				EU3pf - LC1	mLT to faintly bLT	PPM23	Intermediate part of section	
				EU3pf - C1	mT to faintly sT	PPM24	Top of section	
Lagno Molaro (LG)	Sez62_EU3pf_LG	448602.000	4521200.000	EU3pf	lensL	VS99-664	Lens	
				EU3pf - LC1	mLT to faintly bLT	VS99-665	Intermediate part of the section	

				EU3pf	-	VS99-666	Fines-rich level on top of the section	
				EU3pf	lensL	VS99-667	Lens at the bottom of the section	
				EU3pf - C1	mT to faintly sT	VS99-668	Above the lens of VS99-669 sample	
				EU3pf	lensL	VS99-669	Thick lens in the intermediate part of the section	
				EU3pf	lensL	VS99-670	Uppermost lens of the section	
						VS99-671	Bottom of section	
				EU3pf - LC1	mLT to faintly bLT	VS99-672	Intermediate part of the section	
						VS99-673	Top of the section	
				EU3pf - LC1	mLT to faintly bLT	VS99-674	Top of the section	
Lagno Pollena (a)	Sez84_EU3pf_LG	449046.952	4521916.480	EU3pf	-	-	-	140
Lagno Pollena (b)	Sez84b_EU3pf_LG	448753.060	4522128.600	EU3pf	-	-	-	125
Lagno Pollena (c)	Sez85_EU3pf_LG	448427.512	4522116.780	EU3pf	-	-	-	70
Lagno Pollena (d)	Sez86_EU3pf_LG	448226.880	4522103.000	EU3pf	-	-	-	160
Lave 1872-1944	Sez126_EU3pf_LG	448615.116	4520797.060	EU3pf	-	-	-	320

Masseria Carotenuto (a)	Sez09a_EU3pf_LG	458551.110	4514620.855	EU3pf	-	VS99-621	Section located atop a morphological high	-
Masseria Carotenuto (b)	Sez09b_EU3pf_LG	454827.149	4515458.390	EU3pf	-	-	-	150
Masseria Lepre (a)	Sez127a_EU3pf_LG	448773.356	4522344.360	EU3pf	-	-	-	105
Masseria Lepre (b)	Sez127b_EU3pf_LG	448786.728	4522589.770	EU3pf	-	-	-	150
Montevergine (a)	Sez02a_EU3pf_LG	455263.653	4521614.330	EU3pf	-	-	-	22
Montevergine (b)	Sez02b_EU3pf_LG	455940.135	4521938.270	EU3pf	-	-	-	38
Oplontis	Sez11_EU3pf_LG	453778.229	4512032.770	EU3pf	-	RRR3	-	34
					-	RRR5	-	
					-	RRR7	-	
					-	VES 89-1	-	
					-	VES 89-2	-	
Osservatorio	Sez128_EU3pf_LG	449103.329	4520091.940	EU3pf	-	-	-	450
Ottaviano (b)	Sez29b_EU3pf_LG	455908.097	4522213.360	EU3pf	-	-	-	250
Palmentello	Sez92_EU3pf_LG	452846.269	4523300.030	EU3pf	-	-	-	3
Piscinale (a)	Sez105_EU3pf_LG	454925.168	4520402.300	EU3pf	-	-	-	40
Pollena	Sez129_EU3pf_LG	449054.084	4523565.640	EU3pf	-	-	-	150
Pollena Trocchia (a)	Sez130a_EU3pf_LG	449056.175	4522698.150	EU3pf	-	-	-	160
Pollena Trocchia (b)	Sez130b_EU3pf_LG	448726.911	4522827.650	EU3pf	-	-	-	160
Pollena Trocchia (c)	Sez130c_EU3pf_LG	447967.966	4522873.450	EU3pf	-	-	-	200
Pompeii - Necropolis	Sez13_EU3pf_LG	457386.508	4511285.500	EU3pf - LC1	mLT to faintly bLT	ves89-38	Upper 2 cm	5
				EU3pf - LC6	mLBr _{fpoor}	ves89-39	Intermediate 1 cm	
				EU3pf - LC1	mLT to faintly bLT	ves89-40	Lower 2 cm	

Pompeii - Porta Vesuvio	Sez18_EU3pf_LG	456489.561	4511661.330	EU3pf	-	-	-	5
Pompeii - Villa dei Misteri	Sez12b_EU3pf_LG	455972.250	4511708.900	EU3pf	-	-	-	12
Re della Vigna (a)	Sez95_EU3pf_LG	453779.398	4522104.010	EU3pf	-	-	-	80
Re della Vigna (d)	Sez97b_EU3pf_LG	453514.772	4522804.440	EU3pf	-	-	-	95
San Pietro (b)	Sez05b_EU3pf_LG	455420.137	4518939.480	EU3pf	-	-	-	300
San Severino (a)	Sez131a_EU3pf_LG	454311.849	4522053.280	EU3pf	-	-	-	6
San Severino (b)	Sez131b_EU3pf_LG	454293.028	4522265.270	EU3pf	-	-	-	50
Scavoletta (a)	Sez132a_EU3pf_LG	453740.110	4521757.670	EU3pf	-	-	-	10
Scavoletta (b)	Sez132b_EU3pf_LG	453874.527	4521831.420	EU3pf	-	-	-	30
Scudieri	Sez46_EU3pf_LG	456206.000	4520899.000	EU3pf	lensL	VS99-709bis	Lens at the bottom of the section	35
				EU3pf - LC4	xsLT regressive	VS99-710	Fines-rich level on top of the section	
Sez 57D	Sez133_EU3pf_LG	448670.486	4517505.250	EU3pf	-	-	-	30
Sez 69D	Sez81_EU3pf_LG	448496.051	4517782.580	EU3pf	-	-	-	108
Sez 72D	Sez82_EU3pf_LG	448425.190	4517461.580	EU3pf	-	-	-	240
Sez DR10	Sez134_EU3pf_LG	454646.659	4522923.750	EU3pf	-	-	-	150
Sopra Case Brunelle	Sez135_EU3pf_LG	448581.877	4519861.810	EU3pf	-	-	-	120
Sopra Castello	Sez136_EU3pf_LG	449379.694	4521173.750	EU3pf	-	-	-	200
Sopra Masseria Lepre	Sez137_EU3pf_LG	449039.524	4522202.910	EU3pf	-	-	-	20
Sopra Pollena	Sez138_EU3pf_LG	448627.653	4522411.310	EU3pf	-	-	-	48
Sotto Chianatelle	Sez139_EU3pf_LG	449568.502	4521514.970	EU3pf	-	-	-	300
Sotto Cognoli	Sez140_EU3pf_LG	449115.148	4520772.000	EU3pf	-	-	-	150
Strada Osservatorio	Sez141_EU3pf_LG	448463.862	4519419.020	EU3pf	-	-	-	140
Torretta Scozia	Sez90_EU3pf_LG	451855.362	4523763.600	EU3pf	-	-	-	5

Traianello (a)	Sez99_EU3pf_LG	453774.473	4523612.490	EU3pf	-	-	-	110
Traianello (b)	Sez100_EU3pf_LG	453797.903	4523784.710	EU3pf	-	-	-	5
Traversa Forestale	Sez142_EU3pf_LG	453498.448	4519910.850	EU3pf	-	-	-	50
Trecase	Sez111_EU3pf_LG	452818.355	4514023.940	EU3pf	-	-	-	42
Valle Delizie (a)	Sez103_EU3pf_LG	454405.426	4520229.120	EU3pf	-	-	-	10
Vallone Gauda	Sez143_EU3pf_LG	451830.302	4522851.970	EU3pf	-	-	-	100
Vallone Vigna (a)	Sez144a_EU3pf_LG	449929.482	4521728.030	EU3pf	-	-	-	200
Vallone Vigna (b)	Sez144b_EU3pf_LG	449686.015	4521846.130	EU3pf	-	-	-	50
Vergine di Castello	Sez01_EU3pf_LG	454135.189	4522033.810	EU3pf	-	-	-	25
Via Caracciolo	Sez52_EU3pf_LG	448853.423	4522229.500	EU3pf	-	-	-	50
Via Cascetta	Sez48_EU3pf_LG	450973.280	4523584.870	EU3pf	-	-	-	30
Villa Regina	Sez10_EU3pf_LG	455467.664	4512610.150	-	-	VS91-19	-	19.5
Villa Sora	Sez30_EU3pf_LG	446755.716	4514815.530	EU3pf	-	-	-	195
Villa Telesi	Sez04_EU3pf_LG	455992.859	4519299.587	EU3pf - LC6	mlBr _{fpoor}	VS99-705	Lithic-rich level at the bottom of the section	30
				EU3pf	lensL	VS99-706	Lens at the bottom of the section	
				EU3pf - LC5	dbLT to bLT	VS99-707	Cineritic body in the middle of the section	
				EU3pf	lensL	VS99-708	Lens on top of the section	
				EU3pf - C1	mT to faintly sT	VS99-709	Fines-rich level on top of the section	
Voltosanto	Sez26_EU3pf_LG	449677.072	4522882.881	EU3pf - LC2	mLT _i	VS99-718	Pumice-rich level	131
				EU3pf - LC2	mLT _(nl,ip)	VS99-719	Bottom of section	

				EU3pf - LC2	mLT _(nl,ip)	VS99-720	Intermediate part of the section	
				EU3pf - LC2	mLT _(nl,ip)	VS99-721	Top of the section	
				EU3pf - LC2	mLT _i	VS99-722	Uppermost Pumice-rich level (basal fine)	
				EU3pf - LC2	mLT _(nl,ip)	VS99-723	Uppermost Pumice-rich level (base)	
				EU3pf - LC2	mLT _(nl,ip)	VS99-724	Uppermost Pumice-rich level (intermediate)	
				EU3pf - LC2	mLT _(nl,ip)	VS99-725	Uppermost Pumice-rich level (top)	
				EU3pf	mIBr	VS99-726	Lithic-rich level on top of the section	
Zabatta, fabbrica del fuoco	Sez03_EU3pf_LG	455186.611	4521469.260	EU3pf	-	-	-	35

Table 8.4: list of stratigraphic sections and samples used for volume and TGSD estimations for the EU3pf unit. Sections with the suffix “LG” derive from Gurioli (1999).

8.4.2 EU4

Site	Section Name	X UTM coordinate (m)	Y UTM coordinate (m)	Unit	Facies	Sample	Sample location	Partial thicknesses (cm)	Thicknesses levels b and c (cm)	Max total thickness (cm)
Anгри	Sez42_EU4_LG	463788.326	4509863.891	EU4a	-	-	-	5.5-9.5	21.5	27
				EU4b	-	VS99-620	-	11.5		
				EU4c	-	-	-	10		
Boscariello	Sez24_EU4_LG	456202.168	4521097.160	EU4a	-	-	-	8	100	108
				EU4b	-	-	-	100		
				EU4c	-	-	-	-		
Boscoreale (a)	Sez110a_EU4_LG	455591.596	4513406.080	EU4a	-	-	-	<u>38</u>	<u>152</u>	190
				EU4b	-	-	-	<u>142</u>		
				EU4c	-	-	-	<u>10</u>		
Boscoreale, campo sportivo	Sez23_EU4_LG	455023.223	4514384.000	EU4a	-	-	-	3-5	30-100	105
				EU4b	-	-	-	20-70		
				EU4c	-	-	-	10-30		
Boscotrecase	Sez115_EU4_LG	454112.936	4514003.894	EU4a	-	-	-	-	500	500
				EU4b	-	-	-	500		
				EU4c	-	-	-	-		
Brancaccio	Sez31_EU4_LG	460215.893	4514530.900	EU4a	-	-	-	6	33	39
				EU4b	-	-	-	16		
				EU4c	-	-	-	17		
Camaldoli	Sez83_EU4_LG	449693.780	4514655.170	EU4a	-	-	-	<u>30</u>	<u>100</u>	130
				EU4b	-	-	-	<u>93</u>		
				EU4c	-	-	-	<u>7</u>		
Caprai	Sez102_EU4_LG	454447.195	4520634.520	EU4a	-	-	-	<u>5</u>	<u>20</u>	25
				EU4b	-	-	-	<u>19</u>		
				EU4c	-	-	-	<u>1</u>		
Carcovella	Sez101_EU4_LG	454466.603	4521158.590	EU4a	-	-	-	<u>50</u>	<u>200</u>	250
				EU4b	-	-	-	<u>186</u>		
				EU4c	-	-	-	<u>14</u>		
Casa De Falco	Sez60_EU4_LG	456424.684	4514964.260	EU4a	-	-	-	<u>32</u>	<u>126</u>	158
				EU4b	-	VS99-623	-	<u>115</u>		
				EU4c	-	VS99-624	-	<u>9</u>		
Casa Gentile	Sez89_EU4_LG	451383.932	4523461.640	EU4a	-	-	-	-	121	121
				EU4b	-	-	-	113		

				EU4c	-	-	-	8		
				EU4a	-	-	-	<u>29</u>		
Casello	Sez108_EU4_LG	455584.018	4521354.870	EU4b	-	-	-	<u>75</u>	<u>80</u>	100
				EU4c	-	-	-	<u>5</u>		
				EU4a	-	-	-	2		
Cava Iovino	Sez53_EU4_LG	464126.147	4520777.806	EU4b	-	-	-	8	8	10
				EU4c	-	-	-	-		
				EU4a	-	-	-	0-70		
Cava Molara	Sez06_EU4_LG	454711.468	4516858.770	EU4b	-	-	-	150-200	152-204	270
				EU4c	-	-	-	2-4		
				EU4a	-	-	-	2		
Cava Montone	Sez57_EU4_LG	448019.799	4521078.940	EU4b	-	-	-	98	98	100
				EU4c	-	-	-	-		
				EU4a	-	-	-	-		
Cava Pollena (a)	Sez54_EU4_LG	448612.743	4521612.600	EU4b	-	-	-	71-115	73-117	117
				EU4c	-	-	-	2		
				EU4a	-	-	-	-		
Cava Pollena (c)	Sez54c_EU4_LG	448129.045	4522012.200	EU4b	-	-	-	46.5	50	50
				EU4c	-	-	-	3.5		
				EU4a	-	-	-	10-60		
Cava Pozzelle (LG)	Sez08b_EU4_LG	455356.151	4516170.150	EU4b	-	-	-	0-150	0-150	210
				EU4c	-	-	-	-		
				EU4a	-	-	-	40		
Cava Pozzelle (AT)	Sez02_EU4_AT	454678.884	4516418.636	EU4b	xsLT	PPM10	-	300	300	340
				EU4c	-	-	-	-		
				EU4a	-	-	-	40		
Cava San Vito	Sez56_EU4_LG	447993.000	4518588.000	EU4b	-	-	-	400	400	440
				EU4c	-	-	-	-		
				EU4a	-	-	-	1-5		
					xsLT	VS91-80	0-10 cm above level a			
				EU4b			50 cm above level a	60		
Cava Terzigno	Sez07_EU4_LG	457476.599	4516499.850		xsLT	VS91-81			70-73	85
					mTaccr to dbTaccr	VS91-82	-	10-13		

Cinque Vie	Sez40_EU4_LG	454926.063	4514772.268	EU4a	-	-	-	40	150-160	150-170	190-210
				EU4b	-	-	-	-			
				EU4c	-	-	-	0-10			
Cupa Falanga	Sez51_EU4_LG	448773.213	4516960.730	EU4a	-	-	-	-	45-170	50-175	175
				EU4b	-	-	-	-			
				EU4c	-	-	-	5			
Cupa Olivella (b)	Sez87_EU4_LG	450709.138	4522729.500	EU4a	-	-	-	-	21	22	22
				EU4b	-	-	-	-			
				EU4c	-	-	-	2			
Cupa Olivella (c)	Sez88_EU4_LG	450210.892	4523052.770	EU4a	-	-	-	-	84	90	90
				EU4b	-	-	-	-			
				EU4c	-	-	-	6			
Cupa Pallarino	Sez50_EU4_LG	448109.142	4519501.033	EU4a	-	-	-	-	120-210	120-210	210
				-	VS98-553	0-8 cm from bottom					
				EU4b	-	VS98-554	25-30 cm from bottom				
				-	VS98-555	39-45 cm from bottom					
				-	VS98-556						
Discarica Pozzelle	Sez08a_EU4_LG	455085.668	4516416.460	EU4c	-	-	-	-	150	200	
				EU4a	-	-	-	50			
				EU4b	-	-	-	150			
Ercolano - Decumano Massimo	Sez67_EU4_LG	445003.508	4517614.373	EU4a	-	-	-	-	50-60	50-60	50-60
				EU4b	mLT _i mLT	ER 96-39 ER 96-40	-	-			
				EU4c	-	-	-	-			
Ercolano - Palestra	Sez66_EU4_LG	445002.129	4517352.942	EU4a	-	-	-	-	50-60	50-60	50-60
				EU4b	mLT _i	ER 96-35	-	-			
				EU4c	-	-	-	-			
Ercolano - Parete a mare (lapide)	Sez72_EU4_LG	444860.776	4517348.177	EU4a	-	-	-	-	46.5	50	50
				EU4b	-	-	-	-			
				EU4c	-	-	-	3.5			
Ercolano -	Sez68_EU4_LG	444811.207	4517507.309	EU4a	-	-	-	-	500-535	500-535	

Villa dei Papiri, stanza dei triclini				EU4b	mLT _i	ER 96-61	-	500			
				EU4c	-	-	-	0-35			
Fontana	Sez98_EU4_LG	454193.563	4521435.060	EU4a	-	-	-	<u>7</u>	<u>28</u>	35	
				EU4b	-	-	-	<u>26</u>			
				EU4c	-	-	-	<u>2</u>			
Iervolino	Sez28_EU4_LG	461037.912	4521800.221	EU4a	-	-	-	3.5	6	9.5	
				EU4b	-	-	-	3			
				EU4c	-	-	-	3			
La Castelluccia	Sez49_EU4_LG	448701.509	4521230.870	EU4a	-	-	-	-	160	160	160
					-	VS98-550	Bottom of sigmoidal structure				
				EU4b	-	VS98-551	Bottom of sigmoidal structure				
					-	VS98-552	Top of sigmoidal structure				
				EU4c	-	-	-	-			
Lagno Cavone	Sez91_EU4_LG	452595.737	4523167.660	EU4a	-	-	-	-	60	60	
				EU4b	-	-	-	56			
				EU4c	-	-	-	4			
Lagno Macedonia	Sez47_EU4_LG	453619.209	4523249.620	EU4a	-	-	-	1.5-4	20-90	94	
				EU4b	-	-	-	20-90			
				EU4c	-	-	-	-			
Lagno Molaro (a)	Sez01a_EU4_AT	448249.236	4521608.801	EU4a	-	-	-	-	400	400	400
				EU4b	xsLT	PPM3	Pumiceous part				
					xsLT	PPM4	Cineritic part				
Lagno Molaro (b)	Sez01b_EU4_AT	448607.940	4521289.789	EU4c	-	-	-	-	300	300	300
				EU4a	-	-	-	-			
				EU4b	xsLT	PPM12	-				
Lagno Pollena (a)	Sez84_EU4_LG	449046.952	4521916.480	EU4c	-	-	-	-	50	50	
				EU4a	-	-	-	-			
				EU4b	-	-	-	46.5			

Lagno Pollena (c)	Sez85_EU4_LG	448427.512	4522116.780	EU4a	-	-	-	-	210	210
				EU4b	-	-	-	195		
				EU4c	-	-	-	15		
Lagno Pollena (d)	Sez86_EU4_LG	448229.419	4522108.931	EU4a	-	-	-	-	150	150
				EU4b	-	-	-	140		
				EU4c	-	-	-	10		
Massa	Sez116_EU4_LG	455951.759	4514385.273	EU4a	-	-	-	-	308	308
				EU4b	-	-	-	300		
				EU4c	-	-	-	8		
Masseria Carotenuto (a)	Sez09a_EU4_LG	454827.149	4515458.390	EU4a	-	-	-	18-48	430	470
				-	VS98-504	25-32 cm from level a	400			
				-	VS98-505	42-48 cm from level a				
				-	VS98-506	88-93 cm from level a				
				-	VS98-507	189 cm from level a				
				EU4c	-	-		-		
Masseria Carotenuto (b)	Sez09b_EU4_LG	454617.810	4515723.970	EU4a	-	-	-	70	700	
				EU4b	-	-	-	586		630
				EU4c	-	-	-	44		
Mazzamei	Sez45_EU4_LG	455012.820	4520484.647	EU4a	-	-	-	6	426	
				EU4b	-	-	-	300-420		300-420
				EU4c	-	-	-	-		
Montergine	Sez107_EU4_LG	455070.471	4521360.170	EU4a	-	-	-	24	120	
				EU4b	-	-	-	90		96
				EU4c	-	-	-	6		
Montevergine (a)	Sez02a_EU4_LG	455263.653	4521614.330	EU4a	-	-	-	0-20	125	
				EU4b	-	-	-	50-105		50-105
				EU4c	-	-	-	-		
Montevergine (b)	Sez02b_EU4_LG	455940.135	4521938.270	EU4a	-	-	-	35	175	
				EU4b	-	-	-	130		140
				EU4c	-	-	-	10		
Oplontis	Sez11_EU4_LG	453778.229	4512032.770	EU4a	-	-	-	15	145	160

				EU4b	- lensL	RRR 8 VS92-157	- Within xsLT facies	145		
				EU4c	-	-	-	-		
				EU4a	-	-	-	0-10		
					xsLT	VS91-109	10-20 cm above level a			
Ottaviano (a)	Sez29a_EU4_LG	455122.867	4521419.039	EU4b			30-40 cm above level a	42-51	42-53	63
					xsLT	VS91-110				
				EU4c	-	-	-	0-2		
				EU4a	-	-	-	<u>24</u>		
Ottaviano (b)	Sez29b_EU4_LG	455908.097	4522213.360	EU4b	-	-	-	<u>90</u>	<u>96</u>	120
				EU4c	-	-	-	<u>6</u>		
				EU4a	-	-	-	5-7		
Palazzo Baronale- Codola	Sez43_EU4_LG	470865.601	4512824.034	EU4b	-	VS98-520	-	2	2	9
				EU4c	-	-	-	-		
				EU4a	-	-	-	-		
Palmentiello	Sez92_EU4_LG	452846.269	4523300.030	EU4b	-	-	-	114	122	122
				EU4c	-	-	-	9		
				EU4a	-	-	-	<u>42</u>		
Piscinale (a)	Sez105_EU4_LG	454925.168	4520402.300	EU4b	-	-	-	<u>154</u>	<u>165</u>	207
				EU4c	-	-	-	<u>11</u>		
				EU4a	-	-	-	<u>20</u>		
Piscinale (b)	Sez106_EU4_LG	455557.568	4520655.620	EU4b	-	-	-	<u>75</u>	<u>80</u>	100
				EU4c	-	-	-	<u>5</u>		
				EU4a	-	-	-	5-7		
Pompei - Casa dei Casti Amanti	Sez18i_EU4_LG	456934.423	4511220.071	EU4b	-	-	-	136-144	142-150	155
				EU4c	-	-	-	6-14		
				EU4a	-	-	-	4		
					mLT	Ves89-42	First 8 cm			
Pompei - Necropolis	Sez13_EU4_LG	457386.508	4511285.500	EU4b	//LT	Ves89-43	Intermedia te 7 cm	32	35-50	60
					xsLT	Ves89-44	Last 17 cm			
				EU4c	mT _{accr} to dbT _{accr}	Ves89-45	-	3-18		

Pompei - Porta Ercolano	Sez17_EU4_LG	456195.360	4511338.986	EU4a	-	-	-	3		
					mLT	VS91-68	-			
				EU4b	mLT	VS91-69	-	97	115	130
					mLT	VS91-70	-			
				EU4c	mT _{accr} to dbT _{accr}	VS91-71	-	18		
Pompei - Porta Marina	Sez16_EU4_LG	456363.023	4510971.782	EU4a	-	-	-	-		
				EU4b	-	-	-	36-40	36-40	40
				EU4c	-	-	-	-		
Pompei - Porta Nola	Sez12_EU4_LG	457039.742	4511560.475	EU4a	-	-	-	1-6		
					mLT	VS91-66	10 cm from level a			
				EU4b			40 cm from level a	20-130	25-140	140
					mLT	VS91-67				
				EU4c	-	-	-	5-10		
Pompei - Porta San Paolino	Sez14_EU4_LG	456947.579	4510939.547	EU4a	-	-	-	3-4		
				EU4b	-	VS91-46	-	30-58	40-83	90
				EU4c	-	VS91-47	-	10-25		
Pompei - Porta Vesuvio	Sez18_EU4_LG	456489.561	4511661.330	EU4a	-	-	-	3-5		
				EU4b	-	-	-	80-140	92-143	145
				EU4c	-	-	-	12-13		
Pompei - Via Castricio	Sez15_EU4_LG	457005.353	4511125.462	EU4a	-	-	-	3-4		
				EU4b	-	-	-	60-75	72-93	100
				EU4c	-	-	-	12-17		
Pompei - Villa dei Misteri FS	Sez12a_EU4_LG	456182.648	4510972.279	EU4a	-	-	-	2-3		
				EU4b	-	-	-	38-55	58-75	78
				EU4c	-	-	-	20		
Pompei - Villa dei Misteri	Sez12b_EU4_LG	455972.250	4511708.900	EU4a	-	-	-	<u>15</u>		
				EU4b	-	-	-	<u>56</u>	<u>60</u>	75
				EU4c	-	-	-	<u>4</u>		
Raggi	Sez44_EU4_LG	460031.328	4521522.716	EU4a	-	-	-	2		
				EU4b	-	VS98-524	-	13	13	15
				EU4c	-	-	-	-		
Ristorante Le Giare	Sez109_EU4_LG	454289.535	4515347.380	EU4a	-	-	-	<u>62</u>		
				EU4b	-	-	-	<u>230</u>	<u>248</u>	310
				EU4c	-	-	-	<u>18</u>		

Re della Vigna (a)	Sez95_EU4_LG	453779.398	4522104.010	EU4a	-	-	-	<u>20</u>		
				EU4b	-	-	-	<u>75</u>	<u>80</u>	100
				EU4c	-	-	-	<u>5</u>		
Re della Vigna (b)	Sez96_EU4_LG	453825.624	4522444.670	EU4a	-	-	-	-		
				EU4b	-	-	-	23	25	25
				EU4c	-	-	-	2		
Re della Vigna (c)	Sez97a_EU4_LG	453721.072	4522798.660	EU4a	-	-	-	-		
				EU4b	-	-	-	121	130	130
				EU4c	-	-	-	9		
Ruocco	Sez113_EU4_LG	460470.225	4523222.260	EU4a	-	-	-	2		
				EU4b	-	-	-	8	8	10
				EU4c	-	-	-	-		
San Giuseppe - Ottaviano (Sez R46)	Sez79_EU4_LG	455029.467	4519897.020	EU4a	-	-	-	<u>36</u>		
				EU4b	-	-	-	<u>134</u>	<u>144</u>	180
				EU4c	-	-	-	<u>10</u>		
San Giuseppe - Terzigno	Sez80_EU4_LG	454667.195	4519381.450	EU4a	-	-	-	<u>44</u>		
				EU4b	-	-	-	<u>164</u>	<u>176</u>	220
				EU4c	-	-	-	<u>12</u>		
San Giuseppe Vesuviano	Sez112_EU4_LG	460508.293	4521617.565	EU4a	-	-	-	3		
				EU4b	-	-	-	5	23	26
				EU4c	-	-	-	18		
San Pietro (a)	Sez05a_EU4_LG	455086.810	4518970.560	EU4a	-	-	-	8-20		
				EU4b	-	-	-	300	300	320
				EU4c	-	-	-	-		
San Pietro (b)	Sez05b_EU4_LG	455420.137	4518939.480	EU4a	-	-	-	<u>27</u>		
				EU4b	-	-	-	<u>100</u>	<u>108</u>	135
				EU4c	-	-	-	<u>8</u>		
Santa Maria di Pozzano	Sez19_EU4_LG	452640.363	4503617.326	EU4a	-	-	-	2.5-3		
				EU4b	-	AS6	-	7-8	37-46	49
				EU4c	mT _{accr} to dbT _{accr}	VS89-76	-	30-38		
Santa Maria la Carità	Sez22_EU4_LG	458631.394	4507591.494	EU4a	-	-	-	5-6		
				EU4b	mLT //LT	Ves89-70 Ves89-71	-	17	27	35
				EU4c	mT _{accr} to dbT _{accr}	Ves89-72	-	10		

Sant'Antonio Abate	Sez25_EU4_LG	462163.582	4507322.970	EU4a	-	-	-	5		
				EU4b	-	-	-	7	7	12
				EU4c	-	-	-	-		
Scudieri	Sez46_EU4_LG	456126.388	4520952.720	EU4a	-	-	-	<u>5</u>		
				EU4b	-	-	-	<u>53</u>	<u>73</u>	78
				EU4c	-	-	-	<u>20</u>		
Sez 69D	Sez81_EU4_LG	448496.051	4517782.580	EU4a	-	-	-	<u>40</u>		
				EU4b	-	-	-	<u>150</u>	<u>160</u>	200
				EU4c	-	-	-	<u>10</u>		
Sez 72D	Sez82_EU4_LG	448425.190	4517461.580	EU4a	-	-	-	<u>70</u>		
				EU4b	-	-	-	<u>353</u>	<u>380</u>	450
				EU4c	-	-	-	<u>27</u>		
Sotto Osteria	Sez93_EU4_LG	452906.558	4522745.440	EU4a	-	-	-	-		
				EU4b	-	-	-	93	100	100
				EU4c	-	-	-	7		
Terzigno	Sez03_EU4_AT	456229.751	4519198.278	EU4a	-	-	-	-		
				EU4b	xsLT	PPM16	-	180	180	180
				EU4c	-	-	-	-		
Torre del Greco	Sez114_EU4_LG	448445.417	4518082.718	EU4a	-	-	-	-		
				EU4b	-	-	-	210	210	210
				EU4c	-	-	-	-		
Torretta Scozia	Sez90_EU4_LG	451855.362	4523763.600	EU4a	-	-	-	-		
				EU4b	-	-	-	37	40	40
				EU4c	-	-	-	3		
Traianello (a)	Sez99_EU4_LG	453774.473	4523612.490	EU4a	-	-	-	-		
				EU4b	-	-	-	79	85	85
				EU4c	-	-	-	6		
Traianello (b)	Sez100_EU4_LG	453797.903	4523784.710	EU4a	-	-	-	-		
				EU4b	-	-	-	37	40	40
				EU4c	-	-	-	3		
Tricino	Sez27_EU4_LG	459930.608	4512929.200	EU4a	-	-	-	5.5		
				EU4b	xsLT	VS94-219	-			
				EU4b	mLT	VS98-522	Bottom of section	22-24	40-42	45.5-47.5
Trecase	Sez111_EU4_LG	452818.355	4514023.940	EU4c	-	-	-	18		
				EU4a	-	-	-	<u>12</u>		
				EU4b	-	-	-	<u>45</u>	<u>48</u>	60

				EU4c	-	-	-	<u>3</u>		
Valle Delizie (a)	Sez103_EU4_LG	454405.426	4520229.120	EU4a	-	-	-	<u>40</u>		
				EU4b	-	-	-	<u>150</u>	<u>160</u>	200
				EU4c	-	-	-	<u>10</u>		
				EU4a	-	-	-	<u>70</u>		
Valle Delizie (b)	Sez104_EU4_LG	454403.134	4520341.170	EU4b	-	-	-	<u>335</u>	<u>360</u>	430
				EU4c	-	-	-	<u>25</u>		
				EU4a	-	-	-	<u>6</u>		
Vergine di Castello	Sez01_EU4_LG	454135.189	4522033.810	EU4b	mLT mT _{accr} to dbT _{accr}	VS90-2	-	<u>6</u>	<u>11</u>	17
				EU4c	-	-	-	<u>5</u>		
				EU4a	-	-	-	-		
Via Abbadia	Sez94_EU4_LG	453543.083	4522646.700	EU4b	-	-	-	19	20	20
				EU4c	-	-	-	1		
				EU4a	-	-	-	-		
Via Caracciolo	Sez52_EU4_LG	448853.423	4522229.500	EU4b	-	-	-	60	64	64
				EU4c	-	-	-	4		
				EU4a	-	-	-	-		
Via Cascetta	Sez48_EU4_LG	450973.280	4523584.870	EU4b	lensL	VS98-544	Coarse- rich lens at the bottom of level b			
					-	VS98-545	13-18 cm from level a	46.5	50	50
					-	VS98-546	23-28 cm from level a			
					-	VS98-547	Fine ash- rich layer below pisolitic- rich layer			
				EU4c	mT _{accr} to dbT _{accr}	VS98-548	-	3.5		
Villa di Arianna	Sez41_EU4_LG	457615.619	4505932.092	EU4a	-	-	-	2.5-3		
				EU4b	//sLT mLT _{accr}	VS98-514	Bottom of section	23-26	32-35	38
				EU4c	-	-	-	9		

Villa Regina	Sez10_EU4_LG	455467.664	4512610.150	EU4a	-	-	-	6-11	100-150	105-155	155
					xsLT	VS91-28	30-40 cm above level a				
				EU4b	xsLT	VS91-29	40-45 cm above level a				
					xsLT	VS91-30	110-120 cm above level a				
				EU4c	mT _{accr} to dbT _{accr}	VS91-31	-	5			
Villa Sora	Sez30_EU4_LG	446755.716	4514815.530	EU4a	-	-	-	-	117	125	125
					mLT	VS92-133	0-10 cm from level a				
				EU4 b	mLT	VS92-134	10-20 cm from level a				
					xsLT	VS92-135	40-50 cm from level a				
				EU4c	mT _{accr} to dbT _{accr}	VS92-136	-	8			
Villa Telesi	Sez04_EU4_LG	455781.652	4519439.230	EU4a	-	-	-	5-40	96	100	140
				EU4b	xsLT	VS91-102	40 cm above level a				
				EU4c	-	-	-	4			
Voltosanto	Sez26_EU4_LG	448971.022	4522734.790	EU4a	-	-	-	-	300	300	300
				EU4b	xsLT	VS92-183	-				
					mLT	VS92-184	-				
				EU4c	-	-	-	-			
Zabatta, fabbrica del fuoco	Sez03_EU4_LG	455186.611	4521469.260	EU4a	-	-	-	0-20	30-150	30-150	170
				EU4b	-	-	-				
				EU4c	-	-	-				

Table 8.5: list of stratigraphic sections used for volume estimations. Data provided here are the levels found in the section, the lithofacies, the samples collected, the position within the stratigraphic section where the sample was collected, partial thicknesses of the three levels and the total thickness of the section. Sections where partial thicknesses for levels b and c (Bold) or levels a, b and c (Italic and underlined) have been calculated from the total thickness (for details see text). Sections with the suffix “LG” derive from Gurioli (1999).

8.4.3 Fg “Cupa Fontana”

Section	Type	Sample	Density of the deposit (kg/m ³)	Thickness (cm)
28	Real	VS22	1800	200
33	Real	VS24	1690	400
37	Real	-	1800	80
41	Real	VS45	1770	20
43	Real	VS29	1500	30
44	Real	-	1800	60
119	Interpolated	-	1690	289
120	Interpolated	-	1690	330
121	Interpolated	-	1690	330
122	Interpolated	-	1690	110
123	Interpolated	-	1690	300
124	Interpolated	-	1800	480
125	Interpolated	-	1690	300
126	Interpolated	-	1690	200
127	Interpolated	-	1800	100
128	Interpolated	-	1500	25
129	Interpolated	-	1650	25
130	Interpolated	-	1500	25
131	Interpolated	-	1500	1
132	Interpolated	-	1690	194
133	Interpolated	-	1690	124
134	Interpolated	-	1690	120
135	Interpolated	-	1690	120
136	Interpolated	-	1690	50
137	Interpolated	-	1690	300
138	Interpolated	-	1500	130
139	Interpolated	-	1690	100

Table 8.6: list of samples for the “Cupa Fontana” PDC lobe volume and TGSD calculation. Table includes the type of section (real or interpolated – see text for details), samples collected, the density of the deposit and the thickness of the section.

8.5 List of samples used for TGSD estimation

8.5.1 EU3pf

Sample	Site	Section	Φ (wt%)									
			-4	-3	-2	-1	0	1	2	3	4	5
ER 96-10	Ercolano - Parete a mare (tunnel)	Sez71_EU3pf_LG	7.00	10.74	19.92	18.22	18.82	14.91	6.76	1.88	0.60	1.14
ER 96-12	Ercolano - Parete a mare (lapide)	Sez72_EU3pf_LG	9.51	8.58	13.43	12.33	12.47	11.63	8.81	6.33	5.29	11.62
ER 96-16	Ercolano - Palestra	Sez66_EU3pf_LG	0.59	6.46	9.94	11.83	13.21	13.79	11.13	9.16	7.72	16.17
ER 96-38	Ercolano - Cardo III	Sez67_EU3pf_LG	15.97	5.35	9.08	9.47	11.36	11.00	8.93	7.23	6.26	15.35
ER 96-6	Ercolano - Base delle terme	Sez69_EU3pf_LG	9.42	4.99	7.77	5.76	4.85	6.29	7.92	10.20	14.20	28.61
ER 96-7	Ercolano - Angolo terme	Sez70_EU3pf_LG	0.51	3.26	10.52	13.94	16.33	16.17	11.56	8.40	5.86	13.43
ER 97-64	Ercolano - Parete a mare (tunnel)	Sez71_EU3pf_LG	15.63	18.03	18.22	15.61	12.48	9.52	5.58	2.06	0.81	2.06
ER 97-65	Ercolano - Palestra	Sez66_EU3pf_LG	0.44	3.92	9.06	12.32	13.67	14.18	11.28	8.78	7.35	18.99
ER 97-66	Ercolano - Palestra	Sez66_EU3pf_LG	1.43	6.09	9.10	11.68	13.09	14.15	11.13	8.46	7.12	17.74
ER 97-67	Ercolano - Palestra	Sez66_EU3pf_LG	4.80	8.02	10.12	11.83	12.72	12.69	10.41	7.79	6.35	15.27
ER 97-68	Ercolano - Confine giardino di Telefo	Sez73_EU3pf_LG	11.45	5.02	6.96	7.89	8.91	10.15	10.33	9.48	9.49	20.32
ER 97-69	Ercolano - Confine giardino di Telefo	Sez73_EU3pf_LG	0.62	2.44	6.53	10.99	12.64	13.77	11.94	10.13	9.22	21.72
ER 97-70	Ercolano - Confine giardino di Telefo	Sez73_EU3pf_LG	1.72	3.11	10.34	12.79	13.96	13.42	11.61	8.92	7.33	16.79
PPM1	Lagno Molara	Sez01a_EU3pf_AT	0.00	0.91	2.42	5.39	11.40	16.54	16.32	13.11	11.59	22.30
PPM2	Lagno Molara	Sez01a_EU3pf_AT	2.87	29.88	26.96	11.61	8.24	6.30	4.46	2.83	2.06	4.78
PPM11	Lagno Molara	Sez01b_EU3pf_AT	1.41	12.55	15.15	14.01	15.13	13.57	10.15	6.85	5.43	5.75
PPM13	Lagno Amendolare	Sez05_EU3pf_AT	0.00	9.23	16.01	13.07	13.87	14.53	11.75	8.17	6.67	6.70
PPM14	Lagno Amendolare	Sez05_EU3pf_AT	15.85	3.51	7.29	11.29	14.90	14.68	11.70	8.62	6.37	5.79
PPM17	Cava S. Sebastiano	Sez06_EU3pf_AT	0.50	11.11	31.04	15.57	9.04	7.95	7.34	6.11	5.29	6.04
PPM18	Cava S. Sebastiano	Sez06_EU3pf_AT	0.00	1.36	1.85	5.09	11.92	18.72	19.67	16.88	13.39	11.12
PPM19	Cava Pollena	Sez04_EU3pf_AT	3.97	2.93	10.04	14.66	17.86	17.47	13.70	9.12	5.49	4.76
PPM20	Cava Pollena	Sez04_EU3pf_AT	0.00	3.14	4.94	2.50	10.28	14.98	18.17	17.47	12.77	15.75
PPM21	Lagno Molara	Sez01c_EU3pf_AT	4.88	15.41	30.70	18.31	10.46	6.96	4.65	3.81	2.49	2.33

PPM22	Lagno Molara	Sez01c_EU3pf_AT	0.00	0.52	4.17	12.03	18.94	19.69	16.16	12.06	8.86	7.57
PPM23	Lagno Molara	Sez01c_EU3pf_AT	0.00	0.00	1.50	5.75	13.47	17.52	18.60	16.54	14.43	12.19
PPM24	Lagno Molara	Sez01c_EU3pf_AT	0.00	0.28	2.63	7.00	12.37	16.07	16.94	15.72	14.55	14.44
PPM5	Cava Pozzelle	Sez02_EU3pf_AT	0.00	1.92	5.35	16.25	22.37	19.73	13.96	9.02	5.76	5.64
PPM6	Cava Pozzelle	Sez02_EU3pf_AT	17.78	11.55	12.98	13.83	13.28	11.34	7.92	4.82	2.82	3.68
PPM7	Cava Pozzelle	Sez02_EU3pf_AT	3.65	7.03	21.38	17.27	12.45	10.26	6.46	6.42	6.78	8.31
PPM8	Cava Pozzelle	Sez02_EU3pf_AT	0.00	0.14	4.50	9.13	16.94	16.94	14.67	11.69	10.07	15.92
RRR 3	Oplontis	Sez11_EU3pf_LG	0.87	9.12	7.71	12.18	16.62	16.89	14.33	9.97	6.22	6.10
RRR 5	Oplontis	Sez11_EU3pf_LG	3.32	4.76	21.52	15.01	12.56	10.60	8.08	7.55	6.19	10.40
RRR 7	Oplontis	Sez11_EU3pf_LG	9.44	12.66	7.16	9.52	9.64	11.53	12.43	10.41	8.55	8.65
vs 84 33	Cava Pozzelle	Sez08b_EU3pf_LG	5.70	7.50	11.40	12.20	13.60	14.60	9.50	7.70	3.90	13.80
VES 89 1	Oplontis	Sez11_EU3pf_LG	4.13	24.09	33.98	23.97	9.65	2.24	0.44	0.31	0.31	0.88
VES 89 2	Oplontis	Sez11_EU3pf_LG	3.21	6.80	13.24	13.85	17.89	11.23	9.01	8.32	7.03	9.43
ves89-38	Pompei - Necropolis	Sez13_EU3pf_LG	0.00	8.55	8.82	10.69	13.24	11.85	11.71	12.24	9.70	13.22
ves89-39	Pompei - Necropolis	Sez13_EU3pf_LG	0.00	0.00	0.57	2.14	8.74	20.80	21.26	19.61	16.24	10.65
ves89-40	Pompei - Necropolis	Sez13_EU3pf_LG	0.00	2.27	6.45	7.34	12.15	11.20	14.57	13.72	12.83	19.47
VS 91-75	Terzigno	Sez07_EU3pf_LG	14.53	8.87	6.45	6.13	8.26	12.61	12.51	12.17	9.27	9.21
VS 92-173	S. Maria di Pozzano	Sez19_EU3pf_LG	0.00	2.93	8.70	16.95	31.52	20.44	3.64	1.71	1.78	12.34
VS91-19	Villa Regina	Sez10_EU3pf_LG	0.00	34.38	19.31	8.31	6.61	7.09	6.58	5.70	5.41	6.62
VS98-574	Cava Pollena	Sez54_EU3pf_LG	1.45	1.38	2.34	5.97	16.36	21.27	18.49	15.13	11.66	5.95
VS98-575	Cava Pollena	Sez54_EU3pf_LG	2.32	5.66	10.24	13.49	16.73	17.01	13.00	9.74	6.91	4.90
VS98-595	Casa De Falco	Sez60_EU3pf_LG	1.13	13.97	16.61	5.61	5.48	6.93	8.33	9.49	12.15	20.28
VS98-598	Discarica Pozzelle	Sez08a_EU3pf_LG	0.00	0.46	1.02	3.03	8.18	16.56	18.95	15.55	14.09	22.16
VS98-599	Discarica Pozzelle	Sez08a_EU3pf_LG	0.00	0.52	4.34	8.43	11.66	15.78	15.64	12.26	12.23	19.14
VS98-600	Discarica Pozzelle	Sez08a_EU3pf_LG	4.93	9.42	12.35	13.49	13.26	12.87	10.34	7.12	5.50	10.71
VS98-601	Discarica Pozzelle	Sez08a_EU3pf_LG	6.83	9.79	10.70	12.11	12.96	13.05	10.04	7.58	6.12	10.82
VS98-602	Discarica Pozzelle	Sez08a_EU3pf_LG	1.21	1.95	6.87	12.66	15.63	16.11	13.00	9.64	9.29	13.65
VS98-603	Cava Pozzelle	Sez08b_EU3pf_LG	1.87	0.09	1.05	4.20	16.06	23.22	19.42	13.82	8.78	11.48
VS98-603a	Discarica Pozzelle	Sez08a_EU3pf_LG	3.56	6.37	15.13	14.42	14.36	13.51	8.82	6.06	8.67	9.10
VS98-604	Cava Pozzelle	Sez08b_EU3pf_LG	0.00	0.91	4.00	10.65	16.07	18.39	15.09	11.20	9.01	14.66

VS98-605	Cava Pozzelle	Sez08b_EU3pf_LG	3.92	7.05	12.63	13.14	15.66	14.25	11.36	7.74	5.65	8.59
VS98-606	Cava Pozzelle	Sez08b_EU3pf_LG	2.03	3.23	10.08	13.13	11.60	10.70	10.43	9.49	9.37	19.94
VS99-621	Masseria Carotenuto	Sez09_EU3pf_LG	0.59	3.40	6.55	10.94	13.15	14.76	12.45	10.46	10.89	16.81
VS99-636	Cava Pozzelle	Sez08b_EU3pf_LG	0.00	1.45	5.18	10.40	15.79	17.73	15.03	11.66	9.50	13.26
VS99-648	Discarica Pozzelle	Sez08a_EU3pf_LG	3.15	3.84	8.67	15.21	16.73	15.24	11.07	8.21	9.03	8.84
VS99-649	Discarica Pozzelle	Sez08a_EU3pf_LG	0.00	1.64	0.92	4.78	14.08	18.59	15.92	13.62	13.38	17.07
VS99-664	Lagno Molara	Sez62_EU3pf_LG	0.00	0.00	2.32	37.05	30.00	12.97	7.38	4.81	3.25	2.22
VS99-665	Lagno Molara	Sez62_EU3pf_LG	0.00	0.16	2.55	9.06	23.14	26.27	15.83	9.76	6.96	6.26
VS99-666	Lagno Molara	Sez62_EU3pf_LG	0.00	0.86	3.50	7.97	15.53	20.23	16.77	13.27	10.79	11.08
VS99-667	Lagno Molara	Sez62_EU3pf_LG	0.83	19.49	49.85	14.32	5.64	3.22	1.86	1.27	1.18	2.36
VS99-668	Lagno Molara	Sez62_EU3pf_LG	0.00	6.32	6.00	13.14	18.30	16.23	11.86	8.37	6.67	13.11
VS99-669	Lagno Molara	Sez62_EU3pf_LG	15.04	36.77	22.41	8.31	4.75	4.14	3.02	1.93	1.51	2.12
VS99-670	Lagno Molara	Sez62_EU3pf_LG	0.35	15.85	31.81	20.87	10.55	7.61	4.87	3.32	2.25	2.52
VS99-671	Lagno Molara	Sez62_EU3pf_LG	0.00	1.40	3.08	10.63	17.19	24.43	17.31	11.65	7.34	6.98
VS99-672	Lagno Molara	Sez62_EU3pf_LG	0.00	0.67	2.66	5.39	12.14	15.93	15.58	15.25	15.04	17.34
VS99-673	Lagno Molara	Sez62_EU3pf_LG	0.00	0.35	2.04	5.11	11.53	19.80	18.19	15.09	13.37	14.52
VS99-674	Lagno Molara	Sez62_EU3pf_LG	0.00	0.26	0.39	1.93	6.50	17.26	19.14	18.79	18.53	17.19
VS99-679	Cava Pollena	Sez54_EU3pf_LG	0.00	4.52	7.50	11.36	12.81	12.17	11.46	12.23	12.41	15.55
VS99-680	Cava Pollena	Sez54_EU3pf_LG	0.00	0.51	2.25	5.87	11.92	15.97	14.48	12.76	12.61	23.63
VS99-681	Cava Pollena	Sez54_EU3pf_LG	0.00	0.68	3.60	8.98	13.56	15.06	13.37	12.53	12.41	19.81
VS99-682	Cava Pollena	Sez54_EU3pf_LG	2.27	4.11	18.36	24.56	17.53	12.65	6.96	4.33	3.73	5.49
VS99-700	Casa De Falco	Sez60_EU3pf_LG	0.00	1.05	2.59	4.72	8.48	13.25	14.30	14.28	14.77	26.56
VS99-701a	Casa De Falco	Sez60_EU3pf_LG	0.00	25.39	17.19	9.34	6.05	6.63	6.77	6.99	7.55	14.10
VS99-701b	Casa De Falco	Sez60_EU3pf_LG	0.00	2.53	1.78	5.08	9.41	15.24	15.19	14.46	13.90	22.40
VS99-702	Casa De Falco	Sez60_EU3pf_LG	2.78	37.51	16.96	6.32	5.48	6.32	6.09	5.77	5.54	7.23
VS99-705	Villa Telesi	Sez16_EU3pf_LG	0.00	2.61	1.19	7.77	35.67	26.08	12.66	7.00	3.87	3.15
VS99-706	Villa Telesi	Sez16_EU3pf_LG	0.00	7.97	17.33	19.44	15.29	11.64	8.13	5.98	5.72	8.49
VS99-707	Villa Telesi	Sez16_EU3pf_LG	0.00	2.40	3.48	9.79	15.33	16.18	13.15	10.92	10.00	18.76
VS99-708	Villa Telesi	Sez16_EU3pf_LG	0.00	0.83	10.20	45.91	18.26	8.65	5.00	3.74	4.11	3.29
VS99-709	Villa Telesi	Sez16_EU3pf_LG	0.00	22.71	6.59	5.99	6.34	6.74	7.67	8.23	10.01	25.72

VS99-709bis	Scudieri	Sez46_EU3pf_LG	0.00	0.33	13.09	29.98	21.05	14.26	8.69	5.84	4.24	2.52
VS99-710	Scudieri	Sez46_EU3pf_LG	0.00	0.13	2.03	6.50	15.00	23.51	18.43	13.86	10.96	9.57
VS99-714	Cava Pollena	Sez54_EU3pf_LG	4.39	5.79	12.34	16.95	19.16	16.90	10.44	6.65	3.78	3.62
VS99-715	Cava Pollena	Sez54_EU3pf_LG	0.00	0.00	2.24	8.15	18.18	23.44	17.74	13.38	9.88	6.99
VS99-716	Cava Pollena	Sez54_EU3pf_LG	3.95	6.79	7.24	11.81	14.62	15.93	13.20	11.61	9.67	5.18
VS99-717	Cava Pollena	Sez54_EU3pf_LG	12.02	15.68	13.17	13.83	12.63	11.02	7.60	5.33	3.91	4.81
VS99-718	Voltosanto	Sez20_EU3pf_LG	0.00	0.00	2.34	9.92	18.73	17.78	14.47	11.91	9.04	15.80
VS99-719	Voltosanto	Sez20_EU3pf_LG	2.15	5.05	7.51	10.70	11.42	12.80	10.45	10.48	10.95	18.50
VS99-720	Voltosanto	Sez20_EU3pf_LG	1.24	16.31	12.97	10.76	9.04	9.88	8.48	8.15	8.62	14.54
VS99-721	Voltosanto	Sez20_EU3pf_LG	9.15	24.06	12.29	7.43	4.23	3.92	4.49	6.28	7.60	20.55
VS99-722	Voltosanto	Sez20_EU3pf_LG	0.00	5.50	6.09	8.41	11.42	12.75	12.04	10.59	11.58	21.61
VS99-723	Voltosanto	Sez20_EU3pf_LG	10.40	6.07	9.22	13.12	14.00	14.07	10.70	8.15	6.43	7.85
VS99-724	Voltosanto	Sez20_EU3pf_LG	5.30	10.98	13.21	14.41	13.99	12.48	9.07	7.43	6.37	6.75
VS99-725	Voltosanto	Sez20_EU3pf_LG	2.21	11.75	11.43	14.89	15.08	14.27	10.57	7.74	6.10	5.97
VS99-726	Voltosanto	Sez20_EU3pf_LG	0.00	5.24	9.21	16.20	17.18	17.41	12.59	9.04	7.25	5.87

Table 8.7: list of grain size analysis for samples used for the TGSD estimation of the EU3pf unit. Sections with the suffix “LG” derive from Gurioli (1999).

8.5.2 EU4b

<i>Sample</i>	<i>Site</i>	<i>Section</i>	<i>Φ (wt%)</i>									
			-4	-3	-2	-1	0	1	2	3	4	5
AS6	Santa Maria di Pozzano	Sez19_EU4_LG	0.00	1.97	15.67	11.73	11.66	11.33	6.96	5.74	7.60	27.34
ER 96-35	Ercolano - Palestra	Sez66_EU4_LG	10.92	10.24	11.01	10.23	16.19	13.17	8.99	7.64	5.78	5.81
ER 96-39	Ercolano - Decumano Massimo	Sez67_EU4_LG	2.58	8.91	22.33	22.14	15.48	9.79	6.02	4.52	3.63	4.61
ER 96-40	Ercolano - Decumano Massimo	Sez67_EU4_LG	0.00	3.57	4.37	5.25	7.06	8.69	9.34	11.91	16.26	33.56
ER 96-61	Ercolano - Villa dei Papiri, stanza dei triclini	Sez68_EU4_LG	25.64	20.58	17.29	12.60	9.79	4.59	1.83	1.26	1.68	4.74
PPM10	Cava Pozzelle	Sez02_EU4_AT	0.00	5.39	7.61	10.88	16.42	16.53	13.79	11.08	8.44	9.85
PPM12	Lagno Molaro	Sez01b_EU4_AT	0.00	0.11	1.62	9.41	16.25	18.88	18.90	16.16	11.40	7.28
PPM16	Terzigno	Sez03_EU4_AT	0.00	0.19	1.30	2.24	4.65	7.84	14.32	19.61	16.67	33.18
PPM3	Lagno Molaro	Sez01a_EU4_AT	3.21	6.59	15.82	18.45	17.58	14.85	10.38	6.30	4.12	2.69
PPM4	Lagno Molaro	Sez01a_EU4_AT	0.00	0.00	1.03	4.26	11.52	19.12	21.84	19.55	13.29	9.40
RRR 8	Oplontis	Sez11_EU4_LG	3.99	5.68	7.98	8.22	7.33	9.39	10.70	13.43	14.35	18.94
Ves89-42	Pompei - Necropolis	Sez13_EU4_LG	1.28	2.43	6.23	11.36	15.45	11.10	8.33	11.65	12.70	19.48
Ves89-43	Pompei - Necropolis	Sez13_EU4_LG	0.00	0.00	14.16	2.69	7.47	9.55	11.10	15.90	18.78	20.34
Ves89-44	Pompei - Necropolis	Sez13_EU4_LG	0.00	0.38	0.61	1.33	4.14	11.02	14.32	19.85	23.12	25.22
Ves89-70	Santa Maria la Carità	Sez22_EU4_LG	0.00	2.30	17.90	25.50	16.00	7.20	2.70	2.50	3.10	22.80
Ves89-71	Santa Maria la Carità	Sez22_EU4_LG	0.00	0.00	2.50	11.10	14.20	8.90	6.90	8.90	9.20	38.40
VS89-76	Santa Maria di Pozzano	Sez19_EU4_LG	0.00	2.10	13.00	20.60	10.90	3.30	2.00	3.20	5.10	39.60
VS90-2	Vergine di Castello	Sez01_EU4_LG	0.00	0.00	0.32	2.96	6.05	14.65	19.40	22.29	19.59	14.74
VS90-3	Vergine di Castello	Sez01_EU4_LG	0.00	0.00	0.00	1.96	8.47	9.72	8.46	12.40	30.75	28.25
VS91-102	Villa Telesi	Sez04_EU4_LG	0.00	0.00	0.50	2.28	9.59	19.10	21.22	18.86	15.85	12.60
VS91-109	Ottaviano	Sez29_EU4_LG	0.00	0.60	2.45	5.01	10.73	17.89	19.09	16.94	14.90	12.39
VS91-110	Ottaviano	Sez29_EU4_LG	0.00	0.52	3.75	7.63	13.08	18.51	17.86	15.29	12.90	10.44
VS91-28	Villa Regina	Sez10_EU4_LG	0.00	1.07	4.11	6.56	7.58	11.06	15.48	15.74	16.19	22.21
VS91-29	Villa Regina	Sez10_EU4_LG	0.00	0.42	1.79	5.29	8.04	11.91	19.33	16.86	15.61	20.74
VS91-30	Villa Regina	Sez10_EU4_LG	0.00	0.00	0.43	2.48	9.30	18.19	22.76	20.33	14.08	12.42
VS91-46	Pompei - Porta San Paolino	Sez14_EU4_LG	0.00	0.30	3.41	10.64	14.29	13.93	14.63	15.52	14.17	13.12
VS91-66	Pompei - Porta Nola	Sez12_EU4_LG	6.79	17.47	10.43	7.16	4.92	2.96	4.15	6.85	12.92	26.34
VS91-67	Pompei - Porta Nola	Sez12_EU4_LG	0.00	3.41	9.30	8.53	10.96	8.06	11.18	13.11	17.06	18.39
VS91-68	Pompei - Porta Ercolano	Sez17_EU4_LG	0.00	1.56	4.92	7.36	8.74	10.06	12.15	14.24	17.07	23.90

VS91-69	Pompei - Porta Ercolano	Sez17_EU4_LG	0.00	0.48	1.91	3.14	7.14	11.30	14.87	16.80	19.09	25.29
VS91-70	Pompei - Porta Ercolano	Sez17_EU4_LG	0.00	0.12	0.58	2.21	7.08	13.26	17.47	18.65	17.84	22.79
VS91-80	Terzigno	Sez07_EU4_LG	0.00	7.47	8.48	11.50	12.00	12.74	13.00	15.27	14.10	5.42
VS91-81	Terzigno	Sez07_EU4_LG	0.00	1.48	3.88	6.66	11.67	17.96	17.87	15.61	13.22	11.66
VS92-133	Villa Sora	Sez30_EU4_LG	4.97	13.76	5.29	4.24	4.22	5.98	9.62	13.11	14.05	24.80
VS92-134	Villa Sora	Sez30_EU4_LG	0.00	0.88	2.15	3.20	6.91	12.36	14.70	16.27	15.85	27.70
VS92-135	Villa Sora	Sez30_EU4_LG	0.00	3.00	7.53	9.64	13.17	15.23	13.27	11.98	10.28	15.90
VS92-157	Oplontis	Sez11_EU4_LG	7.04	61.82	12.10	2.78	1.66	2.36	2.85	3.14	2.61	3.65
VS92-183	Voltosanto	Sez26_EU4_LG	1.50	7.45	11.57	16.88	18.14	15.06	10.56	7.56	5.52	5.78
VS92-184	Voltosanto	Sez26_EU4_LG	0.00	5.24	7.81	12.62	17.22	18.01	14.08	10.38	7.28	7.36
VS94-219	Tricino	Sez27_EU4_LG	0.00	0.46	0.39	7.38	3.84	5.28	8.40	16.11	23.45	34.70
VS98-504	Masseria Carotenuto	Sez09_EU4_LG	15.68	26.37	16.63	16.51	10.24	4.68	2.26	2.11	2.40	3.11
VS98-505	Masseria Carotenuto	Sez09_EU4_LG	4.23	22.16	22.03	10.41	8.07	8.79	7.56	6.43	4.92	5.40
VS98-506	Masseria Carotenuto	Sez09_EU4_LG	0.00	0.00	2.37	9.97	17.70	18.59	15.13	11.83	10.78	13.64
VS98-507	Masseria Carotenuto	Sez09_EU4_LG	0.00	0.00	0.93	4.93	14.86	24.65	19.32	14.00	10.68	10.63
VS98-514	Villa di Arianna	Sez41_EU4_LG	0.00	1.05	9.67	16.28	12.39	7.14	5.90	7.48	8.74	31.35
VS98-515	Villa di Arianna	Sez41_EU4_LG	0.00	0.00	9.26	18.41	12.59	11.57	7.58	7.29	10.26	23.06
VS98-520	Palazzo Baronale-Codola	Sez43_EU4_LG	0.00	0.00	4.37	12.37	17.23	7.96	4.71	8.37	13.72	31.28
VS98-522	Tricino	Sez27_EU4_LG	0.00	0.00	0.21	2.04	5.10	9.26	11.75	15.22	21.67	34.74
VS98-524	Raggi	Sez44_EU4_LG	0.00	0.00	0.20	0.76	2.48	6.72	13.62	19.73	22.31	34.17
VS98-544	Via Cascetta	Sez48_EU4_LG	0.00	2.58	9.86	21.27	22.51	14.74	10.07	7.88	6.58	4.50
VS98-545	Via Cascetta	Sez48_EU4_LG	0.00	0.00	5.61	18.61	19.02	17.35	13.03	9.95	8.42	8.01
VS98-546	Via Cascetta	Sez48_EU4_LG	0.00	0.89	2.05	3.52	11.21	23.26	20.84	18.45	12.72	7.05
VS98-547	Via Cascetta	Sez48_EU4_LG	0.00	0.00	0.15	5.14	7.24	9.56	10.04	14.08	15.42	38.37
VS98-550	La Castelluccia	Sez49_EU4_LG	0.00	4.31	8.22	11.38	22.68	22.63	14.28	9.24	4.84	2.43
VS98-551	La Castelluccia	Sez49_EU4_LG	0.00	0.00	1.14	4.96	13.60	24.73	23.40	16.31	9.67	6.20
VS98-552	La Castelluccia	Sez49_EU4_LG	0.00	2.47	1.77	4.37	8.84	16.64	18.77	17.67	16.25	13.22
VS98-553	Cupa Pallarino	Sez50_EU4_LG	0.00	0.00	2.11	6.15	15.88	25.48	22.80	13.58	8.04	5.96
VS98-554	Cupa Pallarino	Sez50_EU4_LG	0.00	1.86	11.34	28.60	17.72	14.36	10.35	7.41	4.89	3.48
VS98-555	Cupa Pallarino	Sez50_EU4_LG	0.00	0.00	5.91	21.16	24.07	16.56	10.99	8.58	7.01	5.73
VS98-556	Cupa Pallarino	Sez50_EU4_LG	0.00	0.00	1.41	7.64	14.42	15.53	13.48	14.56	14.51	18.44
VS99-620	Angri	Sez42_EU4_LG	0.00	1.15	5.63	14.09	13.04	8.80	4.29	3.81	6.74	42.44
VS99-623	Casa De Falco	Sez60_EU4_LG	0.00	0.28	3.02	5.76	9.47	14.32	16.15	16.72	15.88	18.41
VS99-624	Casa De Falco	Sez60_EU4_LG	0.00	1.80	3.61	5.61	10.01	14.06	14.80	14.89	15.25	19.96

Table 8.8: list of grain size analysis for samples used for the TGSD estimation of the EU4b unit. Sections with the suffix “LG” derive from Gurioli (1999).

8.5.3 EU4c

<i>Sample</i>	<i>Site</i>	<i>Section</i>	<i>Φ (wt%)</i>								
			-3	-2	-1	0	1	2	3	4	5
Ves89-45	Pompei - Necropolis	Sez13_EU4_LG	0.38	0.61	1.33	4.14	11.02	14.32	19.85	23.12	25.22
Ves89-72	Santa Maria la Carità	Sez22_EU4_LG	0.00	14.16	2.69	7.47	9.55	11.10	15.90	18.78	20.34
VS89-77	Santa Maria di Pozzano	Sez19_EU4_LG	2.10	13.00	20.60	10.90	3.30	2.00	3.20	5.10	39.60
VS91-31	Villa Regina	Sez10_EU4_LG	0.00	0.43	2.48	9.30	18.19	22.76	20.33	14.08	12.42
VS91-47	Pompei - Porta San Paolino	Sez14_EU4_LG	0.30	3.41	10.64	14.29	13.93	14.63	15.52	14.17	13.12
VS91-71	Pompei - Porta Ercolano	Sez17_EU4_LG	0.12	0.58	2.21	7.08	13.26	17.47	18.65	17.84	22.79
VS91-82	Terzigno	Sez07_EU4_LG	0.00	6.51	6.15	6.96	13.63	16.13	17.11	15.84	17.67
VS92-136	Villa Sora	Sez30_EU4_LG	3.00	7.53	9.64	13.17	15.23	13.27	11.98	10.28	15.90

Table 8.9: list of grain size analysis for samples used for the TGSD estimation of the EU4c unit. Sections with the suffix “LG” derive from Gurioli (1999).

8.5.4 Fg Cupa Fontana

<i>Sample</i>	<i>Section</i>	<i>Φ (wt%)</i>									
		-4	-3	-2	-1	0	1	2	3	4	5
VS22	28	10.95	12.20	12.70	12.68	14.24	11.35	10.42	7.03	4.12	4.32
VS24	33	11.49	9.82	13.99	13.80	14.91	13.38	10.18	6.30	3.19	2.95
VS45	41	10.31	13.93	14.08	15.82	16.03	13.30	8.66	4.62	2.00	1.26
VS29	43	13.32	16.73	12.61	10.32	10.34	9.39	8.51	7.07	5.56	6.16

Table 8.10: list of grain size analysis for samples used for the TGSD estimation of the “Cupa Fontana” PDC lobe.

References

- Acocella V., Porreca M., Neri M., Massimi E., Mattei M. (2006a) Propagation of dikes at Vesuvio (Italy) and the effect of Mt. Somma. *Geophysical research letters* 33 (8):L08301
- Acocella V., Porreca M., Neri M., Mattei M., Funicello R. (2006b) Fissure eruptions at Mount Vesuvius (Italy): Insights on the shallow propagation of dikes at volcanoes. *Geology* 34 (8):673-676
- Aiuppa A., Caleca A., Federico C., Gurrieri S., Valenza M. (2004) Diffuse degassing of carbon dioxide at Somma–Vesuvius volcanic complex (Southern Italy) and its relation with regional tectonics. *Journal of volcanology and geothermal research* 133 (1):55-79
- Alberico I., Lirer L., Petrosino P., Scandone R. (2002) A methodology for the evaluation of long-term volcanic risk from pyroclastic flows in Campi Flegrei (Italy). *Journal of Volcanology and Geothermal Research* 116 (1):63-78
- Alberico I., Lirer L., Petrosino P., Scandone R. (2008) Volcanic hazard and risk assessment from pyroclastic flows at Ischia island (southern Italy). *Journal of Volcanology and Geothermal Research* 171 (1–2):118-136. doi:<http://dx.doi.org/10.1016/j.jvolgeores.2007.11.014>
- Alfano G. B. (1924) *Le Eruzioni del Vesuvio tra il 79 e il 1631: studio bibliografico*. Scuola Tipografica Pontifica per i Figli dei Carcerati, Fondata da Bartolo Longo
- Andronico D., Cioni R. (2002) Contrasting styles of Mount Vesuvius activity in the period between the Avellino and Pompeii Plinian eruptions, and some implications for assessment of future hazards. *Bulletin of Volcanology* 64 (6):372-391
- Arrighi S., Principe C., Rosi M. (2001) Violent strombolian and subplinian eruptions at Vesuvius during post-1631 activity. *Bulletin of Volcanology* 63 (2-3):126-150
- Aspinall W. P. (2006) Structured elicitation of expert judgment for probabilistic hazard and risk assessment in volcanic eruptions. *Statistics in volcanology* 1:15-30
- Auger E., Gasparini P., Virieux J., Zollo A. (2001) Seismic evidence of an extended magmatic sill under Mt. Vesuvius. *Science* 294 (5546):1510-1512
- Bachmann O., Bergantz G. W. (2003) Rejuvenation of the Fish Canyon magma body: A window into the evolution of large-volume silicic magma systems. *Geology* 31 (9):789-792
- Barberi F., Cioni R., Rosi M., Santacroce R., Sbrana A., Vecci R. (1989) Magmatic and phreatomagmatic phases in explosive eruptions of Vesuvius as deduced by grain-size and component analysis of the pyroclastic deposits. *Journal of volcanology and geothermal research* 38 (3-4):287-307
- Bardintzeff J. M. (1984) Merapi volcano (Java, Indonesia) and Merapi-type nuée ardente. *Bulletin volcanologique* 47 (3):433-446
- Barsotti S., Neri A., Bertagnini A., Cioni R., Mulas M., Mundula F. (2015) Dynamics and tephra dispersal of Violent Strombolian eruptions at Vesuvius: insights from field data, wind reconstruction and numerical simulation of the 1906 event. *Bulletin of Volcanology* 77 (7):1-19
- Bartolini S., Cappello A., Martí Molist J., Del Negro C. (2013) QVAST: a new Quantum GIS plugin for estimating volcanic susceptibility.
- Baxter P. J., Aspinall W. P., Neri A., Zuccaro G., Spence R. J. S., Cioni R., Woo G. (2008) Emergency planning and mitigation at Vesuvius: A new evidence-based approach. *Journal of Volcanology and Geothermal Research* 178 (3):454-473
- Becerril L., Cappello A., Galindo I., Neri M., Del Negro C. (2013) Spatial probability distribution of future volcanic eruptions at El Hierro Island (Canary Islands, Spain). *Journal of volcanology and geothermal research* 257:21-30

- Berrino G., Corrado G., Riccardi U. (1998) Sea gravity data in the Gulf of Naples: a contribution to delineating the structural pattern of the Vesuvian area. *Journal of Volcanology and Geothermal Research* 82 (1):139-150
- Bertagnini A., Landi P., Santacroce R., Sbrana A. (1991) The 1906 eruption of Vesuvius: from magmatic to phreatomagmatic activity through the flashing of a shallow depth hydrothermal system. *Bulletin of Volcanology* 53 (7):517-532
- Bertagnini A., Landi P., Rosi M., Vigliargio A. (1998) The Pomici di Base plinian eruption of Somma-Vesuvius. *Journal of volcanology and geothermal research* 83 (3):219-239
- Bevilacqua A., Isaia R., Neri A., Vitale S., Aspinall W. P., Bisson M., Flandoli F., Baxter P. J., Bertagnini A., Esposti Ongaro T., Iannuzzi E., Pistolesi M., Rosi M. (2015) Quantifying volcanic hazard at Campi Flegrei caldera (Italy) with uncertainty assessment: I. Vent opening maps. *Journal of Geophysical Research: Solid Earth*
- Bevilacqua A. (2016) Doubly stochastic models for volcanic vent opening probability and pyroclastic density current hazard at Campi Flegrei caldera. PhD thesis, Scuola Normale Superiore, Pisa
- Bianco F., Castellano M., Milano G., Ventura G., Vilardo G. (1998) The Somma-Vesuvius stress field induced by regional tectonics: evidences from seismological and mesostructural data. *Journal of Volcanology and Geothermal Research* 82 (1):199-218
- Bonadonna C., Houghton B. F. (2005) Total grain-size distribution and volume of tephra-fall deposits. *Bulletin of Volcanology* 67 (5):441-456
- Bonadonna C., Costa A. (2012) Estimating the volume of tephra deposits: A new simple strategy. *Geology*. doi:10.1130/G32769.1
- Branney M. J., Kokelaar B. P. (2002) Pyroclastic density currents and the sedimentation of ignimbrites, vol 27, *Memoirs. Geological Society London*
- Brocchini D., Principe C., Castradori D., Laurenzi M. A., Gorla L. (2001) Quaternary evolution of the southern sector of the Campanian Plain and early Somma-Vesuvius activity: insights from the Trecase 1 well. *Mineralogy and Petrology* 73 (1-3):67-91
- Bruno P. P. G., Cippitelli G., Rapolla A. (1998) Seismic study of the Mesozoic carbonate basement around Mt. Somma-Vesuvius, Italy. *Journal of volcanology and geothermal research* 84 (3):311-322
- Bruno P. P. G., Rapolla A. (1999) Study of the sub-surface structure of Somma-Vesuvius (Italy) by seismic reflection data. *Journal of volcanology and geothermal research* 92 (3):373-387
- Bursik M. I., Patra A. K., Pitman E. B., Nichita C., Macias J. L., Saucedo R., Girina O. (2005) Advances in studies of dense volcanic granular flows. *Reports on Progress in Physics* 68 (2):271
- Cappello A., Neri M., Acocella V., Gallo G., Vicari A., Del Negro C. (2012) Spatial vent opening probability map of Etna volcano (Sicily, Italy). *Bulletin of volcanology* 74 (9):2083-2094
- Capra L., Manea V. C., Manea M., Norini G. (2011) The importance of digital elevation model resolution on granular flow simulations: a test case for Colima volcano using TITAN2D computational routine. *Natural hazards* 59 (2):665-680
- Carey S., Sigurdsson H., Mandeville C., Bronto S. (1996) Pyroclastic flows and surges over water: an example from the 1883 Krakatau eruption. *Bulletin of Volcanology* 57 (7):493-511
- Carey S., Bursik M. I. (2000) Volcanic Plumes. In: H. S (ed) *Encyclopedia of Volcanoes* (first edition). Academic Press,

- Carey S., Bursik M. I. (2015) Volcanic Plumes. In: Sigurdsson H (ed) *Encyclopedia of Volcanoes* (second edition). Academic Press,
- Carey S. N., Sparks R. S. J. (1986) Quantitative models of the fallout and dispersal of tephra from volcanic eruption columns. *Bulletin of Volcanology* 48 (2-3):109-125
- Carey S. N., Sigurdsson H. (1987) Temporal variations in column height and magma discharge rate during the 79 AD eruption of Vesuvius. *Geological Society of America Bulletin* 99 (2):303-314
- Carey S. N. (1991) Transport and deposition of tephra by pyroclastic flows and surges.
- Cas R. A. F., Wright J. V. (1987) *Volcanic Successions, Modern and Ancient: A Geological Approach to Processes, Products and Successions*. Allen and Unwin, St Leonards, NSW, Australia
- Cassano E, La Torre P. (1987) *Geophysics. Somma-Vesuvius* CNR, Quaderni de La Ricerca Scientifica, Roma, Italy 8
- Castello B., Selvaggi G., Chiarabba C., Amato A. (2006) CSI Catalogo della sismicità italiana 1981-2002, versione 1.1. <http://csi.rm.ingv.it/>. Accessed July 13, 2014
- Cella F., Fedi M., Florio G., Grimaldi M., Rapolla A. (2007) Shallow structure of the Somma-Vesuvius volcano from 3D inversion of gravity data. *Journal of Volcanology and Geothermal Research* 161 (4):303-317. doi:<http://dx.doi.org/10.1016/j.jvolgeores.2006.12.013>
- Cepeda J., Chávez J. A., Martínez C. C. (2010) Procedure for the selection of runout model parameters from landslide back-analyses: application to the Metropolitan Area of San Salvador, El Salvador. *Landslides* 7 (2):105-116
- Cerminara M., Esposti Ongaro T., Neri A. (2016) Large Eddy Simulation of gas-particle kinematic decoupling and turbulent entrainment in volcanic plumes. *Journal of Volcanology and Geothermal Research*. doi:<http://dx.doi.org/10.1016/j.jvolgeores.2016.06.018>
- Charbonnier S. J., Gertisser R. (2009) Numerical simulations of block-and-ash flows using the Titan2D flow model: examples from the 2006 eruption of Merapi Volcano, Java, Indonesia. *Bulletin of Volcanology* 71 (8):953-959
- Charbonnier S. J., Gertisser R. (2012) Evaluation of geophysical mass flow models using the 2006 block-and-ash flows of Merapi Volcano, Java, Indonesia: towards a short-term hazard assessment tool. *Journal of Volcanology and Geothermal Research* 231:87-108
- Charbonnier S. J., Palma J. L., Ogburn S. (2015) Application of "shallow-water" numerical models for hazard assessment of volcanic flows: the case of TITAN2D and Turrialba volcano (Costa Rica). *Revista Geológica de América Central* (52):107-128
- Christen M., Kowalski J., Bartelt P. (2010) RAMMS: numerical simulation of dense snow avalanches in three-dimensional terrain. *Cold Regions Science and Technology* 63 (1):1-14
- Ciaranfi N., Cinque A., Lambiase S., Pieri P., Rapisardi L., Ricchetti G., Sgrosso I., Tortorici L. (1981) Proposta di zonazione sismotettonica dell'Italia Meridionale. *Rend Soc Geol It* 4:493-496
- Cioni R., Marianelli P., Sbrana A. (1992a) Dynamics of the AD 79 eruption: Stratigraphic, sedimentological and geochemical data on the successions from the Somma-Vesuvius southern and eastern sectors. *Acta Vulcanol* 2:109-123
- Cioni R., Sbrana A., Vecci R. (1992b) Morphologic features of juvenile pyroclasts from magmatic and phreatomagmatic deposits of Vesuvius. *Journal of Volcanology and Geothermal Research* 51 (1):61-78
- Cioni R., Civetta L., Marianelli P., Metrich N., Santacroce R., Sbrana A. (1995) Compositional layering and syn-eruptive mixing of a periodically refilled shallow magma chamber: the AD 79 Plinian eruption of Vesuvius. *Journal of Petrology* 36 (3):739-776

- Cioni R., Santacroce R., Sbrana A. (1999) Pyroclastic deposits as a guide for reconstructing the multi-stage evolution of the Somma-Vesuvius Caldera. *Bulletin of Volcanology* 61 (4):207-222
- Cioni R. (2000) Volatile content and degassing processes in the AD 79 magma chamber at Vesuvius (Italy). *Contributions to Mineralogy and Petrology* 140 (1):40-54
- Cioni R., Gurioli L., Sbrana A., Vougioukalakis G. (2000a) Precursors to the Plinian eruptions of Thera (Late Bronze Age) and Vesuvius (AD 79): data from archaeological areas. *Physics and Chemistry of the Earth, Part A: Solid Earth and Geodesy* 25 (9):719-724
- Cioni R., Levi S., Sulpizio R. (2000b) Apulian Bronze Age pottery as a long-distance indicator of the Avellino Pumice eruption (Vesuvius, Italy). *Geological Society, London, Special Publications* 171 (1):159-177
- Cioni R., Longo A., Macedonio G., Santacroce R., Sbrana A., Sulpizio R., Andronico D. (2003a) Assessing pyroclastic fall hazard through field data and numerical simulations: example from Vesuvius. *Journal of Geophysical Research: Solid Earth* (1978–2012) 108 (B2):2063
- Cioni R., Sulpizio R., Garruccio N. (2003b) Variability of the eruption dynamics during a subplinian event: the Greenish Pumice eruption of Somma–Vesuvius (Italy). *Journal of volcanology and geothermal research* 124 (1):89-114
- Cioni R., Gurioli L., Lanza R., Zanella E. (2004) Temperatures of the AD 79 pyroclastic density current deposits (Vesuvius, Italy). *Journal of Geophysical Research: Solid Earth* 109 (B2)
- Cioni R., Bertagnini A., Santacroce R., Andronico D. (2008) Explosive activity and eruption scenarios at Somma-Vesuvius (Italy): Towards a new classification scheme. *Journal of Volcanology and Geothermal Research* 178 (3):331-346. doi:<http://dx.doi.org/10.1016/j.jvolgeores.2008.04.024>
- Cioni R., Bertagnini A., Andronico D., Cole P. D., Mundula F. (2011) The 512 AD eruption of Vesuvius: complex dynamics of a small scale subplinian event. *Bulletin of volcanology* 73 (7):789-810
- Civetta L., Galati R., Santacroce R. (1991) Magma mixing and convective compositional layering within the Vesuvius magma chamber. *Bulletin of Volcanology* 53 (4):287-300
- Cole P. D., Calder E. S., Druitt T. H., Hoblitt R. P., Robertson R., Sparks R. S. J., Young S. R. (1998) Pyroclastic flows generated by gravitational instability of the 1996–97 lava dome of Soufriere Hills Volcano, Montserrat. *Geophysical Research Letters* 25 (18):3425-3428
- Cole P. D., Calder E. S., Sparks R. S. J., Clarke A. B., Druitt T. H., Young S. R., Herd R. A., Harford C. L., Norton G. E. (2002) Deposits from dome-collapse and fountain-collapse pyroclastic flows at Soufrière Hills Volcano, Montserrat. In: Druitt TH, Kokelaar BP (eds) *The eruption of Soufrière Hills Volcano, Montserrat*, vol 21. vol 1. Geological Society, London, Memoirs, pp 231-262
- Connor C. B., Hill B. E. (1995) Three nonhomogeneous Poisson models for the probability of basaltic volcanism: application to the Yucca Mountain region, Nevada. *Journal of Geophysical Research: Solid Earth* (1978–2012) 100 (B6):10107-10125
- Connor C. B., Connor L. J. (2009) *Estimating spatial density with kernel methods. Volcanic and tectonic hazard assessment for nuclear facilities* Cambridge University Press, Cambridge, UK:346-368
- Connor L. J., Connor C. B., Meliksetian K., Savov I. (2012) Probabilistic approach to modeling lava flow inundation: a lava flow hazard assessment for a nuclear facility in Armenia. *Journal of Applied Volcanology* 1 (1):1-19

- Cook G. W., Wolff J. A., Self S. (2016) Estimating the eruptive volume of a large pyroclastic body: the Otowi Member of the Bandelier Tuff, Valles caldera, New Mexico. *Bulletin of Volcanology* 78 (2):1-11
- Cooke R. M. (1991) Experts in uncertainty: opinion and subjective probability in science.
- Corazzato C., Tibaldi A. (2006) Fracture control on type, morphology and distribution of parasitic volcanic cones: An example from Mt. Etna, Italy. *Journal of Volcanology and Geothermal Research* 158 (1–2):177-194. doi:<http://dx.doi.org/10.1016/j.jvolgeores.2006.04.018>
- Crandell D. R. (1989) Gigantic debris avalanche of Pleistocene age from ancestral Mount Shasta volcano, California, and debris-avalanche hazard zonation. *USGS Bulletin*
- Dade W. B., Huppert H. E. (1995) A box model for non-entraining, suspension-driven gravity surges on horizontal surfaces. *Sedimentology* 42 (3):453-470
- Dade W. B., Huppert H. E. (1996) Emplacement of the Taupo ignimbrite by a dilute turbulent flow. *Nature* 381 (6582):509-512
- Dalbey K. R. (2009) Predictive simulation and model based hazard maps of geophysical mass flows. Dissertation thesis, State University of New York at Buffalo,
- De Natale G., Troise C., Pingue F., Mastrolorenzo G., Pappalardo L. (2006) The Somma–Vesuvius volcano (Southern Italy): Structure, dynamics and hazard evaluation. *Earth-Science Reviews* 74 (1–2):73-111. doi:<http://dx.doi.org/10.1016/j.earscirev.2005.08.001>
- De Siena L., Del Pezzo E., Bianco F., Tramelli A. (2009) Multiple resolution seismic attenuation imaging at Mt. Vesuvius. *Physics of the Earth and Planetary Interiors* 173 (1):17-32
- De Simone G. F., Perrotta A., Scarpato C. (2012) L'eruzione del 472 dC ed il suo impatto su alcuni siti alle falde del Vesuvio. *Rivista di Studi Pompeiani* 22:61-71
- Degruyter W., Bonadonna C. (2013) Impact of wind on the condition for column collapse of volcanic plumes. *Earth and Planetary Science Letters* 377:218-226
- Del Pezzo E., Bianco F., De Siena L., Zollo A. (2006) Small scale shallow attenuation structure at Mt. Vesuvius, Italy. *Physics of the Earth and Planetary Interiors* 157 (3):257-268
- Denlinger R. P., Iverson R. M. (2004) Granular avalanches across irregular three-dimensional terrain: 1. Theory and computation. *Journal of Geophysical Research: Earth Surface* 109 (F1)
- Di Renzo V., Di Vito M. A., Arienzo I., Carandente A., Civetta L., D'antonio M., Giordano F., Orsi G., Tonarini S. (2007) Magmatic history of Somma–Vesuvius on the basis of new geochemical and isotopic data from a deep borehole (Camaldoli della Torre). *Journal of Petrology* 48 (4):753-784
- Dobran F., Neri A., Macedonio G. (1993) Numerical simulation of collapsing volcanic columns. *Journal of Geophysical Research: Solid Earth* 98 (B3):4231-4259
- Dobran F., Neri A., Todesco M. (1994) Assessing the pyroclastic flow hazard at Vesuvius. *Nature* 367 (6463):551-554
- Dóniz J., Romero C., Coello E., Guillén C., Sánchez N., García-Cacho L., García A. (2008) Morphological and statistical characterisation of recent mafic volcanism on Tenerife (Canary Islands, Spain). *Journal of Volcanology and Geothermal Research* 173 (3–4):185-195. doi:<http://dx.doi.org/10.1016/j.jvolgeores.2007.12.046>
- Doyle E. E., Hogg A. J., Mader H. M., Sparks R. S. J. (2010) A two-layer model for the evolution and propagation of dense and dilute regions of pyroclastic currents. *Journal of Volcanology and Geothermal Research* 190 (3):365-378
- DPC (1995) Pianificazione Nazionale d'Emergenza dell'Area Vesuviana, Presidenza del Consiglio dei Ministri-Dipartimento della Protezione Civile, Rome, 157

- DPC (2014) Disposizioni per l'aggiornamento della pianificazione di emergenza per il rischio vulcanico del Vesuvio, Presidenza del Consiglio dei Ministri-Dipartimento della Protezione Civile, Rome, 10
- Druitt T. H. (1992) Emplacement of the 18 May 1980 lateral blast deposit ENE of Mount St. Helens, Washington. *Bulletin of Volcanology* 54 (7):554-572
- Dufek J., Manga M. (2008) In situ production of ash in pyroclastic flows. *Journal of Geophysical Research: Solid Earth* 113 (B9)
- Engwell S. L., Sparks R. S. J., Carey S. (2014) Physical characteristics of tephra layers in the deep sea realm: the Campanian Ignimbrite eruption. *Geological Society, London, Special Publications* 398 (1):47-64
- Engwell S. L., Aspinall W. P., Sparks R. S. J. (2015) An objective method for the production of isopach maps and implications for the estimation of tephra deposit volumes and their uncertainties. *Bulletin of volcanology* 77 (7):1-18
- Esposti Ongaro T., Neri A., Todesco M., Macedonio G. (2002) Pyroclastic flow hazard assessment at Vesuvius (Italy) by using numerical modeling. II. Analysis of flow variables. *Bulletin of volcanology* 64 (3):178-191
- Esposti Ongaro T., Cavazzoni C., Erbacci G., Neri A., Salvetti M. V. (2007) A parallel multiphase flow code for the 3D simulation of explosive volcanic eruptions. *Parallel Computing* 33 (7):541-560
- Esposti Ongaro T., Neri A., Menconi G., De'Michieli Vitturi M., Marianelli P., Cavazzoni C., Erbacci G., Baxter P. J. (2008) Transient 3D numerical simulations of column collapse and pyroclastic density current scenarios at Vesuvius. *Journal of Volcanology and Geothermal Research* 178 (3):378-396
- Esposti Ongaro T., Clarke A. B., Voight B., Neri A., Widiwijayanti C. (2012) Multiphase flow dynamics of pyroclastic density currents during the May 18, 1980 lateral blast of Mount St. Helens. *Journal of Geophysical Research: Solid Earth* (1978–2012) 117 (B6)
- Esposti Ongaro T., Orsucci S., Cornolti F. (2016) A fast, calibrated model for pyroclastic density currents kinematics and hazard. *Journal of Volcanology and Geothermal Research*
- Favalli M., Pareschi M. T. (2004) Digital elevation model reconstruction preserving surface morphological structures. *J Geophys Res* 109:F04004
- Fawcett T. (2006) An introduction to ROC analysis. *Pattern recognition letters* 27 (8):861-874
- Federico C., Aiuppa A., Favara R., Gurrieri S., Valenza M. (2004) Geochemical monitoring of groundwaters (1998–2001) at Vesuvius volcano (Italy). *Journal of Volcanology and Geothermal Research* 133 (1–4):81-104. doi:[http://dx.doi.org/10.1016/S0377-0273\(03\)00392-5](http://dx.doi.org/10.1016/S0377-0273(03)00392-5)
- Ferrucci F., Gaudiosi G., Pino N. A., Luongo G., Hirn A., Mirabile L. (1989) Seismic detection of a major Moho upheaval beneath the Campania volcanic area (Naples, Southern Italy). *Geophysical Research Letters* 16 (11):1317-1320
- Fierstein J., Nathenson M. (1992) Another look at the calculation of fallout tephra volumes. *Bulletin of Volcanology* 54 (2):156-167
- Finetti I., Morelli C. (1974) Esplorazione sismica a riflessione dei Golfi di Napoli e Pozzuoli. *Boll Geofis Teor Appl* 16 (62/63):175-222
- Fischer J.-T., Kowalski J., Pudasaini S. P. (2012) Topographic curvature effects in applied avalanche modeling. *Cold Regions Science and Technology* 74:21-30

- Florio G., Fedi M., Cella F., Rapolla A. (1999) The Campanian Plain and Phlegrean Fields: structural setting from potential field data. *Journal of Volcanology and Geothermal Research* 91 (2):361-379
- Fornaciai A., Bisson M., Mazzarini F. (2008) Detection of Ground Control Points using the SITOGEO-GIS tool to orthorectify Landsat 7 ETM+ images. *Rivista italiana di Telerilevamento* 40 (3):55-63
- Freundt A. (2003) Entrance of hot pyroclastic flows into the sea: experimental observations. *Bulletin of Volcanology* 65 (2-3):144-164
- Fron dini F., Chiodini G., Caliro S., Cardellini C., Granieri D., Ventura G. (2004) Diffuse CO₂ degassing at Vesuvio, Italy. *Bulletin of Volcanology* 66 (7):642-651
- Gaffney E. S., Damjanac B., Valentine G. A. (2007) Localization of volcanic activity: 2. Effects of pre-existing structure. *Earth and Planetary Science Letters* 263 (3):323-338
- Graf H. F., Herzog M., Oberhuber J. M., Textor C. (1999) Effect of environmental conditions on volcanic plume rise. *Journal of Geophysical Research: Atmospheres* 104 (D20):24309-24320
- Granieri D., Carapezza M. L., Avino R., Cardellini C., Donnini M., Ranaldi M., Tarchini L. (2013) Level of carbon dioxide diffuse degassing from the ground of Vesuvio: comparison between extensive surveys and inferences on the gas source. *ANNALS OF GEOPHYSICS*
- Gurioli L. (1999) *Flussi piroclastici: classificazione e meccanismi di messa in posto*. PhD thesis, University of Pisa, Pisa
- Gurioli L., Cioni R., Bertagna C. (1999) I depositi di flusso piroclastico dell'eruzione del 79 dC caratterizzazione stratigrafica, sedimentologica e modelli di trasporto e deposizione. *Atti Soc Tosc Sci Nat Mem Serie A* 106:61-72
- Gurioli L., Cioni R., Sbrana A., Zanella E. (2002) Transport and deposition of pyroclastic density currents over an inhabited area: the deposits of the AD 79 eruption of Vesuvius at Herculaneum, Italy. *Sedimentology* 49 (5):929-953
- Gurioli L., Houghton B. F., Cashman K. V., Cioni R. (2005) Complex changes in eruption dynamics during the 79 AD eruption of Vesuvius. *Bulletin of Volcanology* 67 (2):144-159
- Gurioli L., Zanella E., Pareschi M. T., Lanza R. (2007) Influences of urban fabric on pyroclastic density currents at Pompeii (Italy): 1. Flow direction and deposition. *Journal of Geophysical Research: Solid Earth* 112 (B5)
- Gurioli L., Sulpizio R., Cioni R., Sbrana A., Santacroce R., Luperini W., Andronico D. (2010) Pyroclastic flow hazard assessment at Somma-Vesuvius based on the geological record. *Bulletin of Volcanology* 72 (9):1021-1038
- Hasenaka T., Carmichael I. S. E. (1985) The cinder cones of Michoacán—Guanajuato, central Mexico: their age, volume and distribution, and magma discharge rate. *Journal of Volcanology and Geothermal Research* 25 (1):105-124
- Heidbach O., Tingay M., Barth A., Reinecker J., Kurfeß D., Müller B. (2008) The world stress map database release 2008. WSM Rel2008. doi:10.1594/GFZ
- Hidayat D., Widiwijayanti C., Voight B., Patra A. K., Pitman E. B. TITAN2D analyses of dome-collapse pyroclastic flows on Montserrat. In: AGU Fall Meeting Abstracts, 2007. p 0499
- Hippolyte J. C., Angelier J., Roure F. (1994) A major geodynamic change revealed by Quaternary stress patterns in the Southern Apennines (Italy). *Tectonophysics* 230 (3):199-210
- Hoblitt R. P. (1986) Observations of the eruptions of July 22 and August 7, 1980, at Mount St. Helens, Washington. Professional Papers. USGS,

- Huppert H. E., Simpson J. E. (1980) The slumping of gravity currents. *Journal of Fluid Mechanics* 99 (04):785-799
- Huppert H. E. (2006) Gravity currents: a personal perspective. *Journal of Fluid Mechanics* 554:299-322
- Iacono-Marziano G., Gaillard F., Scaillet B., Pichavant M., Chiodini G. (2009) Role of non-mantle CO₂ in the dynamics of volcano degassing: The Mount Vesuvius example. *Geology* 37 (4):319-322
- IGM (1876) M. Vesuvio.
- IGM (1906) Cono Vesuviano dopo l'eruzione dell'aprile 1906.
- INGV-OV (2014) Database Sismologico dei Vulcani della Campania Osservatorio Vesuviano. sismolab.ov.ingv.it/sismo/index.php?click=1. Accessed September 24, 2014
- Isaia R., D'Antonio M., Dell'Erba F., Di Vito M. A., Orsi G. (2004) The Astroni volcano: the only example of closely spaced eruptions in the same vent area during the recent history of the Campi Flegrei caldera (Italy). *Journal of Volcanology and Geothermal Research* 133 (1):171-192
- ISIDe (2010) Italian Seismological Instrumental and Parametric database <http://iside.rm.ingv.it>. Accessed November 6, 2014
- ISTAT (2011) Censimento popolazione 2011 Istituto Nazionale di Statistica. Accessed March 2015
- Iuliano T., Mauriello P., Patella D. (2002) Looking inside Mount Vesuvius by potential fields integrated probability tomographies. *Journal of Volcanology and Geothermal Research* 113 (3):363-378
- Iverson R. M., Denlinger R. P. (2001) Flow of variably fluidized granular masses across three-dimensional terrain: 1. Coulomb mixture theory. *Journal of Geophysical Research: Solid Earth* 106 (B1):537-552
- Kelfoun K. (2011) Suitability of simple rheological laws for the numerical simulation of dense pyroclastic flows and long-runout volcanic avalanches. *Journal of Geophysical Research: Solid Earth* 116 (B8)
- Kim Y. S., Peacock D.C. P., Sanderson D. J. (2004) Fault damage zones. *Journal of structural geology* 26 (3):503-517
- Klawonn M., Houghton B. F., Swanson D. A., Fagents S. A., Wessel P., Wolfe C. J. (2014) From field data to volumes: constraining uncertainties in pyroclastic eruption parameters. *Bulletin of Volcanology* 76 (839). doi:10.1007/s00445-014-0839-1
- Lee D.T., Schachter B.J. (1980) Two algorithms for constructing a Delaunay triangulation. *Internat J Comput Inform Sci* 3:219-241
- Lirer L., Pescatore T., Booth B., Walker G. P. L. (1973) Two plinian pumice-fall deposits from Somma-Vesuvius, Italy. *Geological Society of America Bulletin* 84 (3):759-772
- Locardi E., Nicolich R. (1988) Geodinamica del Tirreno e dell'Appennino centro-meridionale: la nuova carta della Moho. *Mem Soc Geol It* 41:121-140
- Macedonio G., Costa A., Folch A. (2008) Ash fallout scenarios at Vesuvius: numerical simulations and implications for hazard assessment. *Journal of Volcanology and Geothermal Research* 178 (3):366-377
- Macedonio G., Costa A., Scollo S., Neri A. (2016) Effects of eruption source parameter variation and meteorological dataset on tephra fallout hazard assessment: example from Vesuvius (Italy). *Journal of Applied Volcanology* 5 (1):1

- Malin M. C., Sheridan M. F. (1982) Computer-assisted mapping of pyroclastic surges. *Science* 217 (4560):637-640
- Marianelli P., Metrich N., Santacroce R., Sbrana A. (1995) Mafic magma batches at Vesuvius: a glass inclusion approach to the modalities of feeding stratovolcanoes. *Contributions to Mineralogy and Petrology* 120 (2):159-169
- Marinoni L. B. (1996) Geological and structural evolution of Monte Somma and a study of rheomorphic deformation. Ph.D. Thesis, University of Pisa, Pisa
- Marinoni L. B. (2001) Crustal extension from exposed sheet intrusions: review and method proposal. *Journal of volcanology and geothermal research* 107 (1):27-46
- Marti J., Felpeto A. (2010) Methodology for the computation of volcanic susceptibility: an example for mafic and felsic eruptions on Tenerife (Canary Islands). *Journal of Volcanology and Geothermal Research* 195 (1):69-77
- Matthies H. G. (2007) Quantifying uncertainty: modern computational representation of probability and applications. In: *Extreme man-made and natural hazards in dynamics of structures*. Springer, pp 105-135
- Mazzarini F., Rooney T. O., Isola I. (2013) The intimate relationship between strain and magmatism: A numerical treatment of clustered monogenetic fields in the Main Ethiopian Rift. *Tectonics* 32 (1):49-64
- Mele D., Sulpizio R., Dellino P., La Volpe L. (2011) Stratigraphy and eruptive dynamics of a pulsating Plinian eruption of Somma-Vesuvius: the Pomici di Mercato (8900 years BP). *Bulletin of Volcanology* 73 (3):257-278
- Milia A., Raspini A., Torrente M. M. (2007) The dark nature of Somma-Vesuvius volcano: Evidence from the ~ 3.5 ka BP Avellino eruption. *Quaternary International* 173:57-66
- Milia A., Torrente M. M., Bellucci F. (2012) A possible link between faulting, cryptodomes and lateral collapses at Vesuvius Volcano (Italy). *Global and Planetary Change* 90–91 (0):121-134. doi:<http://dx.doi.org/10.1016/j.gloplacha.2011.09.011>
- Mitchell A. (1999) *The ESRI Guide to GIS Analysis: Geographic patterns & relationships*, vol 1. ESRI, Inc.
- Mundula F., D'Oriano C., Cioni R., Bertagnini A., Casu M. (2014) Ash production within a pyroclastic flow: grain-size variations due to mechanical grinding. Paper presented at the Conferenza Rittmann, Nicolosi (CT), Italy, 29-31 October 2014
- Murcia H. F., Sheridan M. F., Macías J. L., Cortés G. P. (2010) TITAN2D simulations of pyroclastic flows at Cerro Machín Volcano, Colombia: Hazard implications. *Journal of South American Earth Sciences* 29 (2):161-170
- Murrow P. J., Rose W. I., Self S. (1980) Determination of the total grain size distribution in a Vulcanian eruption column, and its implications to stratospheric aerosol perturbation. *Geophysical research letters* 7:893-896
- Nazzaro A. (1997) *Il Vesuvio. Storia eruttiva e teorie vulcanologiche*, Geofisica dell'ambiente e del territorio. Liguori editore Napoli
- Neri A., Esposti Ongaro T., Macedonio G., Gidaspow D. (2003) Multiparticle simulation of collapsing volcanic columns and pyroclastic flow. *Journal of Geophysical Research: Solid Earth* (1978–2012) 108 (B4)

- Neri A., Esposti Ongaro T., Menconi G., De'Michieli Vitturi M., Cavazzoni C., Erbacci G., Baxter P. J. (2007) 4D simulation of explosive eruption dynamics at Vesuvius. *Geophysical research letters* 34 (4)
- Neri A., Aspinall W. P., Cioni R., Bertagnini A., Baxter P. J., Zuccaro G., Andronico D., Barsotti S., Cole P. D., Esposti Ongaro T. (2008) Developing an event tree for probabilistic hazard and risk assessment at Vesuvius. *Journal of Volcanology and Geothermal Research* 178 (3):397-415
- Neri A., Bevilacqua A., Esposti Ongaro T., Isaia R., Aspinall W. P., Bisson M., Flandoli F., Baxter P. J., Bertagnini A., Iannuzzi E. (2015) Quantifying volcanic hazard at Campi Flegrei caldera (Italy) with uncertainty assessment: II. Pyroclastic density current invasion maps. *Journal of Geophysical Research: Solid Earth*
- Newhall C. G., Self S. (1982) The volcanic explosivity index/VEI/- An estimate of explosive magnitude for historical volcanism. *Journal of Geophysical Research* 87 (C2):1231-1238
- Oakey G. (1994) A structural fabric defined by topographic lineaments: correlation with Tertiary deformation of Ellesmere and Axel Heiberg islands, Canadian Arctic. *Journal of Geophysical Research: Solid Earth* (1978–2012) 99 (B10):20311-20321
- Palma J. L., Courtland L., Charbonnier S. L., Tortini R., Valentine G. A. (2014) Vhub: a knowledge management system to facilitate online collaborative volcano modeling and research. *Journal of Applied Volcanology* 3 (1):1
- Papale P., Dobran F. (1993) Modeling of the ascent of magma during the plinian eruption of Vesuvius in AD 79. *Journal of volcanology and geothermal research* 58 (1-4):101-132
- Papale P., Longo A. (2008) Vent conditions for expected eruptions at Vesuvius. *Journal of Volcanology and Geothermal Research* 178 (3):359-365
- Patra A. K., Bauer A. C., Nichita C. C., Pitman E. B., Sheridan M. F., Bursik M. I., Rupp B., Webber A., Stinton A. J., Namikawa L. M. (2005) Parallel adaptive numerical simulation of dry avalanches over natural terrain. *Journal of Volcanology and Geothermal Research* 139 (1):1-21
- Phillips J.C., Hogg A. J., Kerswell R. R., Thomas N. H. (2006) Enhanced mobility of granular mixtures of fine and coarse particles. *Earth and Planetary Science Letters* 246 (3):466-480
- Pitman E. B., Nichita C. C., Patra A. K., Bauer A. C., Sheridan M. F., Bursik M. I. (2003) Computing granular avalanches and landslides. *Physics of Fluids* (1994-present) 15 (12):3638-3646
- Pitman E. B., Le L. (2005) A two-fluid model for avalanche and debris flows. *Philosophical Transactions of the Royal Society of London A: Mathematical, Physical and Engineering Sciences* 363 (1832):1573-1601
- Porreca M., Acocella V., Massimi E., Mattei M., Funicello R., De Benedetti A. A. (2006) Geometric and kinematic features of the dike complex at Mt. Somma, Vesuvio (Italy). *Earth and Planetary Science Letters* 245 (1):389-407
- Porter S. C. (1972) Distribution, morphology, and size frequency of cinder cones on Mauna Kea volcano, Hawaii. *Geological Society of America Bulletin* 83 (12):3607-3612
- Pouliquen O., Forterre Y. (2002) Friction law for dense granular flows: application to the motion of a mass down a rough inclined plane. *Journal of fluid mechanics* 453 (1):133-151
- Principe C., Tanguy J. C., Arrighi S., Paiotti A., Le Goff M., Zoppi U. (2004) Chronology of Vesuvius' activity from AD 79 to 1631 based on archeomagnetism of lavas and historical sources. *Bulletin of Volcanology* 66 (8):703-724
- Principe C., Giordano D., Bisson M., Paolillo A., Gianardi R. (2013) Volcanological map of the southwestern sector of Vesuvius between Torre del Greco and Ercolano. SELCA.

- Procter J. N., Cronin S. J., Platz T., Patra A. K., Dalbey K. R., Sheridan M. F., Neall V. (2010) Mapping block-and-ash flow hazards based on Titan 2D simulations: a case study from Mt. Taranaki, NZ. *Natural hazards* 53 (3):483-501
- Pyle D. M. (1989) The thickness, volume and grainsize of tephra fall deposits. *Bulletin of Volcanology* 51 (1):1-15
- Ricciardi G. P. (2009) *Diario del Monte Vesuvio: Venti secoli di immagini e cronache di un vulcano nella città*. Edizioni scientifiche e artistiche Napoli
- Roche O., Phillips J.C., Kelfoun K. (2013) Pyroclastic density currents. In: Fagents SA, Gregg TKP, Lopes RMC (eds) *Modeling Volcanic Processes: The Physics and Mathematics of Volcanism*. Cambridge University Press,
- Rolandi G., Munno R., Postiglione I. (2004) The AD 472 eruption of the Somma volcano. *Journal of Volcanology and Geothermal Research* 129 (4):291-319
- Rolandi G., Paone A., Di Lascio M., Stefani G. (2008) The 79 AD eruption of Somma: The relationship between the date of the eruption and the southeast tephra dispersion. *Journal of Volcanology and Geothermal Research* 169 (1-2):87-98. doi:<http://dx.doi.org/10.1016/j.jvolgeores.2007.08.020>
- Rose W. I., Pearson T., Bonis S. (1976) Nuee ardente eruption from the foot of a dacite lava flow, Santiaguito Volcano, Guatemala. *Bulletin Volcanologique* 40 (1):23-38
- Rosi M., Santacroce R. (1983) The AD 472 “Pollena” eruption: volcanological and petrological data for this poorly-known, Plinian-type event at Vesuvius. *Journal of Volcanology and Geothermal Research* 17 (1):249-271
- Rosi M., Principe C., Vecchi R. (1993) The 1631 Vesuvius eruption. A reconstruction based on historical and stratigraphical data. *Journal of Volcanology and Geothermal Research* 58 (1):151-182
- Rossano S., Mastrolorenzo G., De Natale G. (1998) Computer simulations of pyroclastic flows on Somma–Vesuvius volcano. *Journal of volcanology and geothermal research* 82 (1):113-137
- Rovida A., Camassi R., Gasperini P., Stucchi M. (2011) CPTI11, la versione 2011 del Catalogo Parametrico dei Terremoti Italiani INGV. <http://emidius.mi.ingv.it/CPTI>. Accessed June 24, 2014
- Santacroce R. (1987) *Somma-Vesuvius, vol 8, Progetto Finalizzato Geodinamica, Monografie Finali*. CNR, Quaderni de la Ricerca Scientifica
- Santacroce R., Sbrana A. (2003) *Geological map of Vesuvius*. SELCA Firenze.
- Santacroce R., Cioni R., Marianelli P., Sbrana A., Sulpizio R., Zanchetta G., Donahue D. J., Joron J. L. (2008) Age and whole rock–glass compositions of proximal pyroclastics from the major explosive eruptions of Somma-Vesuvius: a review as a tool for distal tephrostratigraphy. *Journal of Volcanology and Geothermal Research* 177 (1):1-18
- Savage S. B., Hutter K. (1989) The motion of a finite mass of granular material down a rough incline. *Journal of fluid mechanics* 199:177-215
- Scandone R., Giacomelli L., Gasparini P. (1993) Mount Vesuvius: 2000 years of volcanological observations. *Journal of volcanology and geothermal research* 58 (1):5-25
- Scandone R., Giacomelli L., Speranza F. F. (2008) Persistent activity and violent strombolian eruptions at Vesuvius between 1631 and 1944. *Journal of Volcanology and Geothermal Research* 170 (3-4):167-180

- Scarpa R., Tronca F., Bianco F., Del Pezzo E. (2002) High resolution velocity structure beneath Mount Vesuvius from seismic array data. *Geophysical research letters* 29 (21):36-31-36-34
- Scholz C. H. (2002) *The mechanics of earthquakes and faulting*. Cambridge university press
- Secundus G. P. C., Gigante M., Tacitus C. (1980) *Le lettere di Plinio il Giovane sull'eruzione vesuviana dell'anno 79: testo e traduzione*. Associazione napoletana per i monumenti e il paesaggio
- Selva J., Costa A., Marzocchi W., Sandri L. (2010) BET_VH: exploring the influence of natural uncertainties on long-term hazard from tephra fallout at Campi Flegrei (Italy). *Bulletin of volcanology* 72 (6):717-733
- Selva J., Orsi G., Di Vito M. A., Marzocchi W., Sandri L. (2012) Probability hazard map for future vent opening at the Campi Flegrei caldera, Italy. *Bulletin of volcanology* 74 (2):497-510
- Selva J., Costa A., Sandri L., Macedonio G., Marzocchi W. (2014) Probabilistic short-term volcanic hazard in phases of unrest: A case study for tephra fallout. *Journal of Geophysical Research: Solid Earth* 119 (12):8805-8826
- Sheridan M. F. (1980) Pyroclastic block flow from the September, 1976, eruption of La Soufrière volcano, Guadeloupe. *Bulletin Volcanologique* 43 (2):397-402
- Sheridan M. F., Malin M. C. (1983) Application of computer-assisted mapping to volcanic hazard evaluation of surge eruptions: Vulcano, Lipari, and Vesuvius. *Journal of Volcanology and Geothermal Research* 17 (1-4):187-202
- Sigurdsson H., Carey S. N., Cornell W., Pescatore T. (1985) The eruption of Vesuvius in AD 79. *National Geographic Research* 1 (3):332-387
- Silverman B. W. (1986) *Density estimation for statistics and data analysis*, vol 26. CRC press
- Sparks R. S. J. (1976) Grain size variations in ignimbrites and implications for the transport of pyroclastic flows. *Sedimentology* 23 (2):147-188
- Sparks R. S. J., Wilson L., Sigurdsson H. (1981) The pyroclastic deposits of the 1875 eruption of Askja, Iceland. *Philosophical Transactions of the Royal Society of London* 229:241-273
- Sparks R. S. J., Aspinall W. P. (2004) Volcanic activity: frontiers and challenges in forecasting, prediction and risk assessment. *The State of the Planet: Frontiers and Challenges in Geophysics*:359-373
- Stefanescu E. R., Bursik M. I., Patra A. K. (2012) Effect of digital elevation model on Mohr-Coulomb geophysical flow model output. *Natural hazards* 62 (2):635-656
- Sulpizio R., Mele D., Dellino P., La Volpe L. (2005) A complex, Subplinian-type eruption from low-viscosity, phonolitic to tephri-phonolitic magma: the AD 472 (Pollena) eruption of Somma-Vesuvius, Italy. *Bulletin of volcanology* 67 (8):743-767
- Sulpizio R., Mele D., Dellino P., La Volpe L. (2007) Deposits and physical properties of pyroclastic density currents during complex Subplinian eruptions: the AD 472 (Pollena) eruption of Somma-Vesuvius, Italy. *Sedimentology* 54:607–635. doi:doi: 10.1111/j.1365-3091.2006.00852.x
- Sulpizio R., Cioni R., Di Vito M. A., Santacroce R., Sbrana A., Zanchetta G. (2008) Comment on:“The dark nature of Somma-Vesuvius volcano: Evidence from the~ 3.5 kaBP Avellino eruption” by Milia A., Raspini A., Torrente MM. *Quaternary International* 192 (1):102-109
- Sulpizio R., Dellino P., Doronzo D. M., Sarocchi D. (2014) Pyroclastic density currents: state of the art and perspectives. *Journal of Volcanology and Geothermal Research* 283:36-65

- Tarquini S., Isola I., Favalli M., Mazzarini F., Bisson M., Pareschi M. T., Boschi E (2007) TINITALY/01: a new triangular irregular network of Italy. *Annals of Geophysics* 50 (3)
- Tierz P., Sandri L., Costa A., Zaccarelli L., Di Vito M. A., Sulpizio R., Marzocchi W. (2016) Suitability of energy cone for probabilistic volcanic hazard assessment: validation tests at Somma-Vesuvius and Campi Flegrei (Italy). *Bulletin of Volcanology* 78 (11):79
- Todesco M., Neri A., Esposti Ongaro T., Papale P., Macedonio G., Santacroce R., Longo A. (2002) Pyroclastic flow hazard assessment at Vesuvius (Italy) by using numerical modeling. I. Large-scale dynamics. *Bulletin of volcanology* 64 (3-4):155-177
- Valentine G. A. (1987) Stratified flow in pyroclastic surges. *Bulletin of Volcanology* 49 (4):616-630
- Ventura G., Vilardo G. (1999a) Slip tendency analysis of the Vesuvius faults: implications for the seismotectonic and volcanic hazard assessment. *Geophysical research letters* 26 (21):3229-3232
- Ventura G., Vilardo G. (1999b) Seismic-based estimate of hydraulic parameters at Vesuvius Volcano. *Geophysical research letters* 26 (7):887-890
- Ventura G., Vilardo G., Bronzino G., Gabriele G., Nappi R., Terranova C. (2005) Geomorphological map of the Somma-Vesuvius volcanic complex (Italy). *Journal of Maps* 1 (1):30-37
- Vilardo G., De Natale G., Milano G., Coppa U. (1996) The seismicity of Mt. Vesuvius. *Tectonophysics* 261 (1):127-138
- Vilardo G., Bronzino G., Terranova C. (2009) Sistema Informativo Sismotettonico della Regione Campania (SISCam 2.0) Laboratorio di Geomatica e Cartografia, Istituto Nazionale di Geofisica e Vulcanologia, Osservatorio Vesuviano. <http://ipf.ov.ingv.it/siscam.html>.
- Vogel S., Märker M. (2010) Reconstructing the Roman topography and environmental features of the Sarno River Plain (Italy) before the AD 79 eruption of Somma–Vesuvius. *Geomorphology* 115 (1):67-77
- Von Karman T. (1940) The engineer grapples with nonlinear problems. *Bulletin of the American Mathematical Society* 46 (8):615-683
- Walker G. P. L. (1980) The Taupo Pumice: product of the most powerful known (Ultraplinian) eruption? *Journal of Volcanology and Geothermal Research* 8:69-94
- Weller J. N., Martin A. J., Connor C. B., Connor L. J., Karakhanian A. (2006) Modelling the spatial distribution of volcanoes: an example from Armenia. *Statistics in Volcanology, Special Publications of IAVCEI* 1:77-88
- White J. D. L., Houghton B. F. (2006) Primary volcaniclastic rocks. *Geology* 34 (8):677-680
- Wilson C. J. N., Houghton B. F. (2000) Pyroclastic transport and deposition. In: *Encyclopedia of Volcanoes* (first edition), vol 545. p 554
- Wolff R. G. (1982) *Physical Properties of Rocks: Porosity, Permeability, Distribution Coefficients, and Dispersivity*. U.S. Geological Survey
- Woo G. (1999) *The mathematics of natural catastrophes*. Imperial College press London
- Woods A. W., Bursik M. I. (1991) Particle fallout, thermal disequilibrium and volcanic plumes. *Bulletin of Volcanology* 53 (7):559-570
- Yamamoto T., Takarada S., Suto S. (1993) Pyroclastic flows from the 1991 eruption of Unzen volcano, Japan. *Bulletin of Volcanology* 55 (3):166-175
- Zollo A., D'Auria L., De Matteis R., Herrero A., Virieux J., Gasparini P. (2002) Bayesian estimation of 2-D P-velocity models from active seismic arrival time data: imaging of the shallow structure of Mt Vesuvius (Southern Italy). *Geophysical Journal International* 151 (2):566-582

- Zuccaro G., Cacace F., Spence R. J. S., Baxter P. J. (2008) Impact of explosive eruption scenarios at Vesuvius. *Journal of Volcanology and Geothermal Research* 178 (3):416-453
- Zuccaro G., De Gregorio D. (2013) Time and space dependency in impact damage evaluation of a sub-Plinian eruption at Mount Vesuvius. *Natural Hazards* 68 (3):1399-1423. doi:10.1007/s11069-013-0571-8